

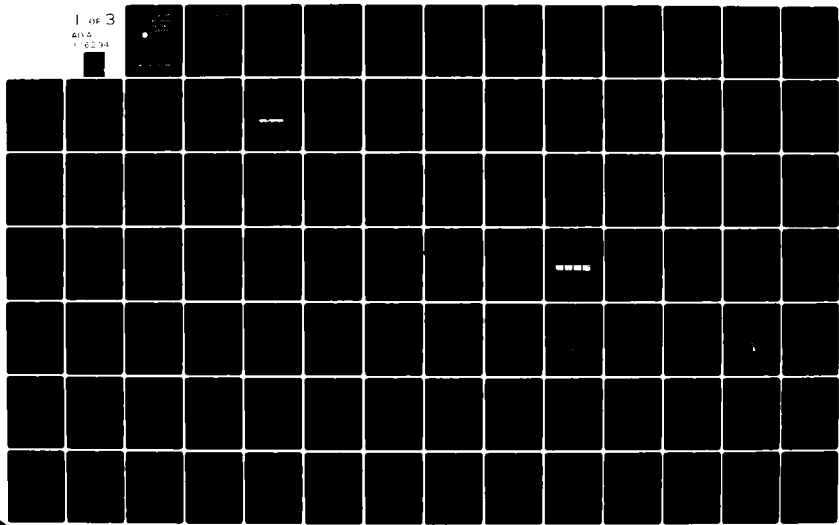
AD-A116 294 NATIONAL AERONAUTICS AND SPACE ADMINISTRATION HAMPTON-ETC F/6 20/5  
ELEVENTH INTERNATIONAL LASER RADAR CONFERENCE, WISCONSIN UNIVER-ETC(U)

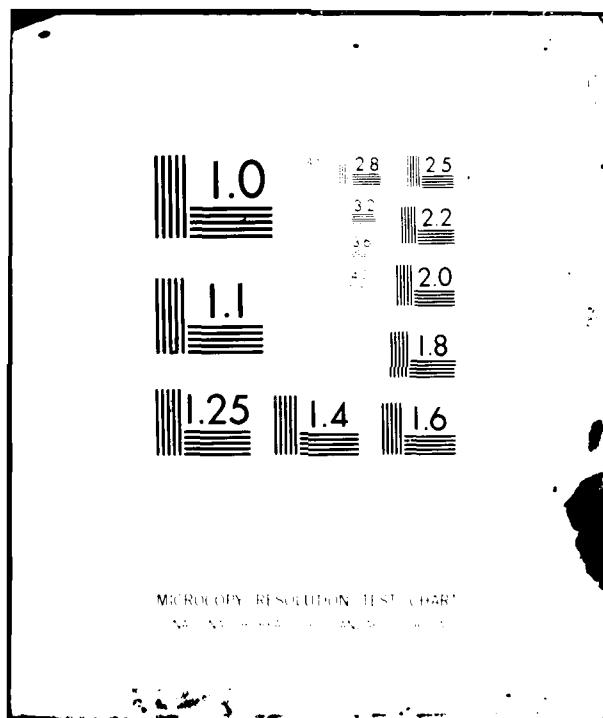
UNCLASSIFIED NASA-L-15380

NASA-CP-2228

NL

1 of 3  
4144  
1-62-94





AD A11 6294

NASA Conference Publication 2228

3

# Eleventh International Laser Radar Conference



Abstracts of papers presented at  
the University of Wisconsin-Madison  
June 21-25, 1982

DTIC  
ELECTED  
JUN 30 1982  
S A D

This document has been approved  
for public release and sale; its  
distribution is unlimited.

FILE COPY

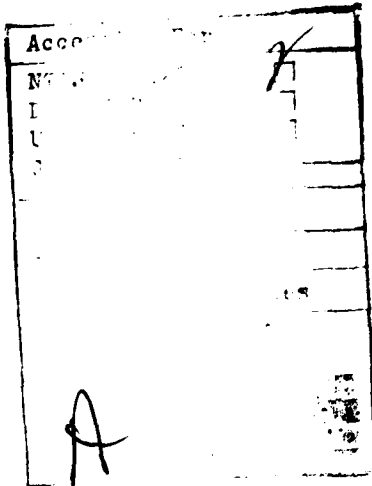
AMS USAF SSEC NASA

82 06 30 031

NASA Conference Publication 2228

# Eleventh International Laser Radar Conference

Abstracts of papers presented at  
the conference held at the University  
of Wisconsin-Madison, June 21-25, 1982,  
and sponsored by the Space Science and  
Engineering Center of the University of  
Wisconsin, the American Meteorological  
Society, the U.S. Air Force Office of  
Scientific Research, NASA Langley  
Research Center, and the U.S. Air Force  
Geophysical Laboratory



National Aeronautics  
and Space Administration

Scientific and Technical  
Information Branch

1982

ELEVENTH INTERNATIONAL LASER  
RADAR CONFERENCE

Sponsored by

Space Science and Engineering Center  
University of Wisconsin

American Meteorological Society (AMS)

U.S. Air Force Office of Scientific Research

U.S. Air Force Geophysical Laboratory

NASA Langley Research Center

Under the auspices of

Committee on Laser Atmospheric Studies  
American Meteorological Society

Radiation Commission  
International Association of Meteorology and Atmospheric Physics (IAMAP)

International Union for Radio Science (URSI)

In cooperation with

Optical Society of America

Geoscience and Remote Sensing Society  
Institute of Electrical and Electronics Engineers, Inc.

## PREFACE

This publication contains abstracts of papers presented at the Eleventh International Laser Radar Conference, held at the University of Wisconsin-Madison, June 21-25, 1982. Eighty-nine papers were presented during ten sessions. These conferences have historically provided lidar researchers from throughout the world with a forum to present their latest achievements and to discuss problems of mutual concern. The conferences have been technique oriented, but always directed toward applications important to the atmospheric sciences.

This eleventh conference manifests a maturing technology. The abstracts discuss laser radar measurements of properties from the Earth's ocean surface to the mesosphere, made with techniques ranging from elastic and inelastic scattering to Doppler shifts and differential absorption.

The conference was sponsored by the Space Science and Engineering Center (SSEC) of the University of Wisconsin, by the American Meteorological Society (AMS), by the Office of Scientific Research and the Geophysical Laboratory of the United States Air Force, and by the Langley Research Center of the National Aeronautics and Space Administration. It was organized under the able leadership of James Weinman of the SSEC, with the assistance of Evelyn Mazur of the AMS during the early planning stages. The Program Committee and Professor Weinman, who chaired the committee, are to be commended for the excellent selection of scientific papers.

This volume was prepared for publication through the efforts of the staff of the Research Information and Applications Division, NASA Langley Research Center, and the staff of the SSEC. In addition, the SSEC staff, in particular Susan Spellman, Joanne Edwards, Robert Fox, and John Roberts, are to be thanked for attending to the diverse tasks required for the success of this conference. The efforts of Ted Barber of the White Sands Missile Range in arranging for session chairpersons are appreciated. Finally, special recognition is made to Don Bedo (USAF Geophysical Laboratory), Herman Gerber (U.S. Naval Research Laboratory) and Chalmers Sechrist (University of Illinois) in arranging for agency sponsorships, and to Horace Furumoto (Candella Corporation) for social sponsorship.

The use of trade names or manufacturers' names in this publication does not constitute endorsement, either expressed or implied, by the National Aeronautics and Space Administration.

M. Patrick McCormick  
Chairman, Committee on Laser Atmospheric Studies  
American Meteorological Society

AMS COMMITTEE ON LASER ATMOSPHERIC STUDIES

M. Patrick McCormick, Chairman  
Aerosol Measurements Res. Branch, M.S. 475  
NASA Langley Research Center  
Hampton, VA 23665

A. I. Carswell  
Dept. of Physics and CRESS  
York University  
4700 Keele St.  
Toronto, Canada M3J 1P3

Giorgio Fiocco  
Istituto di Fisica  
Universita di Roma  
P. delle Scienze  
Roma 00100 Italy

Freeman F. Hall  
WPL/NOAA  
325 Broadway  
Boulder, CO 80303

Takao Kobayasi  
Dept. of Electrical Engineering  
Fukui University  
3-9-1 Bunkyo  
Fukui 910, Japan

Gerard Megie  
CNRS Service d'Aeronomie  
B.P. No. 3  
91370 Verrières-le-Buisson, France

Philip Russell  
Atmospheric Sciences Laboratory  
SRI International  
333 Ravenswood Avenue  
Menlo Park, CA 94025

Kenneth Sassen  
University of Utah  
Salt Lake City, UT 84112

Chalmers Sechrist  
Aeronomy Laboratory  
Dept. of Electrical Engineering  
University of Illinois  
Urbana, IL 61801

Michael Vaughan  
Royal Signals and Radar Establishment  
Gt. Malvern  
Worcestershire, United Kingdom

T. D. Wilkerson  
Institute for Physical Science and Technology  
University of Maryland  
College Park, MD 20742

PROGRAM COMMITTEE

J. A. Weinman, Program Chairman  
Dept. of Meteorology  
Space Science & Eng. Center  
University of Wisconsin-Madison  
Madison, WI 53706

\*H. E. Gerber  
U.S. Naval Research Laboratory  
Washington, DC 20375

M. R. Huffaker  
Wave Propagation Laboratory  
NOAA/ERL  
Boulder, CO 80302

Takashi Igarashi  
Radio Research Laboratories  
Ministry of Posts & Telecommunications  
Koganei, Tokyo, Japan

H. Inaba  
Research Institute of Electrical Communication  
Tohoku University  
Sendai, Japan

\*J. H. Joseph  
Dept. of Planetary & Environmental Science  
Tel Aviv University  
Tel Aviv, Israel

Gerard Megie  
CNRS Service d'Aeronomie  
B.P. No. 3  
91370 Verrières-le-Buisson, France

C. M. R. Platt  
CSIRO  
Division of Atmospheric Physics  
Aspendale, Victoria, Australia

Philip Russell  
Atmospheric Sciences Laboratory  
SRI International  
333 Ravenswood Avenue  
Menlo Park, CA 94025

Chalmers Sechrist  
Aeronomy Laboratory  
Dept. of Electrical Engineering  
University of Illinois  
Urbana, IL 61801

T. D. Wilkerson  
Institute for Physical Science and Technology  
University of Maryland  
College Park, MD 20742

Zhao Yan Zeng  
Institute of Atmospheric Physics  
Academia Sinica  
Beijing, Peoples Republic of China

\*Members of Radiation Commission, IAMAP

TABLE OF CONTENTS AND PROGRAM

PREFACE . . . . .	iii
AMS COMMITTEE ON LASER ATMOSPHERIC STUDIES . . . . .	iv
PROGRAM COMMITTEE . . . . .	iv

Sunday, June 20, 1982	
4:00 p.m. - 8:00 p.m.	Registration at Wisconsin Center
Monday, June 21, 1982	
8:00 a.m. - 3:00 p.m.	Registration at Wisconsin Center
8:30 a.m. - 9:00 a.m.	WELCOME AND OPENING REMARKS
9:00 a.m. - 12:00 noon	SESSION A
	Chairman: G. Megie
	Cochairman: G. W. Grams

MIDDLE ATMOSPHERIC MEASUREMENTS

A1. LIDAR MEASUREMENTS OF THE STRATOSPHERIC AEROSOL: 1974-1982 . . . . .	1
T. J. Swissler and M. Osborn	
A2. MYSTERY CLOUDS IN THE STRATOSPHERE? . . . . .	2
M. P. McCormick	
A3. LIDAR OBSERVATIONS OF THE STRATOSPHERIC AEROSOL OVER CENTRAL EUROPE SINCE JANUARY 1981 . . . . .	4
R. Reiter, H. Jäger, W. Carnuth, and W. Funk	
A4. COMPARISON OF LOW-LATITUDE LIDAR AND SAGE SATELLITE MEASUREMENTS . . . . .	8
G. S. Kent, M. P. McCormick, and M. T. Philip	
A5. LIDAR AND BALLOON-BORNE PARTICLE COUNTER COMPARISONS FOLLOWING THE ERUPTIONS OF MT. ST. HELENS AND ALAID . . . . .	13
D. J. Hofmann, J. M. Rosen, R. Reiter, and H. Jäger	
A6. ATMOSPHERIC DEPOLARIZATION RATIO DECAY AFTER THE ERUPTION OF MOUNT ST. HELENS . . . . .	14
Joseph H. Goad, Jr.	
A7. STEERABLE LIDAR STUDIES OF MESOSPHERIC SODIUM LAYER STRUCTURE . . . . .	17
C. S. Gardner, C. F. Sechrist, Jr., and J. L. Bufton	

Monday, June 21, 1982  
1:00 p.m. - 4:00 p.m.

SESSION B

Chairman: G. Fiocco  
Cochairman: P. B. Russell

METEOROLOGICAL PARAMETERS: TEMPERATURE, DENSITY, HUMIDITY

B1. BALLOONBORNE LIDAR FOR DENSITY MEASUREMENTS . . . . .	21
D. E. Bedo, K. S. W. Champion, and R. A. Swirbalus	
B2. TEMPERATURE MEASUREMENTS IN THE TROPOSPHERE AND LOWER STRATOSPHERE USING A DUAL WAVELENGTH LIDAR . . . . .	23
J. Lefrere and G. Megie	
B3. ADVANCED NEAR IR LIDAR FOR METEOROLOGICAL REMOTE SENSING . . . . .	26
Geary Schwemmer, Mark Dombrowski, and C. Laurence Korb	
B4. REMOTE LASER MEASUREMENT OF TEMPERATURE AND HUMIDITY USING DIFFERENTIAL ABSORPTION IN ATMOSPHERIC WATER VAPOR . . . . .	30
P. Lebow, S. Strobel, T. Wilkerson, L. Cotnoir, and A. Rosenberg	
B5. WATER VAPOR MEASUREMENTS BY USING A FAST-TUNING DIAL SYSTEM . . . . .	33
Zhao Yan-zeng, Wu Shao-ming, Jin Hui-shu, Zhang Chun-lin, Hu Yu-liang, Huang Qi-rong, Huang Zhong-fang, and Zheng Si-ping	
B6. REMOTE MEASUREMENTS OF TROPOSPHERIC WATER VAPOR WITH AN AIRBORNE DIAL SYSTEM . . . . .	34
A. F. Carter, E. V. Browell, C. F. Butler, M. N. Mayo, W. M. Hall, T. D. Wilkerson, and J. H. Siviter, Jr.	
B7. SIMULTANEOUS MEASUREMENTS OF WATER VAPOR MIXING RATIO AND AEROSOL CONTENT USING A DIAL TECHNIQUE AT $0.72 \mu\text{m}$ : COMPARISON WITH RADIOSOUNDINGS AND LIDAR MEASUREMENTS AT $1.06 \mu\text{m}$ . . . . .	37
C. Cahen, J-L. Lesne, J-M. Michelin, and J. Lefrere	
B8. BOUNDARY-LAYER SOUNDING OF HUMIDITY AND AEROSOLS USING RAMAN LIDAR . . . . .	41
D. Renaut, C. Brun, and R. Capitini	
B9. RAMAN WATER-VAPOR LIDAR . . . . .	45
M. Z. Hansen, S. H. Melfi, J. D. Spinhirne, and D. Clem	

Monday, June 21, 1982  
6:30 p.m. - 8:30 p.m.

RECEPTION in rotunda of Wisconsin  
State Capitol, light refreshments

Tuesday, June 22, 1982  
8:30 a. m. - 12:00 noon

SESSION C

Chairman: H. Inaba  
Cochairman: T. Wilkerson

TRACE GASES BY RAMAN AND DIAL TECHNIQUES

C1. TWO YEARS OF EVALUATION AND TESTING OF A MOBILE LIDAR SYSTEM FOR AIR POLLUTION MONITORING . . . . .	47
K. Fredriksson and H. Hertz	
C2. EXPERIMENTAL STUDY OF REMOTE ATMOSPHERIC POLLUTION MONITOR BASED ON DIFFERENTIAL ABSORPTION OF CO <sub>2</sub> LASER RADIATION . . . . .	55
P. Vujkovic Cvijin	
C3. ATMOSPHERIC GAS MONITOR WITH LEAD-SALT DIODE LASER . . . . .	56
Hiroya Sano, Ryuji Koga, Megumi Kosaka, and Koji Shinohara	
C4. AIRBORNE LIDAR MEASUREMENTS OF OZONE AND AEROSOL PROFILES IN THE TROPOSPHERE AND LOWER STRATOSPHERE . . . . .	60
E. V. Browell, S. T. Shipley, A. F. Carter, and C. F. Butler	
C5. SIMULTANEOUS HETERODYNE AND DIRECT DETECTION CO <sub>2</sub> DIAL MEASUREMENTS . . . . .	64
Dennis K. Killinger, Norman Menyuk, and William E. DeFeo	
C6. EXTENSION OF DIAL MEASUREMENTS WITH Nd:YAG-BASED LIDAR SYSTEMS TO SHORT UV AND NEAR IR WAVELENGTHS . . . . .	67
M. Alden, H. Edner, and S. Svanberg	
C7. DAY-TIME DETECTION OF GASEOUS POLLUTANTS BY RAMAN-LIDAR: MEASUREMENTS AND SIMULATIONS . . . . .	70
R. Capitini, E. Joos, and D. Renaut	
C8. DIFFERENTIAL ABSORPTION LIDAR ERRORS CAUSED BY MISALIGNMENT IN COAXIAL SYSTEMS . . . . .	75
William S. Heaps	
C9. THE THEORY AND CORRECTION OF FINITE LASER BANDWIDTH EFFECTS IN DIAL EXPERIMENTS . . . . .	78
C. Laurence Korb and Chi Y. Weng	
C10. CO <sub>2</sub> DIAL SENSITIVITY STUDIES WITH HETERODYNE AND DIRECT DETECTION . . . . .	82
P. Brockman, C. H. Bair, and R. V. Hess	
C11. LIMITATIONS OF SIGNAL AVERAGING OF DIAL MEASUREMENTS DUE TO TEMPORAL CORRELATION . . . . .	87
N. Menyuk, D. K. Killinger, and C. R. Menyuk	

Tuesday, June 22, 1982  
1:00 p.m. - 4:00 p.m.

SESSION D

Chairman: J. D. Lawrence  
Cochairman: T. Kobayasi

TECHNIQUES AND TECHNOLOGY

D1. STATISTICAL PROPERTIES OF CO <sub>2</sub> LIDAR RETURNS FROM TOPOGRAPHIC TARGETS . . . . .	91
P. H. Flamant, R. T. Menzies, and M. J. Kavaya	
D2. MEASUREMENT ERROR IN AIRBORNE CO <sub>2</sub> LASER HETERODYNE SENSOR FOR MONITORING REGIONAL OZONE DISTRIBUTIONS . . . . .	95
Kazuhiro Asai, Toshikazu Itabe, and Takashi Igarashi	
D3. A HIGH PRESSURE LASER FOR LIDAR MEASUREMENTS OF POLLUTANTS IN THE ATMOSPHERE . . . . .	99
John C. Petheram and J. W. van Dijk	
D4. INFRARED DOPPLER LIDAR ANTENNA DESIGN CONSIDERATIONS AND PERFORMANCE CHARACTERISTICS OF THE NOAA GROUND BASED DOPPLER LIDAR . . . . .	103
T. R. Lawrence	
D5. COLOR DISPLAY AND PROCESSING OF DOPPLER LIDAR DATA . . . . .	104
R. Jeffrey Keeler, R. Michael Hardesty, and David K. Churchill	
D6. RM CW LIDAR . . . . .	108
Nobuo Takeuchi, Katsumi Sakurai, Nobuo Sugimoto, Hiroshi Baba, and Masamichi Kondo	
D7. MINIATURE SURFACE CORONA UV PREIONIZATION STABILIZED MULTIKILOHERTZ TEA LASERS . . . . .	111
V. Hasson	
D8. CALIBRATION AND DATA ANALYSIS PROCEDURES FOR THE HIGH SPECTRAL RESOLUTION LIDAR . . . . .	113
J. T. Sroga, E. W. Eloranta, and F. L. Roesler	
D9. ATOMIC AND MOLECULAR BLOCKING FILTERS FOR HIGH-RESOLUTION LIDAR: A PROPOSED METHOD FOR MEASURING ATMOSPHERIC VISIBILITY, TEMPERATURE AND PRESSURE . . . . .	117
H. Shimizu and C. Y. She	
D10. FIELD EVALUATION OF A LASER CLOUD MAPPER . . . . .	120
R. E. Kluchert, B. T. N. Evans, and D. Houston	
D11. DESIGN OF A DIAGNOSTIC TO MEASURE TURBULENT DENSITY FLUCTUATIONS IN ATMOSPHERE . . . . .	122
J. S. Goela	

D12. AIRBORNE LIDAR DUAL WEDGE SCANNER	123
C. DiMarzio, R. Chandler, M. Krause, J. O'Reilly, K. Shaw, and J. Bilbro	
D13. EFFECT OF SEA SURFACE STRUCTURE ON OCEANOGRAPHIC FLUORESCENCE LIDAR SIGNALS	127
U. Gehlhaar	
D14. EVALUATION OF FOUR LASER WAVELENGTHS FOR LIDAR FLUOROSENSING OF OIL SPILLS	129
P. Burlamacchi, G. Cecchi, P. Mazzinghi, L. Pantani, and I. Pippi	
D15. ATMOSPHERIC DERIVATIVE MONITORING: THE EFFECT OF MOLECULAR INTERFERENCE	132
S. E. Taylor and E. L. Thomas	

Wednesday, June 23, 1982

8:30 a.m. - 10:15 a.m.

SESSION E

Chairman: E. Eloranta  
Cochairman: R. Reiter

PLUME DISPERSION

E1. OBTAINING HIGH-QUALITY IMAGE DATA WITH THE LAMP LIDAR	137
Hideaki Nakane, Yasuhiro Sasano, Nobuo Sugimoto, Ichiro Matsui, Hiroshi Simizu, and Nobuo Takeuchi	
E2. AIRBORNE LIDAR MEASUREMENTS DURING THE SOUTH COAST AIR BASIN/SOUTHEAST DESERT OXIDANT TRANSPORT STUDY	141
James L. McElroy	
E3. LIDAR IN ATMOSPHERIC DISPERSION STUDIES: SOME QUANTITATIVE ASPECTS	143
Mervyn J. Lynch, Wynn L. Eberhard, and G. T. McNice	
E4. PLUME DISPERSION TRACKED BY UV LIDAR	145
Wynn L. Eberhard and G. T. McNice	
E5. SUMMARIZED RESULTS OF SHIPBORNE LIDAR MEASUREMENTS CARRIED OUT DURING THREE YEARS OF PLUME DISPERSION OVER SEA SURFACES	149
H. Herrmann, F. Köpp, and Ch. Werner	
E6. CLOUD MAPPING OF SCREENING AEROSOLS	152
B. T. N. Evans	

Wednesday, June 23, 1982  
10:30 a.m. - 12:00 noon

SESSION F

Chairman: A. I. Carswell  
Cochairman: Ch. Werner

BOUNDARY LAYER DYNAMICS

F1. REFRACTIVE TURBULENCE PROFILES BY HIGH-RESOLUTION LIDAR . . . . .	154
Ronald L. Schwiesow and Robert S. Lawrence	
F2. LIDAR MEASUREMENTS OF THE ENTRAINMENT ZONE AND THE TURBULENT KINETIC ENERGY BUDGET OF THE ATMOSPHERIC MIXED LAYER . . . . .	156
R. Boers, E. W. Eloranta, W. P. Hooper, and R. L. Coulter	
F3. CELL STRUCTURES IN THE ATMOSPHERIC MIXED LAYER OBSERVED BY A MIE LASER RADAR . . . . .	157
Yasuhiro Sasano, Hiroshi Shimizu, and Nobuo Takeuchi	
F4. MONITORING ALPINE VALLEY WIND CIRCULATION BY AIRBORNE LIDAR . . . . .	160
W. Renger, P. Mörl, and R. Schellhase	
F5. AIRBORNE LIDAR MEASUREMENTS OF MIXED LAYER DYNAMICS . . . . .	161
S. T. Shipley and E. V. Browell	
F6. THE ESTIMATION OF DIFFUSION PARAMETERS FROM LIDAR MEASUREMENTS . . . . .	165
E. Asculai, A. Cohen, and M. Kleiman	

Wednesday, June 23, 1982  
1:00 p.m. - 4:00 p.m.

SESSION G

Chairman: M. Vaughan  
Cochairman: R. M. Schotland

WIND MEASUREMENTS

G1. WIND MEASUREMENTS OF RADIAL AND TRANSVERSE COMPONENTS - VISIBLE VERSUS INFRARED . . . . .	166
L. Lading, R. L. Schwiesow, and A. Skov Jensen	
G2. LIDAR OBSERVATIONS OF THE DAILY VARIATION OF BOUNDARY LAYER WINDS AND TURBULENCE . . . . .	169
W. P. Hooper, E. W. Eloranta, R. Boers, and R. L. Coulter	
G3. WIND COMPARISON MEASUREMENTS BETWEEN A PULSED DOPPLER LIDAR AND OTHER WIND SENSORS . . . . .	171
R. Milton Huffaker and F. F. Hall, Jr.	
G4. MEASUREMENT OF WINDS, BACKSCATTER, AND RETURN SIGNAL PROPERTIES USING PULSED COHERENT LIDAR . . . . .	172
R. M. Hardesty	

G5. A DIRECT LASER DOPPLER ANEMOMETER FOR REMOTE WIND SENSING . . . . .	176
F. Köpp	
G6. MEASUREMENT OF WIND USING AN AIRBORNE DOPPLER LIDAR SYSTEM (ADLS) - RESULTS OF 1981 CV-990 FLIGHT EXPERIMENTS . . . . .	179
George H. Fichtl, James W. Bilbro, Daniel Fitzjarrald, and Michael Krause	
G7. WINDSAT/ATMOSPHERIC MULTI-USER LIDAR COMPATIBILITY . . . . .	183
John S. Osmundson, R. Milton Huffaker, and Michael McQuirk	
G8. CONICAL LIDAR SCANNING FROM LEO - THE EFFECTS OF MESO $\beta$ AND CONVECTIVE SCALE ATMOSPHERIC PHENOMENA . . . . .	187
G. D. Emmitt	

Wednesday, June 23, 1982

CONFERENCE BANQUET in Great Hall in the  
    Memorial Union (1/2 block from Wisconsin  
    Center)  
    Cocktails  
    Dinner, program to follow

Thursday, June 24, 1982

8:30 a.m. - 12:00 noon

SESSION H  
    Chairman: R. W. Fenn  
    Cochairman: G. Kent

VISIBILITY AND AEROSOL PROPERTIES

H1. PARTICULATE EXTINCTION AND BACKSCATTER PROPERTIES DETERMINED FROM LIDAR MEASUREMENTS . . . . .	191
J. A. Reagan, C. L. Goldsmith, A. J. Anderson, and J. P. Garcia	
H2. ELEVATION-SCANNING LIDAR MEASUREMENTS OF HAZE EXTINCTION AND THEIR RELATIONSHIP TO ALBEDO CHANGES . . . . .	192
Philip B. Russell and John M. Livingston	
H3. REMOTE SENSING OF ATMOSPHERIC PARTICULATE PROPERTIES BY JOINT LIDAR-RADIOMETER OBSERVATIONS . . . . .	196
Qiu Jin-huan, Wang Hong-qi, Sun Jin-hui, Zhang Bei-ying, Xia Qi-lin, Hao Nan-jun, Zhang Jin-ding, Bao Ling-ming, and Zhao Yan-zeng	
H4. LIDAR VISIBILITY MEASUREMENTS . . . . .	197
J. L. Gaumet	
H5. LIDAR MEASUREMENTS OF VERY DENSE FOGS . . . . .	201
L. Stefanutti, F. Castagnoli, and M. Morandi	
H6. EYE-SAFE LASER SLANT VISUAL RANGE MEASURING DEVICE . . . . .	205
Ch. Werner	

H7. AEROSOL SCATTERING AND EXTINCTION MEASUREMENTS WITH LIDAR AT 0,35 $\mu\text{m}$ and 10 $\mu\text{m}$ . . . . .	208
Arne Hågård and Ove Steinvall	
H8. QUANTITATIVE LIDAR MEASUREMENT OF EXTINCTION COEFFICIENT . . . . .	210
Edward Measure and Roberto Rubio	
H9. QUANTITATIVE EXTINCTION MEASUREMENTS WITH THE VISIOCEILOMETER . . . . .	211
W. J. Lentz	
H10. COMMENTS ON THE ANALYSIS OF ATMOSPHERIC LIDAR OBSERVATIONS . . . . .	213
Frederick G. Fernald	
H11. INVESTIGATION OF AEROSOL CHARACTERISTICS USING BISTATIC LIDAR . . . . .	216
B. V. Krishna Murthy and K. Parameswaran	

Thursday, June 24, 1982  
1:00 p.m. - 2:30 p.m.

SESSION H

Chairman: Zhao Yan-zeng  
Cochairman: K. Sassen

VISIBILITY AND AEROSOL PROPERTIES (Cont.)

H12. POLAR NEPHELOMETER MEASUREMENTS OF LASER LIGHT SCATTERING BY NON-SPHERICAL PARTICLES . . . . .	217
Alessandro Coletti and Gerald W. Grams	
H13. THE MODELING OF ATMOSPHERIC AEROSOL BACKSCATTERING AT CO <sub>2</sub> WAVELENGTHS . . . . .	219
G. S. Kent, G. K. Yue, U. O. Farrukh, and A. Deepak	
H14. CO <sub>2</sub> LIDAR FOR ATMOSPHERIC OPTICAL MEASUREMENTS IN THE 8-12 $\mu\text{m}$ WINDOW REGION . . . . .	223
D. M. Winker and R. M. Schotland	
H15. APPLICATION OF COHERENT ANTI-STOKES RAMAN SCATTERING TO DROPLET CHARACTERISTIC MEASUREMENTS IN THE MIE SIZE RANGE . . . . .	224
Abraham Gross and John Cooney	
H16. ALGORITHM FOR OBTAINING AEROSOL BACKSCATTER CROSS-SECTION DISTRIBUTION WITH AN LDV . . . . .	227
L. Z. Kennedy and H. B. Jeffreys	

Thursday, June 24, 1982  
2:30 p.m.

BUSINESS MEETING FOLLOWING SESSION H

Friday, June 25, 1982  
8:30 a.m. - 12:30 p.m.

SESSION I

Chairman: C. M. R. Platt  
Cochairman: B. M. Herman

MULTIPLE SCATTERING, CLOUDS, AND HYDROMETERS

II. MEASUREMENTS OF MULTIPLY SCATTERED RADIATION CONTRIBUTION TO LIDAR AND TRANSMISSOMETER SIGNALS . . . . .	228
P. Bruscaglioni, L. Lachi, L. Lo Porto, L. Pantani, L. Stefanutti, and G. Zaccanti	
II. LIDAR MULTIPLE RAMAN-MIE SCATTERING FROM A CLOUD . . . . .	230
Smadar Egert, Ariel Cohen, and Moshe Kleiman	
II. 2-D LASER PROPAGATION CALCULATIONS USING NEUTRON TRANSPORT METHODS . . .	231
S. A. W. Gerstl, A. Zardecki, and R. C. Shirkey	
II. LIDAR STUDIES OF POLARIZATION ANISOTROPY IN MULTIPLE BACKSCATTERING . . .	234
S. R. Pal and A. I. Carswell	
II. LASER BACKSCATTERING FROM DENSE WATER DROPLET CLOUDS . . . . .	236
A. I. Carswell, R. B. Smith, S. R. Pal, and R. Dubinsky	
II. JOINT POLARIZATION LIDAR AND K <sub>11</sub> -BAND RADAR CLOUD OBSERVATIONS . . . . .	238
Kenneth Sassen	
II. MEASUREMENT OF THE STOKES PARAMETERS FOR CIRRUS CLOUDS USING INCOHERENT AND COHERENT LIDAR SYSTEMS . . . . .	240
Ingar Singstad	
II. LIDAR OBSERVATIONS OF CLOUD TOP STRUCTURE AND SCATTERING POLARIZATION . . . . .	242
J. D. Spinhirne and M. Z. Hansen	
II. A PATH-AVERAGED LASER RAIN GAUGE FOR SATELLITE/EARTH COMMUNICATIONS APPLICATIONS . . . . .	244
D. J. Fang and C. H. Chen	
II. LIDAR BACKSCATTER MEASUREMENTS IN FALLING SNOW . . . . .	245
G. Davidson, A. Bogdan, D. McCaffrey, and John D. Mill	
II. PHASE FUNCTION MEASUREMENTS OF SNOW CRYSTALS . . . . .	247
L. W. Winchester, Jr.	
AUTHOR INDEX . . . . .	251

LIDAR MEASUREMENTS OF THE STRATOSPHERIC AEROSOL: 1974-1982

T. J. Swissler and M. Osborn, Systems and Applied Sciences Corp.  
Hampton, Virginia 23666

Routine ruby lidar observations of the stratospheric aerosol have been obtained at Hampton, Virginia ( $37.1^{\circ}$ N.  $76.3^{\circ}$ W) from 1974 to the present. This period includes a major volcanic increase in 1974 from Volcán de Fuego, a background period of minimal stratospheric aerosol concentrations in 1978-79, and a time of multiple volcanic eruptions during 1980-82. The data are presented in terms of lidar scattering ratio and corresponding temperature profiles, the time history of the peak backscatter mixing ratio, the height of the peak backscatter and temperature minimum, and the aerosol backscatter integrated through the stratosphere. The results are discussed in terms of the increases due to the volcanic eruptions, the decay times of the aerosol following these eruptions, and the possible observations of seasonal variations in the background level concentrations.

This extensive lidar data set has also been combined with aerosol optical modeling techniques to construct an estimate of the stratospheric aerosol mass loading over the 1974-1982 time period.

## MYSTERY CLOUDS IN THE STRATOSPHERE ?

M. P. McCormick  
NASA Langley Research Center  
Hampton, Virginia, 23665, U.S.A.

In late January 1982, an enhancement in lidar backscatter at stratospheric altitudes between 15 and 20 km was reported by Hirono of Kyushu University, Fukuoka, Japan. Subsequently, a number of lidar investigators reported this new enhancement. Although the Smithsonian Institution's Scientific Event Alert Network (SEAN) had received no reports of a large eruption immediately prior to this time, most lidar researchers believed the new layer's origin to be volcanic. The press, on the other hand, reported this layer over a prolonged period of time, most of late February and early March, as a "mystery-layer" of unknown content and origin that could have been from a nuclear detonation, a meteor shower, or a large volcanic eruption.

This paper describes our most recent ground-based (37°N) and airborne lidar measurements (38°N to 10°N) and compares them to past measurements. Figure 1 shows the airborne lidar vertical scattering ratio (SR) measurements after the eruptions of Mount St. Helens (MSH) and Alaid compared to measurement in February 1982. Clearly the profiles are very similar. Note that the first two profiles were taken at different times after their respective eruptions. For the case of MSH, the interval is 4 months and for Alaid, 2 months.

During a mid February flight to Costa Rica (10°N), the lidar SR's were enhanced well over background and became dramatically higher at about 30°N, peaking at about 21°N. The values remained high from there south to Costa Rica. Data were taken serially at two wavelengths, 1.06 and 0.6943  $\mu\text{m}$ . On the return trip 8 days later, the layer was still present over the entire flight path. We conclude from our data and other reported data that the stratospheric enhancement is probably spread over most of the Northern Hemisphere at this time (March 1982) and, based on these data, past lidar signatures, and mass considerations, the layer was probably produced from a low latitude eruption in late December 1981 to mid January 1982.

Measurements by the satellite experiment SAGE, for Stratospheric Aerosol and Gas Experiment, of the dispersion of the MSH effluent are shown in Figure 2 as stratospheric optical depth at 1.0  $\mu\text{m}$ . These data are for the period July 21 to August 26, 2 to 3 months after the eruption, and show the effects of the slow process of global mixing and conversion from sulfur dioxide to sulfuric acid/water particles. A lidar measurement at a specific point, therefore, is not necessarily representative of the entire globe. This will be discussed with reference to the present layer and past volcanically produced layers and the mass calculations inferred from lidar measurements. We have concluded that the stratospheric aerosol mass increase due to the eruption of MSH was about  $0.32 \times 10^6$  tonnes, and that the most recent eruption created at least this amount of enhancement.

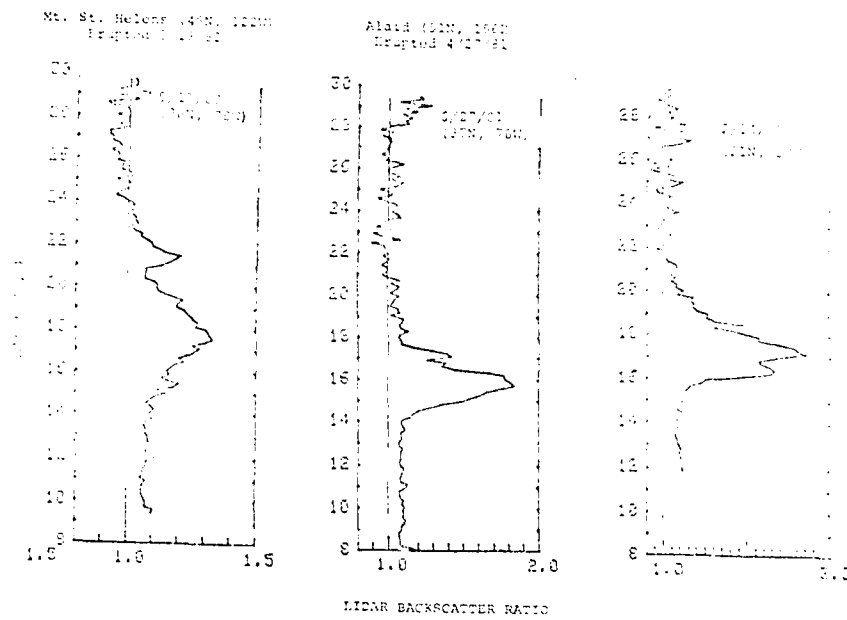


Figure 1 Lidar backscatter ratio profiles at a wavelength of  $0.6943 \mu\text{m}$  after some past volcanic eruptions compared to a recent sounding.

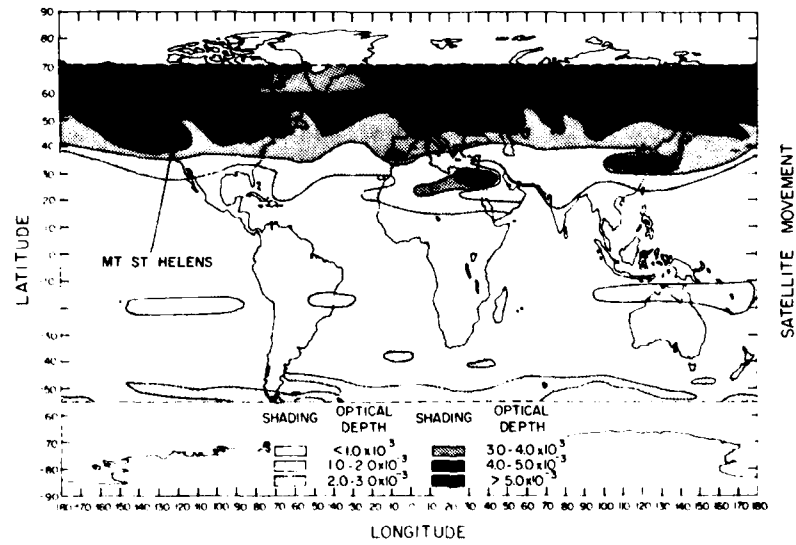


Figure 2 SAGE measurements of stratospheric optical depth for the period July 21 through August 26, 1980. The Northern Hemisphere enhancements are due to the May 18, 1980, eruption of Mount St. Helens ( $46^{\circ}\text{N}$ ,  $122^{\circ}\text{W}$ ).

LIDAR OBSERVATIONS OF THE STRATOSPHERIC AEROSOL OVER CENTRAL EUROPE  
SINCE JANUARY 1981

R. Reiter, H. Jäger, W. Carnuth, and W. Funk

Fraunhofer Institute for Atmospheric Environmental Research,  
Kreuzeckbahnstrasse 19, D-8100 Garmisch-Partenkirchen, FRG

A ruby lidar with a 52 cm receiver telescope and 64 channel photon counter has been used since 1976 at Garmisch-Partenkirchen, Germany ( $47.5^{\circ}\text{N}$ ,  $11.0^{\circ}\text{E}$ ), for continuous monitoring of the stratospheric aerosol (Reiter, et al.; refs. 1 and 2.) The usual matching of the lidar return signal (molecular plus particulate backscatter) with the molecular backscatter profile deduced from a radiosonde ascent results in the net particulate backscattering coefficient. The matching level is 25 to 30 km and a correction for a possible deviation of  $R_{\min}$ , the minimum measured backscattering coefficient, from unity has not been applied. Scattering ratio (ratio  $R$  of total to molecular backscatter), optical mixing ratio ( $R - 1$ ), and particulate backscatter coefficient are the quantities deducable from that single wavelength lidar system.

The aerosol injected into the stratosphere by the St. Helens eruption in May 1980 had almost completely decayed a year later. In May 1981 the backscattering coefficient had decreased to nearly pre-Helens values, so that signals of a new eruption could easily be distinguished from the background. Two volcanic eruptions have been reported to have penetrated into the stratosphere in 1981: the eruptions of Alaid (Kurile Islands,  $50.8^{\circ}\text{N}$ ,  $155.5^{\circ}\text{W}$ ) on April 28 (see ref. 3) and of Pagan (Mariana Islands,  $18.1^{\circ}\text{N}$ ,  $145.8^{\circ}\text{E}$ ) on May 15. (See ref. 4.) In Fig. 1 altitude profiles of the scattering ratio  $R$  are presented. The first profile from April 27 shows the remainder of the Mt. St. Helens aerosol around a 19-km altitude, resulting in a particulate backscatter of about 10% of the molecular backscatter. On May 19 and 20 a peak just above the tropopause gave the first indication of a new stratospheric aerosol cloud. On May 29 this peak was already clearly separated from the tropopause, and further peaks began to develop above 16 km. On June 2 a very strong double peak was observed at 17 km, and with  $R = 3.8$  the highest  $R$  value is measured during the displayed period. It was observed that the stratospheric particulate backscatter decayed fast at first and then slowly decreased along with the vertical inhomogeneity.

As sources of the stratospheric aerosol increase, the eruption of the Alaid volcano on April 18 comes into question. The Pagan volcano is located so far in the south that the arrival of its effluents is not expected before December. In contrast to the situation during the Mt. St. Helens eruption, where the summer easterlies in the middle stratosphere had already fully developed, the stratospheric winter regime was still dominating at midlatitudes at the end of April 1981, and so the upper parts of the Alaid plume were also transported from west to east until even the middle of June. Fig. 2 shows the profile of the westerly wind in the lower troposphere as deduced from the Munich radiosonde data. Additionally, transport velocities of the stratospheric aerosol as a function of height are shown, calculated from the time lags of the observed lidar peaks after the eruption date. Both profiles agree well.

Fig. 3 shows the time variation of the maximum optical mixing ratio ( $R_{\max} - 1$ ) and the height integrated particulate backscatter coefficient between 12 and 23 to 30-km altitude. The former curve rises steeply between the middle of May and the beginning

of June, decreases similarly until the middle of June, and then decreases more slowly until November. The integral curve behaves likewise, but the decline is less steep.

The 1981 aerosol increase has been related to our observations of the Mt. St. Helens eruption cloud and to literature data describing the decay of the Fuego plume (eruption in 1974; see ref. 5). The Alaid eruption seems to have been more intense than the initial Mt. St. Helens eruption, but the Mt. St. Helens effect had been amplified by subsequent eruptions. A comparison of all three volcanic events reveals that both Alaid and Mt. St. Helens eruptions produced a backscattering perturbation of about one third of that caused by the Fuego eruption. No significant climatic changes are to be expected resulting from the recent eruption clouds.

During the preparation of this abstract, from February 2, 1982, on, another stratospheric aerosol peak was observed at 15 km altitude and confirmed by Hirono's group in Japan (private communication). This cloud surely originates from a hitherto unknown volcanic eruption. A preliminary trajectory analysis points at a probable eruption site near the northeastern border of the Pacific ocean in the beginning of 1982.

#### REFERENCES

1. Reiter, R.; Jäger, H.; Carnuth, W.; and Funk, W.: The Stratospheric Aerosol Layer Observed by Lidar Since October 1976. Arch. Met. Geophys. Biokl., Ser. B, 27, 121-149, 1979.
2. Reiter, R.; Jäger, H.; Carnuth, W.; and Funk, W.: Lidar Observations of the Mt. St. Helens Eruption Clouds Over Mid-Europe, May to July 1980. Geophys. Res. Lett., 7, 1099-1101, 1980.
3. EOS, Geophysical Event, EOS, Transactions, American Geophysical Union, 62, 494, 1981.
4. EOS, Geophysical Event, EOS, Transactions, American Geophysical Union, 62, 510, 1981.
5. Russell, P. B.; and Hake, R. D., Jr.: The Post-Fuego Stratospheric Aerosol: Lidar Measurements, With Radiative and Thermal Implications. J. Atmos. Sci., 34, 163-177, 1977.

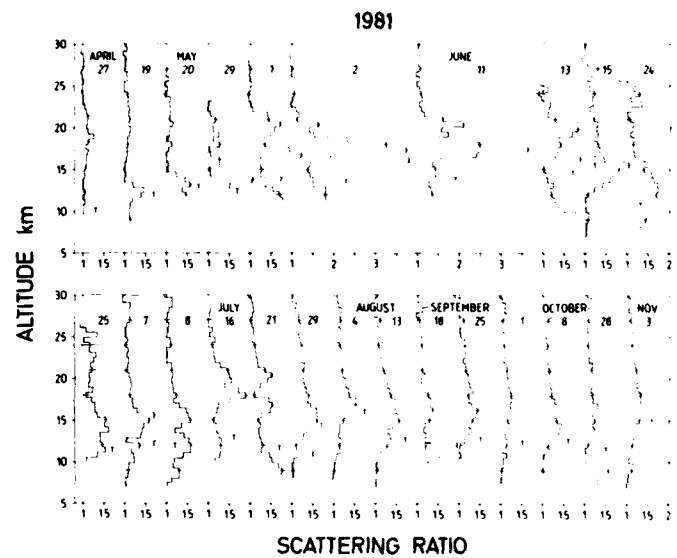


**Fig. 1:**  
 Lidar observations at Garmisch-Partenkirchen showing the formation of aerosol layers following the Alaid eruption. T denotes the Munich radiosonde tropopause.

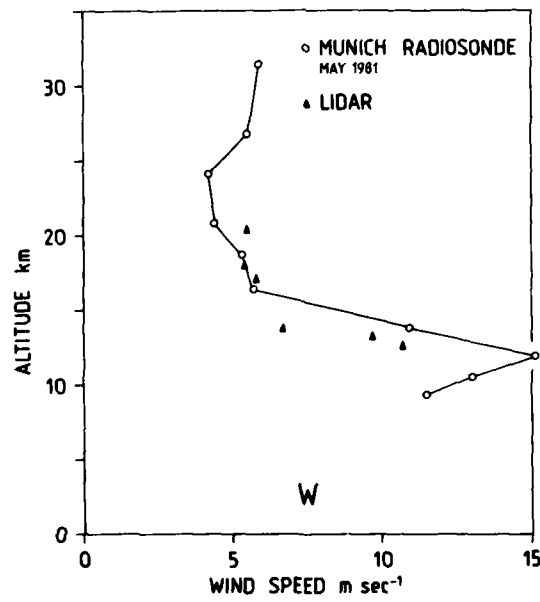


**Fig. 2:**  
 Circulation profile of the stratospheric westerlies deduced from Munich radiosonde data, compared to lidar-determined transport speeds after the Alaid eruption.

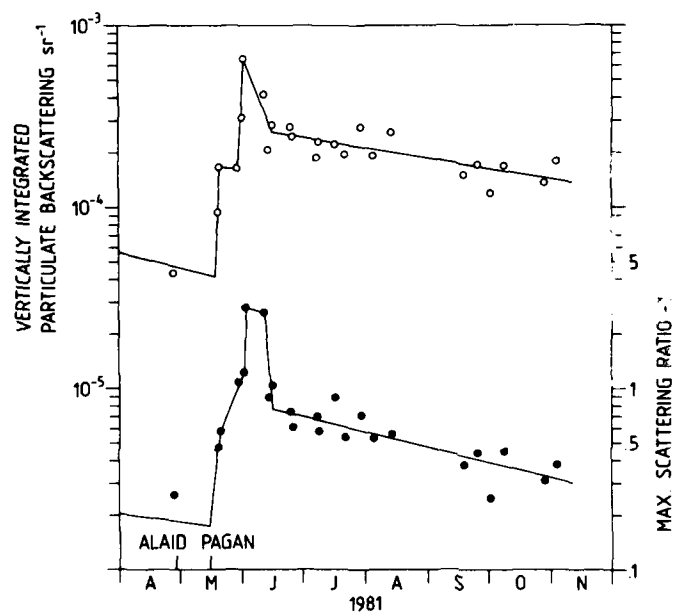


**Fig. 3:**

Time variation of the maximum optical mixing ratio (maximum scattering ratio - 1) and vertically integrated particulate backscattering coefficient.

## COMPARISON OF LOW-LATITUDE LIDAR AND SAGE SATELLITE MEASUREMENTS

G. S. Kent

Institute for Atmospheric Optics and Remote Sensing (IAFORS)  
P. O. Box P, Hampton, Virginia, USA

M. P. McCormick

NASA Langley Research Center  
Hampton, Virginia 23665, USA

M. T. Philip

University of the West Indies  
Kingston, Jamaica

### INTRODUCTION

The low-altitude section of the University of the West Indies, Mark II lidar system (Kent et al., 1971) was used to make observations on the stratospheric aerosol layer during the period February 1978 - November 1979. The system operates at a wavelength of  $0.6943 \mu\text{m}$  and has a vertical resolution of 2 km over the height range 16-52 km. Approximately 90 useful nights' observations were obtained. Because the low latitude aerosol layer extends well above the ceiling of normal meteorological balloon soundings, this data has been normalized to a standard atmosphere over the altitude range 40-52 km. The standard atmosphere chosen is the Air Force Reference Atmosphere (Cole and Kantor, 1978) for the appropriate month and interpolated for the latitude of Kingston, Jamaica ( $18^\circ\text{N}$ ).

The SAGE satellite system was launched in February 1979 to monitor stratospheric aerosol, ozone and nitrogen dioxide over the latitude range  $70^\circ\text{S} \rightarrow 70^\circ\text{N}$  (McCormick et al., 1979). The stratospheric aerosol is measured in terms of the extinction it produces at a wavelength of  $1.0 \mu\text{m}$ . The observation point of the satellite crossed the latitude of Jamaica about 8 times in 1979 making about 150 separate observations within  $5^\circ$  of that latitude.

The data products that have been selected for comparison are the aerosol/molecular backscatter ratio  $R_B$  for the lidar and the aerosol/molecular extinction ratio  $R_E$  for SAGE.

### SHORT TERM PROFILE VARIATION

It is clear, from examination of SAGE data collected at different latitudes, that the low-latitude aerosol layer is very different, in terms of altitude and extinction ratio, from the mid-latitude aerosol layer. Figure 1 shows the mean SAGE profiles for four different latitude zones during the period February-November 1979. The latitude variation is very clear and it shows that Jamaica lies on the edge of the low-latitude region. What is not clear in this diagram is that the boundary between the low- and mid-latitude behavior is sharp and that its position is not fixed. These points are illustrated in Figs. 2(a) and (b). Figure 2(a) shows a succession of lidar profiles obtained in Jamaica on the same night. It can be seen that the layer shape changes and that the height of the maximum scattering ratio may occur over a wide height range extending from about 20 km (typical of mid-latitude) to almost 30 km (typical of low latitude). A similar variation is observed in the SAGE data.

Figure 2(b) shows a succession of SAGE profiles (separated by 24° longitude) obtained on the same day at a latitude of approximately 20°N. Seasonal variations are small at low-latitudes and these data, although taken six months apart, may be regarded as representative. Both sets are taken during periods of low volcanic activity. A more detailed study of SAGE data shows that the low- to mid-latitude boundary changes its position as the longitude is varied and that its latitude is related to the upper-air meteorological conditions; the lidar data shows in addition that the boundary is in a constant shape of movement.

#### MEAN PROFILE

Comparison of the profiles in Fig. 2(a) and (b) shows that, on the average, the lidar profile has higher values in the height range 20-25 km than in the height range 25-30 km, in contrast to the SAGE profile. Analysis shows that the ratio  $R_{BE}$  (backscatter at 0.6943  $\mu\text{m}$ )/(extinction at 1.00  $\mu\text{m}$ ) apparently decreases fairly steadily between 20 and 30 km; the mean value of  $R_{BE}$  is approximately  $0.03 \text{ sr}^{-1}$ , in good agreement with values calculated using Mie theory and standard particle models. The altitude variation has support from SAGE data obtained on an additional aerosol channel at 0.45  $\mu\text{m}$ . A preliminary examination of the ratio (extinction at 0.45  $\mu\text{m}$ /extinction at 1.0  $\mu\text{m}$ ) for the latitude belt 10° - 20°N shows an altitude variation of this ratio similar to that for  $R_{BE}$ , although of somewhat smaller magnitude. The data and possible interpretations are still under study.

#### LONG-PERIOD VARIATION

Although the seasonal variations are small and difficult to detect at low altitudes, both lidar and SAGE show strong long-period changes. Figure 3 shows the variation of  $(R_B-1)$  and  $0.03 (R_E-1)$  for the altitude range (26-30 km) from February 1978 - December 1980. A steady rise in the quantity occurred throughout 1978 and 1979, followed by a sudden drop in December 1979, followed by the start of a new rise. The height range chosen is above that affected by recent volcanic eruptions and the change is apparently that of the background aerosol.

#### REFERENCES

- Cole A. E. and Kantor, A. J.; "Air Force Reference Atmospheres," Air Force Surveys in Geophysics No. 382, AFGL-TR-78-0051, 1978.
- Kent, G. S., Sandland, R., and Wright, R. W.; A second-generation laser radar, *J. Appl. Meteor.* 10, 443-452, 1971.
- McCormick, M. P., Hamill, P., Pepin, T. J., Chu, W. P., Swissler, T. J., and McMaster, L. R., Satellite studies of the stratospheric aerosol, *Bull. Amer. Meteor. Soc.* 60, 1038-1046, 1979.

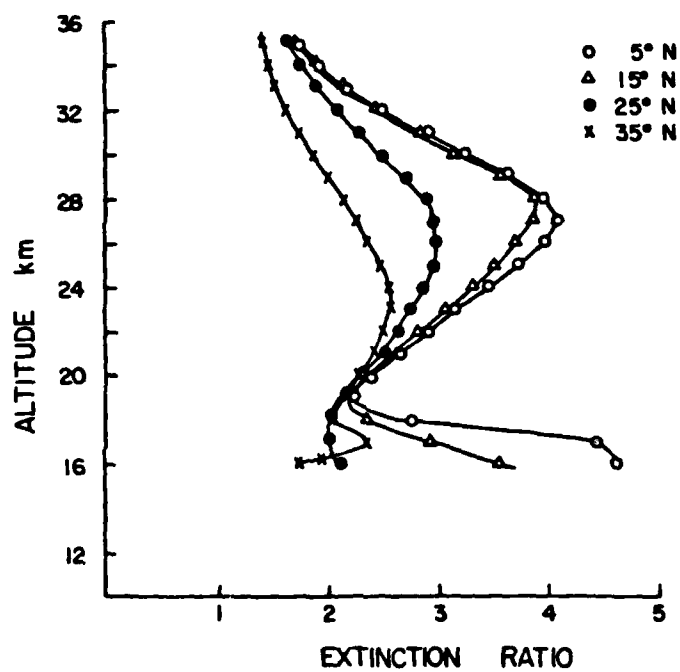


Figure 1.- Mean aerosol extinction ratio profiles for four different  $10^{\circ}$  latitude bands centered at the latitudes shown on the figure.

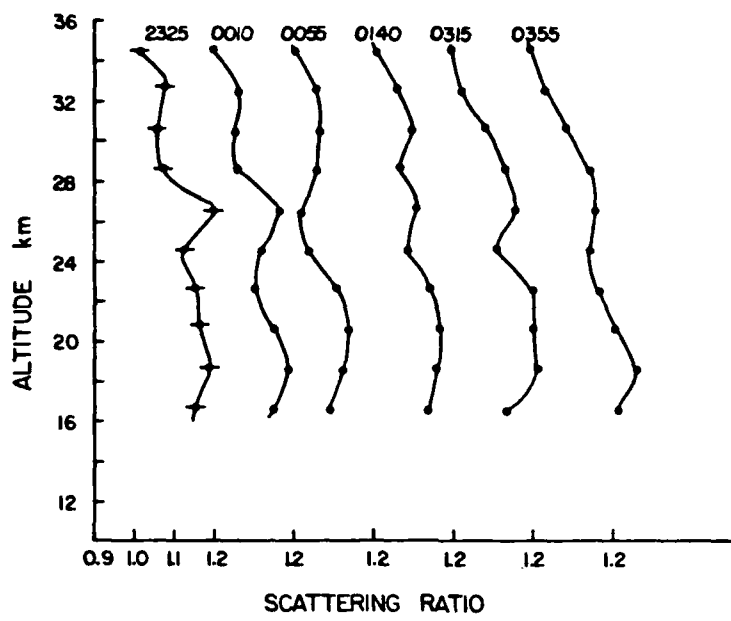


Figure 2(a).- Succession of lidar scattering ratio profiles obtained on 25-26 November 1978.

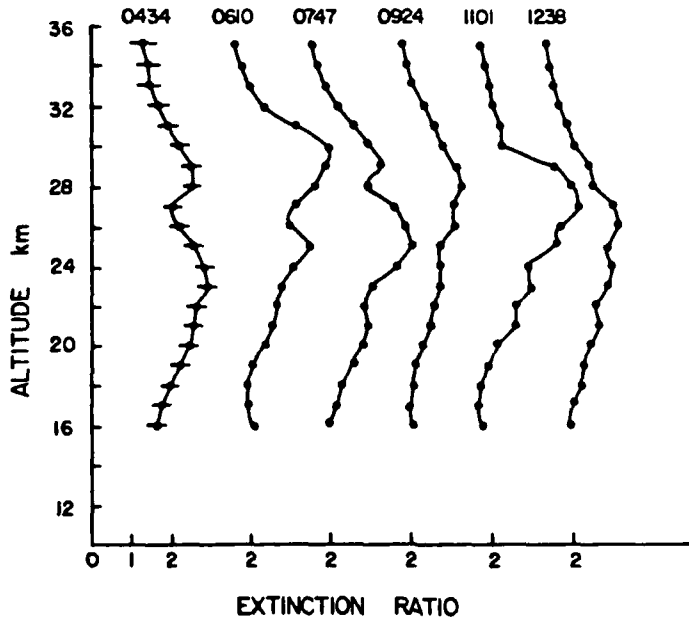


Figure 2(b).- Succession of aerosol extinction ratio profiles obtained on 9 April 1979.

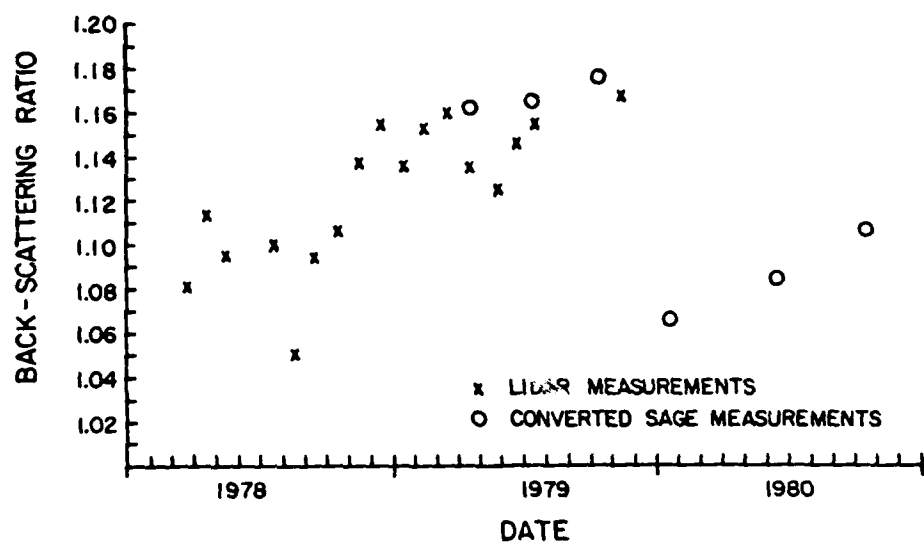


Figure 3.- Variation of  $(R_B - 1)$  and  $0.3 (R_E - 1)$  for the latitude belt  $10^{\circ}$ - $20^{\circ}$ N and the altitude range 26-30 km, from February 1978 - November 1980.

LIDAR AND BALLOON-BORNE PARTICLE COUNTER COMPARISONS  
FOLLOWING THE ERUPTIONS OF MT. ST. HELENS AND ALAID

D.J. Hofmann and J.M. Rosen  
Department of Physics and Astronomy  
University of Wyoming, Laramie WY

R. Reiter and H. Jäger  
Fraunhofer-Institute for Atmospheric Environmental  
Research, Garmisch-Partenkirchen, FRG

Lidar backscatter observations of the stratosphere made at Garmisch-Partenkirchen ( $47.5^{\circ}\text{N}$ ) from mid-1979 to early 1982 are compared with backscatter cross sections as calculated from measurements of condensation nuclei ( $r \geq 0.01 \mu\text{m}$ ) and larger aerosol ( $r \geq 0.15 \mu\text{m}$ ,  $r \leq 0.25 \mu\text{m}$ ) made from balloons over Laramie, Wyoming ( $41^{\circ}\text{N}$ ) during the same period. Log normal size distributions are fit to the three particle sizes measured and spherical droplets consisting of a 75% sulfuric acid solution are assumed in calculating the expected backscatter as a function of time. The results clearly indicate that the lower stratosphere (15-17 km) was disturbed as early as December 1979, prior to the eruption of Mt. St. Helens, probably due to minor volcanic activity.

ATMOSPHERIC DEPOLARIZATION RATIO DECAY AFTER THE  
ERUPTION OF MOUNT ST. HELENS

Joseph H. Goad, Jr.

NASA Langley Research Center

Hampton, Virginia, 23665, U.S.A.

The 1980 eruptions of Mount St. Helens ejected large amounts of volcanic material into the upper troposphere and lower stratosphere. When the fresh volcanic cloud was first observed at our location (37°N.-76.3°W.), the peak depolarization ratios in the volcanic layers were 0.15 to 0.18. From the first observations in June 1980, the depolarization decreased as the volcanic material diffused, sedimented, and changed chemical composition. In 9 months, atmospheric depolarization ratios returned to values measured prior to the Mount St. Helens eruptions.

Figure 1 shows the large depolarization ratios measured in the layers of volcanic material. These ratios are approximately 10 times higher than observed for the atmosphere in nonvolcanic times. The vertical dotted line is the atmospheric molecular depolarization ratio obtained from Young's<sup>1</sup> calculated value by converting from unpolarized incident radiation to polarized incident radiation. In figure 2, the depolarization ratios had decreased to values below 0.05 in a period of 4 months. In figure 3, the depolarization has decreased to similar values measured before the eruptions of Mount St. Helens. The error bars on the figures are the standard deviation of the quotient formed by the ratio of the perpendicular polarized component to the parallel polarized component, which is the depolarization ratio.

These studies have been conducted to measure upper atmospheric lidar depolarization ratios for obtaining additional remote information on the composition and physical state of atmospheric aerosols in the region of the tropopause. In the future, this will provide data inputs for climatic models and for the design of polarization sensors.

1. A. T. Young, "Revised depolarization corrections for atmospheric extinction," Applied Optics, Vol. 19, No. 20, October 15, 1980.

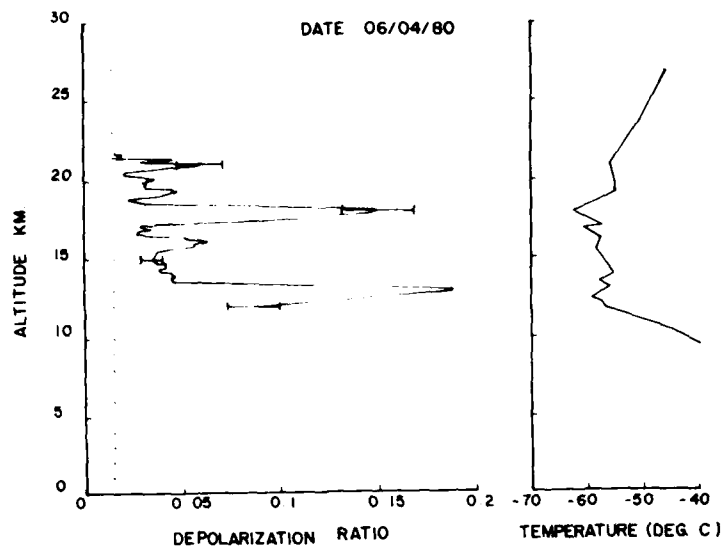


Figure 1 First observed volcanic layers at this location  
(Dotted line - 0.0142 molecular depolarization ratio)

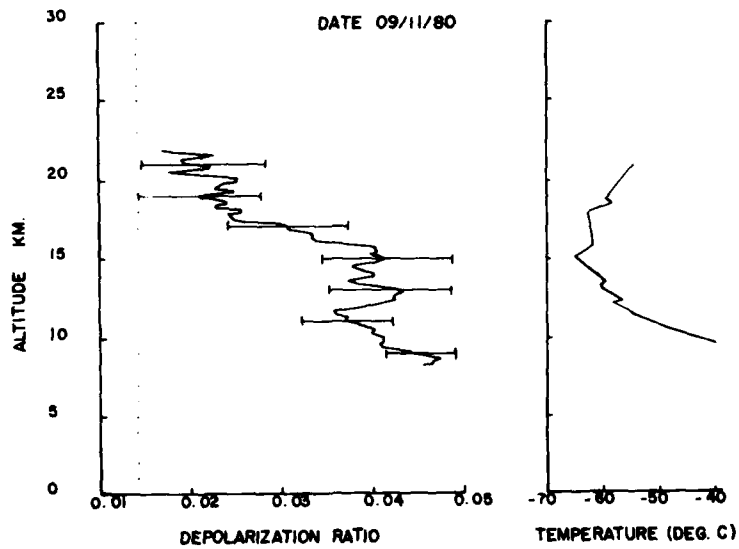


Figure 2 Depolarization ratio has decreased below 0.05  
(Dotted line - 0.0142 molecular depolarization ratio)

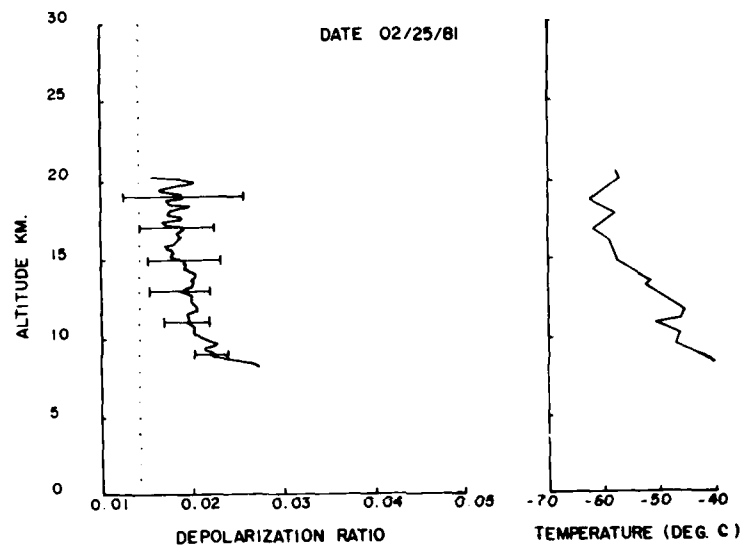


Figure 3 Return to pre-eruption depolarization profile  
(Dotted line - 0.0142 molecular depolarization ratio)

STEERABLE LIDAR STUDIES OF MESOSPHERIC  
SODIUM LAYER STRUCTURE

C. S. Gardner and C. F. Sechrist, Jr.

Aeronomy Laboratory  
Department of Electrical Engineering  
University of Illinois  
Urbana, Illinois 61801

and

J. L. Bufton

NASA  
Goddard Space Flight Center  
Greenbelt, Maryland 20771

ABSTRACT

In May and June, 1981, a 48-inch telescope located at the Goddard Space Flight Center Optical Test Site was used in conjunction with components of the University of Illinois sodium lidar system to make steerable lidar observations of the mesospheric sodium layer. Table 1 lists parameters of the steerable system. The telescope facility, located at  $39.1^{\circ}\text{N}$ ,  $76.8^{\circ}\text{W}$ , consists of a 48-inch Cassegrain astronomical telescope with Coudé focus and supporting equipment which enables this instrument to be used in a variety of laser ranging experiments. The telescope aperture area is approximately the same as the objective area of the Fresnel lens receiving telescope used in Illinois. However, as well as making steerable measurements possible because of the sophisticated telescope mount, the high quality optics permit a small receiver field of view. This serves to reduce the noise counts due to background sky illumination.

The interference filter and PMT are positioned near the focal point of the telescope. No collimating lens is required due to the long focal length of the primary/secondary mirror combination in the telescope. The aperture of the focusing lens in the PMT cooled housing limits the telescope field of view to less than 1 mrad. This field of view can be reduced further by inserting a field stop iris in front of the PMT. The laser head was mounted on the telescope to insure that the laser beam tracked the telescope motions accurately. Coincidence of the transmitted laser beam and the telescope field of view was insured by adjusting the folding mirror. Because the laser beam divergence angle was larger than the telescope field of view, a beam expander was inserted in the optical path between the laser and the folding mirror. This served to reduce the beam divergence to roughly 0.1 mrad. Laser tuning was monitored by examining the scattering of the laser output in a grating spectrometer (for rough tuning) and in a sodium cell (for fine tuning to the sodium D2 line). A fiber optic cable was used to couple the laser output to these instruments.

The position of the telescope was computer controlled and therefore the telescope was easily and rapidly positioned at the desired azimuth

and elevation angles. The range of permissible angles was rather restricted, however, by mechanical considerations related to the laser head. The azimuth angle could be varied by only  $70^\circ$  or  $80^\circ$ . It was not possible to move the telescope past zenith. Steerable measurements were initially attempted on the evening of June 8-9, 1981. The telescope was scanned between three points; point A (azimuth= $277^\circ$ , elevation= $90^\circ$ ), point B (azimuth= $277^\circ$ , elevation= $70^\circ$ ), and point C (azimuth= $307^\circ$ , elevation= $70^\circ$ ). A greater horizontal separation was achieved in later observations of the sodium layer. In order to examine 3 points which were equally spaced horizontally, the observations alternated between zenith measurements and measurements at an elevation angle of  $60^\circ$  while the azimuth angle was varied by  $60^\circ$ . Observations of sodium density at the increased horizontal spacing were made on June 17-18, 1981. Within the mechanical constraints mentioned above, an attempt was made to select points over sparsely populated regions in order to avoid areas where sodium vapor lights were used in large numbers. It should be noted that because data were gathered at depressed elevation angles, the horizontal separation of the observed points was a function of altitude. For the data collected on June 17-18, 1981, the observation points were separated by 50 km at an altitude of 100 km whereas at an altitude of 80 km the separation was only 40 km.

Nine spatial profiles of photocount data were collected on June 8-9, 1981. Each profile consisted of the integrated returns from 500 laser pulses. Because only three photocount profiles were collected at each pointing angle, it was not possible to temporally filter the data. Receiver range gate and delay times of 3  $\mu\text{s}$  and 60  $\mu\text{s}$ , respectively, were utilized at all three pointing angles. The average spatial periodogram of three profiles collected at zenith shows large peaks at  $0.12 \text{ km}^{-1}$ ,  $0.17 \text{ km}^{-1}$ , and  $0.28 \text{ km}^{-1}$ , and indicates that wavelike features are present. The zenith data were processed using a spatial filter with a cut-off at  $0.4 \text{ km}^{-1}$ .

Because of poor weather, additional data could not be collected until June 17-18, 1981. On this evening, a series of 81 spatial profiles were collected. Each spatial profile consisted of the integrated returns from 500 laser pulses. A 3  $\mu\text{s}$  range gate and a 198  $\mu\text{s}$  delay factor were used in obtaining this data. The delay factor was chosen to insure that Rayleigh scattering from 30 km as well as sodium returns could be received as the elevation angle was varied from  $90^\circ$  to  $60^\circ$ . The integration time for each profile was approximately 2 minutes and a profile was obtained every 4 minutes. Thus, 12 minutes separated profiles collected at the same pointing angle. To insure that no temporal variations in sodium density were inadvertently removed, a temporal filter cutoff at  $0.033 \text{ min}^{-1}$  was chosen and applied to the data collected at all three pointing angles. Figure 1 shows the temporal variations in sodium density associated with the zenith measurement.

In October, additional measurements were made at Goddard Space Flight Center by upgrading the receiving system computer to permit

azimuthal scanning of the telescope. Measurements were obtained by pointing the telescope 30° off zenith and repeatedly scanning over a range of 60° in azimuth in 1° or 2° increments. The 60° azimuthal scan required approximately 15 min to complete. Over 3,000 profiles were collected in 3 separate nights of operation revealing information on the horizontal structure of the sodium layer. Pre-sunrise enhancement of the column abundance of more than 100% was observed, corroborating earlier measurements at Goddard in June and at Urbana in Spring 1981. This enhancement is believed to be associated with an increased influx of meteoric material.

TABLE 1  
Steerable Lidar System Parameters

LASER

Type	Tunable Flashlamp Pumped Dye Laser
Output Energy	50 mJ/pulse
Pulse Repetition Frequency	10 Hz
Pulse Width	2 $\mu$ s FWHM
Wavelength	589.0 nm
Linewidth	1 pm FWHM
Beam Divergence	1 mrad

GSFC TELESCOPE

Type	Cassegrain System, f/25 at Coude Focus
Diameter	1.22 m
Bandwidth	5 nm FWHM
Field-of-view	100 $\mu$ rad
Elevation Angle	60°
Azimuthal Range	60°
Azimuthal Scan Time	15 min/60°

JUNE 17-18, 1981

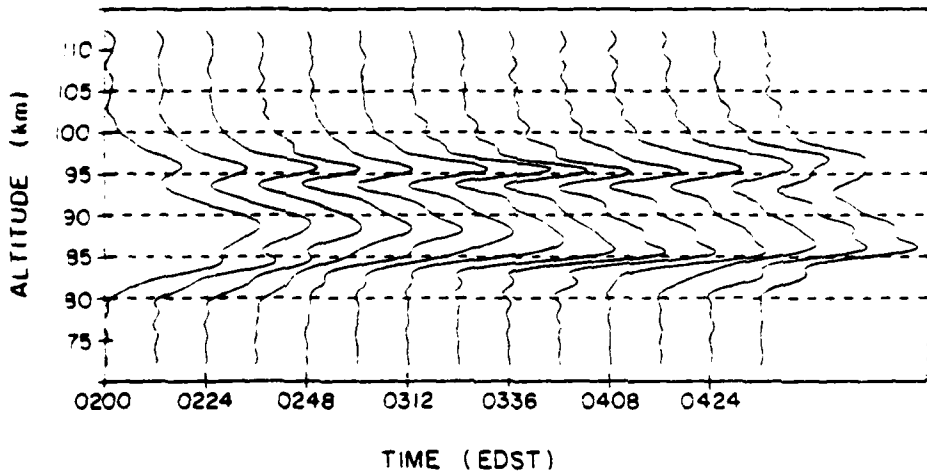
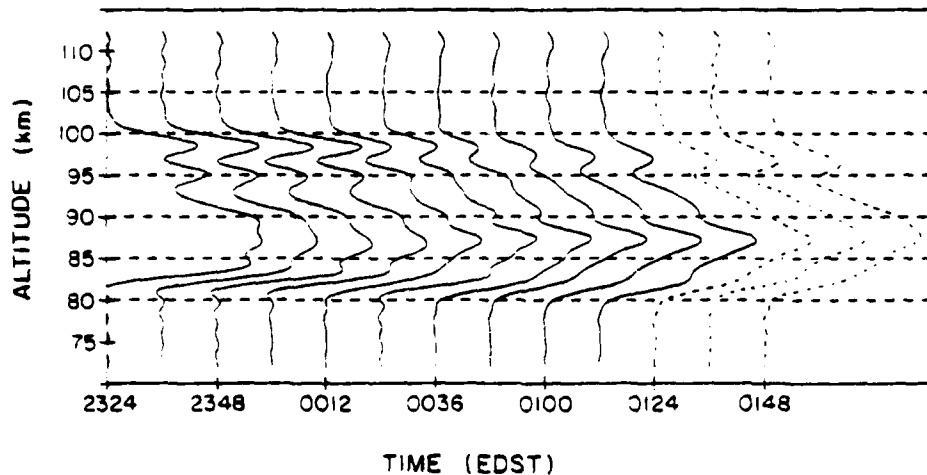


Figure 1. Altitude profiles of sodium density observed at the Goddard Space Flight Center on June 17-18, 1981. The spatial and temporal filter cutoffs were  $0.4 \text{ km}^{-1}$  and  $0.033 \text{ min}^{-1}$  respectively. Profiles are plotted at 12 minute intervals. Interpolated profiles are indicated by dashed curves.

## BALLOONBORNE LIDAR FOR DENSITY MEASUREMENTS

D.E. Bedo, K.S.W. Champion and R.A. Swirbalus  
Air Force Geophysics Laboratory  
Hanscom AFB, MA. 01731

At the present time our balloon measurements emphasize the determination of molecular density and superimposed aerosol concentrations within 40 km of the balloon using simple Rayleigh/Mie backscattering with a two- or three-color lidar. Planned extensions of this system include adding the capability for DIAL measurements of atmospheric pressure, temperature, moisture content and density at low altitudes.

The transmitter section of the balloon lidar consists of a Nd:YAG laser, doubled and tripled, with power levels of 700, 150 and 30 mJ at the emitted wavelengths of 1064, 532, and 355 nm. Throughout the balloon flight the laser remains oriented horizontally and pointing mirrors allow backscatter observations to be made vertically earthward, horizontally and upward at a 35° zenith angle over a 40-km range interval (150-m resolution) within selected altitude segments throughout the flight path. Maximum altitude attainable with the 2400-pound payload is about 35 km. The receiver portion of the lidar includes a 50-cm collector, beam splitters, filters and photomultipliers. Signals at each of three gain levels are taken from each multiplier and digitized by transient A/D convertors for transmission, together with housekeeping data, over a 250 kbit/sec telemetry link. A telemetry frame containing a complete data subset is transmitted for each laser pulse at the firing rate of 10 pps. Thermal control is provided by a liquid cooling system, two large-surface radiators and auxiliary heaters.

Nighttime simulations of backscatter signal levels at 1064 and 355 nm and their translation, based upon a Lowtran 3B model, into error limits in the determination of molecular density have been carried out<sup>1</sup> for a balloon flight of the type described. Results of the error analysis, showing expected errors as a function of altitude, for the nadir viewing configuration are shown in Fig. 1. Three values have been assumed for the uncertainty in the correction of the 355-nm signal for the aerosol scattering as determined at 1064 nm, namely, for 0%, 50% and 100% uncertainties in the backscatter ratio. In general, the Figure shows that reasonable multiple-shot averages can be expected to yield density values accurate to the order of 5% for a balloon lidar at 40-km altitude viewing earthward. A more recent simulation<sup>2</sup> applicable to a satellite lidar and based upon somewhat different aerosol models derived from recent particle data leads, when scaled, to results similar to those shown in Fig. 1 but with improved projected accuracies, approximately 1%.

## REFERENCES

1. Brehm, W.F. and Buckley, J.L.: Design Study of a Laser Radar System for Spaceflight Application. Final Report, General Electric Space Division to Air Force Geophysics Laboratory, AFGL-TR-79-0264, December 1979.
2. Russell, P.B., et al: Improved Simulation of Aerosol, Cloud and Density Measurements by Shuttle Lidar. Final Report, SRI International to National Aeronautics and Space Administration, Contract NAS1-16052, July 1981. (Available from NTIS as NASA CR-3473)

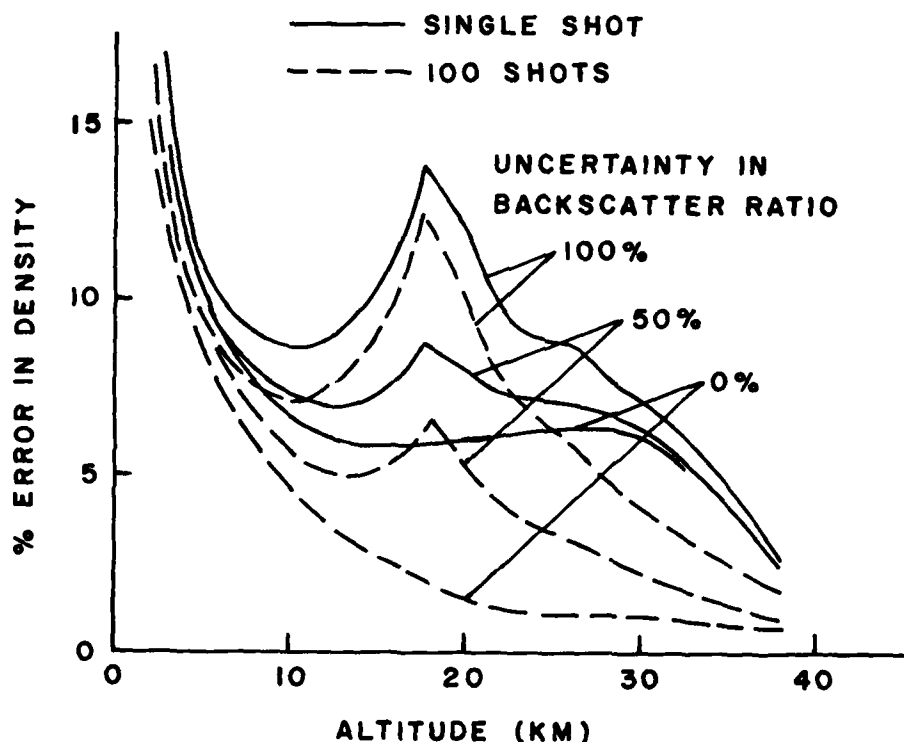


Fig. 1. The error in determining density with a two wavelength lidar (1064 and 355 nm) from a balloon at 40 km (from Ref. 1).

TEMPERATURE MEASUREMENTS IN THE TROPOSPHERE AND  
LOWER STRATOSPHERE USING A DUAL WAVELENGTH LIDAR

J. LEFRERE, G. MEGIE

Service d'Aéronomie du CNRS - BP 3  
91370 - VERRIÈRES-LE-BUISSON - FRANCE

Atmospheric temperature determination in the upper stratosphere and lower mesosphere (30 - 70 km), as derived from the single wavelength lidar measured atmospheric density profile, is now conducted on a routine basis using a ground based system at the Haute Provence Observatory (44°N, 5°E) (ref. 1). To extend these measurements to the lower altitude range and down to the tropopause level, the aerosol scattering contribution to the return signal should be subtracted. This implies the use of a multiwavelength lidar in order to take advantage of the differential spectral variation of the Rayleigh and Mie backscattering coefficients. The main difficulty of the experiment lies in the achievable accuracy on the neutral density profile required to obtain a temperature measurement of geophysical interest. Whereas the statistical error on the backscattered signal can be reduced below 0,1 %, the data reduction and density to temperature conversion will not allow a determination of the temperature profile with an accuracy better than  $\sim 1$  K which will prevent the study of short term fluctuations in this temperature distribution induced by the existence of organized or turbulent motions in the atmosphere. In conducting the temperature measurement described hereafter the main objective was to determine its feasibility using a ground based system. However the principal interest of such a measurement is related to the advent of a space borne system as it will provide temperature determination in such areas where the global rawinsonde network does not allow any measurement (oceans, deserts...) (ref. 2).

To determine the optimum wavelength pair to conduct these measurements among the various laser emission wavelengths available at the Haute Provence Observatory lidar facility, a theoretical optimisation procedure has been conducted : taking into account the overall system efficiency and the sensibility to incertitudes in the nature and shape of the aerosol particles this led to the choice of the second (532 nm) and third (355 nm) harmonics of the Nd<sup>3+</sup> Yag laser (ref. 3). The output laser energies at these wavelengths are respectively 350 mJ and 120 mJ. A 36 cm telescope is used to collect the backscattered signal which is time-analysed using either a Biomation 1010 transient waveform recorder or a 256 channels photon counter. The whole experimental sequence is computer controlled using a PDP 11/34 mini-computer, so that the switching between the two emitted wavelengths which is made every 5 to 10 seconds avoids additional errors due to the fluctuation of the scattering medium. The algorithm used to derive the atmospheric density from the two lidar

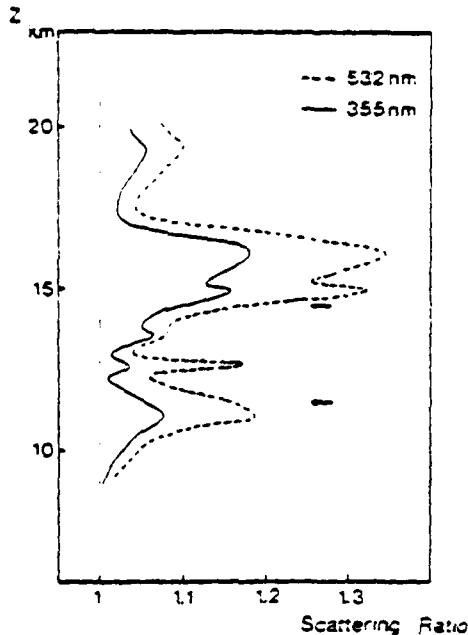


Fig. 1

signals is similar to the one first proposed by P.E. RUSSEL et al. (ref. 4) for space-borne applications.

The figure 1 shows an example of scattering ratios measured at 532 nm and 355 nm respectively. Their constant relationship confirms the homogeneity in terms of nature and shape of the aerosol particles throughout the probed altitude range, except for a thin layer at 11 km altitude which might be attributed to cirrus clouds. These are common features around the tropopause level ; due to their large temporal and spatial variabilities they constitute a major drawback for lidar density measurements as their contribution to the backscattered signal is difficult to evaluate. Taking into account their rather small vertical extension the best procedure will be to extrapolate the data through this

layer, though the temperature determination at lower altitude could be affected by the error propagation due to the integration of the vertical density profile. One has also to notice that the measured scattering ratios in the stratosphere are large : this situation which limits the accuracy of the measurement has been encountered during the past two years due to the enhancement of the volcanic activity in the middle latitude regions of the Northern hemisphere.

The figure 2 shows a vertical temperature profile determined from the lidar sounding within a 10 minutes integration time. The comparison with the rawinsonde measured values at the same location shows a rather good qualitative agreement whereas deviations up to 2K to 3K are observed at those altitudes where the aerosol content is large. The localisation of the tropopause level can be determined from the lidar profile with an accuracy of 200 m which corresponds to the altitude resolution of the system.

As a conclusion to these tentative measurements made during a period of relatively high aerosol loading of the stratosphere, the determination of the temperature profile at the tropopause level using a dual wavelength lidar can be considered as feasible as far as the required accuracy does not exceed 1K to 2K. The localisation of the static tropopause level, which might be of value for the study of the troposphere-stratosphere exchanges on a global scale, can be made within 100 to 200 m.

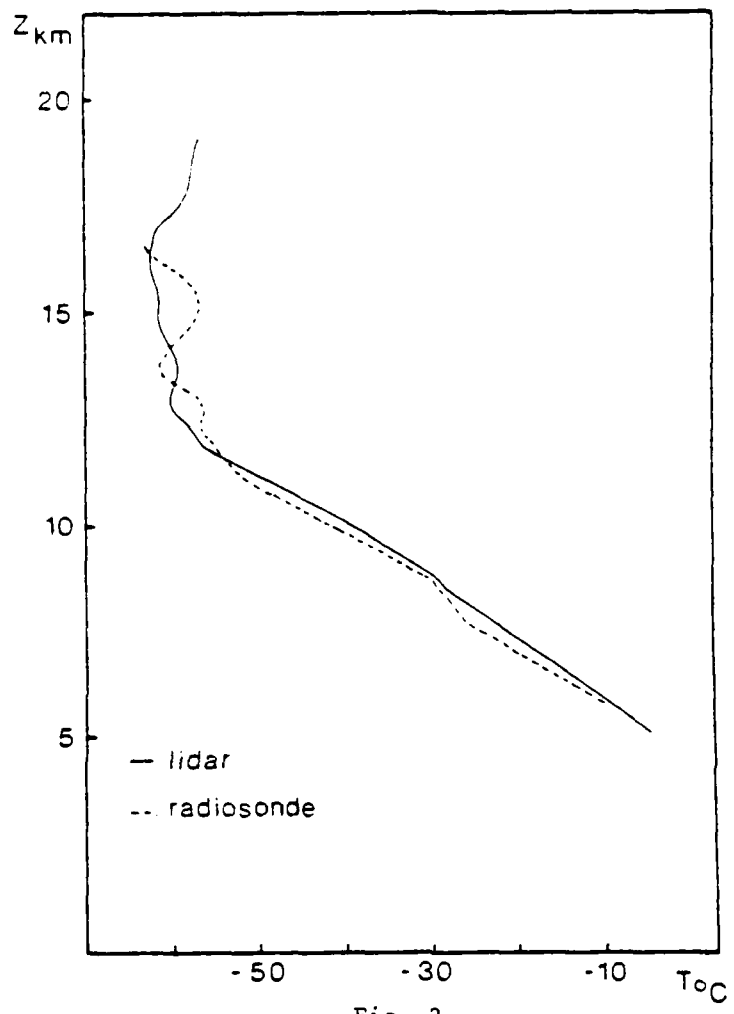


Fig. 2

REFERENCES

1. A. HAUCHECORNE, M.L. CHANIN, *Geophys. Res. Lett.* 7, 565 (1980)
2. NASA SP-433, *Shuttle Atmospheric Lidar Research Program* (1979)
3. J. LEFRERE, *Thèse 3<sup>e</sup> cycle*, Université Paris 6 (1982)
4. P.B. RUSSEL, P. SWISSLER, P. MCCORMICK, *Appl. opt.* 18, 3783, (1979)

## ADVANCED NEAR IR LIDAR FOR METEOROLOGICAL REMOTE SENSING

Geary Schwemmer, Mark Dombrowski, C. Laurence Korb  
NASA/Goddard Space Flight Center, Code 913  
Greenbelt, Maryland 20771

An advanced ground-based and aircraft lidar system has been designed and constructed for making differential absorption profile measurements of pressure and temperature. The high accuracy required for these measurements necessitates a high resolution laser system and a capability for accurately measuring the laser line profile. In addition, the requirements for aircraft operation provide an incentive for the development of a solid state laser system. The system we will describe could also be used to measure atmospheric density, humidity, and aerosols.

We have developed a dual wavelength lidar system (figure 1) which utilizes as the transmitted laser pair two ruby pumped dye lasers, or a solid state Alexandrite laser with a single ruby pumped dye laser. In the former configuration, a high resolution dye laser is used for the on-line measurements which is tuned to a particular resonant absorption feature. It has a spectral bandwidth capability of better than  $0.01 \text{ cm}^{-1}$  and is tunable from 720 to 770 nm using a grazing incidence holographic grating and a single intracavity etalon. A medium resolution dye laser is used for the off-line reference measurement since this channel does not require the high resolution needed for the study of resonant absorption features. Its bandwidth is as narrow as  $0.03 \text{ cm}^{-1}$  and has the same tunability as the high resolution lasers. Both have nominal pulse widths of 40 nsec and a one Hertz repetition rate as dictated by the ruby pump laser. The pulse energies are approximately 350 mJ for the high resolution laser and 100 mJ for the medium resolution laser. The Alexandrite laser operates with high resolution and can be used in place of either of the two dye lasers. Its characteristics are described in a later paragraph.

As shown in figure 1, the system includes provisions for monitoring the laser energies and the detailed spectral characteristics of the on-line laser output. Adjustable beam expanders are used to match the divergence of the two laser beams and a prism polarizer is used to coaxially transmit the orthogonally polarized beams. A quarter wave plate produces circularly polarized radiation to reduce systematic errors induced by any sensitivity to polarization. The laser beams are transmitted coaxially with the receiver telescope axis using a mirror located on the back of the telescope secondary. The energy backscattered from the atmosphere is collected with a 45 cm diameter Newtonian  $f/4.5$  telescope with a  $100 \mu\text{rad}$  minimum field of view.

Interference filters with bandwidths as narrow as 1 nm can be used for daytime measurements. The on-line and off-line laser pulses are separated in time so that a single detector/receiver channel may be used to observe both wavelengths. The temporal separation is adjustable from 100  $\mu\text{sec}$  to 1 sec, but nominal separations of 100  $\mu\text{sec}$  will be used to reduce uncorrelated noise in the return signals due to atmospheric scattering properties changing between the on and off line soundings. Two photomultipliers are used to increase the system dynamic range by

splitting off a small portion of the return signal to a medium gain tube to observe near field returns and sending the majority of the energy to a high gain tube to observe far field returns. Each tube is gated on only during its respective observation period. The times or altitudes at which the PMT's are turned on and off are real-time adjustable parameters so the operator can adjust for changing atmospheric conditions. CAMAC standard instrumentation is used in the data system. Ten bit, 20 MHz A/D converters which were designed in-house are used to digitize the PMT signals and the raw data are recorded on magnetic tape for post analysis. An LSI 11/23 microprocessor controls system functions and monitors all operator adjustable parameters in real time. These parameters are recorded along with the digitized lidar returns, data from the energy and spectral monitors, ground truth data, and housekeeping information.

Synthetic Alexandrite crystal is a relatively new laser material developed by Allied Corporation.<sup>1,2</sup> The Alexandrite laser combines advantages of solid state and dye laser systems. It has the broad tunability and high resolution of dye lasers, the efficiency and energy storage characteristics of Nd:YAG, and is Q-switchable. The Alexandrite laser in our system was developed particularly for our application. It is continuously tunable from 730-790 nm and it can be used to measure the broad range of meteorological parameters mentioned earlier. It has a resolution of better than  $0.02 \text{ cm}^{-1}$ , pulse energies of 100 mJ, pulse widths of 130 nsec and a 10 Hz maximum repetition rate. The spectral narrowing and tuning elements are a birefringent filter and two etalons, one of which is temperature tuned. We are now setting up the spectral instrumentation necessary to make high resolution measurements of the laser line shape, bandwidth and frequency stability to accuracies of  $10^{-3} \text{ cm}^{-1}$ , and will report on the results of these measurements.

In order to make routine measurements of the spectral characteristics of the on-line laser output, a ruggedized, advanced laser spectral wavermeter is being developed for our system by personnel at the University of Maryland. The basic design utilizes two Fizeau etalons and scanning diode arrays. One etalon measures the absolute wavelength to  $0.01 \text{ cm}^{-1}$ . The other will provide the capability to analyze detailed spectral characteristics to  $0.001 \text{ cm}^{-1}$  resolution. This information will be transmitted to the lidar data system for each laser pulse so the lidar data can be analyzed and corrected for finite laser bandwidth effects. The theory and method of analysis for this problem will be presented in a separate paper at this Conference.

Simulations of the performance of our ground-based system for temperature profiling using the P27 line of the oxygen A band are shown in figure 2. The lidar parameters are: a laser pulse energy of 0.1 J, a lidar spectral bandwidth of  $0.02 \text{ cm}^{-1}$ , a telescope area of  $0.2 \text{ m}^2$ , a receiver field-of-view of 0.3 mrad, an optical efficiency of 0.5, a quantum efficiency of 0.24, and a detection bandwidth of 1 nm. Noise sources considered included photon statistics, daytime background levels, and a 1% signal processing error for each layer. The results given are for a 500 shot average which corresponds to a measurement time of 50 seconds. As shown, accuracies generally better than 1 K can be obtained with 200 and 500 m vertical resolution.

A measurement program is now underway with the system described here. Initially, ground-based measurements will be made of vertical

pressure and temperature profiles. Later this year, the system will be flown in the NASA Lockheed Electra multi-user lidar facility, and will measure pressure and temperature profiles from the ground up through most of the troposphere. In addition, surface pressure will be measured or, in the presence of clouds, cloud top pressure heights. The modular nature of the system will allow quick and easy breakdown and setup so that the system can be moved from the laboratory to the aircraft and back with minimum effort. Future development efforts will be made to make the system as reliable, compact and efficient as possible with turnkey operation and a real-time data reduction capability.

#### References

1. J. C. Walling, O. G. Peterson, H. P. Jenssen, R. C. Morris, and E. W. O'Dell, "Tunable Alexandrite Lasers," IEEE J. of Quantum Electronics, QE-16, 1302 (1980).
2. C. L. Sam, J. C. Walling, H. P. Jenssen, R. C. Morris, E. W. O'Dell, "Characteristics of Alexandrite Lasers in Q-switched and Tuned Operations," Proc., Soc. of Photo-Optical and Instr. Eng., 247, 130 (1980).

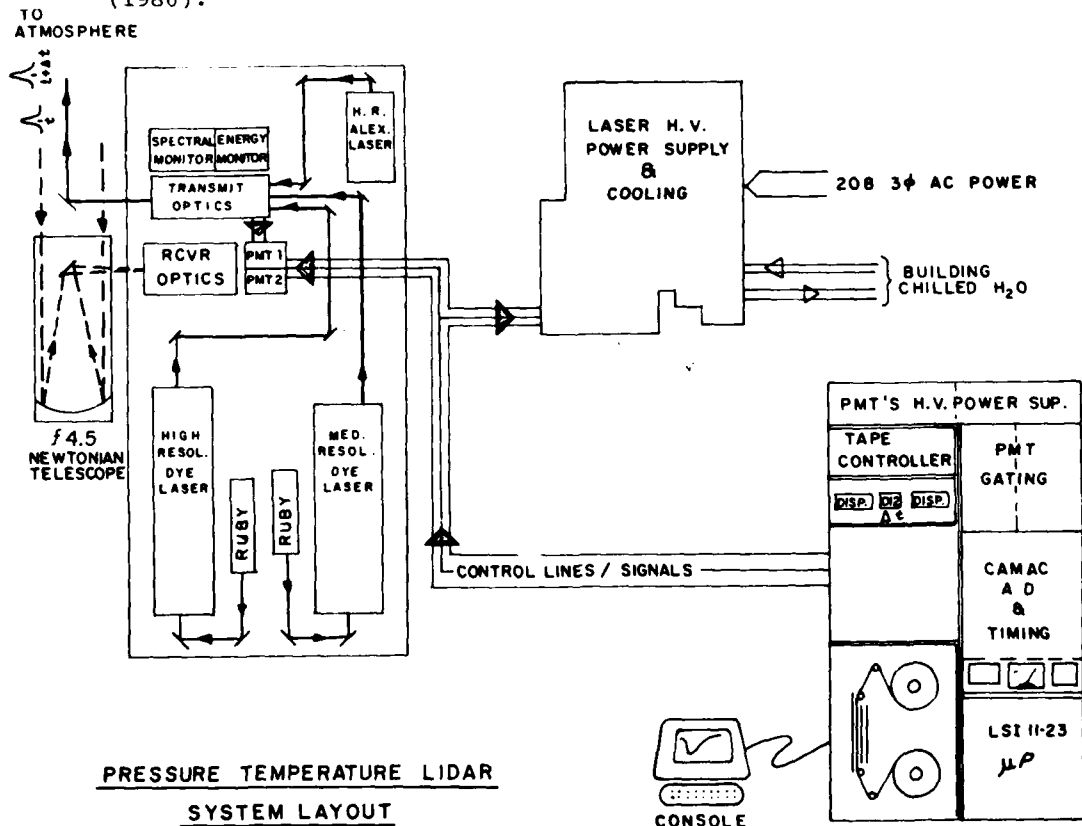


Figure 1. Lidar system layout. Main features include two ruby pumped dye lasers, Alexandrite laser, 45 cm diameter telescope, microprocessor controller and CAMAC data system.

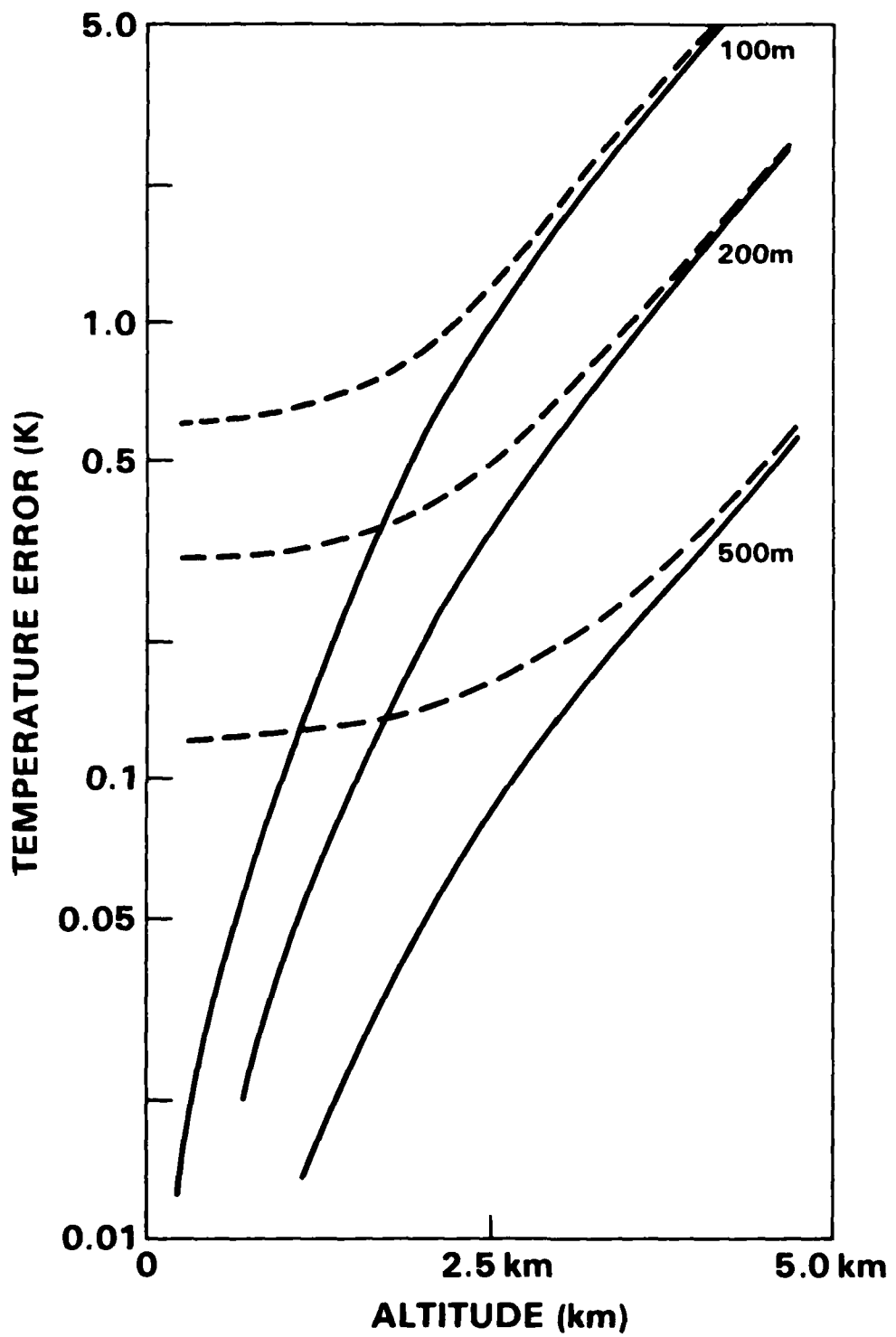


Figure 2. Performance simulations of ground-based lidar system for temperature profiling using the PP27 line of the oxygen A band. The solid curves include only signal shot noise; the dashed curves include all noise sources.

Remote Laser Measurement of Temperature and Humidity  
Using Differential Absorption in Atmospheric Water Vapor\*

P. Lebow<sup>†</sup>, S. Strobel, T. Wilkerson, L. Cotnoir  
Institute for Physical Science and Technology  
University of Maryland, College Park, MD 20742

and

A. Rosenberg  
RCA Corporation Astro Electronics  
P.O. Box 800 Princeton, N.J. 08540

Abstract

We have studied the effects of ambient temperature and humidity on laser beam absorption by atmospheric water vapor. A krypton ion laser pumped CW dye laser (Coherent model 599) with a  $\sim$ 1MHz bandwidth was tuned to selected water vapor vibrational absorption lines near 7200 Å. A second dye laser (Coherent model 595) was used concurrently for normalization of fluctuations in transmittance due to turbulence. Transmission over a 2km outdoor folded path to a 30" Cassegrain receiver was monitored as a function of psychrometer, thermometer and barometer readings for absorption lines of various ground state rotational energies (fig. 1).

This measurement incorporates characteristics of previous investigations, one performed by Endemann and Byer<sup>1</sup> and the other by Kalshoven et al.<sup>2</sup> As described by

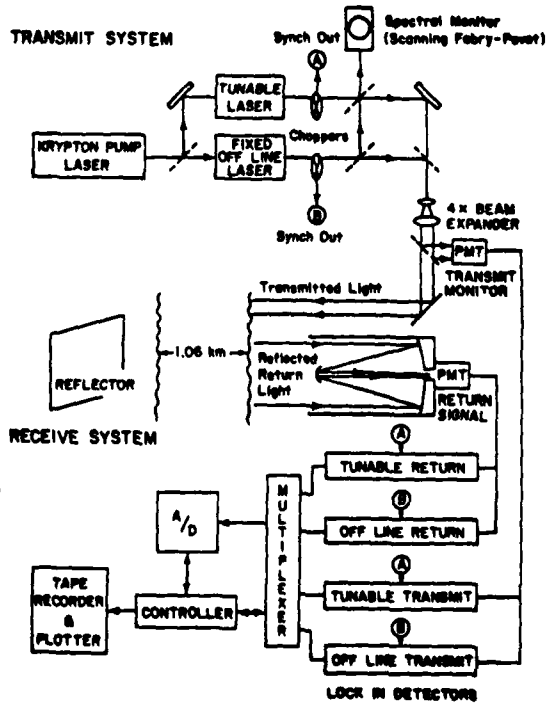


Figure 1. Experimental Arrangement

<sup>†</sup>Present address: Sachs/Freeman Associates c/o Naval Research Laboratory  
Code 6530, Washington, D.C. 20375

\* Research supported by University of Maryland, RCA, and ONR(N00014-78-C-0368).

Mason<sup>3</sup>, the Boltzmann factor temperature dependence of the ground state rotational level populations can measurably affect the line center absorption line strengths. In particular, for water vapor the following approximate relation is used:

$$\tau \equiv \ln(I/I_0) = L \sigma_0 \rho (T/T_0) \cdot 88 \text{ p}^{-1} e^{-E/K^{(1/T-1/T_0)}} \quad (1)$$

where

- $L$  = Path length
- $I$  = Measured intensity with laser tuned to absorption line
- $I_0$  = Measured background intensity with laser tuned away from absorption line
- $\sigma_0$  = Absorption cross section at  $T_0$
- $\rho$  = Water vapor number density
- $T$  = Ambient temperature
- $T_0$  = Reference temperature (296 K usually)
- $P$  = Ambient pressure
- $E$  = Ground state rotational energy
- $K$  = Boltzmann constant

For intensity measurements  $I_1$  and  $I_2$  on two lines of differing ground state energies  $E_1$  and  $E_2$  we have from (1):

$$\ln\{\ln(I_1/I_0)/\ln(I_2/I_0)\} \approx C + (E_2 - E_1)/KT \quad (2)$$

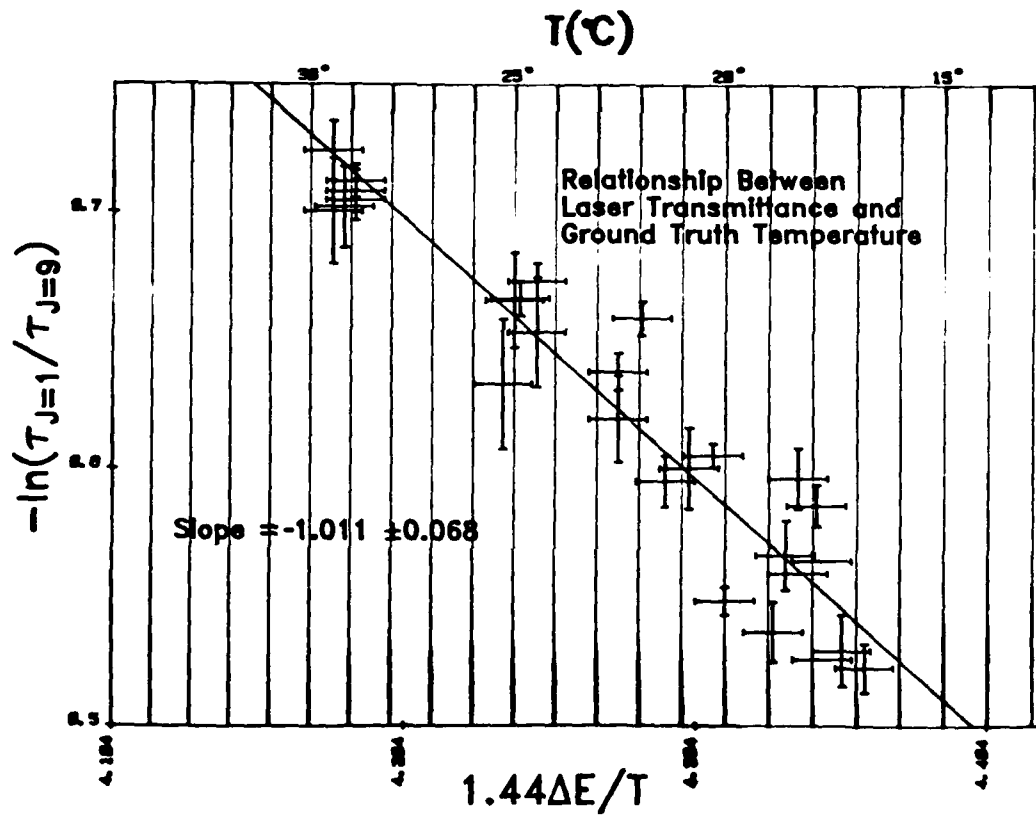


Figure 2.

where  $C$  is a constant which depends upon the individual absorption cross sections,  $\sigma_1$  and  $\sigma_2$ . We have verified the applicability of (1) and (2) to an outdoor measurement and have determined  $\sigma_1$ ,  $\sigma_2$  and  $C$  for a particular pair of lines. Most of our measurements were made on the lines at  $13602.631 \text{ cm}^{-1}$  ( $J=9$ ,  $E=920.169 \text{ cm}^{-1}$ ) and  $13650.017 \text{ cm}^{-1}$  ( $J=1$ ,  $E=42.372 \text{ cm}^{-1}$ ) over a  $15^\circ\text{C}$  temperature range. Figure 2 is an experimental plot of the left hand side of equation (2) verses the right with a linear fit exhibiting the expected slope of  $-1$ .

This experiment demonstrates the feasibility of using water vapor lines in this vibrational band for remote measurements of temperature and humidity. For various reasons, such as increased Mie backscatter, availability of laser sources, proximity to  $\text{O}_2$  lines and a wide range of easily resolved lines to choose from, this region of the spectrum is an attractive candidate for a single ended DIAL backscatter measurement of temperature and humidity. Suggestions for upgrading the technique will be discussed.

This experiment was carried out at the NASA/Goddard Optical Research Facility thanks to the generosity and cooperation of C.L. Korb, J. Kalshoven, and G. Schwemmer.

#### References

1. M. Endemann and R.L. Byer, *Appl. Opt.* 20, 452 (1981).
2. J.E. Kalshoven, Jr., C.L. Korb, G. Schwemmer, and M. Dombrowski, *Appl. Opt.* 20, 1967 (1981).
3. J.B. Mason, *Appl. Opt.* 14, 76 (1975).

## WATER VAPOR MEASUREMENTS BY USING A FAST-TUNING DIAL SYSTEM

Zhao Yan-zeng, Wu Shao-ming, Jin Hui-shu, Zhang Chun-lin, Hu Yu-liang, Huang Qi-rong, Huang Zhong-fang and Zheng Si-ping  
Institute of Atmospheric Physics, Academia Sinica,  
Beijing, China

A computer-equipped fast-tuning DIAL system for water vapor measurement is developed, in which the ruby laser emits two pulses in every fire with one pulse on-line and the other off-line.

Unexpected large fluctuations always exist in the ratio of the on-line and off-line lidar return signals in a single fire, though they can be reduced by averaging over several fires. We cannot attribute these fluctuations to the wavelength or time dependence of the aerosol properties because the wavelength difference of the two pulses is only 0.08 nm and the time intervals between them never exceed 0.3 ms. Neither can we interpret these fluctuations as results of noise or measurement errors. In addition, the fluctuation patterns often last for several minutes with certain range shifts. We expect to extract some new information from them.

Water vapor measurement results related to meteorological conditions are also analyzed in this paper.

REMOTE MEASUREMENTS OF TROPOSPHERIC  
WATER VAPOR WITH AN AIRBORNE DIAL SYSTEM

A. F. Carter, E. V. Browell, G. F. Butler<sup>1</sup>, M. N. Mayo<sup>2</sup>,  
W. M. Hall, T. D. Wilkerson<sup>3</sup>, and J. H. Siviter, Jr.

NASA Langley Research Center  
Hampton, VA 23665

This paper discusses recent measurements of water-vapor profiles in the lower troposphere which have been made with the NASA Langley Airborne Differential Absorption Lidar (DIAL) System. Measurements were made in the vicinity of NASA Langley Research Center and compared with in-situ data obtained from a locally launched radiosonde and with DIAL water-vapor measurement simulations. Remote measurements of water-vapor profiles such as those described in this paper are important for investigations of latent heat flux, air-mass modification over bodies of water, water-vapor transport into the stratosphere, and initialization conditions for weather forecast models.

The airborne DIAL system has been previously described in reference 1 and will only be briefly reviewed here. Two frequency-doubled Nd:YAG lasers are used to pump two independently tunable, high-conversion-efficiency dye lasers tuned in the near IR from 720 to 730 nm. The operational parameters for the DIAL system when measuring water vapor are given in table 1. A high-resolution frequency control system provided by M. L. Chanin of the CNRS, Verrieres le Buisson, France, maintains the "on-line" dye laser tuning coincident with the chosen water-vapor absorption line to within 0.3 pm. The 35-cm receiver system is optimized for water-vapor measurements by using photomultiplier tubes with enhanced response in the 720 nm region and by appropriate narrow-band interference filters. Initial ground preparation tests with the airborne DIAL system consisted of linewidth measurements of the dye laser. Water-vapor absorption measurements were then made in the zenith mode and in horizontal range tests over a 2-km distance to determine the appropriate effective absorption coefficients. The dye laser linewidth was determined to be approximately 25 mA. This was determined from interferometric measurements made in conjunction with an optical multi-channel analyzer and also from the reticon display on the wavelength control unit. Results from the vertical and horizontal water-vapor absorption measurements using the 723.22-nm absorption line gave an effective absorption cross section of  $15.5 \times 10^{-24} \text{ cm}^2$ . This corresponds to 83 percent of the expected cross section. The correlative measurements were made by a locally launched radiosonde for the vertical data and by a thermometer and psychrometer for the horizontal range test.

The first high-spatial-resolution airborne DIAL water-vapor measurements were made in November 1981. The flights were made in the vicinity of

---

<sup>1</sup>Old Dominion University Research Foundation, Norfolk, Virginia.

<sup>2</sup>Kentron Corporation, Hampton, Virginia.

<sup>3</sup>University of Maryland, College Park, Maryland.

Langley Research Center where radiosondes were launched to provide correlative water-vapor profiles. A comparison is shown in figure 1 of a series of measured water-vapor profiles and the correlative radiosonde data. The average of 200 DIAL measurements represents a horizontal resolution of about 4 km. The radiosonde data and the lidar data taken over Langley show agreement within the standard deviation of the DIAL data except in the region from 1500 to 2250 m altitude. The other water-vapor profiles were taken at 2-minute intervals as the aircraft proceeded upwind to Williamsburg, Virginia. These profiles show considerable horizontal inhomogeneity along the 20-km flight path. Aerosol data, taken simultaneously with the water-vapor data and also shown in figure 1, show changes in the vertical aerosol distribution for each of the water-vapor profiles. The horizontal inhomogeneity is not unexpected, as the measurements were made in the vicinity of a cold front. These water-vapor measurements, as well as other water-vapor data obtained during both day and night flights, will be discussed and compared with simulations.

In summary, airborne DIAL water-vapor profile measurements have been made in the lower troposphere and good correlations with radiosonde data obtained. These measurements demonstrated that an airborne water-vapor DIAL system can be used to conduct a broad range of atmospheric investigations.

#### REFERENCES

1. Browell, E. V.; Carter, A. F.; and Wilkerson, T. D.: Airborne Differential Absorption Lidar System for Water Vapor Investigations, Optical Engineering, 20, 84 (1981).

Table 1: Airborne H<sub>2</sub>O DIAL System Characteristics

Transmitter:	Two Pump Lasers -- Quantel Model 482 Pulse Energy -- 350 mJ at 532 nm Repetition Rate -- 10 Hz Pulse Length -- 15 ns Two Dye Lasers -- Jobin Yvon Model HP-HR Output Energy -- 63 mJ (18% Conv. Eff.) at 720 nm Beam Divergence -- 0.2 X 0.6 mrad Linewidth -- < 3 pm Laser Transmitted Energy -- 50 mJ at 720 nm Time Separation Between $\lambda_{on}$ and $\lambda_{off}$ -- 100 $\mu$ s
Receiver:	Area of Receiver -- 0.086m <sup>2</sup> Receiver Bandwidth -- 0.5 nm Receiver Efficiency to PMT - 29% Photomultiplier Type -- RCA Model 7265 with ERMA III Photocathode (Quantum Efficiency -- 4.8% at 720 nm)

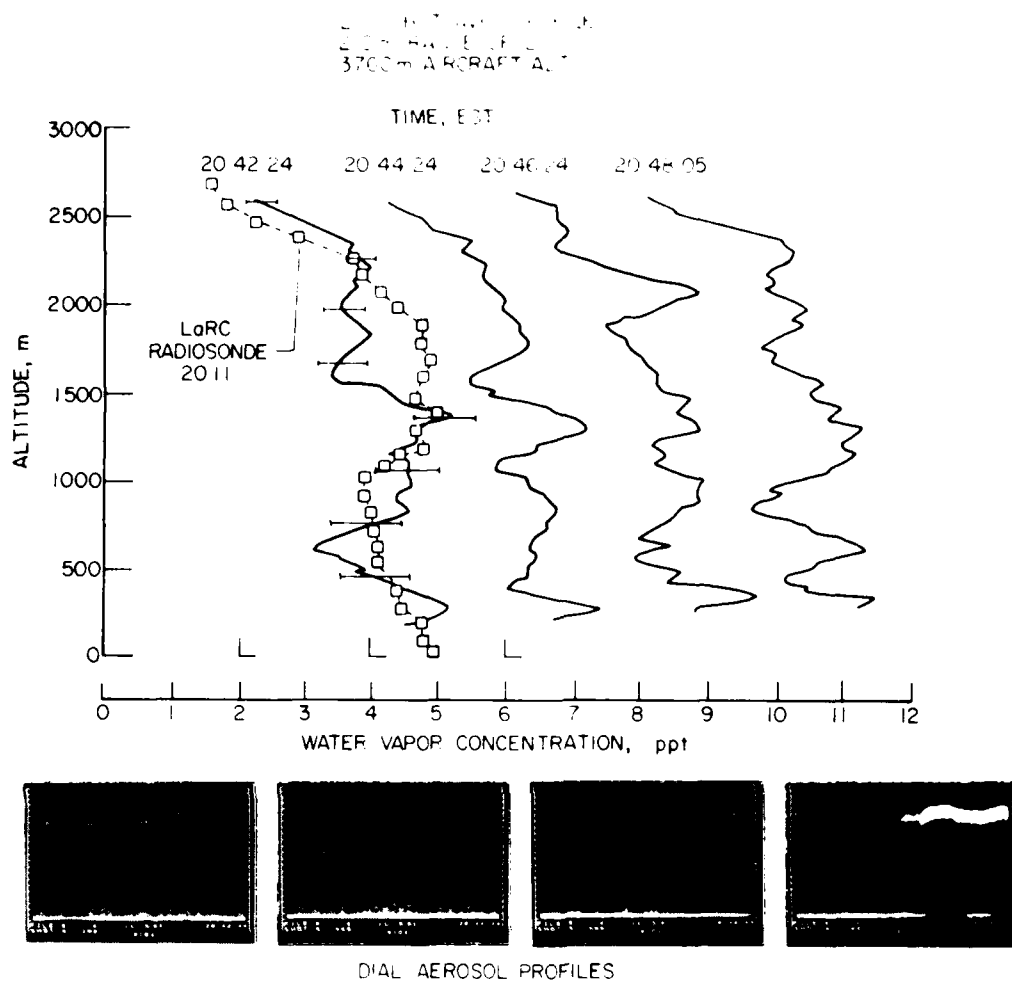


Figure 1: Airborne DIAL sequential water-vapor profiles obtained on November 6, 1981, between Hampton and Williamsburg, Virginia. The water-vapor profiles are offset by 2 ppt, and the sequential aerosol displays (150 m/vertical div.) correspond to the sequential water-vapor profiles.

SIMULTANEOUS MEASUREMENTS OF WATER VAPOR  
MIXING RATIO AND AEROSOL CONTENT USING A DIAL  
TECHNIQUE AT 0.72  $\mu\text{m}$ : COMPARISON WITH RADIOSOUNDINGS  
AND LIDAR MEASUREMENTS AT 1.06  $\mu\text{m}$

C. Cahen, J-L. Lesne, J-M. Michelin and J. Lefrère\*

Direction des Etudes et Recherches  
E.D.F.  
6, Quai Watier, 78400 CHATOU  
FRANCE

\* Service d'Aéronomie  
C.N.R.S.  
BP 3 - 91370 VERRIERE LE  
BUISSON - FRANCE

### 1 - Introduction

Besides the potentiality of the DIAL method at 0.72  $\mu\text{m}$  to monitor tropospheric water vapor up to 7-9 km<sup>(1)</sup>, one of the most attractive features of this method is the simultaneous measurement of water vapor and particle content with high time and vertical resolutions. The correlation between water vapor and particle behaviours leads to studies of perturbative effects of cloud formation or determination of mass transfer coefficient in the mixing layer<sup>(2)</sup>. Unfortunately in this altitude region, the absolute humidity as well as the particle content vary rapidly from one site to another. It is therefore necessary to adapt the choice of the absorption transition to the actual humidity and to account for the specific particle distribution.

Then to confirm the adopted measurement methodology we have organized a comparison campaign between water vapor lidar soundings, radiosoundings and 1.06  $\mu\text{m}$  lidar soundings at Aurillac, France (45°N, 3°E) where the observed absolute humidity is high. Here we present the results relative to the measurement validity: lidar soundings at two different wavelengths leading to spectroscopic calibrations and influence of temporal particle variations on water vapor profile accuracy.

### 2 - Generalities

The measured quantity by the DIAL method is the local optical thickness  $\Delta\tau_w$ <sup>(2)</sup>. To derive the expression of  $\Delta\tau_w$  the usual assumptions have been made: negligible spectral variations of the scattering medium between  $\lambda_{\text{ON}}$  and  $\lambda_{\text{OFF}}$  ( $\lambda_{\text{ON}} - \lambda_{\text{OFF}} \sim 0.05 \text{ nm}$ ), no absorption at  $\lambda_{\text{OFF}}$  (discrete absorption line), quasi-monochromaticity of the laser transmitter with respect to the absorption linewidth (laser linewidth/absorption linewidth  $\sim 0.2$ )<sup>(3)</sup>.

Due to the pressure-temperature dependence (via altitude dependence) of  $\Delta\tau_w$ , the measured quantity is the water vapor mixing ratio  $r_w$  provided that the lowest rotational energy level  $E''$  is  $\sim 330 \text{ cm}^{-1}$ <sup>(2)</sup>.

Combining this criterion with the optimization criterion of the DIAL method,  $\tau_w \sim 1.1$  ( $\tau_w$  integrated optical thickness between 0 and  $z$ )<sup>(4)</sup>, the suitable absorption lines for tropospheric measurements are  $\lambda_{ON} = 723.2$  nm for the upper troposphere and  $\lambda_{ON} = 724.3$  nm for the first hundred meters of the atmosphere.

The lidar system is basically the same as described elsewhere<sup>(1)</sup>. The main improvements to increase the system operability are the total electrical decoupling of the active source and the controlling and processing electronics by means of optical fibers, the change of telescope (dioptric telescope with Fresnel lenses,  $\varnothing = 38$  cm), and a precalibrated absolute positioning of the tuning element of the laser cavity associated with the multibeam Fizeau interferometer servo-loop device for wavelength positioning and switching (0.1 Hz).

### 3 - Comparison with radiosoundings - Spectroscopic measurements

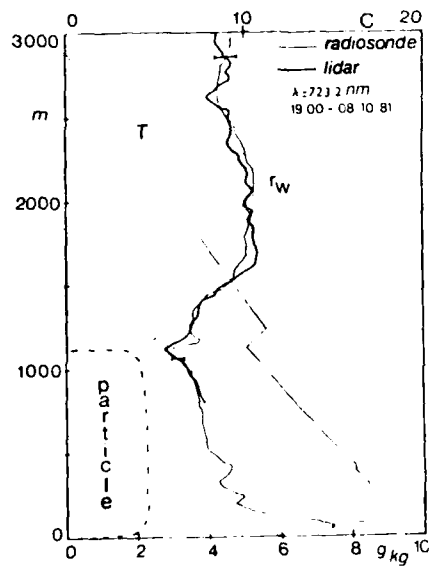


Fig.1 : Comparison LIDAR  
radiosounding at  $\lambda_{ON} = 723.2$  nm

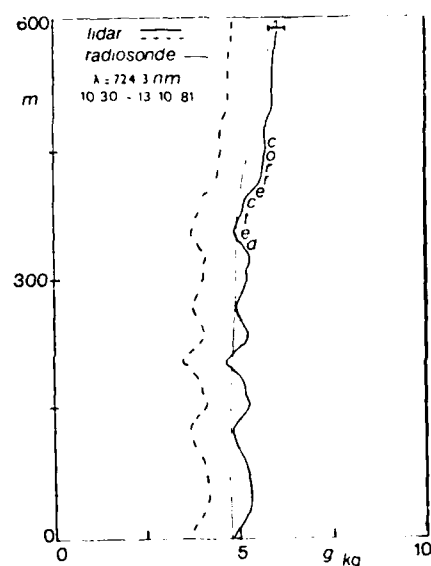


Fig.2 : Comparison LIDAR  
radiosounding at  $\lambda_{ON} = 724.3$  nm

- In the altitude region between 600m and 3000m, we show the comparison of laser soundings at  $\lambda_{ON} = 723.2$  nm with simultaneous radiosoundings (Fig.1). The time acquisition of the two methods is comparable ( $\sim 10$ mn), the vertical resolution is 15 m, the accuracy better than 15%. The agreement between the two profiles is good. Note that the two profiles exhibit a noticeable decrease of humidity at the top of the mixing layer the altitude of which is determined both by the temperature inversion measured by radiosounding and lidar measurements of particle content (Fig.1).
- For measurements in the first hundred meters of the atmosphere (0-600m) we use another transition,  $\lambda_{ON} = 724.3$  nm (the associated absorption cross section is higher). The comparison between laser soundings and radiosoundings is shown on Fig.2.

We note a systematic discrepancy ( $\sim 40\%$ ) at any altitude levels between the two profiles, a discrepancy which has been confirmed by several soundings. The good agreement between laser soundings and radiosoundings at  $\lambda_{ON} = 723.2$  nm demonstrates that there is no bias due to the lidar system. This discrepancy was then attributed to the adopted value of the absorption cross section  $\sigma$  at  $\lambda_{ON} = 724.3$  nm ( $\sigma = 910^{-23} \text{ cm}^2$  at S.T.P.)<sup>(5)</sup>. Therefore we have performed absolute humidity measurements with the laser system by means of a multipass cell (measurement of the ratio input energy/output energy). This ratio is averaged over 100 shots and the standard deviation is calculated from several series of 100 shots at a given wavelength controlled by the interferometric device. The equivalent path  $L = 450 \pm 15\text{m}$  of the multipass cell was exactly measured by means of a photomultiplier tube and a fast oscilloscope triggered by the laser pulse entering the cell. This procedure enables us to verify that the measured output energy corresponds to the light which has traveled exactly through the equivalent path.

The measured values at the two wavelengths ( $\lambda_{ON} = 724.3$  nm,  $\lambda_{ON} = 723.2$  nm) are reported in table 1 where corrections have been made to account for the departure of  $T$ ,  $p$  from S.T.P. for which cross sections are given ( $T = 292 \pm 0.5$  K,  $p = 954 \pm 10$  mb,  $U = 60 \pm 5\%$  - classical instruments plus radiosonde).

	$\lambda_{ON} = 724.3$ nm	$\lambda_{ON} = 723.2$ nm	reference
number density $10^{17} \text{ cm}^{-3}$	$2.15 \pm 0.08$	$3.17 \pm 0.12$	$3.32 \pm 0.17$

Table 1

Good agreement is obtained between the measured humidity at  $\lambda_{ON} = 723.2$  nm and the reference value for soundings, while at  $\lambda_{ON} = 724.3$  nm the discrepancy is  $\sim 35\%$ , a value comparable with the observed discrepancy for atmospheric measurements ( $\sim 40\%$ ). A similar discrepancy ( $\sim 20\%$ ) appears between the measured and theoretically deduced linestrength of this transition (C.Camy-Peyret and J.M. Flaud, private communication). Complementary spectroscopic measurements are needed.

#### 4 - Elimination of the temporal variations of the aerosol content

To determine exactly  $r_w$ , the assumption of the correct elimination of the temporal variations of the scattering medium between the sequentially emitted pulses at  $\lambda_{ON}$  and  $\lambda_{OFF}$  due to atmospheric transport is necessary. The short scale fluctuations are supposed to be random and to vanish on averaging.

We have compared successive water vapor profiles corresponding to a rather large acquisition time (10 min) recorded between 0-600 m where the

aerosol content is high. The aerosol variations are monitored with the 1.06  $\mu\text{m}$  lidar with a time resolution of 1 min.

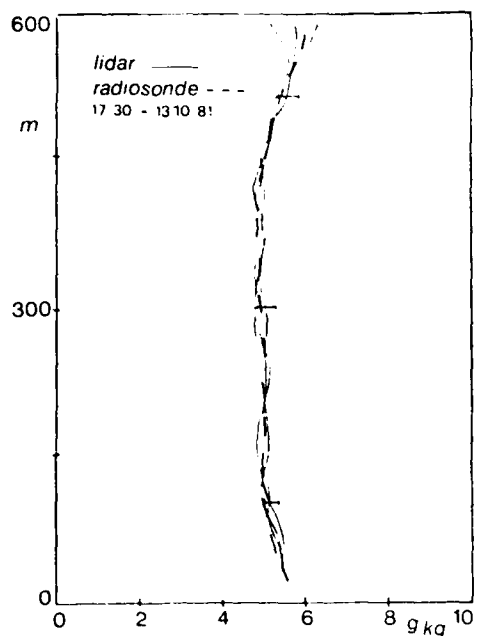


Fig. 3 : Successive  $r_w$  profiles

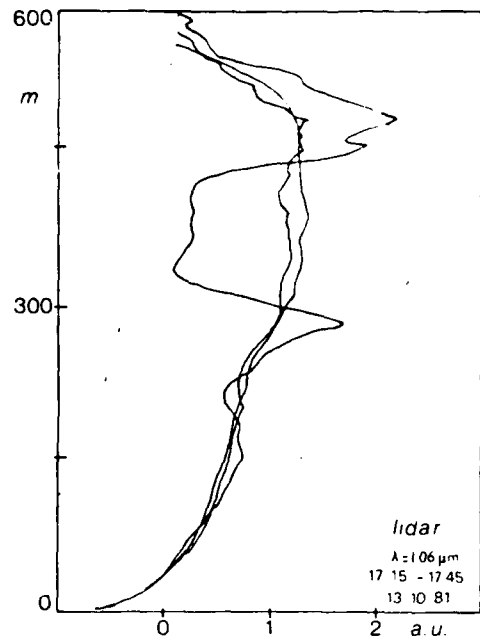


Fig. 4 : Observed temporal particle variations

While the aerosol content rapidly varies, we observe no significant variation of the water vapor profiles which are quite comparable with the radiosounding profile recorded simultaneously (Fig. 3, 4).

The adopted switching time (0.1 Hz) is short enough to take into account the modification of the backscattering medium though in the immediate vicinity of a cloud the simultaneous emission of the two wavelengths is probably required.

### 5 - Conclusion

The results obtained during this campaign demonstrate (1) the operationality of the lidar system leading to the development of a mobile lidar as required by our agency, (2) the necessity of complementary spectroscopic measurements, and (3) the validity of the DIAL method to determine both water vapor profiles and aerosol content, confirming its potentiality to deliver input data for meteorological studies such as transport and diffusion modeling.

References :

1. C.Cahen, G.Megie, P.Flamant, 1981-Proceedings of the IAMAP Symposium, Hamburg(Germany)ESA SP 165, p. 149.
2. C.Cahen, G.Megie, P.Flamant, 1982 subm. to J.Appl.Meteo.
3. C.Cahen, G. Megie, 1981, J.Quant.Spectroscop.Radiat. Transfer, 25, pp. 151 - 157.
4. E.E Remsberg,L.L Gordley, 1978, Appl Opt.17, pp.624 - 630.
5. T.D.Wilkerson,G.Schwemmer,B.Gentry, 1979, J.Quant.Spectroscop.Radiat.Tr. 22, pp. 315 - 331.

BOUNDARY-LAYER SOUNDING OF HUMIDITY  
AND AEROSOLS USING RAMAN LIDAR

D. RENAUT, C. BRUN  
Météorologie Nationale, EERM, 78470 St-Rémy-les-Chevreuse, FRANCE

R. CAPITINI  
Commissariat à l'Energie Atomique, CEN Saclay, DPC, FRANCE

SUMMARY

This paper presents some results of an experimental program conducted to check the possibilities of the Raman lidar for boundary-layer studies. Water vapor and aerosol profiles are measured within a range of 3 kilometers. Two Raman lidar systems are employed: the first one emits at 347 nm; at this wavelength, Raman detection is possible only at nighttime. The second one emits at 266 nm; in this "solar-blind" portion of the spectrum, Raman signals can also be measured during daytime.

NIGHTTIME MEASUREMENTS

The water vapor mixing ratio  $r(z)$  is obtained by ratioing the  $\text{H}_2\text{O}$  and  $\text{N}_2$  Raman signals:

$$r(z) = k_1 \cdot S(\text{H}_2\text{O}, z) / S(\text{N}_2, z)$$

where the constant  $k_1$  is determined by comparison with in situ measurements. Once the feasibility of the method was shown (1), a Raman lidar was designed at the EERM Center for meteorological use. The laser is a doubled-frequency ruby laser and the receiver is equipped with a double-path focal assembly in order to avoid errors due to temporal variations in atmospheric transmittance. Table I gives the technical specifications of the lidar and the equipment is fully described in (2). Alternatively, the profile of the aerosol scattering ratio  $R_d$  is measured using the Rayleigh-Mie and the  $\text{N}_2$  Raman signal:

$$R_d(z) = k_2 \cdot S(\text{RM}, z) / S(\text{N}_2, z)$$

The constant  $k_2$  is determined in very clear air, assuming that aerosol scattering is negligible. The two parameters  $r$  and  $R_d$  are measured at nighttime, and the experimental performances are summarized in table II. The self-consistency of the measurements has been verified by successive vertical soundings in stable conditions and by scans.

DAYTIME MEASUREMENTS

More recently, it was decided to extend the Raman measurements to daytime by means of a UV solar blind lidar. In the solar blind portion of the spectrum, boundary-layer ozone loading is large enough to produce a notable attenuation of UV light; moreover, this absorption is strongly wavelength-dependent and has to be taken into account. The water vapor mixing ratio is determined with the help of the three Raman signals for  $\text{O}_2$ ,  $\text{N}_2$ ,  $\text{H}_2\text{O}$  (3):

$$r(z) = k_3 \cdot [S(\text{H}_2\text{O}, z) / S(\text{N}_2, z)] \cdot [S(\text{O}_2, z) / S(\text{N}_2, z)]^\gamma$$

where  $\gamma = \Delta\sigma(\lambda_{\text{H}_2\text{O}}, \lambda_{\text{N}_2}) / \Delta\sigma(\lambda_{\text{N}_2}, \lambda_{\text{O}_2})$  is the ratio of the ozone differential absorption cross sections. The constant  $k_3$  is measured by comparison with in situ measurements. The UV Raman lidar was designed by the CEA for pollution measurements (4). The laser is a quadrupled-frequency YAG laser and the receiver is equipped with a monochromator. Table I gives the technical specifications of the lidar.

Qualification of the measurements was made previously using a laser with a slow repetition rate (5). Experiments with a 10 Hz laser began recently; experimental performances are summarized in table II.

## EXPERIMENTAL RESULTS

A general experiment was conducted in November and December 1981 at the Meteorologie Nationale Research Center in order to qualify and compare various boundary-layer monitoring systems; it involved the two Raman lidars together with a triple Doppler sonar, radio-sounding equipment, wind radar, and ground sensors. Results are now under examination. Examples of comparison with radio soundings are shown for the 347 nm lidar (fig. 1) and the 266 nm lidar (fig. 2). The daytime lidar elevation angle is now limited to 45 degrees, thus limiting its height range to about 1.5 km.

Preliminary conclusions of the experiment for the lidar measurements are the following:

- For water vapor measurements, the agreement is good between the 347 nm lidar and the radio sounding. However, the poor average power of the laser limits the accuracy of the lidar measurement. For the daytime lidar, the agreement is generally good but some cases of discrepancy have been evidenced. Up to now they are attributed to a relative inaccuracy in signal digitizing, to an aerosol fluorescence effect in hazy atmospheres and to the sequential measurement of the three Raman lines.
- The aerosol profile (nighttime) gives very useful information on the structure of the boundary layer (inversion layers, mixed layers, cloud cover and air masses limits), well correlated to the temperature-humidity profile. Daytime measurements have been tried with a method similar to that for  $H_2O$  determination; good retrieval of the aerosol profile is made difficult by the great sensitivity to ozone attenuation.
- The time continuity of the lidar measurements allows one to describe short-lived evolutions which are not seen by the conventional sounding.
- Technical improvements (multicanal detection, signal electronic processing) are planned to get a better viability of daytime measurements; beyond, the lidar system should be automatic to allow continuous monitoring without human intervention.

- (1) J. C. POURNY, D. RENAUT, A. ORSZAG - Applied Optics, vol. 18, 1141 (1979).
- (2) D. RENAUT and others - note technique EERM n° 94 (1981).
- (3) D. RENAUT, J. C. POURNY, R. CAPITINI - Optics Letters, vol. 5, 233 (1980).
- (4) R. CAPITINI, E. JOOS, D. RENAUT Paper at 3rd IAMAP, lidar session Hambourg (1981).
- (5) D. RENAUT, R. CAPITINI, J. C. POURNY La Météorologie VIe série n° 25 (1981).

TABLE I  
Technical specifications of the two Raman-lidar systems

	EERM Raman-lidar	CEA Raman-lidar
lidar configuration	parallel	coaxial
laser	doubled ruby 347 nm	quadrupled Nd YAG 266nm
laser energy	800 mJ	80 mJ
laser repetition rate	1/60 Hz	10 Hz
telescope	Cassegrain Ø 40 cm	Cassegrain Ø 60 cm
Optical filter	double path, interference + blocking filters	one path, double monochromator
Optical bandwidth	2 nm	1.8 nm
Optical transmission	1% (RM) - 9% (N <sub>2</sub> ) 3% (N <sub>2</sub> ) - 16% (H <sub>2</sub> O)	15%
PM efficiency	25%	25%
acquisition system	biomation 8100 (8 bits, 2 x 100 ns)	Tektronix 7612 D (8 bits, 2 x 5 ns)
processing system	Intel MDS - 800	Tektronix CP 4165

TABLE II  
Experimental performances for the measurements

	aerosol scattering ratio	water vapor mixing ratio
laser wavelength	347 nm	347 nm
operation	night	night
maximum range	3 km	3 km
range resolution	30 m 150 m at 2 km 400 m at 3 km	30 m at 1 km
accuracy	10% at 1.5 km 20% at 3 km	10% constant
sounding duration	4 mn	10 mn
		8 mn

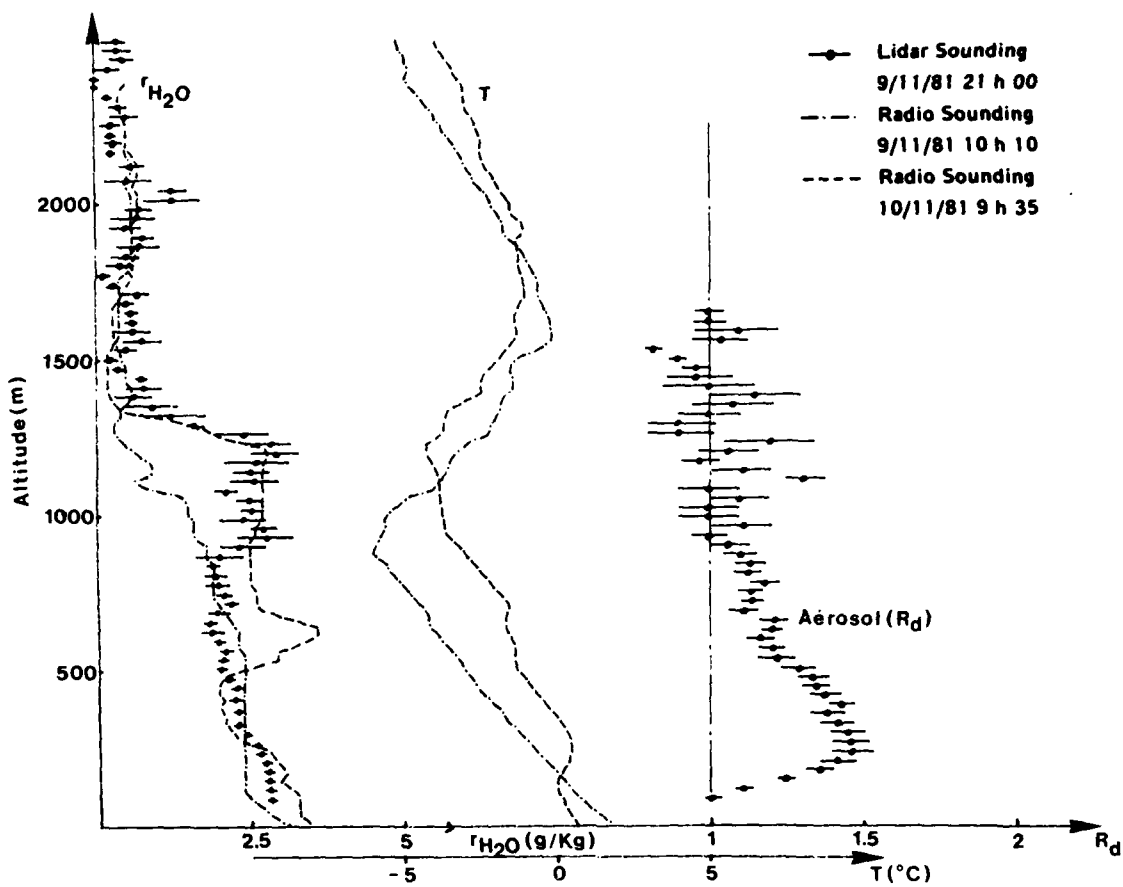


Fig. 1 : Comparison of the nighttime lidar profiles with two aerological soundings

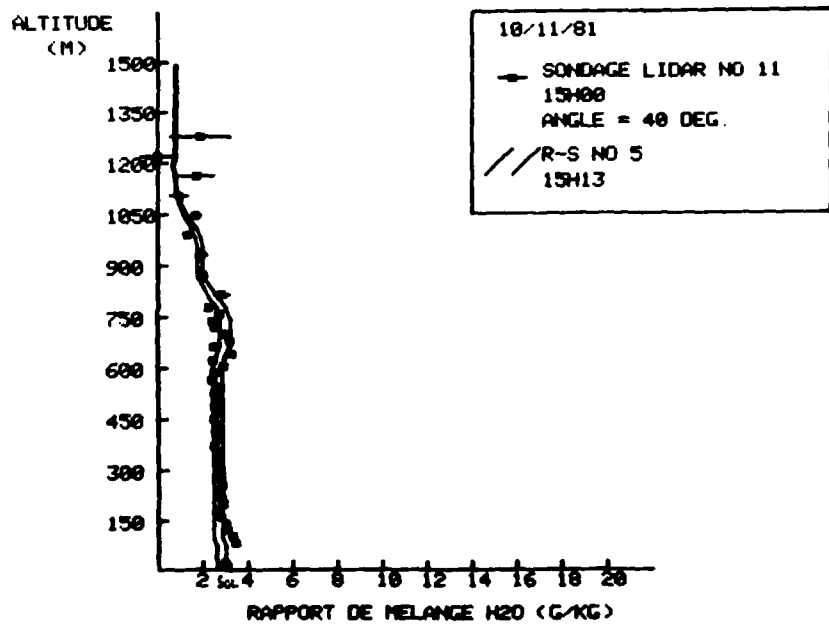


Fig. 2 : Comparison of the daytime lidar profile with an aerological sounding

## RAMAN WATER-VAPOR LIDAR

M. Z. Hansen, S. H. Melfi, J. D. Spinhirne  
and D. Clem  
NASA/Goddard Space Flight Center, Code 913  
Greenbelt, MD 20771

One of the most important mechanisms for the transfer of energy from the earth's surface to the atmosphere is through latent heat due to the evaporation of water from the surface into the atmosphere. This transfer process involves highly structured water vapor mixing in the boundary layer which requires maximum observation times of about one minute and vertical resolution of 50 meters. A knowledge of this structure is needed as input to global climate models and mesoscale severe storm models.

The objective of this research is to observe the vertical structure of water vapor utilizing a high spatial and temporal resolution lidar. The ultimate goal is to develop an improved parameterization scheme for water-vapor fluxes in the boundary layer.

An evaluation of the two most promising lidar methods for remote water vapor measurements (Raman and differential absorption) was performed. Analyses show that when short range, high spatial resolution measurements of reasonably high concentration molecular species are required (as for water-vapor measurements in the boundary layer), the Raman lidar technique is preferred (Fig. 1). This is particularly true of nighttime measurements when the background levels are low.

Based on the theoretical evaluation, construction of a Raman lidar system was undertaken. Due to the difficulty of the measurement, a powerful transmitter and a large receiver were required. The major area of hardware improvement in recent years has been the laser technology, where reliability and power have greatly increased. Details of the equipment are presented in Table I. The system was installed in a trailer to make it mobile. Presently, the lidar is undergoing initial testing. The results of these first measurements will be presented. Future plans include taking the equipment to the Eastern coast for marine boundary-layer water-vapor measurements.

TABLE I.- LIDAR CHARACTERISTICS

Transmitter

laser	ND:YAG III
wavelength	355 nm
pulse energy	150 mJ
repetition rate	20 Hz maximum

Receiver

mirror	60 inch diameter
H <sub>2</sub> O return	408 nm
N <sub>2</sub> return	387 nm

Data Acquisition

digitizers	8 bit/20 MHz
computer	LSI 11/23

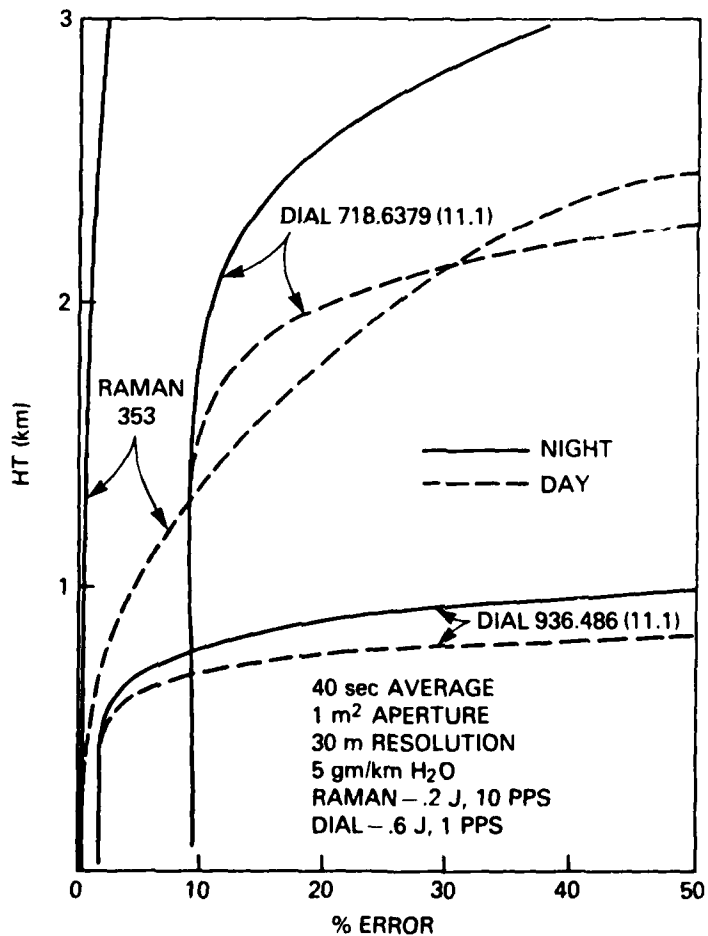


Figure 1.- Ground-based water-vapor measurement.

TWO YEARS OF EVALUATION AND TESTING OF A MOBILE  
LIDAR SYSTEM FOR AIR POLLUTION MONITORING

K. Fredriksson and H. Hertz

National Swedish Environment Protection Board,  
Studsvik, S-611 82 Nyköping, Sweden

A national mobile lidar laboratory was developed in 1979 at the Chalmers University of Technology, which was then the base for our research activities. The laser remote sensing was recently reviewed (1), and the mobile lidar system was described in detail in a recent paper (2). When the construction of the mobile system was completed in 1980 we began an evaluation and development phase for the system and its applications at the Research Department of the Env. Prot. Board. For a period of two years the system was further developed and operated at several field tests. The results of the field work were presented in national reports and in papers being prepared. A paper on the conclusions from the complete testing and evaluation phase will also be published.

The goal for the evaluation period was to be a guidance and also to form the basis for the future research and routine measurement program with the lidar techniques in Sweden. The emphasis on the work was to develop operational routines for the monitoring of  $\text{NO}_2$ ,  $\text{SO}_2$ ,  $\text{O}_3$ , and particulates, but the activities was also directed towards the future research in this field, including extensions of the DIAL technique to include other gaseous pollutants and also meteorological applications of the lidar techniques. From the experiences and conclusions from the work, decisions will be made on the forming of an organization for routine monitoring of air pollutants. In this conference contribution, examples of results from the field work and the experiences from the evaluation phase will be given. The directions for the future activities in the Swedish lidar program will also be presented.

The mobile lidar laboratory is based on an Nd:YAG laser and a dye laser. The basic design of the system is shown in Fig. 1. The laser beam is emitted from a rotatable dome structure on the roof of the covered truck. The optical and electronic arrangements of the mobile laboratory were given in Ref.(2). The entire system is run automatically utilizing a minicomputer. It has proved to be very reliable and well suited for field work. The set-up time for the system at a new measurement location is reduced to only a few minutes. The system was operated for a period of two years. In Table I, a summary of the activities is given. Besides the field work and laboratory studies, large efforts were made to develop efficient evaluation routines to convert measurement data into suitable forms of presentation.

A few examples of measurements from the field work are given here. Fig. 2. is a DIAL measurement of the  $\text{NO}_2$  concentration in a spreading smoke-stack plume from a saltpetre plant. The measurement curves at an absorption wavelength of  $\text{NO}_2$  and at a reference wavelength are given on a logarithmic scale. The divided DIAL curve is shown at top right in the figure. The  $\text{NO}_2$  concentration is evaluated as a function

of the distance in the fourth diagram. The range resolution for the evaluation is adequate for the physical situation in this case.

From a set of measurements of the type shown in Fig. 2. a charting of a plume in a vertical section can be made. Such a charting is shown in Fig. 3., where a horizontal map of the measurement site is also given. The vertical section of the plume in the direction indicated by the horizontal axis is shown. The plume is at an altitude of about 100 m in the vertical section.

In Fig. 4. an example of a DIAL measurement of ambient  $\text{SO}_2$  at a sulphuric acid plant area is shown. A map of the measurement site is shown in the figure. The diagram displays the  $\text{SO}_2$  concentration along a local street at 3-5 m height above the ground. The direction of the laser beam is given by the horizontal axis of the diagram. The concentration of  $\text{SO}_2$  originates from diffuse emissions in this case. A horizontal charting of  $\text{SO}_2$  in a paper-mill area is shown in Fig. 5. The charting is made from DIAL measurements in 16 different directions.

Table I Measurement programs for mobile lidar system

Studied parameter	No. of field tests	No. of measurement days (effective)
$\text{SO}_2$ at industrial plants (emissions and ambient)	3	12
$\text{NO}_2$ at industrial plants (emissions)	3	10
$\text{NO}_2$ in urban areas	6	17
$\text{O}_3$ (ambient)	3	8
Particulates (plume spreading, charting)	4	12
$\text{H}_2\text{O}$ vapour	1	4

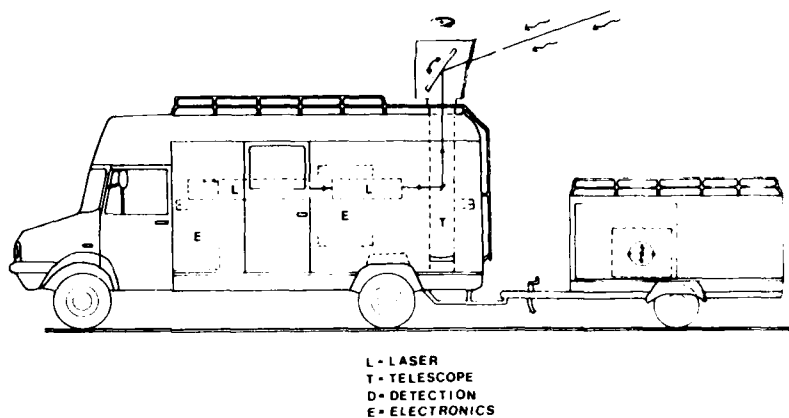


Fig. 1. Mobile lidar laboratory.

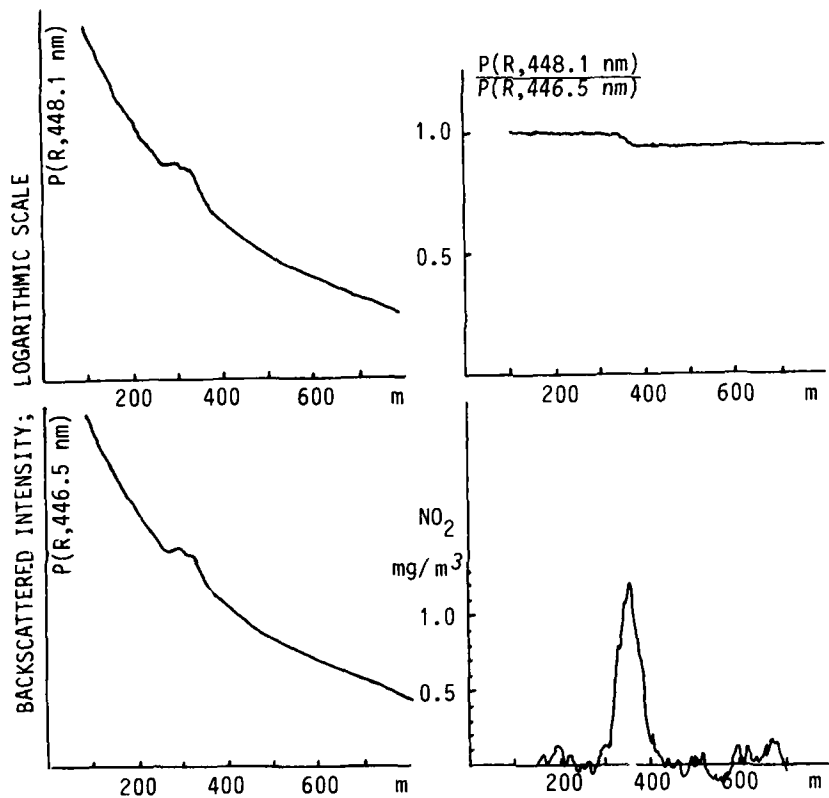


Fig. 2. DIAL measurement of a spreading plume from a saltpetre plant. The evaluation of the concentration, which is shown in the fourth diagram, was made with a distance resolution of 50 m.

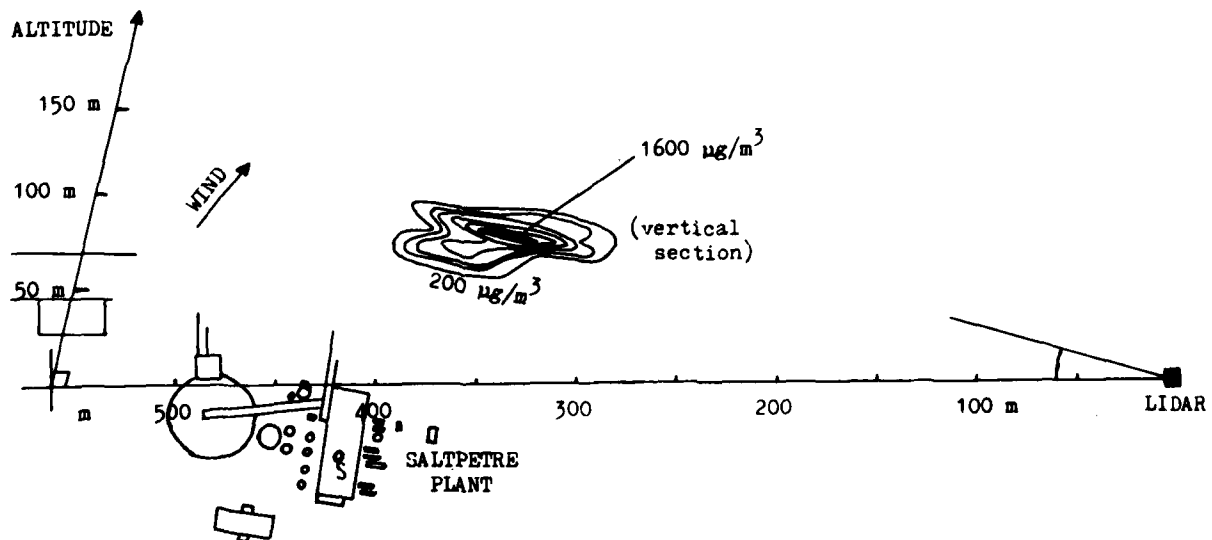


Fig. 3. Charting of  $\text{NO}_2$  in a spreading plume. The vertical section in the direction given by the horizontal axis is displayed. The main source is marked with an S in the figure.

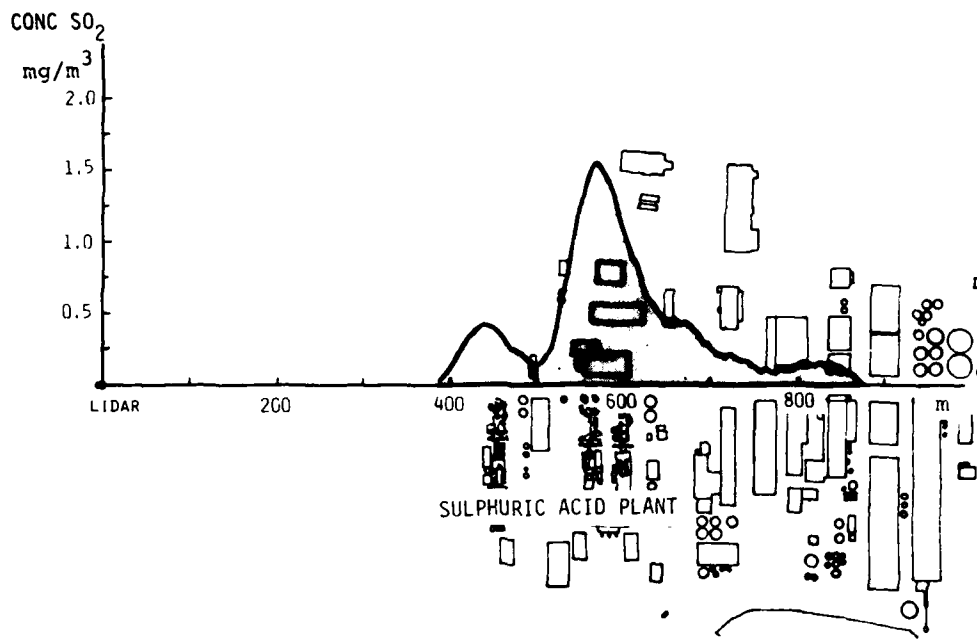


Fig. 4. DIAL measurement of  $SO_2$  in the ambient air at a local street in a sulphuric acid plant area. The direction for the laser beam is given by the horizontal axis.

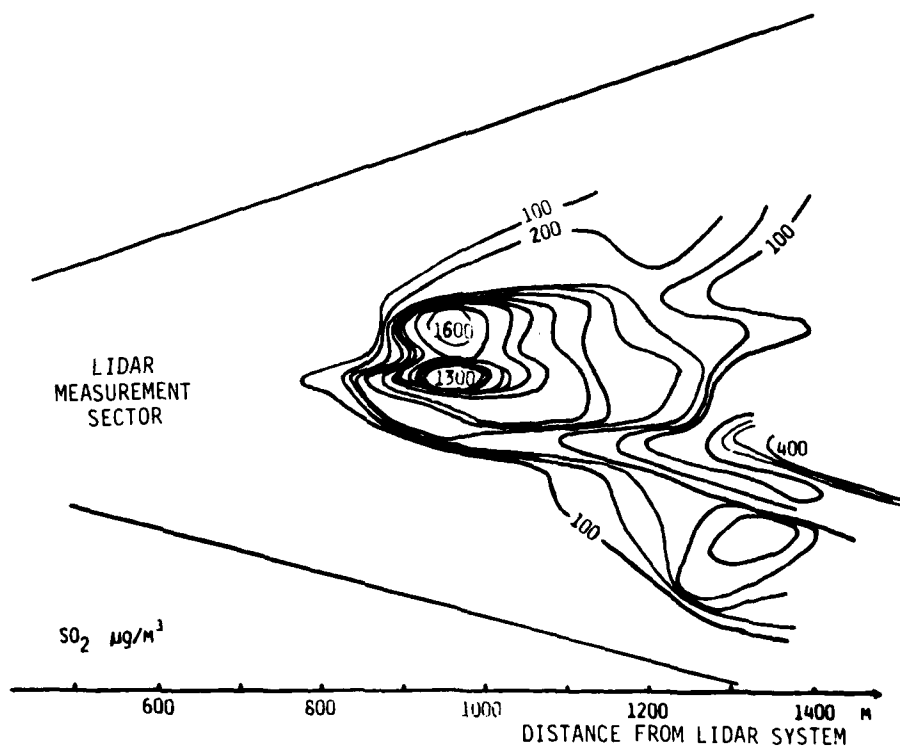


Fig. 5. Charting of  $SO_2$  concentrations in a paper-mill area. Each level represents  $100 \mu\text{g}/\text{m}^3$ . DIAL measurements in 16 directions were made for the charting.

Fig. 6. shows a study of the  $\text{NO}_2$  concentration along a city street. The laser beam was directed along the street and the mean concentration for a 500 m path was determined. The results from a large number of 2-minute measurements are summarized in the diagram. In this study the differences in subsequent single measurements were found to be very low.

The DIAL technique can be very useful for the determination of the total flow of a gas from an area or in a smoke-stack plume. The diagram in Fig. 7. is a charting of the  $\text{SO}_2$  concentration in a vertical section downwind of a chemical factory area. The distributed plume is due to diffuse emissions from a sulphur acid plant, whereas the dense plume at a higher altitude comes from a stack. The readings in the diagram give the total concentration in the vertical section. These numbers times the wind velocity yield the flows of  $\text{SO}_2$  from the area. Fig. 8. shows another form of presentation of a measurement of the  $\text{SO}_2$  flow through a vertical section. In this case an integration of the  $\text{SO}_2$  concentration with the altitude is made. The diffuse emissions from the plant area and a dense plume are displayed in the diagram. The readings in the diagram give the same type of information as in the former example, Fig. 7. Whereas a complete charting of a gas of the type shown in Fig. 7. is rather time-consuming, this type of measurement integrated with the altitude is a rather rapid way of determining the flow. Sofar wind data has been obtained from alternative measurements. A technique for measuring the wind based on lidar is planned.

In the near future the mobile lidar system will be used for routine measurements and for special atmospheric studies in cooperation with other research groups. We will also strengthen our efforts in the lidar research by relocation of our facilities to Lund, where we will establish a joint center for laser studies of air pollutants at the Lund Institute of Technology. Further, we are planning to construct a new version of the mobile lidar laboratory, which will be somewhat bigger and will extend the possibilities to study other gaseous pollutants in the UV and IR wavelength regions.

This work was sponsored by the Swedish Space Corporation and the National Environment Protection Board.

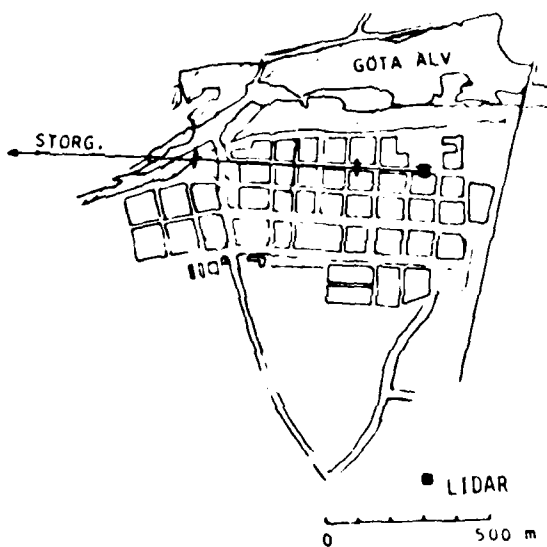
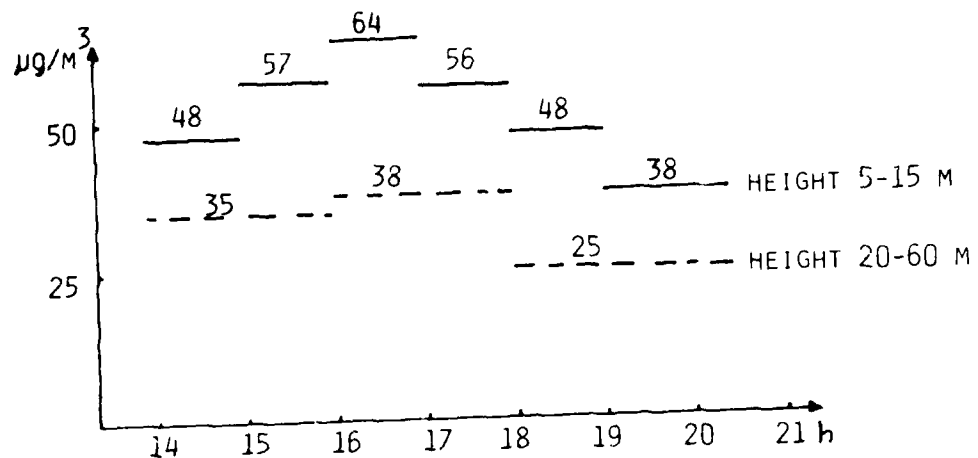


Fig. 6. Study of  $\text{NO}_2$  concentrations in an urban area. The laser was directed along a city street according to the map in the figure. The mean concentration from 300 to 700 m was evaluated. The diagram is a summary of a large number of 2-minute measurements.

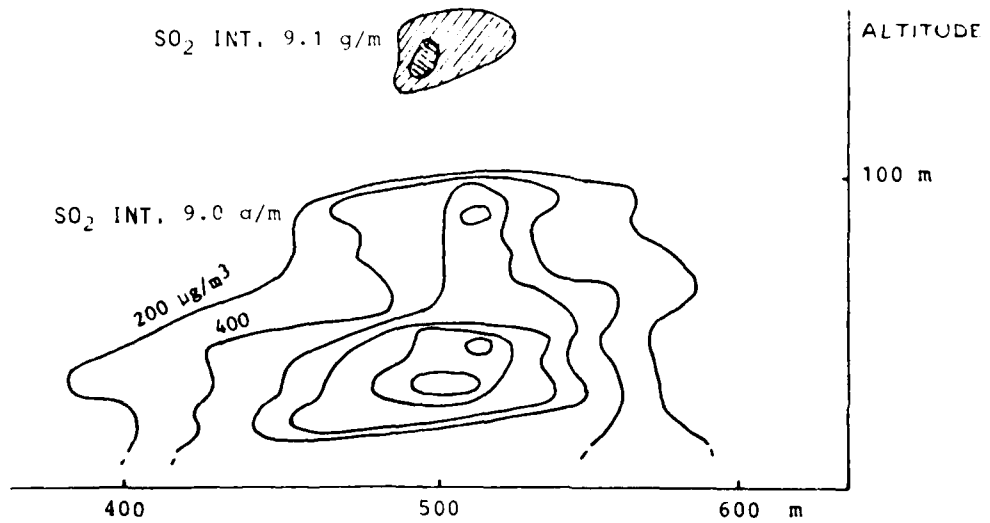


Fig. 7. Charting of  $\text{SO}_2$  in a vertical section downwind from an industrial area. The total flow of  $\text{SO}_2$  from the area can be calculated from the gradient in the figure and the wind data.

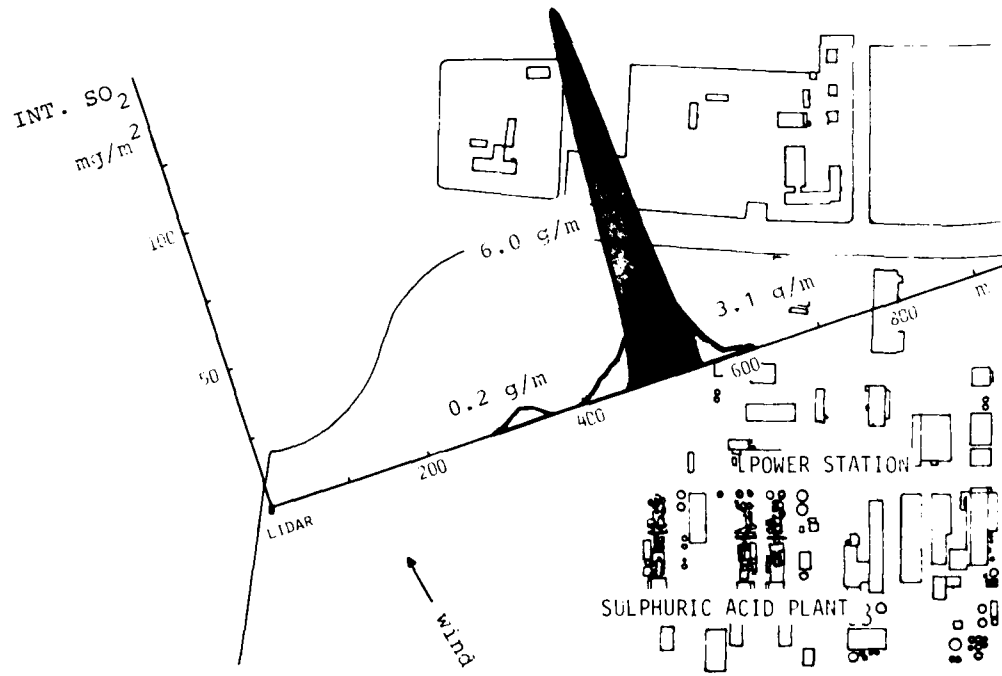


Fig. 8. Measurement of the integrated vertical profiles of the  $\text{SO}_2$  flow from an industrial area. Two diffuse emissions and one dense plume are displayed in the figure. The direction of the vertical section is given by the horizontal axis. This measurement and the wind data yield the flow of  $\text{SO}_2$ .

### References

1. K. Fredriksson, Laser spectroscopy applied in studies of alkali-atom structures and in environmental monitoring, Ph.D. dissertation, Göteborg 1980.
2. K. Fredriksson, B. Galle, K. Nyström, and S. Svanberg, Mobile lidar system for environmental probing, *Appl. Opt.* 20, 4181 (1981).

EXPERIMENTAL STUDY OF REMOTE ATMOSPHERIC POLLUTION MONITOR BASED ON  
DIFFERENTIAL ABSORPTION OF CO<sub>2</sub> LASER RADIATION

P. Vujković Cvijin  
Institute of Applied Physics  
P.O. Box 58, 11071 Novi Beograd, Yugoslavia

The necessity for a practically usable remote atmospheric pollution monitoring device has been well recognized for a long time. Designs for three versions of a remote pollution monitor intended for field applications in urban and industrial environments are reported.

A CO<sub>2</sub> laser-based differential absorption technique was chosen because of its ability to measure trace amounts of pollutant gases present in urban and industrial atmospheres, with ethylene being the most interesting one because of its presence in motor vehicle exhaust and in the polluted atmosphere over some chemical plants. The differential absorption technique is a spectroscopic one and relies on the use of selected laser wavelengths in coincidence with the absorption features of pollutant gas.

Three experimental models were investigated in the course of this study. The first two models were based on the long-path bistatic scheme where the return radiation was provided by distant retroreflectors. This approach resulted in the design of a rugged remote pollution monitor of moderate cost. A small-scale low-powered pulsed CO<sub>2</sub> laser was used as the tunable radiation source. The retro-reflected radiation was collected by 6.5-cm and 20.3-cm aperture telescopes for the two models, respectively. The received radiation was focused onto a lithium-tantalate pyroelectric detector. Due to its ruggedness and ambient temperature operation, the pyroelectric detector made the whole system advantageous for field applications. A signal averaging technique was used for return radiation intensity measurements. Experimental investigations were carried out at retroreflector distances up to 1200 m with the sample chamber immediately in front of the retro-reflector. System sensitivity defined as the equivalent concentration-pathlength product for which the measured average uncertainty equals concentration was found to be of the order of several ppb-km of ethylene. Test measurements with ammonia and freon 12 were also performed.

The third experimental model investigated in this study was a monostatic one with backscattering from topographic targets providing the return radiation. Back-scattered radiation was collected by a 20.3-cm-aperture Newtonian telescope and detected by a liquid nitrogen cooled Pb Sn Te detector. In this system the operation of the CO<sub>2</sub> laser including the sequential tuning of selected wavelengths was controlled by a microprocessor. System sensitivity in this case was found to be comparable with previous models.

Due to the spectral region of operation, systems described here are favorable from the standpoint of eye safety, allowing their use for atmospheric pollution monitoring in populated urban and industrial environments.

## ATMOSPHERIC GAS MONITOR WITH LEAD-SALT DIODE LASER

Hiroya SANO<sup>†</sup>, Ryuji KOGA<sup>†</sup>, Megumi KOSAKA<sup>†</sup>, and Koji SHINOHARA<sup>‡</sup>

<sup>†</sup>Department of Electronics, Okayama University: Okayama 700, JAPAN

<sup>‡</sup>Fujitsu Laboratories Ltd.: 2-28, 1-Chome, Goshō-dori, Hyogo-ku, Kobe 652, JAPAN

**Abstract** - A portable, open-air, point atmospheric-gas monitor based on diode-laser absorption spectrometry was developed to attain high sensitivity by employing new techniques for suppression of optical-fringe noises. Methane density has been measured experimentally with 0.3 ppm sensitivity, and 4.7 ppb sensitivity is expected theoretically.

### I Introduction

A gas monitor which is (1) sensitive (below 0.01 ppm for  $\text{NO}_2$ ), (2) real-time (one datum every second), (3) non-contacting, and (4) local ( $1 \text{ m} \times 1 \text{ m} \times 1 \text{ m}$ ) is useful for personal safety and for studies of microscopic dynamics of the atmosphere including chemical reactions, according to the authors' opinion. Reid and his coworkers [1]-[4] have developed a point monitoring system with laser diodes and depressurized White cells to attain line separations. The White cell has a very long optical path length. They attained a very high sensitivity which is limited by optical fringes or standing waves at optical frequencies. The authors have examined a system employing a dye laser as a tunable light source [5]. Some fundamental techniques applied to the system are stated here.

The present system features a short optical path in open air that enables local and non-contacting monitoring with a small sized apparatus, and a spectrum scanning operation of the tunable lead-salt (PbSnTe) diode laser which leads to fast measurement (4 seconds for a datum) and high sensitivity (0.3 ppm proved and 4.7 ppb expected theoretically for methane) [6]. Employing a built-in computer which performs a density calculation based on the "adjoint spectrum" [7] gives an immunity to spectral interferences including window contaminations.

### II System description

A schematic diagram of the system is given in Fig. 1. The PbSnTe diode laser operates at  $\lambda = 7.7 \mu\text{m}$  and about 100  $\mu\text{W}$  power [8]. The laser is finely tuned over  $7 \text{ cm}^{-1}$  within a mode. Infrared detectors are of pc-type HgCdTe. These are mounted on Dewar vessels and cooled by liquid nitrogen. The optical beam for measurement is folded back with a corner-cube mirror system on a separate base plate. Thus, the optics can be mounted on a small sized base plate, which results in a light-weight apparatus. Behind the beam-splitter a cell is filled with a standard gas of the concerned species.

Optical components are of Ge and AR-coated, except the beam-splitting surface. The electronic systems are designed for second derivative spectrometry. The diode laser current is a sum of  $I_D$  (a nominal wavenumber in the spectrum which is kept constant over 1/60 s) and  $\delta_i$  (a periodic waveform of frequency  $f = 7.68 \text{ kHz}$ ). The

diode current is sharply cut off for 2  $\mu$ s after every 1/60 s. Two infrared detectors and independent but similar electronic signal processors are in the two optical legs. The output of each detector is fed to a lock-in amplifier tuned to a second harmonic frequency of 2f and to a pulse-height detector that gives a beam power impinging on the detector.

In order to obtain density data, 256 different values of  $I_D$  are scanned and two second-derivative absorption spectra,  $S_x$  for the measurement leg and  $S_r$  for the reference, are obtained. Both of these are already normalized by the optical input to each detector and are independent of the optical transmittance of the system at that wavenumber or at each time slot.

The desired density of the atmospheric gas is calculated by

$$c_x^{L_x} = c_r^{L_r} \frac{\langle S^*, S_x \rangle}{\langle S^*, S_r \rangle}, \quad (1)$$

where the symbol  $\langle \rangle$  denotes an inner product between two vectors, and  $c_x^{L_x}$  is the density-length product of the measurement path and  $c_r^{L_r}$  is that of the reference path. A weight distribution  $S^*$ , which is named an adjoint spectrum by the authors [7], has been generated from the measured  $S_r$  by

$$S^* = S_r - \sum_{j=1}^J \langle S_r, U_j \rangle U_j, \quad (2)$$

where  $U_j$ 's are an orthonormalized set of spectra that have been predicted to take part. Examples of them are a constant, a linear function or a known absorption spectrum of an interfering gas species.

### III Measurement accuracy

In development, efforts were made to reduce optical fringes in the obtained spectra. This phenomenon takes place due to the appearance of an unexpected cavity for the laser beam formed between two partially reflecting surfaces. It has been found theoretically that, for less vulnerability to optical fringes, the laser current modulation profile  $\delta_i$  should have spikes at its extreme and a repeated hyperbolic sine profile is preferable under a limited bandwidth of electronic circuits [9]. Effects produced by controlling the modulation profile are shown in Fig. 2. For the same response to a methane line, the response to the fringe is remarkably reduced from (a) for the sinusoidal profile to (b) for the triangular and further in (c) for a reflected hyperbolic sine.

Various modes of optical fringes can exist simultaneously. Among them, a mode provided by a cavity, one part of which is the laser, is usually most intense due to the amplification of the laser. An optical fringe of this type, however, can be suppressed by putting a quarter wave plate just in front of the laser, since the laser operates in a linearly polarized mode. A single-mode operation is required of the laser. If not, a span error appears, because Eq. (1) is based on the monochromatism of the laser light.

In experiments without the wave plate, the system sensitivity was about 0.3 ppm for methane, which is decided by a still persisting optical fringe despite the modulation-profile control. A statistical characteristic of fringe-induced noise resembles a so-called 1/f noise, which cannot be suppressed with numerical accumulation.

If the etalon fringe is reduced to its minimum, a random noise from the ir-detector is intrinsically dominant in our system. A resultant fluctuation in methane density is calculated to be 4.7 ppb in the value of standard deviation for the employed components. Owing to the density calculation with Eq. (1), the window contamination scarcely causes a base-line drift or a span error. This value will be reduced further if a more powerful diode laser [10] is employed.

#### IV Concluding Remarks and Further Problems

In diode-laser spectrometry for atmospheric-gas monitoring, optical fringes can be reduced by controlling the profile of the diode-current modulation and by a quarter wave plate. Numerical treatment with a  $\mu$ -computer along with the electronic normalization process lends an immunity from a spectral interference which gives a zero-drift in the measurement system.

The above results were obtained on an optical bench. A portable apparatus has been built and is being tested. Alteration of the diode-laser to one with shorter wavelength is planned for applications to NO or NO<sub>2</sub>.

#### References

- [1] J. Reid, J. Shewchun, B. K. Garside, and E. A. Ballik, *Appl. Opt.*, 17 (1978) 300-307.
- [2] J. Reid, B. K. Garside, J. Shewchun, M. El-Sherbiny, and E. A. Ballik, *Appl. Opt.*, 17 (1978) 1806-1810.
- [3] J. Reid, B. K. Garside, and J. Shewchun, *Opt. Quant. Electron.*, 11 (1979) 385-391.
- [4] J. Reid, M. El-Sherbiny, B. K. Garside, and E. A. Ballik, *Appl. Opt.*, 19 (1980) 3349-3354.
- [5] R. Koga, M. Kosaka, and H. Sano, *IEEE Trans. Instrum. Measurem.* (submitted).
- [6] H. Sano, R. Koga, M. Kosaka, and K. Shinohara, *Jap. J. Appl. Phys.*, 20 (1981) 2145-2153.
- [7] H. Sano, R. Koga, Y. Tanada and M. Kosaka, *Mem. Sch. Eng.*, Okayama Univ., 13 (1979) 181-193.
- [8] M. Yoshikawa, K. Shinohara, and R. Ueda, *Appl. Phys. Lett.*, 31 (1977) 699-701.
- [9] R. Koga, M. Kosaka and H. Sano, *Mem. Sch. Eng.*, Okayama Univ., 16 (1982) (to be published).
- [10] K. Shinohara, Y. Nishijima and T. Akamatsu, *Conf. Lasers and Electro-Optics, CLEO'82* (Phoenix 1982) FM6.

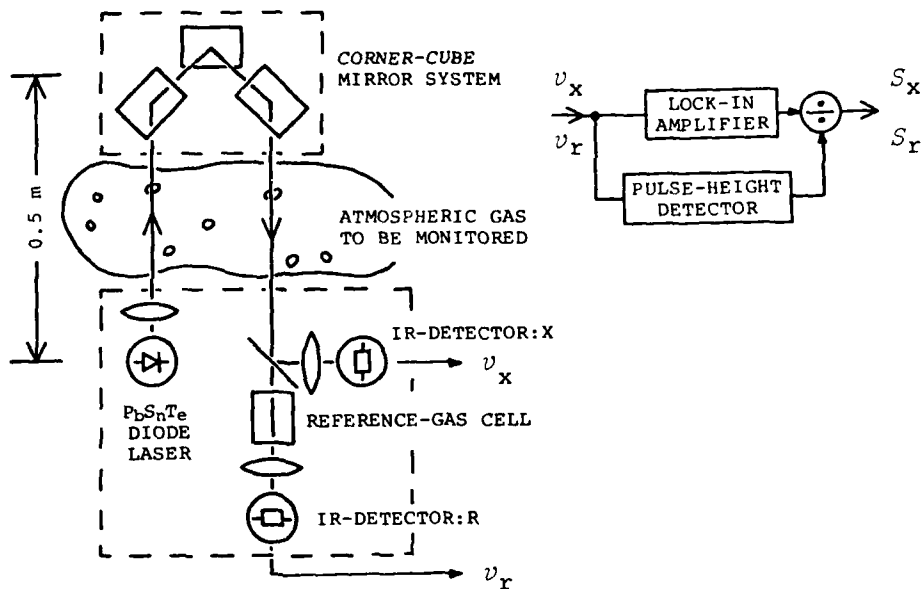


Fig.1 Schematic diagram of an optical head(left) and an electronic signal processor(right).

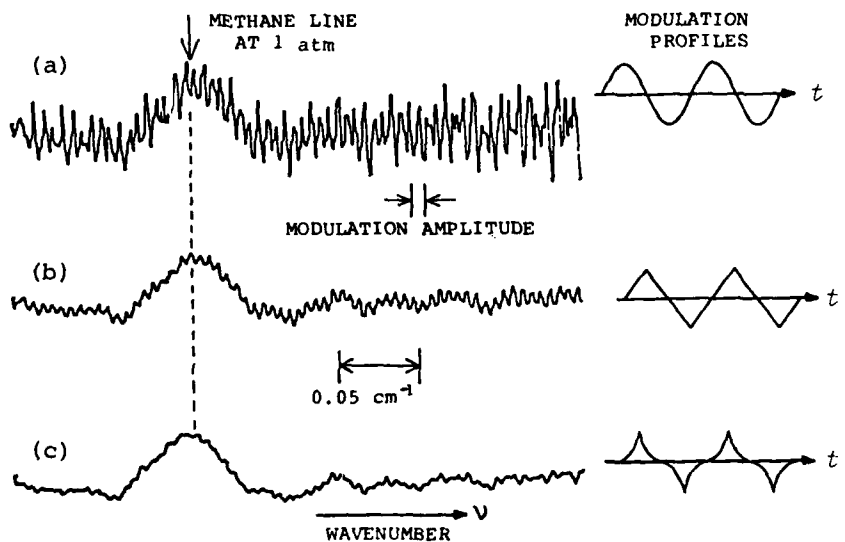


Fig.2 Effects of the laser frequency-modulation profile on an immunity from fine pitched optical fringes.

AIRBORNE LIDAR MEASUREMENTS OF OZONE AND  
AEROSOL PROFILES IN THE TROPOSPHERE AND LOWER STRATOSPHERE

E. V. Browell, S. T. Shipley, A. F. Carter, and C. F. Butler<sup>†</sup>  
NASA Langley Research Center  
Hampton, VA 23665

Introduction

This paper describes the first application of an airborne lidar to measurements of ozone and aerosol profiles in regional- and global-scale atmospheric investigations. In January 1980, an airborne differential absorption lidar (DIAL) system was developed at the NASA Langley Research Center for the remote profiling of  $O_3$  and aerosols in the troposphere. The DIAL system made the first  $O_3$  profile measurements from an aircraft platform in May 1980. In the summer of 1980, the airborne DIAL system was used during an EPA field experiment to study Persistent Elevated Pollution Episodes (PEPE) in the Eastern United States. Simultaneous  $O_3$  and aerosol profiles were measured with the DIAL system on long-range flights during several PEPE episodes. A NASA-sponsored global tropospheric instrument test flight to San Juan, Puerto Rico, was conducted on July 14-16, 1981. Data on  $CO$ ,  $CH_4$ ,  $NO$ ,  $NO_2$ ,  $O_3$ ,  $T$ , and dew point temperature were collected by in situ sensors in altitude step increments along the flight path. The DIAL system provided remote measurements of  $O_3$  and aerosol distributions below the aircraft. Recent flights have been made with the DIAL system operating in a zenith-viewing mode for measurements of  $O_3$  and aerosols in the lower stratosphere.

The airborne DIAL system uses two dye lasers that are pumped by frequency-doubled Nd:YAG lasers. The dye laser wavelengths are frequency doubled into the UV to produce the on and off wavelengths for the DIAL measurement of  $O_3$ .<sup>1</sup> The dye laser outputs at 286 and 300 nm and a portion of the dye laser energy at 600 nm are directed into the atmosphere coaxially with a 35-cm diameter receiving telescope. The system is mounted in the NASA Wallops Electra aircraft and can be pointed in either a nadir- or zenith-viewing orientation through 40-cm diameter quartz windows. The backscattered lidar returns in the UV and visible are collected by the telescope, optically separated in the detector package, and detected by separate photomultiplier tubes. The signals from the photomultiplier tubes are digitized and stored on high-speed magnetic tape. Ozone concentrations can be calculated in real-time by means of a minicomputer. In addition, displays of ozone and aerosol distributions can be produced to precisely locate atmospheric features for real-time experiment control.

Lower Tropospheric  $O_3$  and Aerosol Measurements

The first remote measurements of ozone profiles in the lower troposphere with the airborne DIAL system were made in May 1980 over the Chesapeake Bay.<sup>1-3</sup> Subsequent to these initial measurements, a major field experiment with the Environmental Protection Agency was conducted in July-August 1980 to study large-scale pollution events in the Eastern United States. The airborne DIAL system was used in the study of ozone and aerosols

---

<sup>†</sup>Old Dominion University Research Foundation, Norfolk, Virginia.

during this program.<sup>4</sup> The objective of this experiment included the characterization of persistent elevated pollution episodes (PEPE) and the evaluation of a four-layer regional oxidant model. A comparison of  $O_3$  measurements made with the airborne DIAL system and in situ instruments on a Cessna aircraft is given in Figure 1. The variation in  $O_3$  concentration from 42 ppb above the mixed layer to 100 ppb within the mixed layer was measured remotely by the DIAL system from an altitude of 3200 m. The horizontal bars on the DIAL data represent the standard deviation for the average  $O_3$  profile obtained from 300 laser shots. The Cessna data were obtained during an aircraft spiral performed in the vicinity of Snowhill, Maryland. The in situ data are shown as averages over 200 m vertical increments, and the standard deviation of all measurements in that altitude interval is given. The precision of the in situ measurements was estimated to be about 2 percent, while the absolute accuracy was estimated at 10 percent. The DIAL and in situ  $O_3$  measurements agree very well in the free troposphere and in the boundary layer. Ozone DIAL measurements made during the PEPE/NEROS field experiment are discussed in this paper. These data will be used to investigate the regional distribution, production, and transport of  $O_3$  in elevated pollution episodes.

Aerosol backscatter profiles at 600 nm are also obtained simultaneously with the UV DIAL data. The aerosol data are processed by subtracting the background signal from the lidar-plus-background signal and then multiplying by range-squared, which removes the geometrical dependence of the lidar return signal with range. The resulting lidar backscatter profile is indicative of the distribution of aerosols below the aircraft. The backscatter signal level is converted into a 16-level gray scale display line, where stronger scattering is indicated by higher brightness. Sequential gray scale lines are then used to construct a picture of the aerosol vertical distribution along the Electra flight path. The aerosol data discussed in this paper were obtained during the NASA-sponsored Global Tropospheric Instrument Test Flight-1 (GTIT-1) from Wallops Island, Virginia, to San Juan, Puerto Rico, on July 14-16, 1981. Data on in situ measurements of  $CO$ ,  $CH_4$ ,  $NO_x$ , temperature, and dew point are compared with the vertical distribution of aerosol scattering and atmospheric layering obtained with the airborne DIAL system.<sup>5</sup> Implications for long-range transport of gases and aerosols are also examined. A companion paper discusses airborne lidar measurements of mixed layer dynamics from aerosol profile data.<sup>6</sup>

#### Profiles of $O_3$ and Aerosols in Lower Stratosphere

The first airborne DIAL measurements of  $O_3$  and aerosol profiles in and above the tropopause region of the atmosphere were made on August 6, 1981, over Maine. This was the first flight experiment conducted with the DIAL system operating in a zenith-viewing mode from the Electra. The Loring Air Force Base, Maine, site was selected for the tropopause experiment because of its location on the northern side of the jet stream. A National Weather Service station at Caribou, Maine, 17 miles from Loring AFB, was selected for an ozonesonde launch. An ozonesonde launch team from the Wallops Flight Center was flown to Loring AFB along with the DIAL system on the afternoon of August 6.

An ozonesonde was launched at 2209 EDT, and the data showed a tropopause located at a geopotential altitude of 11.1 km. Two prominent  $O_3$  enhanced

layers were found at altitudes of 12.5 and 13.5 km. The peak  $O_3$  concentrations in these layers were about twice the average concentration outside the layers. The depth of the lower layer was about 500 m, and the upper layer had a depth of only 350 m. The airborne DIAL system was flown at an altitude of 8230 m to make  $O_3$  and aerosol profile measurements in and above the tropopause region. The flight over Maine was completed by flying over the ozonesonde launch site at 2348 EDT. A comparison of the DIAL  $O_3$  profile and the ozonesonde data is shown in Figure 2. Also shown in the figure are the potential temperature data from the ozonesonde. The DIAL data represent the average  $O_3$  profile obtained from 300 DIAL measurements along a 6 km horizontal path. The horizontal bars designate the standard deviation of the average  $O_3$  profile. The magnitude and relative position of the  $O_3$  layers are in excellent agreement between the DIAL and ozonesonde measurements. The altitude agreement for these layers is within 150 m, which is very good considering that the DIAL measurements were only in the vicinity of the ozonesonde ascent path. Features in the minimum between the two layers are also accurately determined by the DIAL system. Simultaneous lidar measurements of aerosol scattering were made at a wavelength of 600 nm. The  $O_3$  layers seen by both the DIAL system and the ozonesonde were found to have an increase in aerosol scattering associated with them. Aerosol scattering ratios of 0.15 and 0.2 were found for the lower and upper  $O_3$  layers, respectively. A cross-sectional map of these layers is being constructed along the Electra flight path, which went from the northwestern corner of Maine southeast to the coast. A detailed discussion of these measurements is presented in this paper.

#### References

1. Browell, E. V.; Carter, A. F.; Shipley, S. T.; Siviter, Jr., J. H.; Hall, W. M.; Allen, R. J.; Butler, C. J.; and Mayo, M. N.: The NASA Langley Multipurpose Airborne DIAL System and Measurements of Ozone and Aerosol Profiles. To be submitted to Appl. Opt.
2. Browell, E. V.; Carter, A. F.; and Shipley, S. T.: An Airborne Lidar System for Ozone and Aerosol Profiling in the Troposphere and Lower Stratosphere. Proceeding of the IAMAP International Quadrennial Ozone Symposium, NCAR, Boulder, CO, August 4-9, 1980.
3. Browell, E. V.: Lidar Measurements of Tropospheric Gases. Opt. Eng., 21, 128 (1982).
4. Browell, E. V.; Shipley, S. T.; Carter, A. F.; Butler, C. F.; and Ismail, S.: Airborne DIAL Measurements of Ozone, Aerosols, and Mixed Layer Heights during the 1980 PEPE/NEROS Summer Field Experiment. NASA TP in preparation.
5. Hinton, R. R.; Browell, E. V.; Gregory, G. L.; and Harriss, R. C.: CO,  $O_3$ , and Aerosol Measurements from NASA Global Tropospheric Experiment: Test Flights 1981. Proceedings of the Second Symposium on Composition of the Nonurban Troposphere. Williamsburg, VA, May 25-29, 1982.
6. Shipley, S. T. and Browell, E. V.: Airborne Lidar Measurements of Mixed Layer Dynamics. Eleventh International Laser Radar Conference, NASA CP-2228, 1982. (Paper F5 of this compilation.)

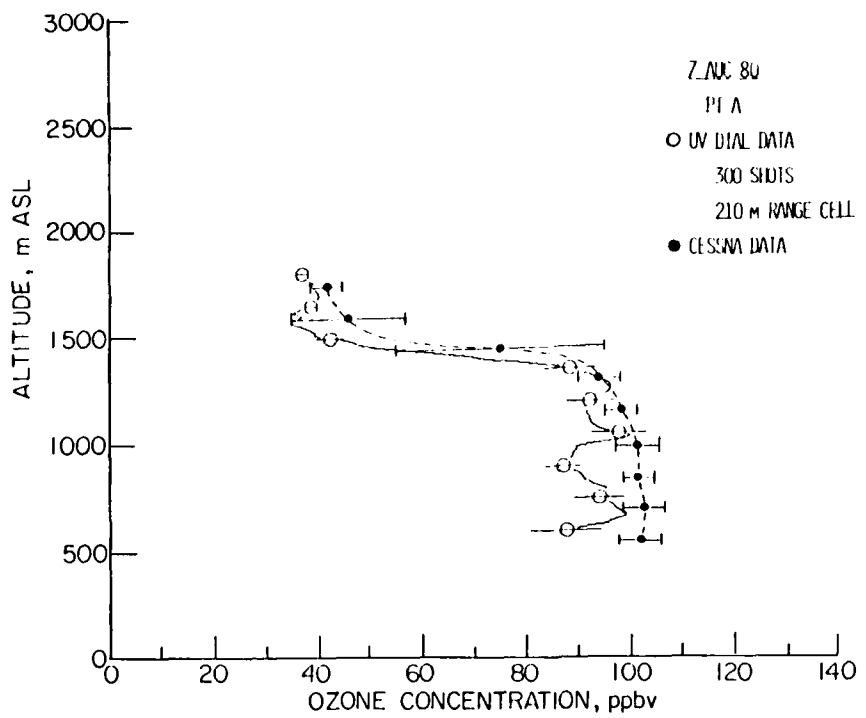


Figure 1: Comparison of DIAL and in situ  $O_3$  measurements above and in the boundary layer.

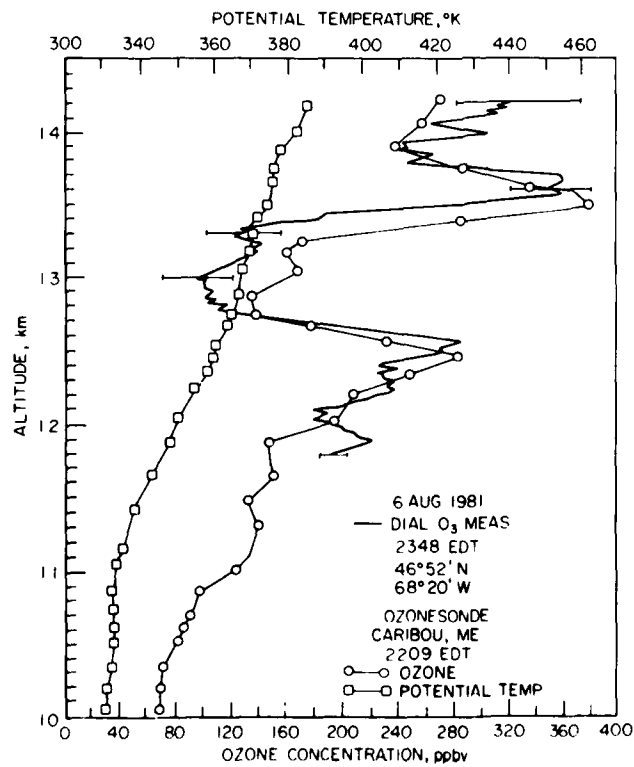


Figure 2: Comparison of DIAL and ozonesonde measurements of  $O_3$  in the vicinity of the tropopause.

## SIMULTANEOUS HETERODYNE AND DIRECT DETECTION CO<sub>2</sub> DIAL MEASUREMENTS\*

Dennis K. Killinger, Norman Menyuk and William E. DeFeo  
Lincoln Laboratory, Massachusetts Institute of Technology  
Lexington, Massachusetts 02173

A dual-CO<sub>2</sub> laser differential-absorption LIDAR (DIAL) system has been developed which incorporates both direct detection<sup>1</sup> and heterodyne detection of the same LIDAR returns. This system has been used to obtain preliminary measurements of the statistical and temporal properties of the DIAL returns in order to experimentally quantify these properties. Comparison of these results with theory for dual-wavelength operation is currently being conducted. An overview of the system and current status of the experimental measurements will be presented.

Figure 1 shows a schematic of the dual-laser DIAL system. Two tunable, hybrid-TEA CO<sub>2</sub> lasers provide the pulsed primary radiation. The TEA laser operates at a PRF of 100 Hz, with a pulse energy of 10 mJ per pulse and a pulse length of approximately 300-400 nsec. The low-pressure gain cell is operated slightly above threshold with a cw output laser power of about 100 mW.

The frequency of the hybrid-TEA laser is adjusted to an offset frequency of approximately 20 MHz relative to that of the CO<sub>2</sub> laser local oscillator (L.O.). A room-temperature HgCdTe detector and a 1  $\mu$ sec gated frequency counter were used to monitor the heterodyne beat frequency between the cw portion of the hybrid-TEA laser radiation and the local oscillator; this value was found to be within 1~2 MHz of that obtained with a precision frequency counter and transient digitizer which measured the frequency of the pulsed portion of the heterodyne LIDAR return. The measurements established that the pulse-to-pulse frequency stability of the hybrid-TEA laser was approximately 10 MHz and the intrapulse stability (chirp) was approximately 1 MHz. The TEA discharge disrupted the lasing of the cw gain cell, which limited the PRF of the system to approximately 100 Hz, dependent upon discharge and gas-mixture conditions.

The outputs from the two lasers were joined with a 50/50 beamsplitter, expanded by an X10 beam expander, and directed out the laboratory window. The backscattered LIDAR radiation was collected using a Cassegrain telescope and split with a 50/50 beamsplitter; half of the returned beam was directed toward a cooled direct-detection HgCdTe detector, and the other half mixed with the CO<sub>2</sub> local oscillator output and directed toward a cooled heterodyne-detection HgCdTe detector. The output signals from the detectors were sent to a high-speed data acquisition system. This system monitored the frequency offset of each laser pulse to ensure that it fell within the bandpass of the detector.

\*This work was sponsored by the National Aeronautics and Space Administration and the Air Force Engineering and Services Center.

amplifiers, normalized the LIDAR returns to the laser pulse energy, and calculated the statistical and temporal characteristics of the returns. Heterodyne returns have been obtained from topographic targets at ranges up to 10 km and from atmospheric aerosols at ranges of approximately 0.5 km.

Reference

1. D. K. Killinger and N. Menyuk, "Remote Probing of the Atmosphere Using a CO<sub>2</sub> DIAL System," J. Quant. Elect. QE-17, 1917 (1981).

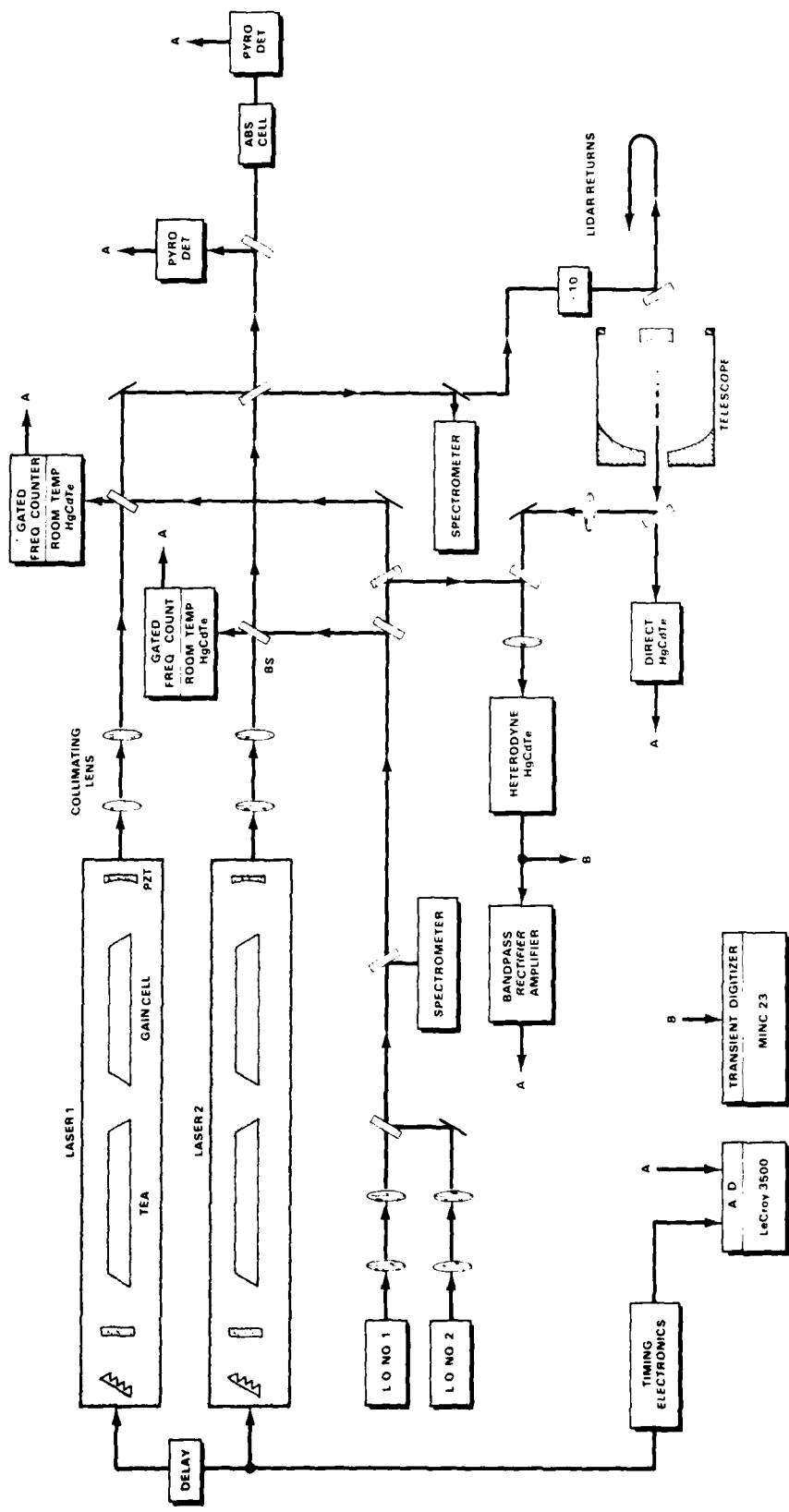


Figure 1. - Schematic of dual-0<sub>2</sub> laser heterodyne and direct detection DIAL system.

EXTENSION OF DIAL MEASUREMENTS WITH  
Nd:YAG-BASED LIDAR SYSTEMS TO  
SHORT UV AND NEAR IR WAVELENGTHS

M. Aldén, H. Edner and S. Svanberg  
Department of Physics  
Lund Institute of Technology  
P.O. Box 725  
S-220 07 Lund  
Sweden

The DIAL technique as applied employing Nd:YAG  $\rightarrow$  dye-laser technology is quite powerful for monitoring  $\text{NO}_2$ ,  $\text{SO}_2$  and  $\text{O}_3$  and some measuring systems are approaching operational status<sup>1-3</sup>. However, it is of considerable interest to extend the applicability of such systems to a number of other atmospheric molecular constituents, e.g.  $\text{NO}$ ,  $\text{HCHO}$ ,  $\text{Hg}$ ,  $\text{CO}$ ,  $\text{HCl}$ ,  $\text{HF}$  and  $\text{CH}_4$ . While  $\text{NO}_2$ ,  $\text{SO}_2$  and  $\text{O}_3$  absorb in the visible and the easily accessible UV region ( $\sim 300$  nm), the measurement of the additional gases requires extensions of the wavelength region to short UV and IR wavelengths. With the high peak powers available with Nd:YAG based laser systems this is possible using Raman-shifting and frequency-mixing techniques. We are presently involved in a program aiming at the exploitation of these possibilities. At short UV wavelengths the atmospheric attenuation due to scattering is strong whereas low back-scattering is instead a problem in the IR region. Clearly, the pulse energies will be limited outside the well established wavelength regions and therefore the use of topographic targets or even retro-reflectors rather than atmospheric back-scattering can be necessary in many cases. Whereas low pulse energies can be problematic with a down- or up-converted dye-laser source, the continuous tuning capability is an attractive feature. It is advantageous to use close-lying optimal on/off-resonance wavelengths, which eliminates differential albedo effects present for  $\text{CO}_2$ -laser systems.

We perform lidar measurements with a laboratory-based system and also make the necessary spectral investigations of the studied molecules. A Nd:YAG laser with more than 200 mJ output at 532 nm is used for pumping a dye laser with amplifier. Tunable radiation in 100 mJ pulses is produced using the most favourable dyes. A Raman shifter, operating with  $\text{H}_2$  at about 20 atm. pressure is used for Stokes shifting in normally three steps into the near IR region ( $< 3 \mu\text{m}$ ), where overtones of molecular absorption are employed. For UV generation, anti-Stokes shifting is employed after frequency-doubling of the dye-laser output.

Dial measurements of atomic mercury were performed at the 253.65 nm resonance line<sup>4</sup>. The correct wavelength was achieved by frequency-doubling of 567.06 nm dye-laser light and first anti-Stokes shifting by  $4155 \text{ cm}^{-1}$  in  $\text{H}_2$ . Typical pulse energies were 0.7 mJ. The detection system has been described in Ref. 5. In Fig. 1 on- and off-resonance curves are shown for a remote open-ended cell containing  $\text{Hg}$  vapour in a concentration of about  $100 \mu\text{g}/\text{m}^3$ . An analysis of the dial sensitivity for  $\text{Hg}$  indicates that even the low background concentrations of about  $4 \text{ ng}/\text{m}^3$  can be measured if a pathlength of  $2 \times 1 \text{ km}$  is used. Mercury is of great interest regarding the

increased utilization of coal and in connection with volcanic eruptions prediction.

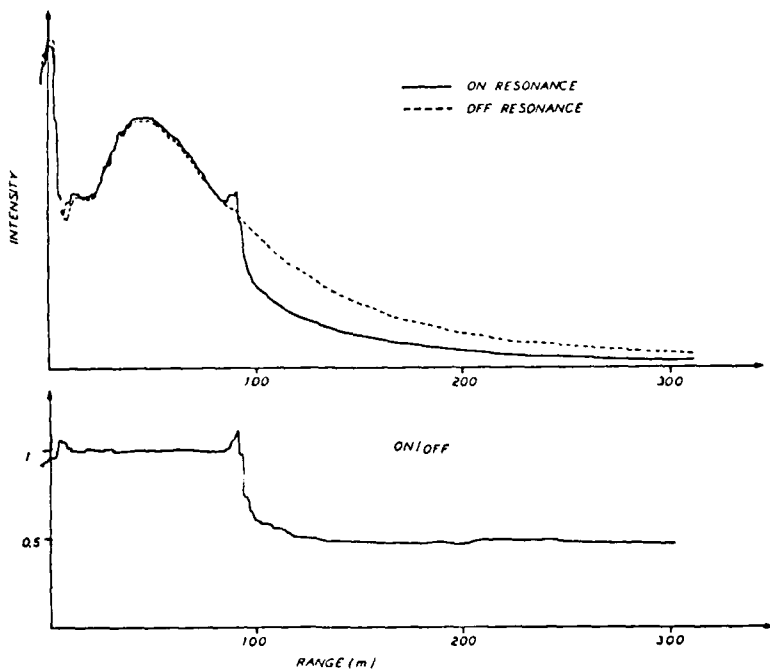


Figure 1. Dial measurement of atomic mercury at the Hg resonance line 253.65 nm. The lower curve is a divided representation.

Nitrogen oxides are primarily emitted into the atmosphere as NO and a subsequent oxidation to  $\text{NO}_2$  then occurs. For monitoring NO and for studies of the chemical transformation process, lidar techniques are very desirable. We have generated UV light in the region of the NO band-head at 227 nm by second anti-Stokes shifting of 279 nm frequency-doubled dye-laser light. Transmitted pulse energies in first dial measurements were about 0.1 mJ. In Fig. 2 a lidar curve is shown for a measurement against a topographic target 420 m distant. Determinations of proper NO cross sections are in progress. Using frequency-mixing techniques it should be possible to increase output energies at 227 nm to about 3 mJ.

Spectral studies for CO, HCl and  $\text{CH}_4$  have been performed in the 1-3  $\mu\text{m}$  range. In Fig. 3 an absorption spectrum for a 30 cm cell containing 400 torr of  $\text{CH}_4$  is shown. Third Stokes generation starting with a Rhodamine 640 dye-laser output was employed. The increase in level from low to high wavelengths reflects the gradual increase in the dye-laser output. Lidar measurements employing an InSb detector are in preparation. Of particular interest are CO, HCl and HF.

This work is supported by the Swedish Board for Space Activities and the Swedish Environment Protection Board.

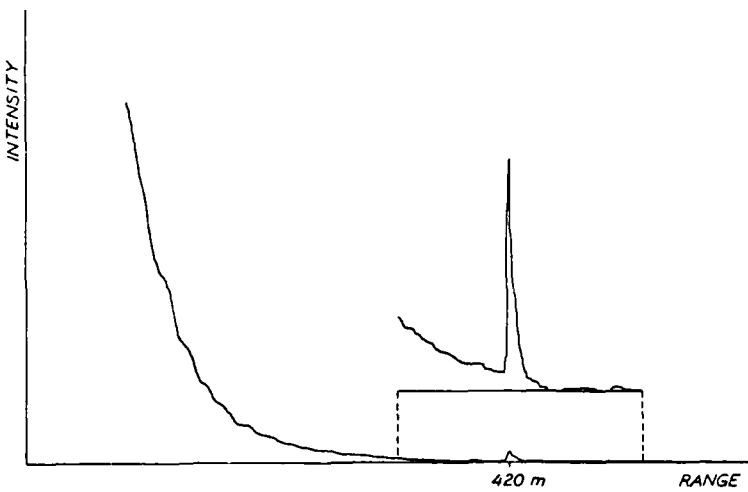


Figure 2. Lidar curve at the 226.8 nm resonance line of NO. Atmospheric backscattering and the echo from a topographic target are shown.

$CH_4 \quad (v_1 + v_4, v_3 + v_4)$

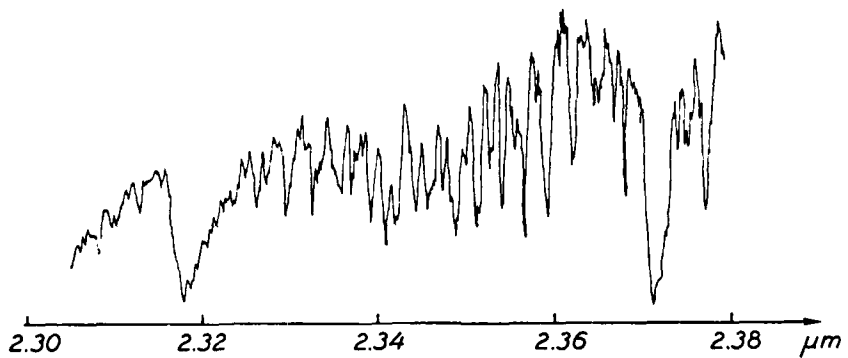


Figure 3. Absorption spectrum of methane, recorded using third-Stokes shifted dye-laser radiation.

#### References

1. K. Fredriksson, B. Galle, K. Nyström and S. Svanberg, *Appl. Opt.* 20, 4181 (1981); K. Fredriksson and S. Svanberg, *Proc. of the Workshop on Optical and Laser Remote Sensing, Monterey, Febr. 9-11 1982.*
2. J.G. Hawley, L.D. Fletcher and G.F. Wallace, *Proc. of the Workshop on Optical and Laser Remote Sensing, Monterey, Febr. 9-11 1982.*
3. E. Browell, *ibid.*
4. M. Aldén, H. Edner and S. Svanberg, *Opt. Letters* in press (scheduled for May 1982).
5. K. Fredriksson, B. Galle, K. Nyström and S. Svanberg, *Appl. Opt.* 17, 1998 (1979).

DAY-TIME DETECTION OF GASEOUS POLLUTANTS  
BY RAMAN-LIDAR: MEASUREMENTS AND SIMULATIONS

R. CAPITINI  
Commissariat à l'Energie Atomique  
CEN/Saclay  
Département de Physico-Chimie  
91191 Gif-sur-Yvette Cedex (France)

E. JOOS  
Laboratoire de Spectrochimie Infrarouge-Raman  
CNRS  
Université de Lille (France)

D. RENAUT  
Météorologie Nationale  
EERM  
(France)

SUMMARY

This paper presents Raman-Lidar experimental results in minor species detection. That mainly concerns two kinds of measurements:

- detection of ozone in the atmosphere, using resonance Raman Scattering and of  $\text{CO}_2$  using Raman scattering;
- identification and measurement of pollutant gases ( $\text{SF}_6$ ,  $\text{SO}_2$ , and  $\text{CO}_2$ ) in a simulation tank.

From these preliminary results, the detection limits of the system are estimated and simulations of pollutant plume measurements are performed taking spectroscopic problems into account.

EQUIPMENT

The CEA Raman-Lidar is described in this publication (1). For pollutant gas studies, a simulation tank is located about 100 m from the Lidar. This tank is a 2-m long inox cylinder with a 15-cm diameter. Both ends are closed with quartz windows slanted at Brewster's angle.

EXPERIMENTAL RESULTS

For these measurements, the digitizer averages a given number of lidar signals depending upon the intensity of the Raman line. The average signal corresponding to each point of the spectrum is transmitted to the computer without signal correction, except for the average laser energy emitted.

Detection of Atmospheric  $\text{CO}_2$  and  $\text{O}_3$

Figure 1 shows a remote atmospheric spectrum measured with the Raman Lidar. The three Raman lines for  $\text{O}_2$  ( $1556 \text{ cm}^{-1}$ ),  $\text{CO}_2$  ( $2\nu_2$ ,  $1286 \text{ cm}^{-1}$ ) and  $\text{O}_3$  ( $1100 \text{ cm}^{-1}$ ) are

apparent, the  $\text{CO}_2$  ( $\nu_1$ ,  $1388 \text{ cm}^{-1}$ ) line is masked by the  $\text{O}_2$  wing. Atmospheric concentrations were not measured at this time; nevertheless one can observe the strong enhancement for  $\text{O}_3$  scattering ( $\sim 1200$ ) which agrees with our laboratory measurements (2). Due to resonance, ozone profiles have been measured with a 500-m range and an 80-m range resolution (3). For  $\text{CO}_2$ , only ordinary Raman scattering occurs and, assuming a 350 ppm mixing ratio, one gets  $\sigma(\text{CO}_2)/\sigma(\text{O}_2) = 0.6$ .

#### Detection of Pollutant Gases ( $\text{SF}_6$ , $\text{CO}_2$ , and $\text{SO}_2$ ) in a Simulation Tank

Accurate measurements have been obtained with  $\text{SF}_6$  and the results were recently published (3). In the same way,  $\text{CO}_2$  has been detected. Figure 2 presents pure  $\text{CO}_2$  Raman spectra with the  $2\nu_2$  and  $\nu_1$  bands. The scattering volume is limited to the tank length. The measured ratio  $\sigma(\text{CO}_2, \nu_1)/\sigma(\text{CO}_2, 2\nu_2)$  is 1.55.  $\text{SO}_2$  presents a strong absorption in the 266 nm range, so that resonance Raman is to be expected. Experiments are now in progress.

#### SPECTROSCOPIC SIMULATIONS AND SNR CALCULATIONS

Calculations require pollutant concentrations inside a plant plume at a few hundred meters from the stack. Spatial distribution of concentrations of gaseous pollutants and aerosols in a plume are calculated using the classical Pasquill-Gifford plume dispersion model (4) and the Turbigo plant data (5).

Two kinds of calculations are performed. First, Raman spectra are computed using model concentrations in the plume, Raman cross sections (measured or extrapolated to 266 nm), and the transfer function of the spectrometer for a given slitwidth. The purpose is to verify the spectroscopic feasibility of the detection. It is assumed that aerosols do not absorb and that no fluorescence occurs. The backscattering cross section of aerosols are calculated at 266 nm using Mie theory and McCormick tables for a monodispersion of spherical particles with a radius of  $0.5 \mu\text{m}$ , specific gravity of  $10^{-12} \text{ g}/\mu\text{m}^3$  and a refractive index of 1.5. The spectrum shown in figure 3 is computed with model concentrations at 100 m from the stack on the plume axis. Data used to get this spectrum are gathered in table 1.

Assuming that  $\sigma(\text{SO}_2)/\sigma(\text{N}_2) = 100$ , the  $\text{SO}_2$  line is resolved enough and can be detected; with  $\sigma(\text{SO}_2)/\sigma(\text{N}_2) = 10$ , continuous background does not allow detection. In spite of a resonant Raman cross section,  $\sigma(\text{NO}_2)/\sigma(\text{N}_2) = 75$ , the  $\text{NO}_2$  line does not emerge enough to be detected.

Continuous background which limits signal detection is due to the great concentration of aerosols and to the rejection rate of our spectrometer. To get down to the minimal noise level (PM dark current and background sky light), a  $10^{-12}$  rejection rate would be necessary.

In a second step, calculations of SNR can be performed, assuming that on a vertical axis orthogonal to the plume axis, aerosols and gas concentrations are constant on lengths equal to the maximal lidar range resolution of 2.5 m.

$\text{SO}_2$  model concentrations and statistical SNR are shown for points located on a vertical axis 100 m from the stack (fig. 4). Difference between height of maximum concentration and height of maximum SNR is due to  $\text{SO}_2$  absorption and aerosol diffusion in the plume. SNR are high enough to allow detection.

At 250 m from the stack, calculations show that detection is still possible. It must be noted that an extrapolation from fluorescence intensity observed during water vapor soundings gives a fluorescence level in the plume of the same order as the  $\text{SO}_2$  peak in figure 3.

#### REFERENCES

- (1) - D. RENAUT, C. BRUN, R. CAPITINI  
Eleventh International Laser Radar Conference, NASA CP-2228, 1982.  
(Paper B8 in this compilation.)
- (2) - J.C. POURNY, D. RENAUT, J. ENGLENDER,  
C.R. n° 8/77, Météorologie Nationale, Ecole Polytechnique
- (3) - R. CAPITINI, E. JOOS, D. RENAUT  
Paper at 3rd IAMAP, Lidar Session, Hambourg, 1981
- (4) - D.B. TURNER  
Workbook of Atmospheric Dispersion Estimates -  
Environmental Protection Agency, Publication n° AP-26 (1970)
- (5) - A. LONGHETTO and others  
Final Report on the Remote Sensing Exercise at Turbigo (1979).

TABLE I.- SIMULATION DATA

Scattering species	Raman shift ( $\text{cm}^{-1}$ )	$\sigma / \sigma_{\text{H}_2}$ (266 nm)	concentration ( $\text{m}^{-3}$ )
molecules (Rayleigh scattering)	0	1240 $\times$	$2.5 \cdot 10^{25}$
Aerosols (Mie scattering)	0	$3.9 \cdot 10^{20} \text{xx}$	$2.6 \cdot 10^{10}$
$\text{N}_2$	2340	1	$3.0 \cdot 10^{25}$
$\text{O}_2$	1570	$2.1 \times$	$4.6 \cdot 10^{24}$
$\text{H}_2\text{O}$	3660	$3.1 \times$	$6.0 \cdot 10^{23}$
$\text{CO}_2$	1270	$1.2 \times$	$4.8 \cdot 10^{23}$
$\text{CO}_2$	1390	$1.9 \times$	$4.8 \cdot 10^{23}$
$\text{O}_3$	1120	$2500 \times$	$2.2 \cdot 10^{18}$
$\text{SO}_2$	1150	$100 \text{xxx}$	$6.3 \cdot 10^{21}$
$\text{NO}_2$	750	$5 \times$	$9.6 \cdot 10^{20}$

Spectrometer : slitwidth : 2 nm, maximum rejection rate :  $10^{-3}$ .

( $\times$ ) experimental values  
(xx) calculated value  
(xxx) hypothesis

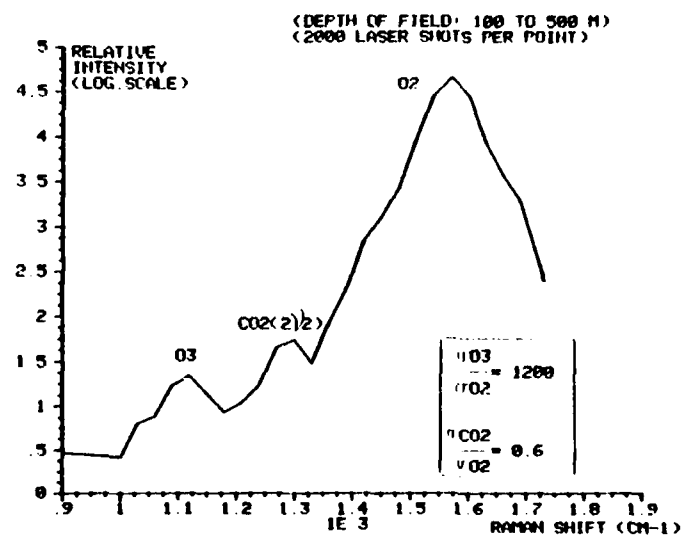


Figure 1.- Atmospheric Raman spectrum.

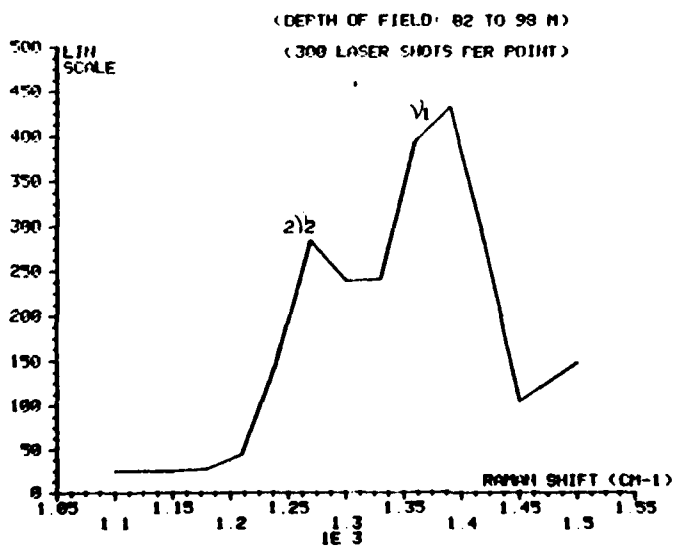


Figure 2.-  $\text{CO}_2$  Raman lines.

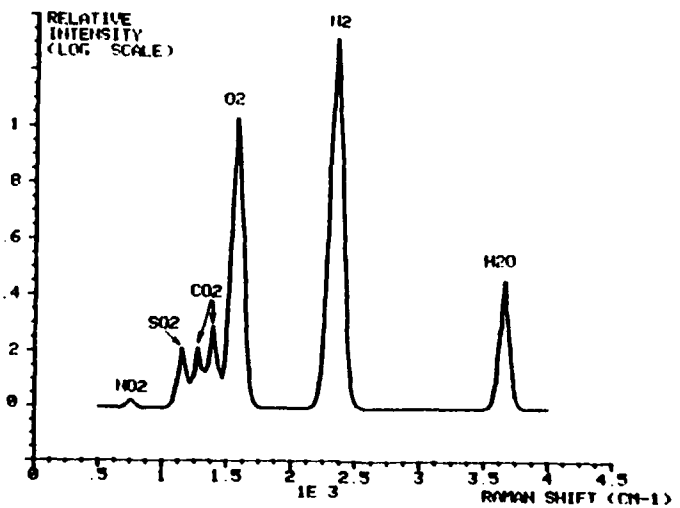


Figure 3.- Computed Raman spectrum in the model plume.

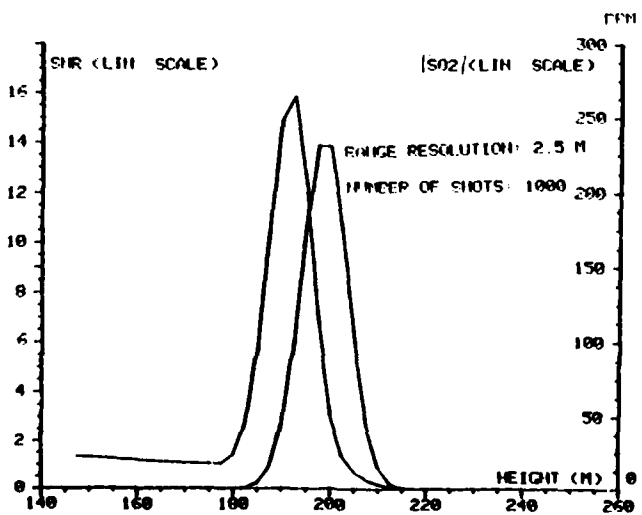


Figure 4.-  $\text{SO}_2$  detection SNR and concentration in the plume.

DIFFERENTIAL ABSORPTION LIDAR ERRORS CAUSED  
BY MISALIGNMENT IN COAXIAL SYSTEMS

William S. Heaps  
NASA/Goddard Space Flight Center  
Code 963  
Greenbelt, Maryland 20771

In the conduct of a LIDAR experiment, one is always limited at the short range end by the distance required for the transmitted beam and the receiver field of view to overlap. When return signals are very large this blind spot can be advantageous in that it protects the receiver from saturation by the very strong near return. However in the limit of weak signals it would be very attractive to be able to see at short ranges before the inverse square law has greatly attenuated the signal. In any case it is usually desirable to operate the LIDAR receiver with a very narrow field of view in order to minimize the background signal due to scattered solar flux. Reducing the field of view of the receiver, however, increases the range at which total overlap is achieved as well as aggravating the sensitivity of the system to misalignment. A model has been developed which calculates the degree of overlap of a LIDAR system as a function of range. Using this model one can show that under some circumstances in which the receiver and beam are misaligned, the form of the overlap function can affect the interpretation of differential absorption LIDAR (DIAL) data giving rise to substantial errors which may be of either sign.

Consider a LIDAR system composed of the following elements:

- a) A Cassegrain receiver with an outer radius of  $R_1$ , a central obstruction radius of  $R_2$  and a full angle field of view of  $\theta_1$ , focussed at infinity.
- b) A steerable flat located on the axis of the telescope used to align the transmitted beam with the receiver.
- c) A Gaussian beam with a waist  $w_1$  located at the steering flat and a full angle beam divergence of  $\theta_2$ . The alignment of the receiver with the beam can be described in terms of three parameters:
  - 1)  $r$  is the distance of the beam center from the axis of the telescope at the steering flat (range equals zero).
  - 2)  $\delta$  is the angle between the beam axis and the receiver axis if the beam axis were projected into a plane containing the receiver axis.
  - 3)  $\phi$  is the angle between the radial displacement of the beam center from the telescope axis and the projection of the beam axis in a plane perpendicular to the receiver axis. This is to say if  $\phi=0$  the misaligned beam points away from the receiver axis and if  $\phi=180^\circ$  it points toward the receiver axis. If there is no radial displacement ( $r=0$ ) then  $\phi$  is meaningless.

One may now define an overlap function  $O(z)$  as an additional term in the LIDAR equation:

$$\text{Return signal} = C \propto (O(z) \exp(-\beta z)) / z^2$$

When the receiver field of view completely encompasses the transmitted beam  $O(z)=1$ . This is the region in which one normally operates. Assuming  $\beta$  is constant in a range interval from  $z_1$  to  $z_2$  one can solve for it:

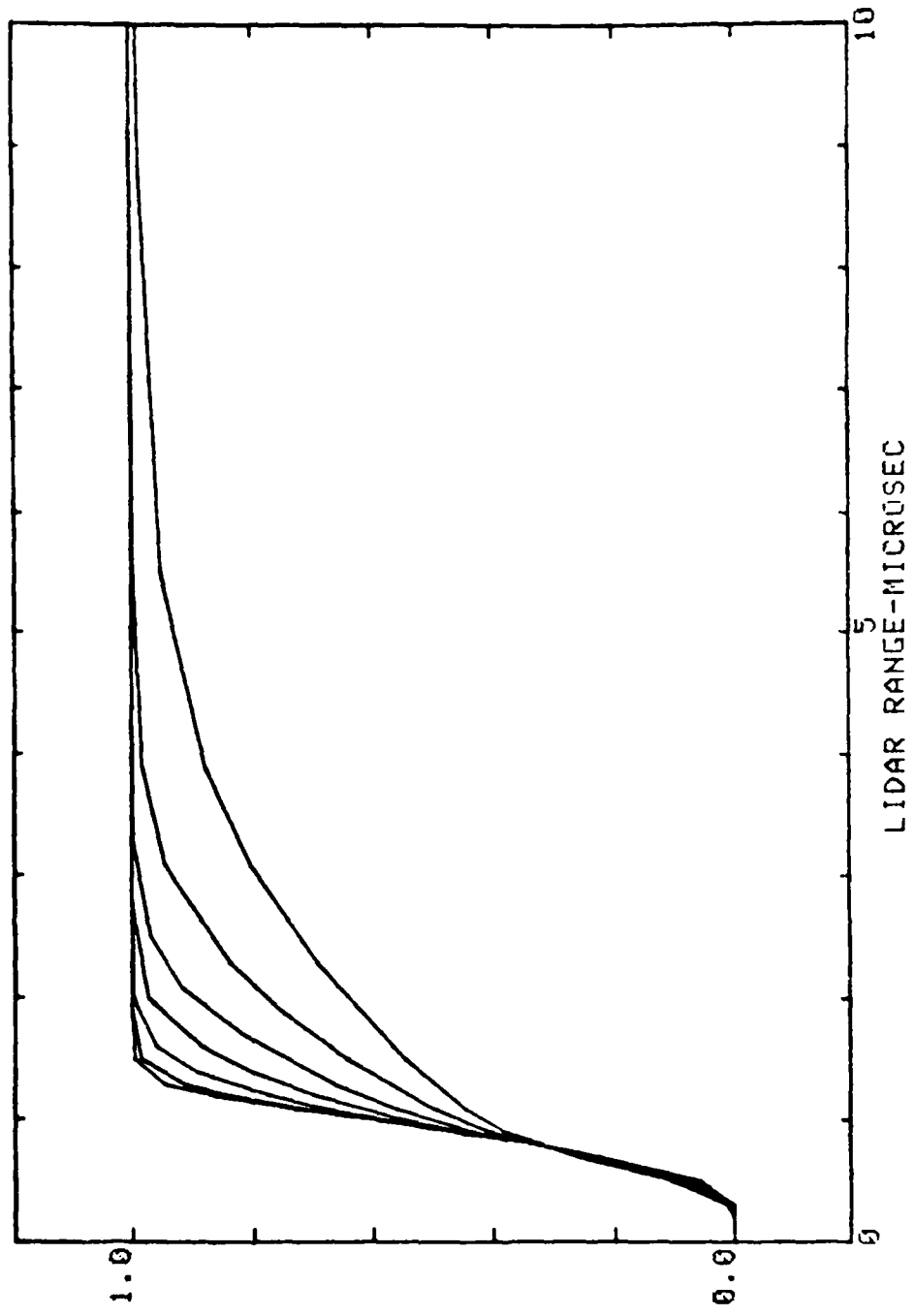
$$\beta = \frac{\ln(O(z_2)/O(z_1)) - \ln(z_2^2 C(z_2)/z_1^2 C(z_1))}{z_2 - z_1}$$

Clearly if  $O(z)$  is constant over the interval its contribution is zero; however under some conditions of misalignment  $O(z)$  can be a slowly increasing or slowly decreasing function. This makes it hard to tell from the backscatter data that the overlap is incomplete, but can generate a sizeable error in the determination of  $\beta$ . For best signal-to-noise ratio in an absorption measurement  $\beta(z_2-z_1)$  should be approximately one. If  $O(z)$  changed from .8 to .9 over the interval from  $z_1$  to  $z_2$ , this would give rise to an error on the order of 10% in  $\beta$ .

The figure illustrates change in the overlap function with range for a typical LIDAR system. The outer radius of the telescope is 15 cm, the central obstruction radius is 5 cm, and the field of view is 1.6 milliradians. Beam diameter is 2 cm at the source and has a divergence of .2 milliradians. The top curve shows the overlap for a perfectly aligned system and each successive curve shows the effect of increasing  $\delta$  in steps of .1 milliradian out to a maximum of .6. One can see that a misalignment as large as .3 milliradians would be difficult to detect, indeed difficult to prevent, during the initial alignment. However, if the interval chosen for a DIAL measurement were 2 to 6 microseconds ( $\sim 300$ -900 meters) the value of  $\ln(O(900)/O(300))$  would be .025. For a weak absorption, necessary if one wished to measure at long ranges, even this small change could cause a significant error in  $\beta$ .

Clearly this effect depends on the other parameters of the system as well and can amount to a very substantial error. When the misalignment,  $\delta$ , exceeds one half of the field of view,  $O(z)$  can become a decreasing function giving errors of the opposite sign. The model permits all such cases to be considered and could be useful as a diagnostic tool when one is attempting to align a LIDAR system.

LIDAR OVERLAP FUNCTION



THE THEORY AND CORRECTION OF FINITE LASER  
BANDWIDTH EFFECTS IN DIAL EXPERIMENTS

C. Laurence Korb  
NASA Goddard Space Flight Center  
Greenbelt, Maryland 20771

and

Chi Y. Weng  
Science Systems & Applications, Inc.  
Seabrook, Maryland 20801

The effects of finite laser bandwidth can cause very large errors in range-resolved measurements of differential absorption (DIAL) and, therefore, must be accounted for accurately. No method of solution to this problem has been reported for the case of pure elastic scattering. In addition, processes which redistribute the frequencies of photons during scattering have not previously been considered for DIAL experiments. This paper describes a general method of solution for treating the effects of finite laser bandwidth in DIAL experiments with pure elastic scattering. In addition, methods for treating the problem of Rayleigh scattering, which redistributes the photon frequencies, are considered.

We consider first the case of elastic scattering. For a DIAL experiment with finite bandwidth, the absorption coefficient as measured by the experiment over the layer  $Z_1$  to  $Z_2$ ,  $K_{obs}$ , is defined in the conventional manner as

$$K_{obs} = -0.5(z_2 - z_1)^{-1} \ln \left[ \frac{E_\ell(z_2)/E_r(z_2)}{E_\ell(z_1)/E_r(z_1)} \right] \quad (1)$$

where  $E_\ell$  and  $E_r$  are the backscattered signals at the on-line and reference frequencies, respectively, and the measurement extends across the effective altitude range from  $Z_1$  to  $Z_2$ . The transmission of the atmosphere,  $T(z_0, z)$ , as measured with a laser along the two-way vertical path from the laser at height  $Z_0$  to height  $Z$  is given as

$$\frac{T(z_0, z)}{T(z_0, z_0)} = \frac{\int_{v_1}^{v_2} h(v) \exp \left[ -2 \int_{z_0}^z K(v, z) dz \right] dv}{\int_{v_1}^{v_2} h(v) dv} \quad (2)$$

where  $h(\nu)$  is the laser spectral line shape which contributes on the interval from  $\nu_1$  to  $\nu_2$ , and  $K(\nu, Z)$  is the absorption coefficient. For absorption in the atmosphere, the absorption coefficient must generally be represented by the Voigt line profile which is a convolution of independent Doppler and Lorentz profiles<sup>(1)</sup>. It follows from Eqs. (1) and (2) that

$$K_{\text{obs}} = -0.5(Z_2 - Z_1)^{-1} \ln \left[ \frac{\overline{T(Z_0, Z_2)}}{\overline{T(Z_0, Z_1)}} \right] \quad (3)$$

where the resonant absorption at the reference frequency is assumed to be negligible compared to that at the on-line frequency.

The physical significance of Eq. (3) can be seen by evaluating the difference between the absorption coefficient observed for various lidar bandwidths and for a monochromatic measurement at line center. Figure 1 gives the resultant errors as a function of altitude for several bandwidths for a high-altitude aircraft measurement on a typical atmospheric line. We assume a two-way atmospheric optical depth of 3, a ratio of collision to Doppler width near 4 at the surface and 0.3 at 20 km, and a collision broadening coefficient of  $0.05 \text{ cm}^{-1}/\text{atm}$ . As shown, errors as large as 25% occur near 10 km for a laser bandwidth of  $0.04 \text{ cm}^{-1}$ .

$K_{\text{obs}}$  depends primarily on the transmission of the particular layer in question, averaged over the spectral bandwidth of the laser. As a result of the finite bandwidth, however,  $K_{\text{obs}}$  also has a dependence on the transmission properties of the intervening layers between the laser and the measured layer, i.e., from  $Z_0$  to  $Z_1$ . The effects of the intervening layers are shown explicitly in Figure 1 for the same line discussed previously. As shown, the magnitude of this effect is generally small; it is less than 3% for a  $0.04 \text{ cm}^{-1}$  laser bandwidth.

The combined effects of finite laser bandwidth can be accurately treated in a lidar differential absorption experiment using the following iteration procedure which requires a detailed knowledge of the laser spectral line shape. 1) A profile of the absorption coefficient measured by the lidar,  $K_{\text{obs}}$ , is determined from Eq. (1). 2) The absorption coefficient observed with finite bandwidth for the case of independent atmospheric layers is found from Eq. (2) on the interval  $Z_i$  to  $Z_{i+1}$  as

$$K = -(1/2)(Z_{i+1} - Z_i)^{-1} \ln \left[ \overline{T(Z_i, Z_{i+1})} \right] \quad (4)$$

and an estimate of the desired atmospheric parameter,  $X_i(Z)$ , e.g., the absorption coefficient or species density, is found using numerical or graphical methods to solve Eq. (4) for  $X_i(Z)$  with  $K = K_{\text{obs}}$ . 3) The transmission and absorption coefficient as given by Eqs. (2) and (3) are determined using  $X_i(Z)$ , thus including the effect of the intervening layers. Eq. (3) is then solved for  $X_{i+1}(Z)$  using numerical or graphical methods and measured values of  $K_{\text{obs}}$ . 4) Step 3 is repeated until the residuals,  $X_{i+1}(Z) - X_j(Z)$ , are sufficiently small.

After applying this procedure to the absorption line previously considered, the residual error in the absorption coefficient is found to be less than 0.035% for a bandwidth of  $0.02 \text{ cm}^{-1}$  and less than 0.2% for a bandwidth of  $0.04 \text{ cm}^{-1}$  if the absorption coefficient of the intervening layers is measured to 5% accuracy. The only limitations to the accuracy of the method are the knowledge of the laser spectral line shape on a per pulse basis and the accuracy of the experimental measurements of the observed absorption on the intervening layers and the measurement layer.

Prior studies of differential absorption have assumed that Rayleigh scattering produces no change in the photon frequency distribution. It is well known, however, that the molecules which produce Rayleigh scattering have a velocity distribution which, through the Doppler effect, causes the intensity of an incident monochromatic frequency to be spectrally redistributed in a Gaussian profile<sup>(2)</sup>. For a monochromatic laser centered on an absorption line at  $\nu_0$ , the energy backscattered from a molecular atmosphere at frequency  $\nu$  from height  $z$  is given as

$$E(\nu) = h_0 \beta(z) T_{\nu_0}(z_0, z) T_{\nu}(z, z_0) \exp[-\ln 2(\nu - \nu_0)^2/4b^2] \quad (5)$$

where  $h_0$  is a constant,  $\beta(z)$  is the Rayleigh backscatter coefficient,  $T_{\nu}(z, z_0)$  is the one-way transmission of the atmosphere at frequency  $\nu$  for the path from  $z$  to  $z_0$ , and  $b$  is the Doppler width of air at frequency  $\nu_0$  and temperature  $T$ . Thus, even for the case of a monochromatic laser source, DIAL measurements utilizing Rayleigh backscatter produce finite spectral bandwidth effects on the return path from the atmosphere to the receiver.

For laser bandwidths which are small compared to the atmospheric-absorption line width, the Rayleigh scattering problem for DIAL measurements can be treated using the same method of solution as was developed earlier in this paper. Namely, the transmission of the laser beam along the return path through the atmosphere is treated as an equivalent finite bandwidth problem. The spectral spread function in this case is the convolution of the actual laser line shape and the Rayleigh scattering spectral function. The solution then follows as was previously discussed.

#### References

1. Penner, S. S., 1959: Quantitative Molecular Spectroscopy and Gas Emissivities (Addison-Wesley Pub. Co., Inc., Reading, MA), Chap. 3.
2. Benedetti-Michelangeli, G. and G. Fiocco, 1974: Active and passive optical Doppler techniques for the determination of atmospheric temperature, 2: A highly coherent laser radar. In: The Structure and Dynamics of the Upper Atmosphere, F. Verniani, Ed. (Elsevier, Amsterdam, pp. 211-219).

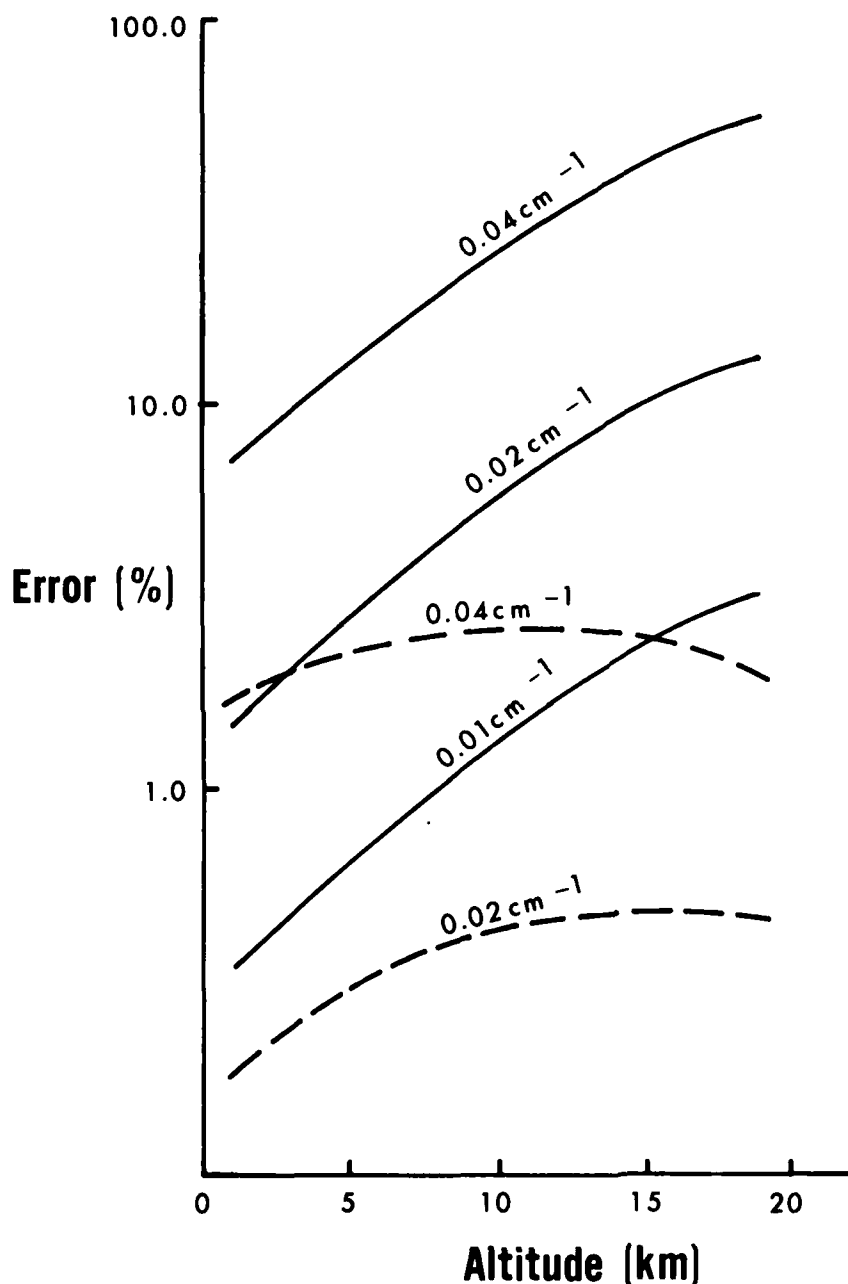


Fig. 1. The solid lines show the errors introduced by finite laser bandwidth for DIAL measurements of absorption coefficient for a typical atmospheric line. The dashed lines give the errors due to the effects of the intervening atmospheric layers.

CO<sub>2</sub> DIAL SENSITIVITY STUDIES WITH HETERODYNE AND DIRECT DETECTION

P. Brockman, C. H. Bair, and R. V. Hess

NASA Langley Research Center, Hampton, Virginia 23665

There is a great need for atmospheric trace constituent measurements with higher resolution than attainable with passive radiometers. Infrared (IR) differential absorption lidar (DIAL), which depends on Mie scattering from aerosols, has special advantages for tropospheric and lower stratospheric applications and has great potential importance for measurements from Shuttle and aircraft (refs. 1,2,3, and 4). DIAL data reduction involves comparing large amplitude signals which have small differences. The commonly used SNR expression (signal divided by noise in the absence of signal) is not adequate to describe DIAL-measurement accuracy and must be replaced by an expression which includes the random coherent (speckle) noise within the signal (refs. 5 and 6). A comprehensive DIAL computer algorithm for heterodyne and direct detection including speckle noise is used to calculate DIAL measurement sensitivities. Results are presented for measurement of ground-level plumes using direct and heterodyne detection and distributed ambient trace gases using heterodyne detection.

In differential absorption the double ratio of signals at adjacent scattering cells, at two frequencies, yields information about absorption in the region between the scattering cells:

$$2 \int_{R_1}^{R_2} (\rho \Delta \sigma) dr = \ln \left( \frac{P_{22}}{P_{12}} \frac{P_{11}}{P_{21}} \right) + \ln \left( \frac{\beta_{12}}{\beta_{11}} \frac{\beta_{21}}{\beta_{22}} \right) - 2 \int_{R_1}^{R_2} (\Delta \xi) dr$$

where  $P_{ij}$  = expectation value of measured return from cell j at frequency i,  $\beta_{ij}$  = backscatter coefficient from cell j at frequency i,  $\Delta \sigma$  = absorption coefficient difference between frequencies 1 and 2,  $\Delta \xi$  = extinction coefficient difference between frequencies 1 and 2 (not including gas being measured), i = 1 or 2 frequencies on or off absorption line, respectively, and j = 1 or 2 for distances  $R_1$  and  $R_2$ , respectively. The  $\beta$  term is negligible for range-resolved measurements if the type of scatterers does not vary with range. The  $\Delta \xi$  term can be predicted if the distribution of interferents is known. Both terms can be reduced by use of closely spaced frequencies. For scattering cells of equal length the resolution length  $R_2 - R_1$  equals the scattering cell length  $\Delta R$ . For narrow plumes of density  $\rho_p$ , length  $L < (R_2 - R_1)$ , and  $\sigma_{on} > > \sigma_{off}$ , the random error in two-way plume optical depth due to the measurement process is

$$\delta(2\rho_p L \sigma_{on}) = \left[ \frac{1}{N} \sum_{i=1}^2 \sum_{j=1}^2 \frac{1}{(\text{SNR})_{ij}^2} \right]^{1/2}$$

where N is the number of pulse pairs per measurement and SNR is the single-pulse signal-to-noise ratio.

AD-A116 294

NATIONAL AERONAUTICS AND SPACE ADMINISTRATION HAMPTON-ETC F/6 20/5  
ELEVENTH INTERNATIONAL LASER RADAR CONFERENCE, WISCONSIN UNIVER--ETC(U)  
JUN 82

UNCLASSIFIED

NASA-L-15380

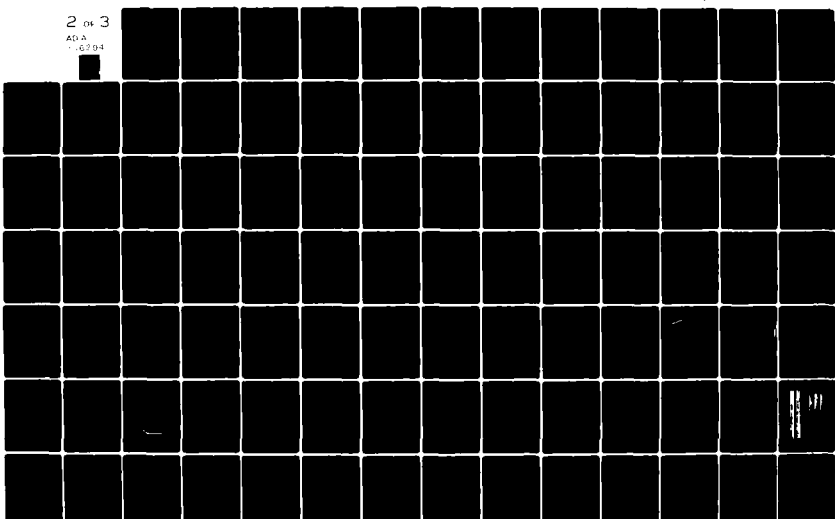
NASA-CP-2228

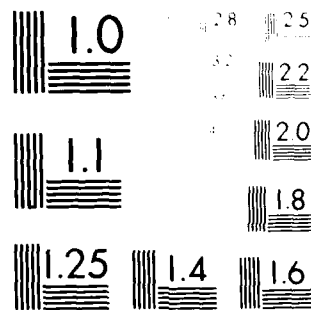
NL

2 of 3

ADA

-6294





McROBBIE Y. REED, BFA, NCEP, CPE, LEED AP

The heterodyne single-pulse signal-to-noise ratio with a single detector is

$$(\text{SNR})_{\text{HET}} = \frac{P_{ij}}{P_{ij} + BT} \sqrt{BT}$$

where B is the post-detection bandwidth and is set equal to the reciprocal of the pulse duration. T is the integration time across a scattering cell;  $T = 2\Delta R/c$ . BT is equal to the number of independent samples per scattering cell.

Direct detection can have advantages over single-detector heterodyne detection when signal levels are high since direct detection allows averaging over multiple coherence areas with a single detector. The direct-detection signal-to-noise ratio can be written as a function of the number of coherence areas M, the measured signal  $P_{ij}$ , and the detector thermal noise figure  $D_T^*$ . The direct-detection single pulse SNR is

$$(\text{SNR})_{\text{DD}} = \frac{P_{ij} \sqrt{BT}}{\left[ \frac{n^2 A_D B T^2}{(h\nu D_T^*)^2} + P_{ij} B T + (G F M T) B T + \frac{P_{ij}}{M} \right]^{1/2}}$$

Where G is the background signal in detected photons/sec/Hz per coherence area, M is the number of coherence areas, F is the bandwidth in Hz of the optical filter,  $A_D$  is detector area, and  $\eta$  is detector efficiency. Direct detection accuracies can exceed heterodyne accuracies by  $\sqrt{M}$ . An additional set of independent statistics can be achieved for direct detection by operating multimode and transmitting  $M'$  frequencies for the purpose of examples in this paper,  $M = 1000$  and  $M' = 1$ .

The assumption that the SNR improves with  $\sqrt{BT}$  implies that there are no major nonuniformities across a scattering cell. The assumption that the measurement error is reduced by  $\sqrt{N}$  implies that the range distribution of scatterers does not vary during the measurement period. This assumption will remain valid if the measurement period is short compared to time scales of atmospheric nonuniformities.

For the examples of plume-measurement sensitivity shown, the optical efficiency is 20% and quantum efficiency is 50%. Telescope area is  $.01 \text{ m}^2$  and the optical bandwidth is  $1.5 \times 10^{11} \text{ Hz}$ . The "on" and "off" frequencies have been selected to be at the R(30) ( $1084.63 \text{ cm}^{-1}$ ) and R(28) ( $1083.479 \text{ cm}^{-1}$ ) normal isotope  $\text{CO}_2$  laser lines. The "on" absorption is  $48 \text{ (atm cm)}^{-1}$  and the "off" absorption is  $.3 \text{ (atm cm)}^{-1}$ . For these frequencies the only significant interference is from  $\text{CO}_2$ ; and laser pulse energies are .01 to 10 Joules/pulse for horizontal ground-based measurements and .01 to 1 Joule/pulse for vertical measurements. M = 1 for heterodyne measurements and 1000 for direct-detection measurements. The range to the plume center is 3000 m for horizontal cases, and the range to the ground is 3500 m for vertical cases. The resolution length is 500 m for the horizontal case with  $T = 3.3 \times 10^{-6} \text{ sec}$ . Pulse width is set at  $10^{-7}$  and bandwidth at  $10^7 \text{ Hz}$ . Ground reflectivity is 1%. Figures 1 and 2 show sensitivities of plume measurements for horizontal range resolved and vertical column content measurements. The percent of error in measuring the two-way optical depth  $100 \times \delta (2\rho_p L_{\text{on}})$  of the plume is plotted against laser energy and measured photons per range cell. The figures are based on  $\text{NH}_3$  measurements where a 2% two-way optical-depth error would imply an

error in  $(2\rho_p L)$  of  $4.2 \times 10^{-4}$  atm cm or a NH<sub>3</sub> density error of  $\approx 21$  ppb in a 100 m plume. The results can be extended to other chemicals if the absorption coefficients are known. The results cannot be extended to plumes with high optical densities due to the loss of signal from behind the plume.

DIAL measurements can benefit from operating at rare isotope laser frequencies and utilizing collision broadening in the laser to tune the frequencies across atmospheric absorption lines. The use of closely spaced on and off frequencies also minimizes errors due to frequency variation in backscattering and to interfering species. An example of ambient trace gas measurement is given in figure 3 (ref. 1) which displays O<sub>3</sub> concentration in STP-ppb and measurement error in the same units versus altitude for measurement from Shuttle at 250 km. The pulse energy is 5 Joules per pulse with 1000 pulse pairs per measurement. Telescope area is 1 m<sup>2</sup>, bandwidth is 10<sup>7</sup> Hz, quantum efficiency is 50%, optical efficiency is 25%, and resolution is 1.5 km below 30 km and 3 km above 30 km. Simulations are for an "off" frequency of 1058.01 cm<sup>-1</sup> and "on" frequencies of 1058.17, 1058.11, and 1058.19 cm<sup>-1</sup>. It should be noted that a fine tuning of the "on" frequency results in a sharp variation of altitude at which the best measurement can be accomplished.

#### REFERENCES

1. Brockman, P.; Hess, R. V.; Staton, L. D.; and Bair, C. H.: DIAL with Heterodyne Detection Including Speckle Noise: Aircraft/Shuttle Measurement of O<sub>3</sub>, H<sub>2</sub>O and NH<sub>3</sub> with Pulsed Tunable Lasers. Heterodyne Systems and Technology Part II, p. 557. NASA CP-2138, 1980.
2. Hardesty, R. M.: A Comparison of Heterodyne and Direct Detection CO<sub>2</sub> DIAL Systems for Ground Based Humidity Profiling. NOAA Technical Memorandum ERL WPL-64, October 1980.
3. Megie, G.; and Menzies, R. T.: Complementarity of UV and IR Differential Absorption Lidar for Global Measurement of Atmospheric Species. Applied Optics, Vol. 19, p. 1773, 1980.
4. Hess, R. V.: CO<sub>2</sub> Lidar for Measurements of Trace Gases and Wind Velocities. SPIE 25th Annual Technical Symposium, Physics and Technology of Coherent Infrared Radar. Paper 300-05, Aug. 1981.
5. Elbaum, M.; and Teich, M. C.: Heterodyne Detection of Random Gaussian Signals in the Optical and Infrared: Optimization of Pulse Duration. Opt. Commun., Vol. 27, no. 2, pp. 257-261, Nov. 1978.
6. Rye, B. J.: Differential Absorption Lidar System Sensitivity with Heterodyne Reception. Appl. Opt., Vol. 17, no. 24, pp. 3862-3864, Dec. 1978.

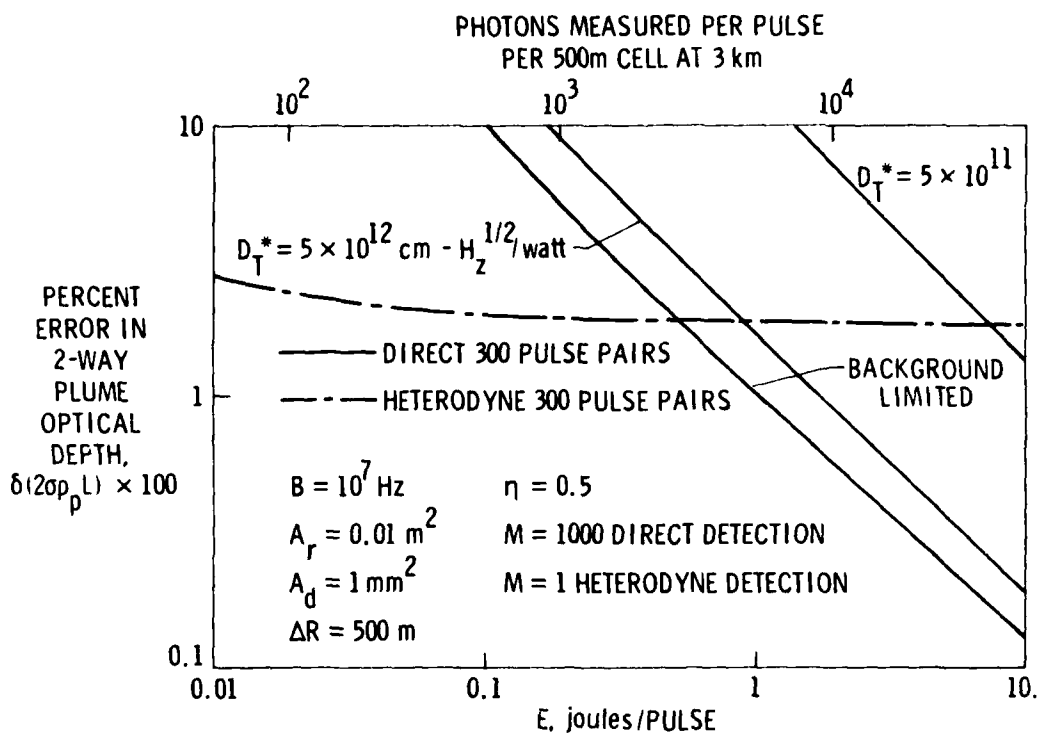


Figure 1.- Sensitivity of horizontal-range-resolved plume measurements.

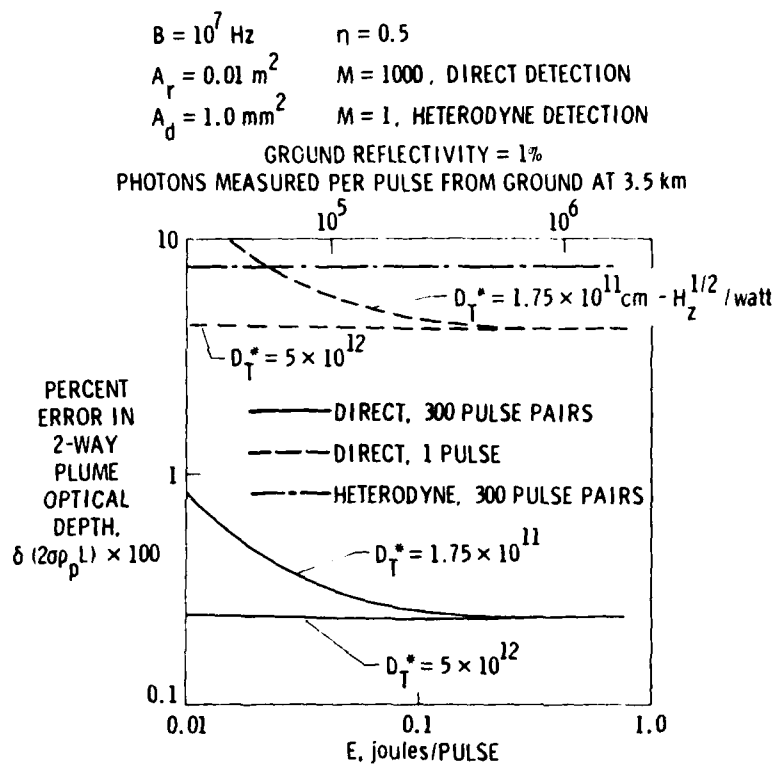


Figure 2.- Sensitivity of vertical-column-content plume measurements.

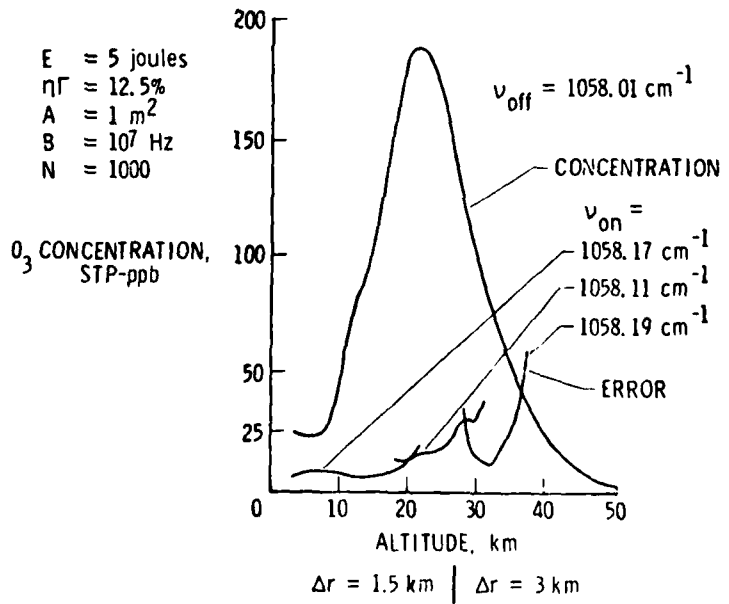


Figure 3.- Sensitivity of range-resolved ozone measurements from 250 km.

LIMITATIONS OF SIGNAL AVERAGING OF DIAL MEASUREMENTS  
DUE TO TEMPORAL CORRELATION\*

N. Menyuk and D. K. Killinger  
Lincoln Laboratory, Massachusetts Institute of Technology  
Lexington, Massachusetts 02173

and

C. R. Menyuk\*\*  
Laboratory for Plasma and Fusion Energy Studies  
University of Maryland  
College Park, Maryland 20742

The accuracy of the remote sensing of species in the atmosphere using a differential-absorption LIDAR (DIAL) system is dependent upon the determination of the value of the "on-resonance" DIAL return compared to the "off-resonance" value. The accuracy of such measurements can generally be improved by increasing the number of measurements and taking average values. This paper describes the results of an experiment which directly measured the effect of averaging on the measurement uncertainty, where the uncertainty is defined by the standard deviation of the mean value of the returns. Our results show that the reduction of the standard deviation by signal averaging over increasing numbers of pulses is much smaller than would be anticipated for independent measurements and is due to small but long-term temporal correlation. The results are shown to be in excellent agreement with a theoretical analysis which takes the correlation of successive LIDAR returns into account.

A dual mini-TEA CO<sub>2</sub> DIAL system was employed for the experiment.<sup>1</sup> The first of the two CO<sub>2</sub> lasers in the dual-laser system (laser 1) was fired on the P(28) laser transition, and 50  $\mu$ s later laser 2 was fired on the P(22) transition, both in the 10.6  $\mu$ m band. The atmosphere is effectively 'frozen' over this time interval.<sup>2</sup> The laser outputs were directed along identical beam paths to a flame-sprayed aluminum plate at a range of 2.7 km, which served as a diffusely reflecting target. A total of 22,528 LIDAR return pulses from the target were recorded for each of the two lasers. The process took 40 minutes, corresponding to a pulse repetition frequency of slightly under 10 Hz. Due to computational constraints, analysis was limited to sets of 12,288 pulses from each laser. The results obtained from the initial and final sets of data are therefore presented separately.

The measured normalized standard deviations of the LIDAR return pulses averaged over every successive  $N$  pulses,  $\sigma_N$ , are presented in Figs. 1(a) and 1(b) for the initial and final sets of data, respectively. In all four sets of data the reduction of  $\sigma_N$  with increasing  $N$  is much slower than the  $N^{-1/2}$  dependence expected for uncorrelated signals. In addition, the near

\*The Lincoln Laboratory portion of this work was supported by the National Aeronautical and Space Administration and the Air Force Engineering and Services Center.

\*\*The University of Maryland portion of this work was supported by the Department of Energy.

"flattening" of  $\sigma_N$  with large  $N$  seen in Fig. 1(b) is consistent with the long-term atmospheric drift observed during this period.

These results can be explained by a theoretical analysis which considers the effect of pulse averaging in the presence of temporal correlation. Let us define  $I_k = I(t_k)$  as the normalized deviation of the  $k$ th pulse return (occurring at time  $t_k$ ) from its mean value over the full set of data. That is,

$$I_k = \frac{J_k - \bar{J}}{\bar{J}} \quad (1)$$

where  $J_k$  is the  $k$ th LIDAR pulse return signal. Then, the temporal correlation function for a delay time equal to  $j\tau$  is given by

$$\rho_j = \frac{1}{\sigma^2} \langle I(t_k) I(t_k + j\tau) \rangle \equiv \frac{1}{\sigma^2 (\Gamma - j)} \sum_{k=1}^{\Gamma-j} I_k I_{k+j} \quad (2)$$

where  $\sigma$  is the normalized standard deviation of the full set of individual pulses ( $N=1$ ),  $\Gamma$  is the total number of pulses in the set, and  $\tau$  is the interval between pulses.

It can be shown that, to a good approximation, the pulse-averaged standard deviation is related to the temporal correlation by the equation

$$\sigma_N = \frac{\sigma}{\sqrt{N}} \left[ 1 + 2 \sum_{j=1}^{N-1} (1 - j/N) \rho_j \right]^{1/2} \quad (3)$$

It should be noted that in the absence of correlation ( $\rho_j=0$ ), Eq. (3) predicts the expected  $N^{-1/2}$  dependence.

The LIDAR data were used to evaluate the temporal correlation coefficients  $\rho_j$  for  $j=1, 2, 4, 8, \dots, 1024, 2048$ , with a linear interpolation used for the intermediate values. These values were then used in Eq. (3) to calculate  $\sigma_N^2$ , and the results were compared with the measured values of  $\sigma_N^2$  shown in Figs. 1(a) and 1(b). The agreement was found to be excellent.

These results serve to validate Eq. (3) and indicate that the improvements available through signal averaging of LIDAR returns reflected from hard targets can be severely limited by the presence of small but long-term temporal correlation. In addition to presenting the correlation functions obtained from our data, a discussion of the nature of these limitations will be presented.

REFERENCES:

1. D. K. Killinger and N. Menyuk, "Remote Probing of the Atmosphere Using a CO<sub>2</sub> DIAL System," IEEE J. Quantum Electron. QE-17, 1917 (1981).
2. N. Menyuk and D. K. Killinger, "Temporal Correlation Measurements of Pulsed Dual CO<sub>2</sub> LIDAR Returns," Opt. Lett. 6, 301 (1981).

114892-R

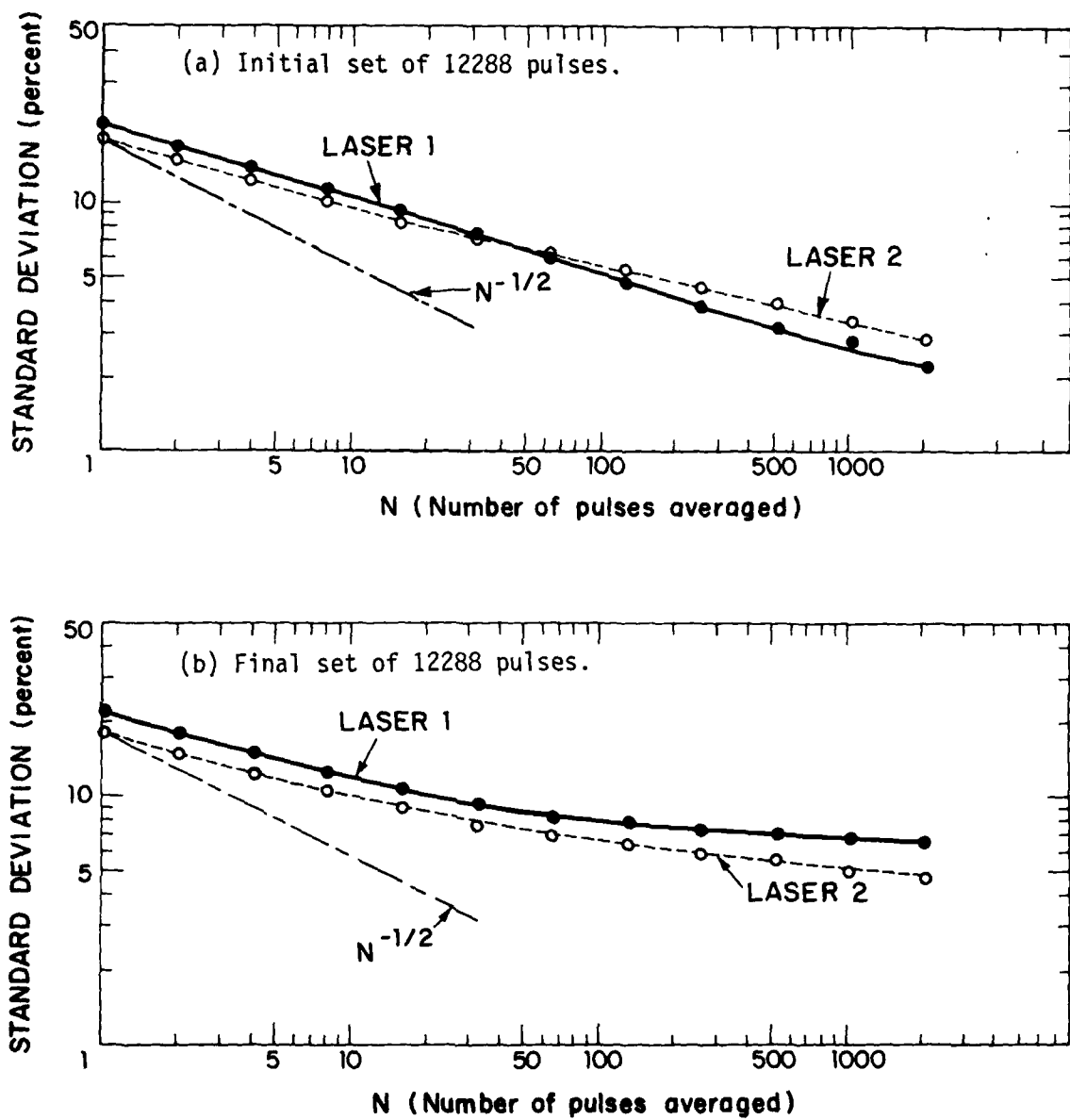


Fig. 1. Standard deviation of LIDAR return signals as a function of the number of pulses averaged.

## STATISTICAL PROPERTIES OF CO<sub>2</sub> LIDAR RETURNS FROM TOPOGRAPHIC TARGETS

P. H. Flamant

R. T. Menzies

M. J. Kavaya

Jet Propulsion Laboratory  
California Institute of Technology  
Pasadena, CA 91109

### Abstract

Due to the many potential applications of infrared lidar to measurements of gaseous and aerosol composition in various atmospheric regions, the influence of diffuse (optically rough) topographic targets on the return signal intensity fluctuations must be well characterized. Often topographic targets are the most convenient means of providing a backscattered signal when measurements are to be made over an atmospheric path. Yet the far-field speckle pattern which is produced when a rough surface is illuminated by coherent radiation produces intensity fluctuation effects which are not always well understood and are often difficult to separate from effects of atmospheric turbulence or transmitter beam jitter. The statistics of fully developed speckle patterns are well understood [1,2]. The reduction of the variance in detected intensity through aperture averaging is straightforward [1,3] and has been employed in many DIAL systems which use direct detection [4]. For coherent detection systems, aperture average is not an option, and one would normally expect to observe the effects of fully developed speckle when using topographic targets. However, when short-pulse laser transmitters are used, there are cases for which the coherence length of the radiation is not large compared to the depth variation of the ensemble of scatterers which provide the backscatter. In such cases, the statistical properties of the lidar signal change significantly.

We report the results of a study of the probability distribution function (pdf) of detected intensity when using a TEA CO<sub>2</sub> laser transmitter and various topographical targets at a distance of approximately 2 km from the instrument. The receiver optics were designed for coherent detection; consequently there was no aperture averaging. However, the receiver was used in a direct detection mode, making it possible to study speckle effects on return signal intensity for two cases: (1) a free-running, multi-longitudinal-mode TEA laser, emitting pulses with a spectral bandwidth of approximately 4 GHz (0.13 cm<sup>-1</sup>) and pulse duration of 200 nsec., and (2) an injection-locked TEA laser, emitting a single-longitudinal-mode (SLM) with a spectral bandwidth dictated by the

Fourier transform of the pulse duration, also 200 nsec. Histograms were plotted depicting the pdf of detected intensity when scattering from various topographic targets, for each of the two cases. Examples are shown in Figures 1 and 2.

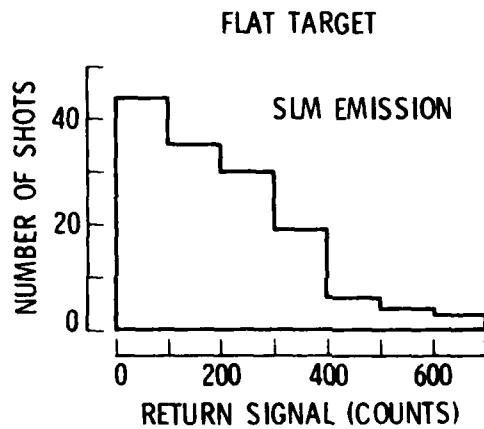


Figure 1. Histogram of return signal intensity from "flat" target.

In Figure 1 are shown the results when scattering from a painted structure attached to a reservoir dam. Although this surface is rough compared to the  $10 \mu\text{m}$  wavelength, it is a flat surface when compared with the pulse coherence length. The resulting pdf is approximately exponential, as expected.

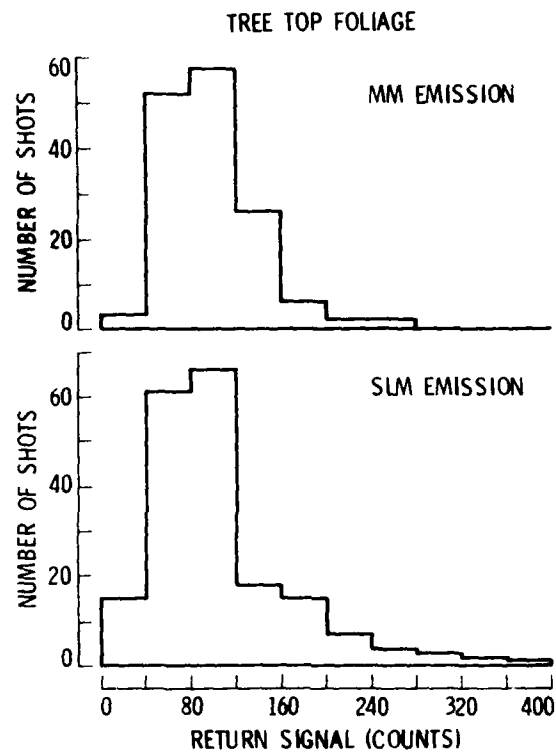


Figure 2. Histograms of return signal intensities from tree top foliage.

In Figure 2 are shown the results when scattering from tree top foliage in a wooded region near the reservoir dam. The pdf's for both the multi-mode and SLM cases are closer to a log-normal distribution than an exponential distribution. This is to be expected for the multi-mode case, in which the coherence length is short compared with the depth variation of the tree foliage target. However, the results for the SLM case are mildly surprising. Apparently the

tree top target significantly alters the pdf from that expected for a fully developed speckle pattern. An estimate of the mean intensity (to an uncertainty level of 10%, for example) can be determined with fewer pulses as a result. These and other examples will be discussed.

#### References

- (1) J. C. Dainty, editor, Laser Speckle and Related Phenomena (Springer, Topics in Applied Physics, Vol. 9, 1975).
- (2) R. M. Hardesty, R. J. Keeler, M. J. Post, and R. A. Richter, Applied Optics 20, 3763 (1981).
- (3) J. F. Holmes, "The Effects of Target Induced Speckle, Atmospheric Turbulence, and Beam Pointing Jitter on the Errors in Remote Sensing Measurements," paper presented at the Workshop on Optical and Remote Sensing, Monterey, CA, February, 1982.
- (4) N. Menyuk and D. K. Killinger, Optic Letters 6, 301 (1981).

MEASUREMENT ERROR IN AIRBORNE CO<sub>2</sub> LASER HETERODYNE  
SENSOR FOR MONITORING REGIONAL OZONE DISTRIBUTIONS

Kazuhiro Asai, Toshikazu Itabe, and Takashi Igarashi  
Radio Research Laboratories  
Ministry of Posts and Telecommunications  
Koganei, Tokyo 184, Japan

1. Introduction

The airborne laser remote sensing has been featured as a powerful and useful technique for measuring regional distributions of ozone concentrations in a short time. Several groups have worked on developments of airborne remote-sensing systems with cw CO<sub>2</sub> lasers and pulsed CO<sub>2</sub> lasers. (1-7)

This paper will discuss a measurement error in the airborne CO<sub>2</sub> laser heterodyne sensor for ozone measurements. A brief description is given of our airborne system and of flight experiments for the differential albedo and various ground surfaces.

2. Analysis of Measurement Error

We assume that there is no interference from other gases. When the aircraft is flying toward the x-direction, ozone column density between the aircraft and the ground at point x is estimated by using the differential absorption technique as follows:

$$N(x) = \frac{1}{2 \Delta \sigma H} \{ \ln R_I(x) + \ln R_A(x) \} \quad (1)$$

$$R_I(x) = \frac{I_{if_2}(x)/I_2}{I_{if_1}(x)/I_1}$$

$$R_A(x) = \frac{\gamma_1(x)}{\gamma_2(x)}$$

where N(x) is a column density of ozone at point x,  $\Delta \sigma$  is the differential absorption cross section of ozone molecule, H is an aircraft altitude,  $I_{if}(x)$  is an intensity of if beat signal in the sky at the point x, I is the laser power,  $\gamma$  is the albedo of the ground surface at the point x, and subscripts 1 and 2 correspond to on-resonance line and off-resonance line, respectively.  $R_A$  defined as the ratio of albedo should strongly depend on materials of ground surfaces. Knowledge about  $R_A$  at various ground surfaces, e.g., town, suburbs, country, sea, etc., is required in advance for calculation of the ozone density from eq. (1).

According to "a law of error propagation", a square of the relative standard error of ozone number density  $(\Delta N/N)^2$  is given by

$$\left( \frac{\Delta N}{N} \right)^2 = \left( \frac{\Delta H}{H} \right)^2 + \frac{1}{(2 \Delta \sigma \bar{N} \bar{H})^2} \left\{ \left( \frac{\Delta R_I}{R_I} \right)^2 + \left( \frac{\Delta R_A}{R_A} \right)^2 \right\} \quad (2)$$

where  $\Delta N$ ,  $\Delta H$ ,  $\Delta R_I$ , and  $\Delta R_A$  are standard deviations of  $N$ ,  $H$ ,  $R_I$ , and  $R_A$  and  $\bar{N}$ ,  $\bar{H}$ ,  $\bar{R}_I$ , and  $\bar{R}_A$  are averages of  $N$ ,  $H$ ,  $R_I$ , and  $R_A$ , respectively. We will discuss each term as follows:

(i) Term of  $\Delta H/\bar{H}$ : this term is resulting from random changes of pitch and roll angles of the aircraft during flights. However, even if these angles randomly change  $\pm 5$  degrees,  $\Delta H/\bar{H}$  gives only an error of 0.8% in  $\Delta N/\bar{N}$ .

(ii) Term of  $\Delta R_I/\bar{R}_I$ : this  $\Delta R_I/\bar{R}_I$  is divided into two factors. One of these is due to changes of optical axes of transmitter, heterodyne receiver optics by mechanical vibrations, and heating in the aircraft. The other factor is resulting from instabilities of signal processing and recording electronics instruments. The error caused by these factors is called the systematic error. This error should be reduced by careful designs and alignments for the system.

(iii) Term of  $\Delta R_A/\bar{R}_A$ : this term is due to the fact that the albedo of the ground surface depends on laser lines. The error caused by this frequency dependence of ground surface's albedo is an uncontrollable factor. Measurement error of this airborne system might be eventually determined by this term.

Fig. 1 shows a calculated result for the relative standard error of  $R_A$  vs  $\Delta N/\bar{N}$ . As shown in Fig. 1, the fluctuations of  $R_A$  will be serious problems in the flight operations for measuring regional ozone concentrations.

### 3. Experiments

A block diagram of our airborne laser heterodyne sensor is shown in Fig. 2. The system under development is divided into three sections: i.e., transmitting-receiving optics including two waveguide CO<sub>2</sub> lasers, the heterodyne receiver, data acquisition electronics and recording instruments. P(14) is used for on-resonance line, P(24) for off-resonance line. Both outputs of each laser are about 500 mW. Two laser beams are pointed the direction of 7 degrees back of nadir. Frequency of if beat signal from the HgCdTe mixer was 1.5-2.5 MHz at the flying speed of 250 km/hour. The if beat signals were detected by an envelope detector through a pre-amplifier and a if bandpass filter, then recorded in an analog data recorder. Off-line data analysis were made by a computer in the laboratory for all data recorded in the aircraft during flights. The experiments were made over 20 hours observing various ground surfaces; i.e., big cities, suburbs, countries, forest, sea, and ground covered with snow. The aircraft used in the flight was Grand Commander 685. Table 1 shows  $R_A$  normalized by  $\bar{R}_A$  of a doppler shifter in aluminum for big cities and countries.

### 4. Summary

We discussed the importance of preliminary knowledge about the ratio of the albedo,  $R_A$  and  $\Delta R_A$ , of various places for minimizing the measurement errors. We don't think that our experimental data are enough to determine  $R_A$  and  $\Delta R_A$  for the above places (big cities and countries). It is still necessary to fly for the determination of this  $R_A$  at various ground surfaces.

Further analyzed data including Fourier transforms will be discussed at the conference.

#### References

- (1) R. T. Menzies and M. S. Shumate; *J. Geophys. Res.*, 89 4039 (1978)  
M. S. Shumate, R. R. Menzies, W. B. Grant and D. S. McDougal; *Appl. optics*,  
20, 545 (1981)
- (2) R. B. Wiesemann, W. English and K. Gurs; *Appl. Phys.* 15, 257 (1978)
- (3) R. W. Stewart and J. Bufton; *Optical Eng.*, 19, 503 (1980)
- (4) P. Brockman, R. V. Hess, L. D. Staton and C. H. Bair; *NASA CP-2138*, 1980.
- (5) J. Boscher and F. Lehmann; *Battelle Institute e.V.*, D-6000 Frankfurt am Main,  
West Germany (1979)
- (6) K. Asai, T. Itabe, T. Matsui and T. Igarashi; *Symposium on Laser Radar in  
Japan at Hamana*, Feb. (1981)
- (7) K. Asai, T. Itabe and T. Igarashi; *Workshop on optical and laser remote  
sensing in Monterey Cal.*, Feb. 9-11, 1982

TABLE I.- MEASURED  $\bar{R}_A$  IN THE FLIGHT EXPERIMENT

	$\bar{R}_A$ normalized by aluminum doppler shifter
Big cities	0.9
Country	1.26

Fig. 1.- Estimated curves for measurement error,  $\Delta N / \bar{N}$  vs.  $\Delta R_A / \bar{R}_A$  with parameters of aircraft altitude.

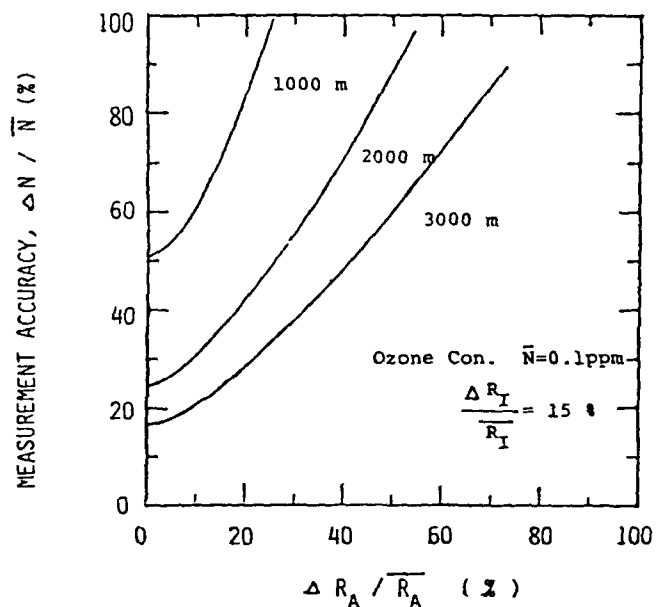
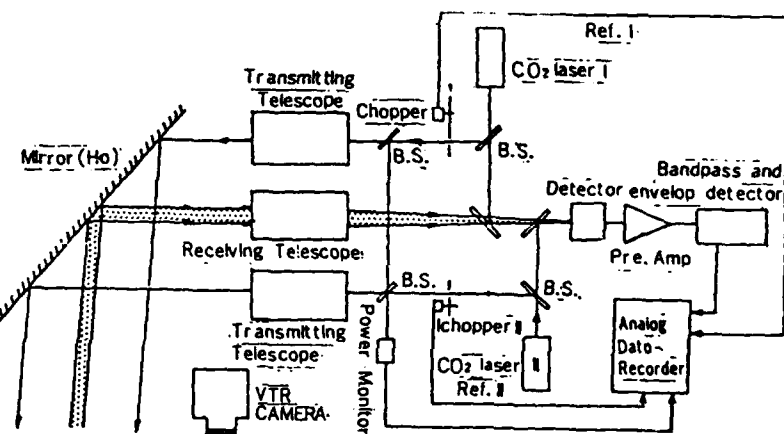


Fig. 2.- Block diagram of airborne  $\text{CO}_2$  laser heterodyne sensor for monitoring regional ozone concentrations.



A HIGH PRESSURE LASER FOR LIDAR MEASUREMENTS  
OF POLLUTANTS IN THE ATMOSPHERE

John C. Petheram and J.W. van Dijk

University of Hull, Dept. of Applied Physics, Hull, UK, HU6 7RX.

INTRODUCTION

Until the invention of the TEA CO<sub>2</sub> laser in 1969 only ozone and sulphur dioxide (in the UV) and nitrogen dioxide (in the blue) were considered accessible to laser monitoring by virtue of the fortunate coincidence of possessing an absorption spectrum which overlapped an existing laser wavelength. The TEA laser immediately offered high peak powers on many regularly spaced emission lines between 9 and 11 microns where many more chemicals of interest absorb. The lasers were easy to fabricate, the laser medium was of low cost, and the dual properties of high pulse energy and high repetition frequency made the data collection task easier. The operational capability of LIDAR systems was also enhanced by the improved propagation characteristics at this wavelength. A number of CO<sub>2</sub> LIDAR systems were constructed, both for anemometry and differential absorption (DIAL), and operated more or less successfully.

Recently, however, it has been suggested that CO<sub>2</sub> lasers operating at a pressure above atmospheric might be more suitable for future pollution monitoring systems. The reason is that although the TEA CO<sub>2</sub> laser emits a multiplicity of individually selectable wavelengths, these wavelengths are fixed to within a few tens of megahertz. Thus, a laser frequency will often probe more than one molecular absorption feature at a time making the specific identification of a particular chemical species difficult. Also, if the background interfering species is water vapour, as is likely to be the case in the troposphere, variations in the absolute humidity will lead to an inaccurate estimation of the target chemical concentration [1]. A further complication for DIAL systems which use the atmospheric aerosol as the reflector is that absorption by the aerosol makes the backscattering term a sensitive function of frequency and relative humidity [2]. This leads to systematic errors in determining the chemical species concentration. These effects may be minimised if we have available a tunable source such that by judicious selection of the laser frequency we only probe a single spectral line belonging to a single chemical species at any one time.

Increasing the gas pressure in a CO<sub>2</sub> laser causes the individual vibrational-rotational transitions to broaden. At a pressure >10 atmospheres the gain curve is essentially continuous over the 9-11 micron region and the output broadly tunable allowing the desired laser frequency selection to be made. Unfortunately this virtually uniform gain gives rise to increased linewidth and decreased stability and, in order to probe

atmospheric absorption lines (which possess a halfwidth of  $\approx 3\text{GHz}$ ) a laser linewidth and stability of  $\approx 100\text{ MHz}$  is necessary. This has led to the laser which has been constructed at the University of Hull, specifically for DIAL applications, containing many novel design features in an effort to produce a stable, narrow line output.

#### LASER DESIGN

High pressure lasers require a pressure vessel to contain the gas and traditionally this has been simply a metal tube with end plates bolted on to flanges. The plates are perforated to allow access for the essential services: gas, electricity and water if required. Our design is fundamentally different in this respect, however, since it consists of two concentric cylinders the space in between being filled with water. The water will eventually act as the main energy storage capacitor but initially serves just to add mass to the laser head and damp-out acoustic vibrations.

The concentric cylinders are pierced at 6 places around their circumference with three pairs of diametrically opposed access slots; these allow electrode supports or windows to be positioned in place. The fact that the electrodes can be moved between different pairs of slots allows for future insertion of an amplifier if need be. The provision of the windows means that the discharge can be viewed and interferometry, Schlieren photography or holography used diagnostically. The slots also allow the high voltage supply to be fed in the side rather than the end, substantially reducing the firing circuit inductance.

The electrodes in a TE laser need to be manufactured to very high tolerances and aligned very carefully. The electrode is an equipotential surface and careful alignment reduces the possibility of the glow discharge degenerating into an arc with consequent non-uniform energy deposition and loss of efficiency. This is important because arcs damage the electrodes and non-uniform energy deposition leads to refractive index discontinuities and poor output mode quality. The electrodes in the Hull laser are Chang profiles [3] and have been manufactured using numerically controlled machinery assuring that at all times the material was strain free. They may be aligned by screw adjusters when they are in position in the vessel, unlike the normal practice of resorting to shims and washers. This arrangement also lends itself to the possibility of the electrodes being deliberately inclined by known amounts to parametrically study the intrapulse chirp.

To prevent the discharge forming arcs when the main voltage is applied the gas needs to be preconditioned, i.e., preionised to aid formation of a uniform glow. There are many ways of doing this but one of the simplest and cheapest is UV photoionisation (UVPI). Here, subsidiary discharges (sparks) are struck at some distance away from the lasing volume and UV photons propagate towards the gap. Electrons produced by one-step photoionisation

of impurities in the gas serve to seed the discharge. Palmer [4] has shown that at a pressure of 10 atmospheres an electron density  $n_e = 10^7$  e/cm<sup>3</sup> is required and Babcock et al [5] have derived expressions for the number of electrons produced by a single spark as a function of energy(J), peak spark current(j), inductance(L) and pressure(P). Babcock's equations together with Palmer's criterion have allowed us to model the UVPI electron density distribution in three dimensions and select the best combination of parameters to achieve as uniform a distribution as possible.

The empirical equation used is:

$$n_e = 4 \times 10^{-4} j (CV^2 P/2N)^{0.5} \sum_{i=1}^N d_i^{-2} N_e(P, d_i)$$

where N is the total number of sparks and  $d_i$  can be found by Pythagoras.  $N_e(P, d_i)$  is derived from Babcock. Controllable parameters, voltage, inductance and capacitance enter via  $j = V(C/L)^{0.5}$  and  $J = 0.5CV^2$ . Typical results are shown in figs. 1 and 2. Fig. 1 shows the configuration used in our laser (15 sparks opposite 14) and fig. 2 the effect of too few sparks. In general we conclude:

(i) the sparks should be in a double row opposite one another and offset to give improved uniformity.

(ii) in order to achieve a flat distribution along the electrode and across the width a spark is required every  $\approx 2$  cm.

(iii) the spark array must be longer than the electrodes to avoid the tail-off effect, with 25-cm electrodes we use a 30-cm PI.

(iv) the most sensitive parameter is the distance of the spark array from the electrode center line. Our PI is adjustable between 2 and 5 cm. The figs. show the case for  $d = 3$  cm.

Preliminary testing of the device is in hand and some early results will be presented.

#### REFERENCES

- (1) J.C. Petheram, at Tenth International Laser Radar Conference, Silver Spring, Md (1980), post deadline paper
- (2) J.C. Petheram, Appl. Opt. 20, 3941 (1981)
- (3) T.Y. Chang, Rev. Sci. Instrum. 44, 405 (1973)
- (4) A.J. Palmer, Appl. Phys. Lett. 25, 138 (1974)
- (5) R.V. Babcock et al., IEEE Jo. Quant. Electr. QE-12, 29 (1976)

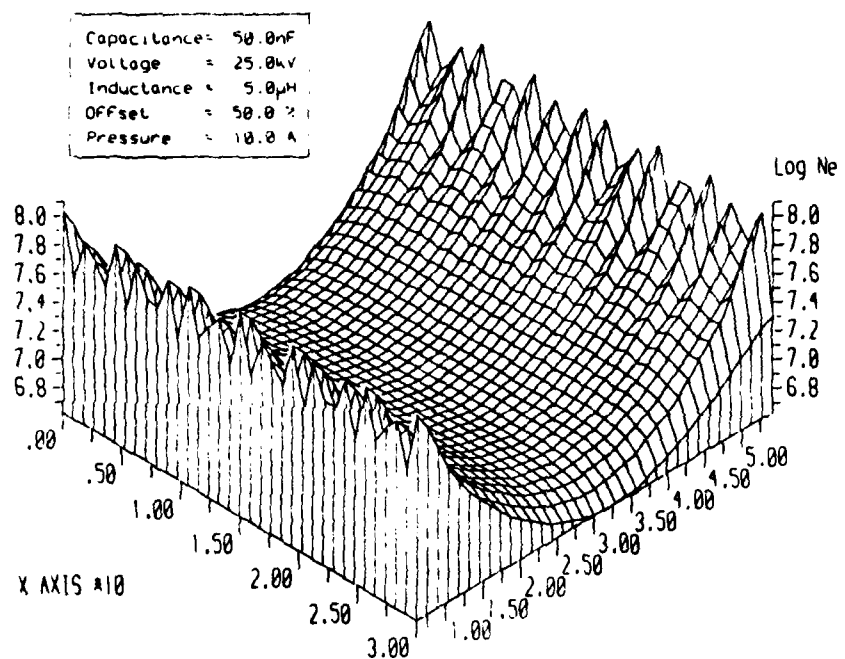


FIG. 1

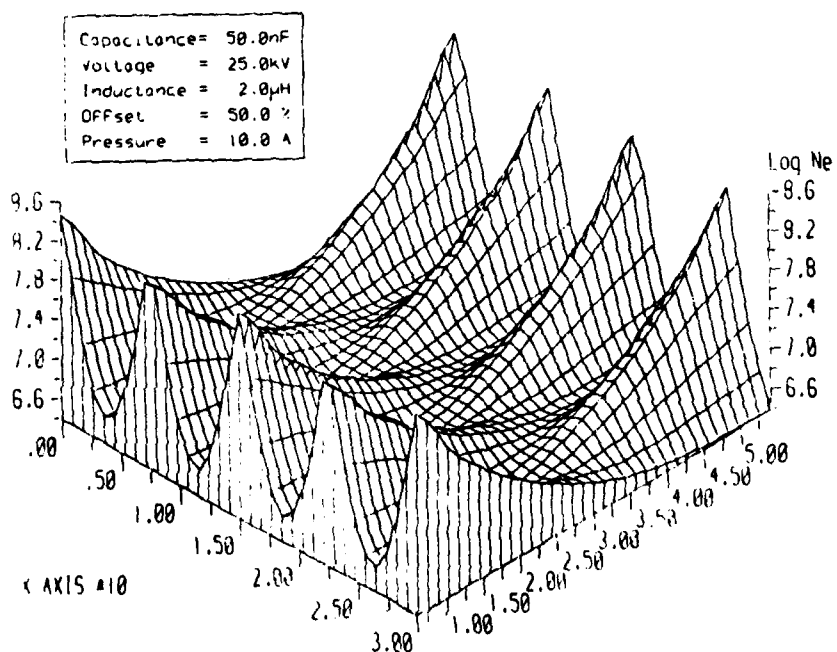


FIG. 2

Infrared Doppler Lidar Antenna Design Considerations and  
Performance Characteristics of the NOAA Ground Based Doppler Lidar

T. R. Lawrence  
National Oceanic and Atmospheric Administration  
Environmental Research Laboratories  
Wave Propagation Laboratory  
Boulder, Colorado 80303

ABSTRACT

Inference of target properties from Doppler lidar returns requires precise knowledge of system efficiency, attenuation and degradation due to atmospheric propagation effects and system parameters respectively. Within the latter category, the parameters that determine the range dependence of the system response function (the antenna gain function) are the telescope diameter, the range at which the telescope is focused and the beam illumination irradiation patterns on the transmitting and receiver apertures. The results of an analysis of the antenna gain function dependence on these parameters will be presented and the predictions compared with experimental data. The results presented are useful as guidelines in design of systems for applications requiring a match of the antenna gain function to the requirements of a particular application, or for what is usually the requirement, that of maximizing performance at long range.

It is shown that the heterodyne signal calculation can be accomplished at the target plane using transmitter and local oscillator fields transformed to that plane. To retain flexibility in assignment of beam apodizations, the FFT algorithm as described by Sziklas and Siegman is used to calculate the fields in the target plane. The results show a marked dependence of the range dependence of the lidar response on system parameters. Performance characteristics of the NOAA Doppler lidar are considered and compared with predictions. For detection of calibrated diffuse targets, the signal return is within 6 dB of theoretical after compensation for easily measured system losses.

## COLOR DISPLAY AND PROCESSING OF DOPPLER LIDAR DATA

R. Jeffrey Keeler  
National Center for Atmospheric Research  
Field Observing Facility  
P.O. Box 3000  
Boulder, CO 80307

and

R. Michael Hardesty and David K. Churchill  
National Oceanic and Atmospheric Administration  
Wave Propagation Lab, R45x2  
325 Broadway  
Boulder, CO 80303

Several research groups have built pulsed coherent CO<sub>2</sub> Doppler lidars that are capable of obtaining clear air aerosol returns in the boundary layer at ranges in excess of 20 km. The Wave Propagation Lab of the National Oceanic and Atmospheric Administration has developed one such system that is described elsewhere in these abstracts(1). This lidar system produces field data tapes which contain the sampled complex time series of returns from each pulse. Coherent lidar returns from a single pulse are processed off-line to extract the backscatter and velocity at all ranges within a single pulse.

In the last few years radar meteorologists have been able to study the detailed structure of atmospheric flow fields both in real time and during post-processing by utilizing color-coded plan position indicator (PPI) displays(2). Similar PPI displays of lidar backscatter and velocity would allow one to readily detect meteorologically significant structures such as wind shear, gust fronts, downbursts and mesocyclones in the clear air and to qualitatively estimate the profile of the horizontal wind field. Such measurements and event detection would be much more difficult using only one-dimensional velocity plots along a single beam or scanning a processed set of velocity azimuth display (VAD) outputs. The color aspect of the display allows the viewer to see fine fluctuations in the field more readily as well as presenting an image that is pleasing to view. The two dimensional display contains spatial information that is not available in one dimensional plots and color provides the psychological effect of making us want to look at the meteorological information contained in the image.

The meteorological radar (microwave) community has a well developed technology and mature data analysis procedures for processing multiple Doppler radar (or lidar) data. In particular they have developed a common Doppler radar exchange format for insuring compatible data sets collected from different radars(3). The National Center for Atmospheric Research (NCAR) has developed a sophisticated color image display and processing capability which accepts these universal exchange format data

tapes(4). The Research Data Support System (RDSS) is a dual-processor, multi-user computing facility based around a DEC VAX and PDP 11/60. The total disk storage is over 2 Gbytes and memory is over 4 Mbytes. This large mass storage can hold several thousand images for sequential image processing and rapid access of different images. The images are displayed on two COMTAL programmable display and processing systems. Standard image processing features (roam and zoom, range-azimuth grids, alphanumeric labelling, color table definition, add/subtract images, etc.) are available as well as special features (intensity of the velocity image enhanced by the reflectivity image and two- or three-dimensional spatial filtering). The images can be recorded on 35 mm or Polaroid film or a color printer.

We have converted field data tapes from NOAA's lidar to the universal exchange format for display and further processing on NCAR's RDSS. We will present color images of lidar backscatter, radial velocity, and a measure of reliability. The backscatter (beta) will be displayed on a logarithmic scale,  $\text{dB}\beta = 10 \log_2 \beta$  with  $\beta$  in  $(\text{m str})^{-1}$  and the velocity in  $\text{m s}^{-1}$ . We will compare lidar-derived images with radar-derived images to show how the two remote sensor systems differ in sensitivity to various meteorological targets, different wavelengths, and different target volumes.

Although real atmospheres are three-dimensional, many remote sensing systems treat the data as if it were one-dimensional. Specifically, a coherent Doppler lidar system gives a backscatter and radial velocity measurement at each range gate along the beam. The small beam diameter and short coherence time of atmospheric targets that are typical of coherent infrared lidars prevent our performing coherent integration over three-dimensional volumes of a size larger than the pulse volume. Consequently, we are justified in performing coherent processing in only one dimension to estimate the aerosol density, the radial velocity, and even the spectral width, which gives an indication of shear and turbulence within the sampled volume. Any additional processing of the range-gated data can most easily be done off-line after the data are recorded.

For many purposes spatial averaging techniques are adequate; however, the detailed aerosol or velocity structure is lost. When detailed spatial relationships are required, we desire a true three-dimensional display or an effective two-dimensional presentation (an image) of the three-dimensional information. Perhaps 3D holograms could be implemented directly with optical waves, but the technology for achieving such displays may not be practical.

Digital imaging systems, however, are commonplace. A set of PPI image displays taken at different elevation angles contains an enormous store of three-dimensional information presented as a sequence of two-dimensional images. Present lidar systems can measure accurately both the aerosol density and the radial velocity over a very large dynamic

range. By color encoding the range gated data in each image, we may readily observe the fine structure in the lidar reflectivity and velocity fields. If many of the two-dimensional fields (taken at constant elevation angles) are stored in a computer having a sufficiently large memory and if the data base can be accessed appropriately, then 2D images corresponding to any plane slice through the 3D volume scan can be displayed. This capability is entirely satisfactory for many atmospheric science investigations.

Color coded PPI plots of range-corrected lidar intensity allows us to observe the structure and behavior of aerosol masses in the clear air. The structure of aerosol "clouds" in and above the boundary layer needs to be better understood in order to properly estimate the performance of various proposed infrared lidar systems. Because the aerosol targets characteristic of clear air returns decorrelate within a few microseconds under typical atmospheric conditions, the returns from consecutive pulses are uncorrelated. However, many times the aerosol returns from consecutive pulses have the same mean power and velocity, and pulse-to-pulse averaging provides a more precise measurement of these values. By displaying the lidar data in a two-dimensional PPI format, we can visually detect changes in the mean value of backscatter or velocity. If we desire to smooth fluctuations caused by noise or by the Rayleigh target, we can perform spatial smoothing on the image field plus a host of other well known image processing algorithms.

An immediate question that comes to mind when displaying lidar data having a narrow beamwidth of approximately 1 m at a range of 20 km and a beam separation approximately one degree is "Should we fill in the area between the actual sensed volumes or leave them blank?" We have found from preliminary image displays that overlaying multiple scans of narrow beamwidth data so that random filling yields a fully illuminated image provides a useful display. We will show examples.

NCAR's RDSS includes an interactive editing capability(5) that allows the user to explore the above question and to evaluate various other data transformations and presentations. For example, we can remove the mean wind motion from a velocity image and see the circulation and convergence areas more readily. We can perform gate-to-gate differencing to detect shear regions. We can perform three-dimensional smoothing to remove speckle from closely spaced beams. We can "unfold" aliased velocities based on spatial continuity. And we can construct RHI (Range Height Indicator) or CAPPI (Constant Altitude PPI) scans from a volume of PPI scans. The flexibility of this interactive editing facility has been demonstrated for microwave radar data. We will extend these capabilities and show how the RDSS color imaging system will enhance the meteorological applications of a scanning Doppler lidar system.

## REFERENCES

1. Hardesty, R. M., "Measurement of Winds, Backscatter and Return Signal Properties Using Pulsed Coherent Lidar," Eleventh International Laser Radar Conference, NASA CP-2228, 1982. (Paper G4 of this compilation.)
2. Gray, R.G., R.J. Serafin, D. Atlas, R.E. Rinehart, J.J. Boyajian; "Real Time Color Doppler Radar Display", Bulletin of AMS, Vol. 56, No. 6, June 1975, p. 580-588.
3. Barnes, S. "Report on a Meeting to Establish a Common Doppler Radar Data Exchange Format," Bulletin of AMS, Vol. 61, No. 11, Nov. 1980, p. 1401-1404.
4. Brown, R.C. and V.F. Borgogno, "A Laboratory Radar Display System," Preprints 19th Radar Meteorology Conference, 1980, Miami, FL., AMS, p. 272-277.
5. Oye, R. and R.E. Carbone, "Interactive Doppler Editing Software", Preprints 20th Radar Meteorology Conference, 1981, Boston, MA, AMS, p. 683-689.

## RM CW LIDAR

Nobuo TAKEUCHI\*, Katsumi SAKURAI, \*\* Nobuo SUGIMOTO\*,  
Hiroshi BABA, \*\* and Masamichi KONDO\*\*

\*National Institute for Environmental Studies,  
Yatabe, Tsukuba, Ibaraki 305 Japan

\*\*University of Tokyo, Komaba, Meguro, Tokyo 153 Japan

### 1. Introduction

In lidar the range resolution is usually obtained by the measurement of return time of a scattered laser pulse. This pulse technique belongs to the impulse response method. It is also possible to obtain the response function by demodulating the scattered signal of modulated CW laser light. In the case of modulation by a pseudorandom code, demodulation can be performed by taking correlation with the modulation signal itself.

In this paper, we report on a new lidar technique pseudorandom-code modulated CW lidar. Although Doppler lidar and long-path absorption method use CW lasers, they lack the ability of obtaining spatial resolution. An FM (frequency modulation) CW lidar<sup>1)</sup> was proposed, and a preliminary experiment<sup>2)</sup> was reported. However, an FM CW lidar requires the detection of frequency beat. On the other hand, the pseudorandom-code modulated CW lidar (hereafter we call this lidar random modulation (RM) CW lidar, named after FM CW lidar) does not necessarily require phase sensitive detection (in principle, incoherent detection is enough). The RM CW lidar is an analogy to a coded pulse radar in the microwave range<sup>3)</sup>. The latter is operated interruptedly to get rid of the strong influence from the short distance. In the RM CW lidar, we can remove the short range effect by adjusting nonoverlapping range between the laser beam and the telescope field-of-view.

### 2. Theory

The principle of the RM CW lidar is shown in Fig.1. The lidar equation for the RM CW lidar is written as

$$\begin{aligned} P(t) = & \\ & P_0 \int_{t-T}^t S(t-t')M(t')dt' \\ & + b_0(t) \end{aligned} \quad (1)$$

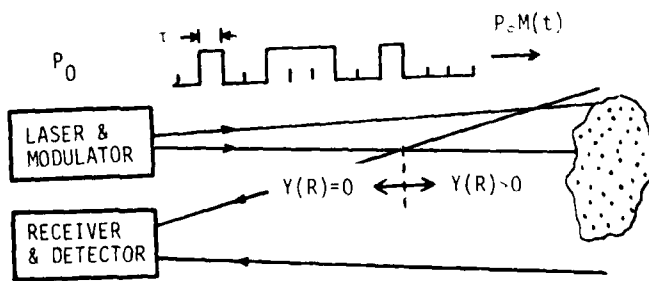


Fig.1 Principle of RM CW lidar

Here  $P(t)$  is the signal power, and  $P_0$  is an amplitude of a CW laser. The noise term  $b_0(t)$  is mainly from background

radiation and noises of a detector and an amplifier and is treated to be completely random. The pseudorandom modulation code  $M(t)$  has a period  $T$ , and here we use the maximum-length sequence (M-sequence) in the  $p$ -th order (in our experiment,  $p=10$ ). The response function  $S(t)$ , corresponding to an A-scope in a pulsed lidar, is given by

$$S(t) = n(c/2)A_r\beta_r(R)T^2(R)Y(R)/R^2, \\ R = t(c/2) \quad (2)$$

The usual lidar equation in pulsed operation is described in terms of  $S(R)$  (eq. (2)) as

$$P_r(R) = P_{pulse} \tau_p S(R) + b_0(R) \quad (3)$$

The M-sequence has the following feature:

$$\frac{1}{T} \int_{t-T}^t M(t')M(t'-t_s)dt' = \begin{cases} 1 & (t_s = 0, T, 2T, \dots) \\ -1/N & (\text{otherwise}) \end{cases} \quad (4)$$

where  $N = 2^p - 1$ .

Using the above relation, the response function (spatial distribution profile of the scatterers) can be obtained from

$$S(t) = \frac{1}{P_0} \int_0^T P(t')M(t'-t)dt' \quad (5)$$

### 3. Characteristics of the RM CW lidar

The RM CW lidar has the following characteristics:

- 1) the ability same as a pulsed lidar with the averaged power of  $P_0/2$ ,
- 2) better stability due to CW operation,
- 3) great improvement in induction noise from laser discharge,
- 4) automatic zero-level correction by no correlation between pseudorandom code and random noise,
- 5) compactness of the system,
- 6) hindrance by large contribution from the short range, which is reduced by adjusting  $Y(R)$  so that  $Y(R)$  is zero up to a long distance. The use of  $Y(R)$  for eliminating the short range influence can be possible due to the small laser-beam divergence.

### 4. Experimental

In Fig.2, the block diagram of the experimental setup is shown. The Argon ion laser has an output power of about

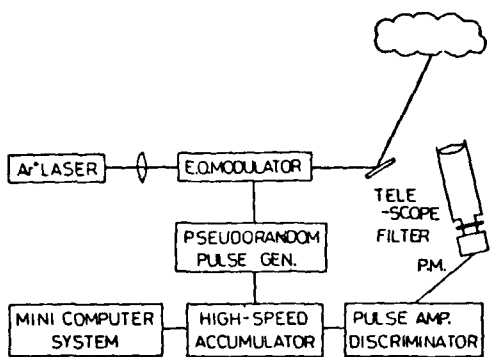


Fig.2 Block diagram of the experimental setup

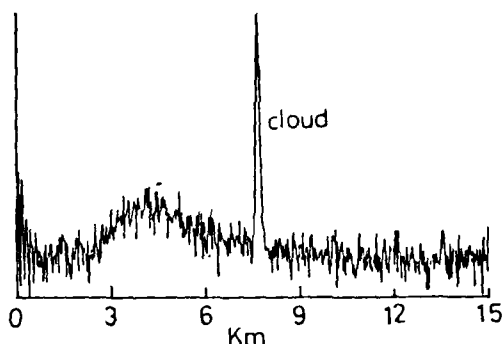


Fig.3 An example of the measurement

one watt. A pseudorandom pulse generator provides the modulation code of the 10th-order M-sequence, which has 1023 ( $2^{10}-1$ ) elements. Each element has the gatetime longer than 80 ns. We used the gate time of 200 ns, which corresponded to the range resolution of 30 m. A CW laser light, modulated at an electro-optical modulator, is emitted to the atmosphere. Scattered light is collected by a Newtonian-type telescope with a 15 cm aperture. Scattered-light signal is passed through a narrow-band interference filter, is detected by a photon-counter, and is cyclically summed into a high-speed accumulator with 1023 segments. After cyclic summation, they are transferred to a minicomputer and the delayed correlation with the modulation code is taken. An example of the processed data with gradual increase in the delay time is shown in Fig.3. From the data it is found that  $Y(R)$  departs from zero at the distance of 2.4 km and that it reaches the maximum at  $R = 4.2$  km. Using an Argon ion laser with a power of less than 1 W, aerosol quantity was recognized up to 12 km. In conclusion, we are convinced that the RM CW lidar is an excellent system to have very low noise-level and to detect small amount of scatterers.

#### Reference

- 1) R.A.Ferguson: "Feasibility of a cw lidar technique for measurement of plume opacity," Final Report SRI Project 1979; EPA No 650/2-73-037 (Nov. 1973).
- 2) T.Kobayashi et al: Proc. of 10th ILRC p77-78, Silver Spring (1980).
- 3) M.I.Skolnik ed: Radar Handbook, Chapt. 16, McGraw-Hill (1970).

MINIATURE SURFACE CORONA UV PREIONIZATION<sup>+</sup>  
STABILIZED MULTIKILOHERTZ TEA LASERS<sup>+</sup>

V. Hasson

Avco Everett Research Laboratory, Inc.  
Everett, MA 02149

SUMMARY

The surface corona UV preionization stabilized discharge scheme developed by the author and co-workers has been applied successfully to a variety of low-rep-rate IR and UV TEA lasers<sup>1-2</sup>. The basic concept has also been used to energize waveguide and miniature lasers (plasma volume < 1 cm<sup>3</sup>)<sup>3-4</sup>; a miniature N<sub>2</sub>-laser has been operated with axial gas flow at rep-rates of up to ~ 1 kHz<sup>5</sup>.

The main objective of the present program has been to develop a high repetition rate discharge technology suitable for the excitation of miniature TEA lasers at 10-15 kHz. The surface corona UV preionization scheme has been successfully adapted to a transverse flow geometry to achieve rapid hot-gas-clearing. The scheme is presently being applied to the development of a very compact 10 kHz helium-free CO<sub>2</sub> laser with average powers of 100 watts and peak powers of >100 kW in the TEM<sub>∞</sub> mode; the total discharge volume is <1 cm<sup>3</sup> and the discharge length is only 10 cm.

The paper will review the discharge stabilization, pulsing and transverse flow scheme and highlight important phenomena which control key system performance parameters such as specific energy loading, flush factor and medium homogeneity. The paper will review discharge and time-resolved interferometric data which were taken to identify and resolve issues which have hitherto limited the performance of TEA lasers operating at high rep-rates.

The various flow, discharge and pulsing concepts developed in this program are appropriate to closed-cycle laser systems and can also be scaled to substantially larger devices.

REFERENCES

1. Hasson, V. and von Bergmann, H.M., 1976, "High pressure flow discharges for nanosecond excitation of gas lasers and low inductance switching applications," J. Phys. E.: Sci. Instrum. 9, 73-76.

---

<sup>+</sup>Work accomplished under company-sponsored IRAD.

2. Hasson, V. and von Bergmann, H.M., 1979, "Simple and compact photopreionization stabilized excimer lasers," *Rev. Sci. Instrum.* 50, 1542-1544.
3. Hasson, V. and von Bergmann, H.M., 1979, "Ultraminiature high-power gas discharge lasers," *Rev. Sci. Instrum.* 50, 59-63.
4. Brink, D. J. and Hasson, V., 1978, "High-power photopreionization-stabilized carbon dioxide waveguide lasers operating at gas pressures of up to 13 atm," *J. Appl. Phys.* 49, 2250-2253.
5. Von Bergmann, H. M. and Penderis, A. J., 1977, "Miniatuized atmospheric pressure nitrogen laser," *J. Phys. E.: Sci. Instrum.* 10, 602-604.

Calibration and Data Analysis Procedures for the  
High Spectral Resolution Lidar

J.T. Sroga<sup>1</sup>, E.W. Eloranta<sup>1</sup>, and F.L. Roesler<sup>2</sup>

1) Department of Meteorology, 2) Department of Physics

University of Wisconsin  
Madison, WI 53706

This paper discusses calibration and data analysis procedures developed for the High Spectral Resolution Lidar (HSRL). Calculations of the range dependence in the calibration coefficients for the HSRL receiver will be presented. Examples of HSRL data analyzed using these procedures will be shown.

The HSRL measures the aerosol to molecular backscatter ratio, the aerosol-backscatter cross section, and the total-extinction cross section by separating the elastically scattered aerosol signal from the thermally Doppler broadened molecular contribution. The aerosol-molecular backscatter separation is achieved by tuning the transmission peak of a high-resolution ( $\lambda/\delta\lambda = 10$ ) Fabry-Perot optical interferometer to the wavelength of the narrow-band laser transmitter. Lidar backscatter contributions near the laser wavelength (primarily aerosol contributions) are transmitted through the interferometer to an "aerosol" channel detector. Light not transmitted through the interferometer is reflected to a "molecular" channel detector which measures light which is predominantly Doppler shifted. The signals  $S_a$  and  $S_m$ , measured in the "aerosol" and "molecular" channels, respectively, are linear combinations of aerosol,  $N_a$ , and molecular,  $N_m$ , backscattering contributions:

$$S_a(R) = C_{aa}(R) \cdot N_a(R) + C_{ma}(R) \cdot N_m(R)$$
$$S_m(R) = C_{am}(R) \cdot N_a(R) + C_{mm}(R) \cdot N_m(R)$$

The calibration coefficients ( $C_{ij}$ ,  $i,j = a,m$ ) are calculated using the known spectral distributions for light backscattered from aerosols and molecules along with the measured spectral bandpass characteristics of the receiver channels. The spectral bandpass for each of the receiver channels can be calculated from the Fabry-Perot spectrometer design parameters and the backscatter intensity distribution in the spectrometer entrance aperture. (See reference 1.) The illumination of the HSRL spectrometer aperture is not uniform and it changes with range to the backscatter volume. The calibration coefficients,  $C_{ij}$ , are therefore slightly range dependent. A model of the transmitter-receiver telescope geometry is used to estimate the range dependence of the aperture illumination.

Fig. 1 illustrates the measured transmission of each channel as a function of transmitter detuning for uniform illumination of the spectrometer entrance aperture with diffuse laser light. The solid and dashed curves represent model calculations for the transmission of each channel. Fig. 2 illustrates the range dependence of the calibration coefficients computed from the theoretical models of the HSRL spectrometer and range-dependent intensity distribution in the spectrometer entrance aperture.

The importance of the range dependence in the HSRL calibrations can be seen in analysis of HSRL data. Figs. 3 and 4 show analysis of data obtained during a 7 Aug 1980 evaluation flight. The backscatter cross sections, backscatter ratio and extinction cross section are shown using the range-dependent calibration. Also shown are the extinction cross sections calculated with uniform calibration coefficients; these indicate the sensitivity of HSRL results to the range dependence of the calibrations. The in situ scattering cross-section measurements were obtained in reference 2.

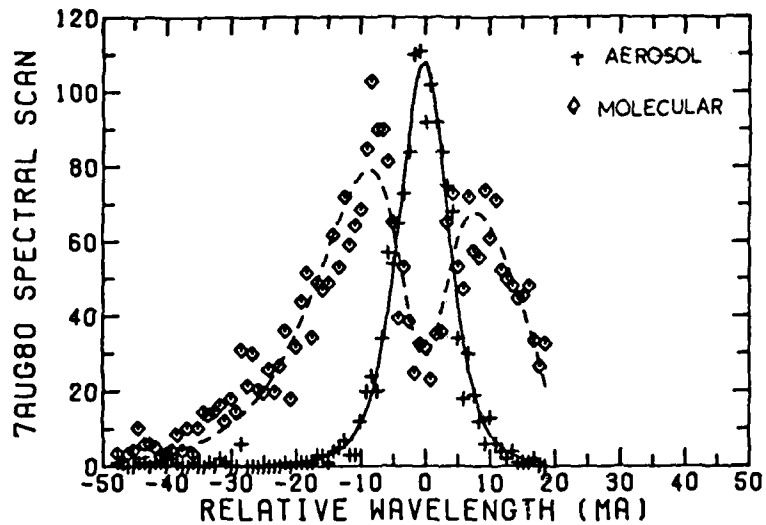


Fig. 1. The spectral distribution of the "aerosol" (+) and "molecular" passbands of the HSRL spectrometer. This data was obtained during 7 Aug 1980 flight experiments using diffuse, laser light inserted into the spectrometer entrance aperture. The solid ("aerosol") and dashed ("molecular") lines are theoretical calculations of the passbands obtained by a least-squares technique.

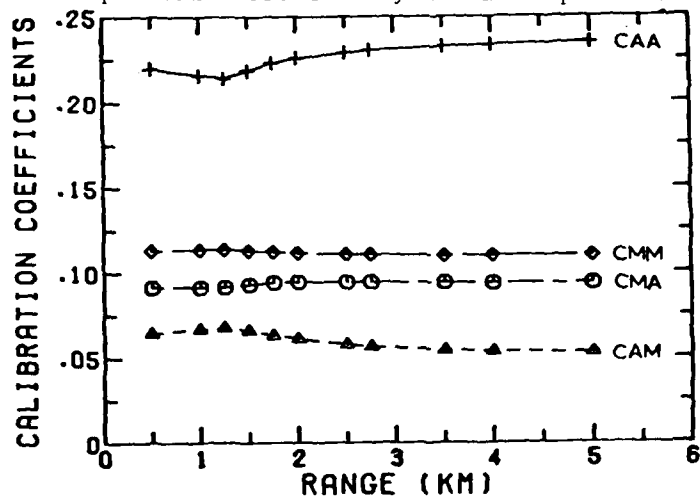


Fig. 2. Range dependence of the HSRL calibration coefficients calculated from the spectral distributions of the two-channel spectrometer passbands and a simple model of the range-dependent intensity distribution in the spectrometer entrance aperture. This range dependence is calculated from calibration data obtained on 7 Aug 1980 flight experiment.

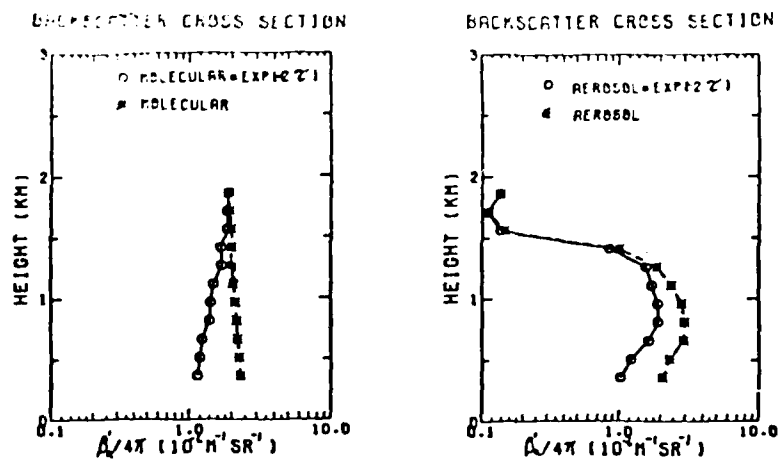


Fig. 3. Height profiles of molecular and aerosol backscatter cross sections obtained with the HSRL between 18:38 and 18:51 EDT on 7 Aug. 1980. The dashed line on the left is the molecular backscatter cross section for a summer, mid-latitude atmospheric model described in reference 3. The open circles on the left show the observed molecular return normalized to the model of reference 3 at a height of 2.2 km. A direct measure of atmospheric extinction is provided from the decrease of the HSRL molecular measurements with increasing range from the aircraft. The open circles on the right graph show the aerosol return before correction for attenuation. The dashed line on the right is the aerosol backscatter cross section corrected for the two-way attenuation measured from the molecular signals on the right.

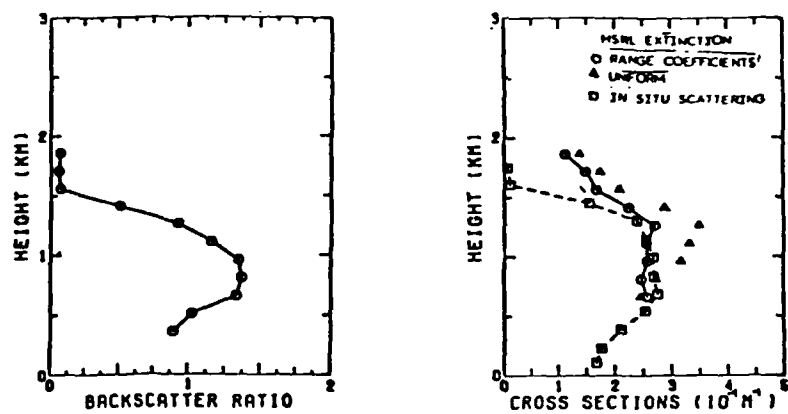


Fig. 4. The ratio of aerosol to molecular backscattering measured with the HSRL is shown on the left. On the right a height profile of the extinction cross section measured with the HSRL,  $\square$ , is compared with simultaneous in situ nephelometer measurements,  $\triangle$ . Also shown is the HSRL derived extinction profile,  $\Delta$ , calculated without correction for the range dependence of the spectrometer passbands.

#### REFERENCES

1. Mack, J. E.; McNutt, D. P.; Roesler, F. L.; and Chabbal, R.: App. Opt. 2, 1963, pp. 873-885.
2. Gregory, G. L.; Beck, S. M.; and Mathis, J. J., Jr.: NASA TM 83107, 1981.
3. McClatchey, R. A.; Fenn, R. W.; Selby, J. E. A.; Volz, F. E.; and Garing, J. S.: AFCRL-71-0279, 1971.

Atomic and Molecular Blocking Filters for High-Resolution Lidar:  
A Proposed Method for Measuring Atmospheric Visibility,  
Temperature and Pressure

H. Shimizu and C. Y. She  
Department of Physics, Colorado State University  
Fort Collins, Colorado 80523

SUMMARY

The use of atomic and molecular blocking filters for high-resolution lidar is proposed because of its simplicity, stability and high dynamic range. By analyzing the high-resolution lidar return corresponding to elastic and quasi-elastic scattering at two widely separated wavelengths, a potentially accurate method for simultaneous determination of atmospheric visibility, temperature and pressure is suggested.

A basic lidar system performs the expected function of light detection and ranging via Rayleigh scattering of atmospheric gas (mainly air) molecules and Mie scattering of suspended aerosol particles (including water droplets and ice crystals). As such, lidar can be used to determine the location and distribution of cloud layers, haze layers, smoke plumes and inversion layers.<sup>1</sup> Although the differential backscattering coefficient,  $\beta_g$ , and the extinction coefficient,  $\alpha_g$ , of atmospheric gas molecules are known, a basic lidar does not have enough resolution to determine the volume differential backscattering coefficient  $\beta = \beta_g + \beta_p$  and the volume extinction coefficient  $\alpha = \alpha_g + \alpha_p$  of the atmospheric aerosol (particles plus gas molecules) simultaneously. Here,  $\beta_p$  and  $\alpha_p$  are, respectively, backscattering and extinction coefficients due to aerosol particles. Therefore, the desired meteorological information of aerosol particle scattering and atmospheric visibility cannot be determined quantitatively, not to speak of atmospheric temperature and/or pressure.

It has been known and its preliminary experiment carried out for quite some time<sup>2</sup> that while Mie scattering may be regarded as truly elastic, Rayleigh scattering of air molecules in visible wavelengths is quasi-elastic with its main component (called Cabannes Line)<sup>3</sup> spread over a spectral width of approximately 1.5 GHz. This suggests that if the elastic and quasi-elastic components of the lidar signal can be detected simultaneously and separately, the contributions of gas molecules and aerosol particles can be separated and the visibility and atmospheric transmission can be unambiguously determined. Obviously, a narrow-band laser should be used to confine the Mie scattering to within a bandwidth much narrower than 1.5 GHz. At the same time, a high-resolution detection system with a narrow-band blocking filter should be used to discriminate against particle

scattering, thus relatively enhancing molecular scattering. Preliminary measurements using the concept of high-resolution lidar from an airborne system with a copper laser and an elaborated system of Fabry-Perot interferometry to block the Mie scattering signal have recently been made with encouraging results.<sup>4</sup> In order to improve the sensitivity and reliability of the high-resolution lidar, we believe that research seeking for a simpler blocking filter with high resolution and higher rejection ratio should be conducted.

Therefore, in this paper, we propose a high resolution lidar system using a single-mode tunable pulsed laser system and a narrow-band atomic (or molecular) blocking filter to measure quantitatively range-resolved  $\beta_p$  and  $\alpha$  (thus visibility). We further propose that if the Rayleigh spectrum of the lidar return is analyzed by a simple Fabry-Perot interferometer along with the atomic blocking filter, the proposed high-resolution lidar can be used to measure range-resolved atmospheric temperature and pressure as well. We will present preliminary laboratory experimental results with a single-frequency argon-ion laser and an  $I_2$  cell as blocking filter to measure its rejection-ratio of Mie scattering and to demonstrate the feasibility of the proposed concept. We will also discuss the potential of using the proposed high-resolution lidar for ground-based long-range measurements of visibility, temperature and pressure. Our search for and proposal of using atomic blocking filters for available laser systems will also be presented.

One great advantage of using atomic and/or molecular absorption as a narrow-band laser blocking filter is its stability in absorption wavelength which does not depend on critical optical alignment. Another advantage is the high dynamical range in rejection-ratio of Mie scattering which can be achieved by simply changing the atomic concentration in the filter cell. However, the absorption line in question should satisfy several conditions in order to be useful for high-resolution lidar. (1) The atomic absorption line should coincide with the laser line and the use of a tunable laser will be helpful. (2) Atomic or molecular weight in question should be much larger than that of air molecules to minimize the Doppler broadening of the atomic absorption line. (3) The atom or molecule should have zero nuclear spin so that there is no hyperfine-broadening in the atomic transition in question. (4) The oscillator strength of the atomic transition in question should be large enough to strongly absorb Mie scattering at low atomic or molecular concentration.  $I_2$  molecule is only marginal in satisfying these conditions. Atomic transitions in Ba at 7913.5 Å and 5537.0 Å are ideal if single-mode alexandrite and pulsed dye lasers are used, respectively. Our suggested list of other atomic blocking filters will be presented and discussed at the conference.

Simultaneous measurements of  $\beta_p$  and  $\alpha$  can be and have been made with simultaneous Raman scattering of nitrogen molecules.<sup>5</sup> The proposed technique of using Rayleigh scattering is, however, much better because of its three orders-of-magnitude larger scattering cross-section. Indeed, our estimate shows that using Mie/Rayleigh scattering, the simultaneous measurement of  $\beta_p$  and  $\alpha$  at 10 km range

and 30 km visibility should be possible with available ground-based lidar systems.<sup>6</sup>

When the Rayleigh scattering spectrum is analyzed, the temperature and pressure of the atmosphere can be measured because the central Cabannes line is broadened by both Doppler effect (temperature dependent) and pressure broadening. The principles behind these temperature and pressure measurements are similar to those recently proposed.<sup>7,8,9</sup> Our technique offers simplicity and reliability in analysis of Rayleigh spectrum<sup>7</sup> and unlike the methods of differential absorption,<sup>8,9</sup> it in principle permits the use of any laser wavelength. Since according to recent high-resolution Raman results,<sup>10</sup> Doppler broadening and pressure broadening at atmospheric pressure are comparable in the visible and near infrared, the determination of temperature and pressure using resonance absorption requires a careful analysis of the spectral shape and the weak spectral wing. We note that Doppler broadening depends on scattering frequency used and that pressure broadening is independent of the laser frequency. This fact can be used to advantage in our method and we propose the use of two wavelength high-resolution lidar for atmospheric temperature and pressure measurements. For example, a simultaneous analysis of Rayleigh scattering spectra at 1.06  $\mu\text{m}$  and 0.266  $\mu\text{m}$  should reveal a pressure broadening component of the same width plus a Doppler broadening component having widths differing by a factor of 4, leading to unambiguous determination of atmospheric pressure and temperature.

1. R. T. H. Collis and P. B. Russell, "Lidar Measurement of Particles and Gases by Elastic Backscattering and Differential Absorption," in Laser Monitoring of the Atmosphere, Hinkley, ed., Springer-Verlag (1976).
2. F. Fiocco, G. Benedetti-Michelangeli, K. Maischberger and E. Madonna, "Measurement of Temperature and Aerosol to Molecule Ratio in the Troposphere by Optical Radar," Nature 229, 78 (1971).
3. A. T. Young, "Rayleigh Scattering," Phys. Today, pp. 42-48, January 1982.
4. E. Eloranta, "High Resolution Lidar Measurements," Workshop on Optical and Laser Remote Sensing, Monterey, California, February 1982.
5. H. Shimizu, T. Kobayashi and H. Inaba, "The Laser Radar System for Measuring and Processing of Multiple Atmospheric Parameters in Troposphere," Trans. IECE 60-C, 162 (1977).
6. N. Takeuchi, H. Shimizu, Y. Sasano, N. Sugimoto, I. Matsui, and H. Nakane, "Wide-Area Air Pollution Measurement by the NIES Large-Aperture Lidar," Workshop on Optical and Laser Remote Sensing, Monterey, California, February 1982.
7. R. L. Schwiesow and L. Lading, "Temperature Profiling by Rayleigh-Scattering Lidar," Appl. Opt. 20, 1972 (1981).
8. J. E. Kalshoven, Jr., C. L. Korb, G. K. Schwemmer, and M. Dombrowski, "Laser Remote Sensing of Atmospheric Temperature by Observing Resonant Absorption of Oxygen," Appl. Opt. 20, 1966 (1981).
9. M. Endemann and R. L. Byer, "Simultaneous Remote Measurements of Atmospheric Temperature and Humidity Using a Continuously Tunable IR Lidar," Appl. Opt. 20, 3211 (1981).
10. A. Owyong, "CW Stimulated Raman Spectroscopy," in Chemical Applications of Nonlinear Spectroscopy, Harvey ed., New York: Academic Press (1981).

FIELD EVALUATION OF A LASER CLOUD MAPPER

R.E. KLUCHERT, B.T.N. EVANS AND D. HOUSTON\*

DEFENCE RESEARCH ESTABLISHMENT, VALCARTIER  
P.O. BOX 8800, COURCELETTE, QUEBEC, CANADA  
GOA 1R0

\* OPTECH INC., 701 Petrolia Road, Downsview Ont. Canada M3J 2N6

A cloud mapping LIDAR system has been acquired by the Defence Research Establishment, Valcartier Quebec. Its performance was evaluated during recent field trials which indicated that it is capable of mapping dense and rarefied clouds. The main results of these trials will be discussed in another paper delivered in this conference.

The computer controlled LIDAR consists of a 30 mJ Nd: YAG laser operating at  $1.06 \mu\text{m}$  and 100 Hz, a scanning mirror, a receiver consisting of a silicon avalanche diode plus dual logarithmic amplifiers (6.5 decades of dynamic range) and a transient digitizer (see schematic in Figure 1). Figure 2 gives the general set up of the field experiment during a typical run. The horizontal sweep is  $90^\circ$  and the vertical sweep is up to  $10^\circ$ . Returns from co-operative targets plus a peak sensor are used for obtaining additional transmission measurements on the lowest sweep.

The paper will also include an examination of the temporal and spatial resolution, concentration limits and useful range of the system.

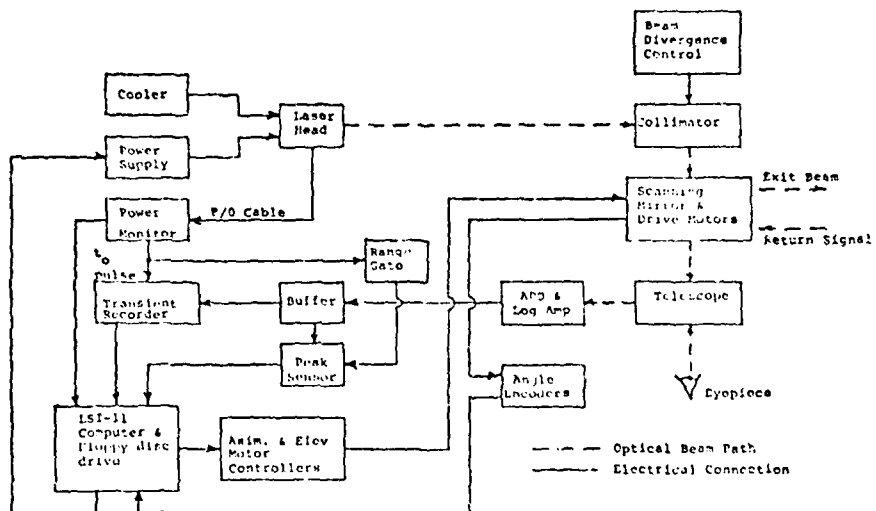


Figure 1.- Block schematic of cloud mapper system.

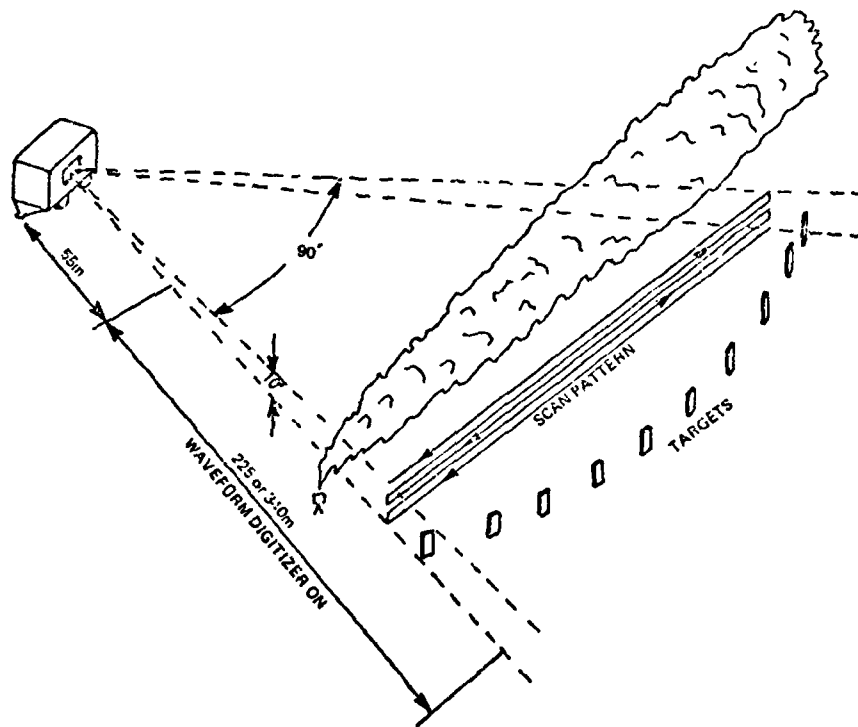


Figure 2.- Experimental field set up.

DESIGN OF A DIAGNOSTIC TO MEASURE TURBULENT DENSITY  
FLUCTUATIONS IN ATMOSPHERE\*

J. S. Goola  
Department of Mechanical Engineering  
Indian Institute of Technology Kanpur  
Kanpur 208 016, India

The results of a theoretical study carried out to explore the possibility of obtaining quantitative information about density fluctuations in a turbulent air flow is presented. The specific technique considered for analysis is a new three-level gain measurement scheme which consists of using a high-power pulse laser to saturate one transition of a molecule and then measuring gain on a coupled transition of the same molecule with a probe laser. It is shown that the most promising of all the three-level schemes considered in  $\text{CO}_2$  and  $\text{H}_2\text{O}$  is the one which involves pumping the R(12) line of the  $021 \leftrightarrow 000$  band in  $\text{CO}_2$  with an HF laser and measuring the gain on the P(16) line of the  $021 \leftrightarrow 020$  band with a CW diode laser. Our study shows that in the case of random and isotropic turbulent flow fields, the energy and power spectrum can be obtained with the use of commercially available lasers. The possibility of conducting a simulation experiment in the laboratory is discussed, and the use of this diagnostic to measure turbulent density fluctuations behind an airplane is explored.

---

\*Work performed under AFOSR contract No. F 49260-78-C-0099 at Physical Sciences Inc., Woburn, Massachusetts.

AIRBORNE LIDAR DUAL WEDGE SCANNER

C. DiMarzio  
R. Chandler  
M. Krause  
J. O'Reilly

ELECTRO-OPTICS SYSTEMS LABORATORY  
EQUIPMENT DIVISION  
RAYTHEON COMPANY  
SUDSBURY, MASS. 01776

K. Shaw

ADVANCED COMPUTER  
BILLERICA, MASS. 01821

J. Bilbro

NATIONAL AERONAUTICS AND SPACE ADMINISTRATION  
MARSHALL SPACE FLIGHT CENTER  
HUNTSVILLE, AL 35802

ABSTRACT

Coherent Doppler lidars have been used extensively over the past decade to measure a variety of atmospheric phenomena such as clear air turbulence, wake vortices, and boundary layer winds. For the most part, these systems have been either ground-based or non-scanning airborne systems. To overcome these limitations, the NASA-MSFC Airborne Doppler Lidar System has been developed which combines the flexibility of a scanning system with the mobility of an aircraft platform to produce in real time a two-dimensional vector wind velocity (Bilbro et al., 1982).

The purpose of the two-dimensional scanner is to permit velocity measurements to be made with the lidar system over a plane in space in such a way that at least two velocity measurements are made in different directions at each point on the plane. The density of data points must be sufficient to provide meaningful atmospheric velocity fields while the time between the different measurements at each point should be sufficiently short that the velocity does not change appreciably.

The design of such a scanner required a thorough evaluation of the inter-relations among scan configuration and rates, spatial and velocity resolution, time, and aircraft velocity. In addition, it was necessary to evaluate the problems of aircraft roll, pitch, and yaw, the flight stability of the aircraft and the design constraints imposed by the aircraft.

It became obvious early in the program that the scanner itself was only part of the system required to meet the design requirements and that a relatively sophisticated control system was also necessary. This control system, which is an integral part of the concept, eventually evolved into a Central Timing and Control System (CTCS).

As one of the key elements in the Airborne Lidar Systems, the scanner/CTCS had to meet the following criteria:

- 1) Scan a 30 cm. diameter, 10.6- $\mu$ m wavelength lidar beam in a horizontal plane, 20° forward and aft of a centerline perpendicular to the aircraft flight path
- 2) Minimize degradation or power loss to the input/output path
- 3) Provide variable scan time points at rates up to .25 seconds and variable delay time delays at end points
- 4) Maintain roll and pitch stabilization over  $\pm$  5 to 10 degrees with a pointing accuracy of 0.1°
- 5) Minimize size, weight and aircraft modification while containing the system completely within the aircraft

The CTCS portion of the system provided the following additional functions:

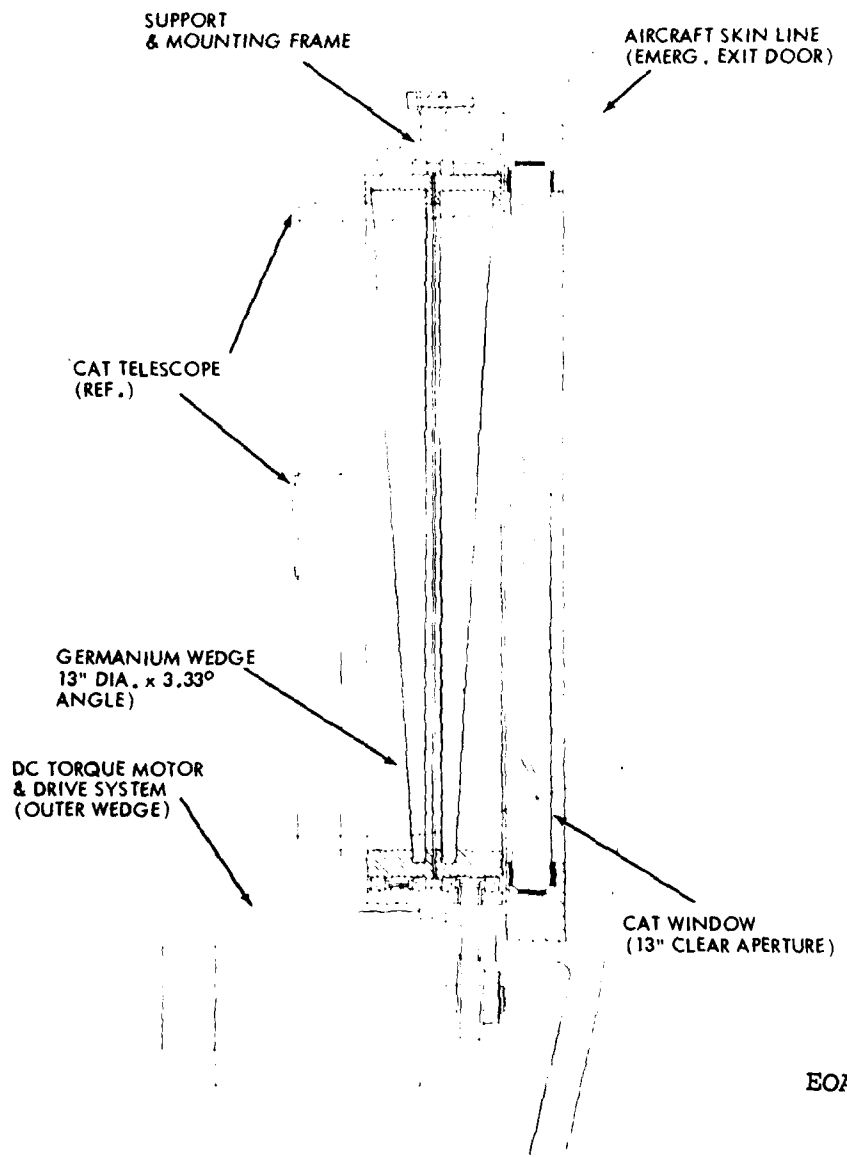
- 6) Interface with the Central Air Data Computer (CADC), the wedge scanner, the PDP 11/35, the Inertial Navigation System (INS), and the signal processor, sequence (transmitter), ADDAS and Aircraft Time Code system
- 7) Calculate coordinates of A/C along track to 50 m accuracy with respect to an initial point for a traveled distance of 12 km
- 8) Develop a correction to eliminate Doppler shift due to aircraft velocity for the signal processor
- 9) Provide means of storing and formatting A/C coordinates, scan position, etc., until processing of each frame of data is complete
- 10) Apply drift angle correction to data
- 11) Provide expansion capability such that the generation of more complex scanning patterns may be added to the system at a later date

While the obvious advantages of a dual rotating wedge scanner (i.e., compact size, single axis of rotation, etc.) are immediately apparent, questions of optical quality, cost and survivability of 30 cm diameter wedges posed possible risks to the program. As designed, the scanner incorporates two  $3.33^{\circ}$  wedge angle germanium wedges which produce a maximum combined deviation angle of  $20^{\circ}$ . Although a larger angle was desirable to reduce the error in deriving the crosswind component, the  $20^{\circ}$  angle allowed utilization of an existing 14-inch clear aperture germanium window for a pressure bulkhead. Also, thicker wedges would greatly increase motor torque requirements or possibly restrict scanner performance.

Ultimately, the wedge scanner performance met all design goals. Optical performance was better than specified with  $<0.5$  dB two-way signal-to-noise reduction per wedge and a deviation angle of  $10.24^{\circ}$ . The scanner system was calibrated onboard the aircraft prior to initiation of the flight test program, and aligned relative to the aircraft centerline and INS by surveying five lines of sight to a range of 1200 feet.

#### Reference

Bilbro, James W., G. H. Fichtl, D. Fitzjarrald, and M. Krause (1982)  
Airborne Doppler Lidar Wind Field Measurements. Submitted to Bull. Am. Meteorol. Soc.



EOA-72

WEDGE SCANNER CONCEPT

## EFFECT OF SEA SURFACE STRUCTURE ON OCEANOGRAPHIC FLUORESCENCE LIDAR SIGNALS

U. Gehlhaar  
University of Oldenburg  
FB 8, Physik,  
D-2900 Oldenburg, FRG

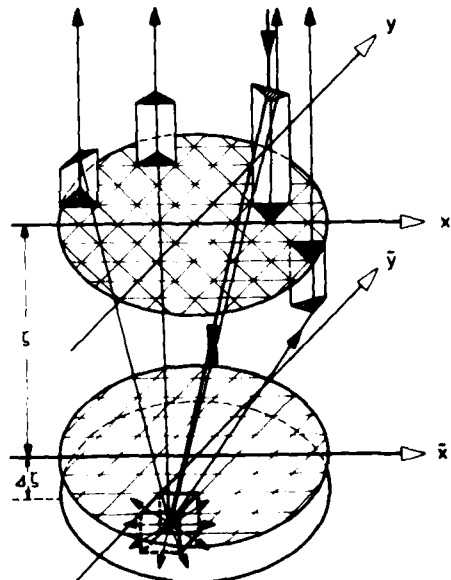
### ABSTRACT

Oceanographic fluorescence or Raman lidar systems offer the chance to investigate the surface layer of the oceans synoptically with high sensitivity /1-4/. Usually the surface structure of the sea is not taken into account or is assumed to be planar, when performing such measurements, and the Fresnel losses are considered constant /5/. The physical situation discussed in the following shows however that the surface considerably interacts with that part of the excited fluorescence or Raman radiation contributing to the detector signal.

The process of fluorescence generation by laser light at a certain depth in the water column and the path of fluorescence radiation to the detector can be simulated by the model shown in Fig. 1.

Fig. 1

Model of computer simulations.

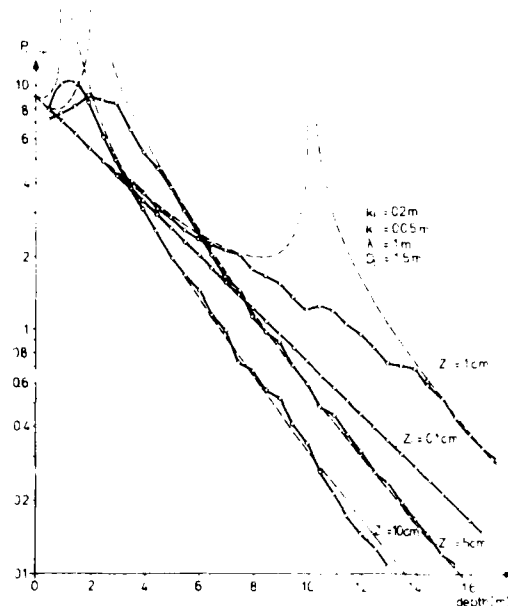


The indicated surface is decomposed into triangular facets, which are small enough to preserve the surface curvatures /6/. The relative signal contribution from different depths for the simple case of plane sine waves at the surface is shown in Fig. 2.

The curves correspond to different amplitude-to-wavelength ratios of the waves. The dashed lines are obtained by the theory discussed below.

Fig. 2

Depth-resolved (rel.) fluorescence lidar signals for different amplitude-to-wavelength ratios ( $z/\lambda$ ).  $k_F, k_L$  are effective extinctions at the fluorescence resp. laser wavelength;  $D_L$  is diameter of excited area at the surface. Dashed lines correspond to theory.



The depth-resolved and depth-integrated signals obtained by simulation may be interpreted theoretically, if one considers the transformation of solid angles by curved boundaries. The concave and convex parts of the surface and their statistics determine the transformation of the fluorescence or Raman radiation, when passing the boundary on the way to the remote detector. The transformation of solid angles is not symmetric with respect to the concave and convex parts of the surface, although the statistical weights of these parts are equal. General expressions for surface induced signal modifications are found and calculated for different experimental parameters, e.g., solid angle of detector, optical penetration depth, etc.

#### REFERENCES

- 1) H. R. Gordon, ed., NOAA Technical Memorandum ERL PMEL-18 (1980).
- 2) H. H. Kim, Appl. Opt. 12, 1454 (1973).
- 3) F. E. Hoge and R. N. Swift, Appl. Opt. 20, 3197 (1981).
- 4) U. Gehlhaar, K. P. Guenther and J. Luther, Appl. Opt. 20, 3318 (1981).
- 5) E. V. Browell, NASA TN D-8447, (1977).
- 6) U. Gehlhaar, Thesis, University of Oldenburg, Oldenburg (1980).

EVALUATION OF FOUR LASER WAVELENGTHS FOR LIDAR FLUOROSENSING  
OF OIL SPILLS

P. Burlamacchi, G. Cecchi, and P. Mazzinghi  
Istituto di Elettronica Quantistica of the C.N.R.  
Via Panciatichi 56, I 50127 FIRENZE (Italy)

L. Pantani and I. Pippi  
Istituto di Ricerca sulle Onde Elettromagnetiche of the C.N.R.  
Via Panciatichi 64, I 50127 FIRENZE (Italy)

ABSTRACT

The fluorescence lidar technique is one of the most promising for the remote sensing of oil spills on the sea and other natural waters. The purpose of this paper is the evaluation of the potential of different laser wavelengths in this application. Since the most used wavelength is the 3371 Å line of the N<sub>2</sub> laser this one was compared with two shorter wavelengths of excimer lasers, KrF (2495 Å) and XeCl (3080 Å), and with a longer wavelength of a dye laser, Stilben-3 (4200 Å). Particular attention was given to the capability of detecting very-low-thickness oil films.

Laboratory measurements were carried out at the four wavelengths on five different crude oils and a light oil. From each oil sample, films with thicknesses ranging from 1 mm to 100 Å were spilled on a water tank. The film was then irradiated with the selected laser radiation and the fluorescence spectrum was recorded by means of a polychromator and an optical multichannel analyzer. The emission spectra of different water samples were separately measured in order to determine the expected value of the background radiation. Fig. 1 shows the fluorescence emission spectra at 3080 Å of different thickness films obtained from a sample of Russian crude oil while fig. 2 shows the fluorescence emission spectra of the same sample at the four wavelengths with a fixed thickness of the film.

The data obtained from the laboratory experiments were processed in order to calculate the expected performances of lidar fluorosensors in the detection and characterization of oil spills having different origin and thickness, taking into account the oil signal, the background noise, the atmospheric absorption and scattering. The calculation results were used, with other data as the laser efficiency and reliability, for the evaluation of the potential of the four laser wavelengths in the remote sensing of oil spills. Between the four wavelengths taken into account, the 3080 Å line of the XeCl laser seems to have the highest potential in the detection of oil films also with low thickness, while the use of more than one wavelength could allow the identification of the film thickness.

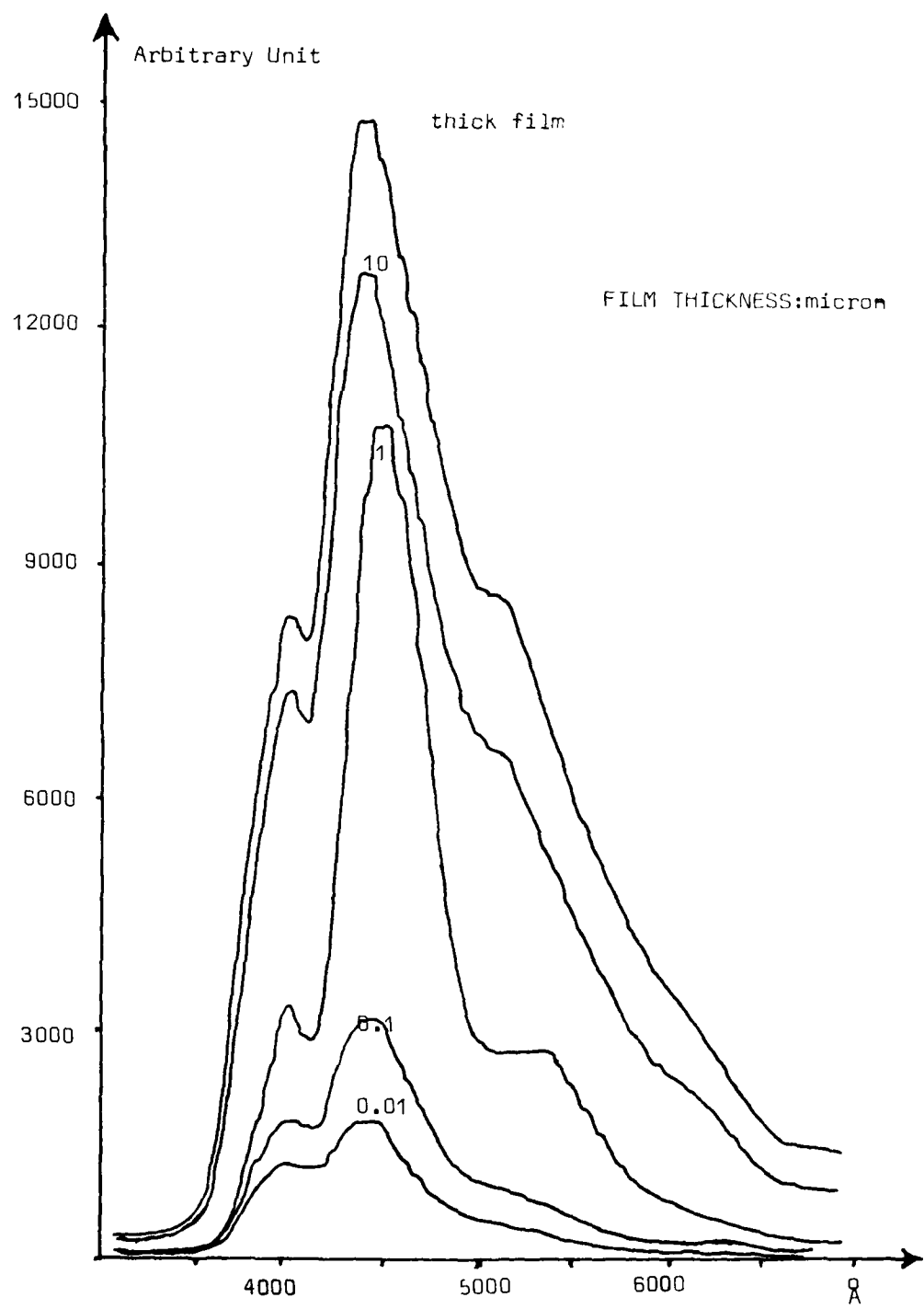


Fig. 1 - Fluorescence spectra of a Russian crude sample as a function of wavelength and film thickness. Excitation wavelength: 3080 Å. The vertical scale has to be divided by 3 for the three lower thicknesses.

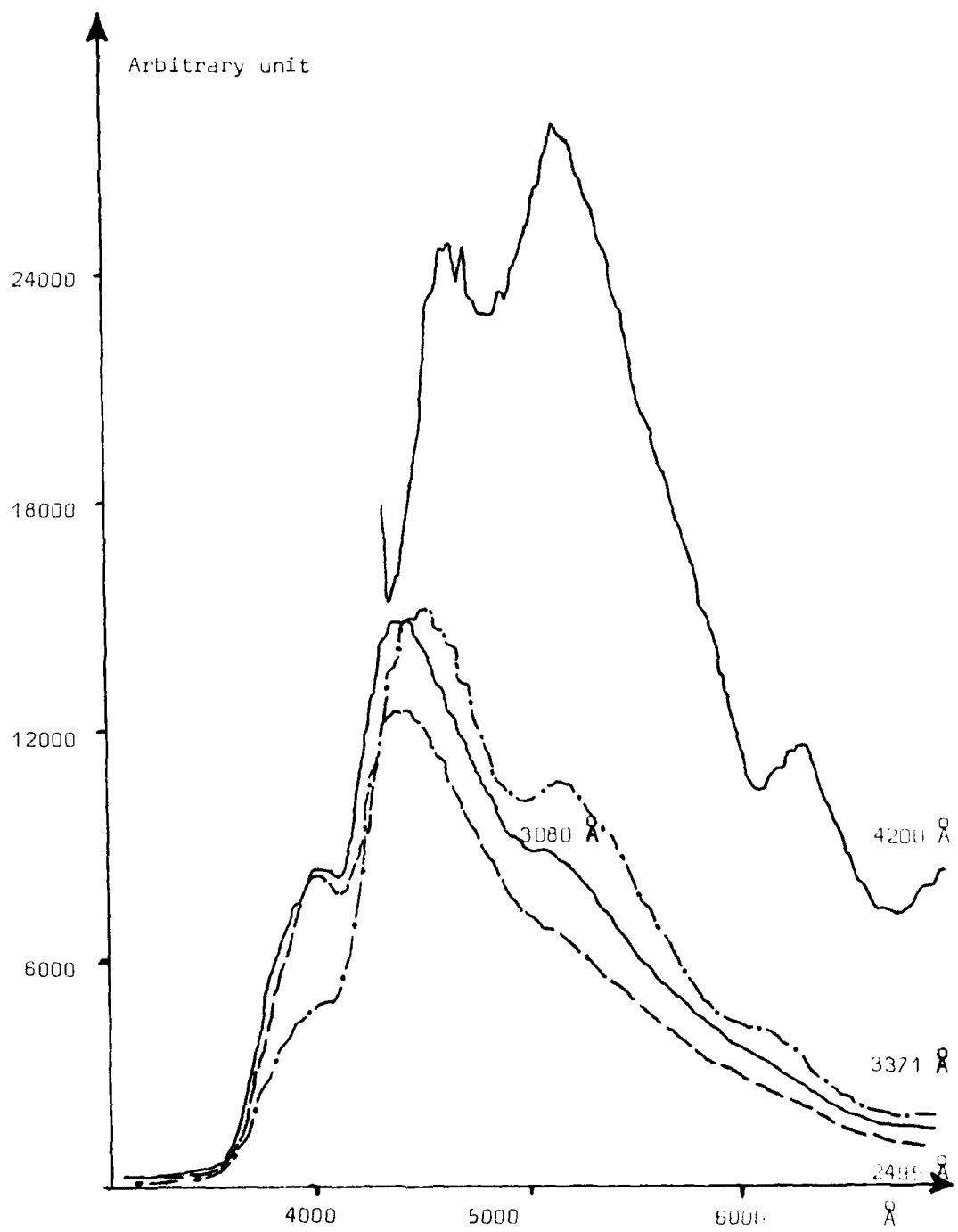


Fig. 2 - Fluorescence spectra of a Russian crude sample as a function of the fluorescence wavelength and the excitation wavelength. The vertical scale has to be multiplied by 2 for the 4200 Å excitation. Exciting energy: 1 mJ. Thick film.

ATMOSPHERIC DERIVATIVE MONITORING:  
THE EFFECT OF MOLECULAR INTERFERENCE

S. E. Taylor and E. L. Thomas  
The University of Hull  
Dept. of Applied Physics  
England, HU6 7RX

Introduction

Many continuously tunable lasers are now available in the infrared atmospheric transmission windows at 3-5  $\mu\text{m}$  and 8-14  $\mu\text{m}$ . As the power output of these devices is improved, the effect of detector noise on sensitivity becomes less important, and the limit to measurement accuracy is caused by unwanted interference from changing molecular constituents and changing pressure and temperature. In general, the best line for monitoring a particular species is not necessarily the strongest. This paper suggests a useful criterion for optimum line selection for a ratio-type derivative spectrometer.

The Ratio-Derivative Technique

This technique is being increasingly used for atmospheric and industrial monitoring because of its selectivity and lack of dependence on non-dispersive extinction. Its application to tunable diode lasers has been described elsewhere.<sup>1</sup> In general, a sinusoidal frequency modulation ( $W_m$ ) is applied to a laser source at optical frequency  $\nu$ :

$$\nu = \nu + a \sin(W_m t) \quad (1)$$

The transmission  $T(\nu)$  is given by

$$T = \frac{I}{I_0} = \exp(-L\alpha_T) \quad (2)$$

where  $\alpha_T$  is the absorption from all the molecules. From Taylor's expansion,

$$T(\nu') = T(\nu) + T'(\nu) a \sin(W_m t) + T''(\nu) \frac{a^2}{2} \sin(W_m t) \dots$$

Hence the power at the second harmonic of the modulation frequency is given by

$$P(2W_m) = I_0 T''(\nu) \frac{a^2}{4} \quad (3)$$

The output  $R$  is obtained from the ratio of the second harmonic power (at  $2W_m$ ) and the received average power. Hence

$$R = \frac{P(2W_m)}{I_0 T} = \frac{T''(v)}{T(v)} = [ (L\alpha_T')^2 - L\alpha_T'' ] \quad (4)$$

The change in output is given by

$$dR = 2L^2 \alpha_T' d\alpha_T' - L d\alpha_T'' \quad (5)$$

where  $dR$  is the change in absorption arising from interfering lines. The effect of detector noise on the output of a practical system is given by  $NEP\sqrt{B}/I_0 T$ . Hence when

$$NEP\sqrt{B} \ll dR \quad (6)$$

the errors in measurement are systematic errors associated with molecular interference rather than from random thermal noise. In order to provide a stable frequency of operation, derivative monitors are locked to a frequency standard by utilising the first derivative output. This frequency standard may be derived from an external device, for example a gas cell or spectrometer, or from the atmosphere itself. For ease of operation, a low pressure gas cell is frequently used,<sup>2</sup> and this is the case considered here.

From equation (5), we see that  $dR$  depends on both the first and second derivative spectra. In practice, however,  $2L\alpha_T' d\alpha_T' \ll d\alpha_T''$  so that the change in output arising from a variation in molecular concentration  $dn$  is

$$dR = |M_i'' dn_i| \quad (7)$$

where  $M$  is the extinction from the interfering species 'i'. This change will be attributed to a change in concentration of target species  $dn_a$  given by

$$dn_a(v_a) = \frac{1}{M_a''} \sum |M_i'' dn_i| \quad (8)$$

Here the interference has been summed over many species, and the subscript 'a' refers to the target species. The optimum wavelength for monitoring a molecular species occurs when  $dn_a(v_a)$  is nearest zero. The  $v_a$  are taken as being the center of each absorption line, since the system is considered locked to a low pressure cell. Clearly there will be no change of output provided that the molecular constituents remain constant, and hence static concentrations will not affect measurement. However, in practice atmospheric gaseous concentrations vary by a considerable amount, often by as much as the average concentrations themselves. Owing to the lack of reliable data on the typical deviations from the mean to be expected in atmospheric gaseous constituents, the  $dn$  have been taken to be the absolute concentrations themselves. The calculated interference therefore corresponds to the absolute amount of second harmonic of the modulation frequency  $W$

generated from interference. The second derivative lineshape obtained from a Lorentzian profile is given by

$$M'' = 2S_i \frac{3f_i^2 - \gamma_i^2}{(f_i^2 + \gamma_i^2)^3} \quad (9)$$

where  $f = v_a - v$ . Substitution of equation (9) into equation (8) results in a number of unsatisfactory line selections, since for an isolated line,  $M''$  is zero at  $\gamma/\sqrt{3}$  from line centre. Although no second harmonic is produced at this point, uncertainties in halfwidth and in variation of pressure and temperature will cause a large change in output. Thus, operation is to be preferred in the tails of interfering lines, rather than near line centres, where  $dn$  may be zero but may vary rapidly. A weighting function  $W$  was used which tends to  $M''$  when off resonance, but which does not change sign. In order to allow selection in the case where a very weak interfering line is close to the line centre of the molecule of interest, the absolute value of the function  $W$  should be the same as  $M''$  when nearly on resonance. An expression for  $W$  which meets these requirements is given below.

$$W = 2S_i \frac{3f_i^2 + \gamma_i^2}{(f_i^2 + \gamma_i^2)^3}$$

Hence

$$dn_a = \frac{\sum_{\text{all } i} S_i \frac{3f_i^2 + \gamma_i^2}{(f_i^2 + \gamma_i^2)^3} dn_i}{\sum_{\text{all } a} \frac{3f_a^2 - \gamma_a^2}{(f_a^2 + \gamma_a^2)^3}} \quad (10)$$

### Results

Two atmospheric models were used: one for a rural and one for an urban environment. These are shown in Table 1. The minimum value of equation (10) has been calculated for all the molecules listed on the AFCRL absorption line compilation<sup>3</sup> in the 8-14  $\mu\text{m}$  and 3-5  $\mu\text{m}$  regions. (See Tables 2 and 3.) The results show the equivalent background in terms of concentration of the molecule to be measured, in parts per billion.

From Table 2 we can see that nitric oxide, methane, carbon monoxide and nitrous oxide can be measured in the 3-5  $\mu\text{m}$  band with little interference. However the measurement of ozone, sulphur dioxide and nitrogen dioxide in a normal environment may prove difficult since the background is either equal to or greater than the corresponding ambient level. In the 8-14  $\mu\text{m}$  band ozone, nitrous oxide, methane and ammonia can all be measured to ambient levels, while nitrogen dioxide, and especially sulphur dioxide will suffer interference.

### Conclusion

Careful consideration of the effects of interference is required when using the infrared absorption of some species to monitor their concentrations at ambient levels. A simple and computationally fast criterion has been developed for the selection of optimum wavelength at which measurements should be carried out. In cases where the laser source has only a limited tuning range, for example with diode lasers, the application of this selection procedure should prove especially valuable.

### References

1. E. D. Hinkley, Ed., *Laser Monitoring of the Atmosphere* (Springer, Berlin, 1976).
2. W. Wiesman and W. Diehl, *Appl. Opt.*, 20, 2230 (1981).
3. Air Force Cambridge Research Labs., AFCRL-TR-76-0033, AFCRL-TR-73-0096, Compilation edn: Atmospheric Oct. 1978, Trace Oct. 1977.
4. R. M. Tennent, Ed., *Science Data Book*, (Oliver and Boyd, Edinburgh, 1971).
5. A. C. Stern, Ed., *Air Pollution*, 1, 30 (Academic Press, New York, 1968).
6. P. L. Hanst, *Advances in Environmental Science and Technology* (J. Wiley, New York, 1971).

Table 1. Model Atmospheres. t=288 deg k, p=1000 mbar

Molecule	Rural (ppm)	Urban (ppm)	Reference
H <sub>2</sub> O	8000	8000	for 50% rh & 15 deg c
CO <sub>2</sub>	318	354	4,5
O <sub>3</sub>	0.01	0.3	6
N <sub>2</sub> O	0.5	0.5	4
CO	0.1	5.0	6
CH <sub>4</sub>	1.4	3.0	6
O <sub>2</sub>	2*10 <sup>5</sup>	2*10 <sup>5</sup>	4
NO	0.002	0.2	6
SO <sub>2</sub>	0.002	0.2	6
NO <sub>2</sub>	0.001	0.1	6
NH <sub>3</sub>	0.002	0.004	6
HNO <sub>3</sub>	0.003	0.003	3
OH	0.01	0.01	
H <sub>2</sub> CO	0.001	0.05	6

Table 2. Interference from 1800-2900 cm(-1)

Molecule	Rural Model		Urban Model	
	v cm(-1)	dn(ppb)	v cm(-1)	dn(ppb)
O <sub>3</sub>	2126.466	23.38	2126.466	64.39
N <sub>2</sub> O	2195.633	0.02	2559.083	0.04
CO	2099.035	0.22	2169.201	1.04
CH <sub>4</sub>	2917.653	0.49	2668.85	0.79
NO	1929.023	0.21	1929.023	0.22
SO <sub>2</sub>	2507.832	16.51	2507.832	16.97
NO <sub>2</sub>	2882.279	1.09	2882.279	1.11

Table 3. Interference from 700 - 1400 cm(-1)

Molecule	Rural Model		Urban Model	
	v cm(-1)	dn(ppb)	v cm(-1)	dn(ppb)
O <sub>3</sub>	1001.894	0.22	1001.894	0.23
N <sub>2</sub> O	1274.620	1.79	1278.105	2.91
CH <sub>4</sub>	1202.509	1.74	1233.453	6.79
SO <sub>2</sub>	1124.499	5.85	1144.125	20.08
NO <sub>2</sub>	843.683	0.45	843.688	0.49
NH <sub>3</sub>	867.945	0.03	867.945	0.08

## Obtaining High-Quality Image Data with the LAMP Lidar

Hideaki Nakane, Yasuhiro Sasano, Nobuo Sugimoto,  
Ichiro Matsui, Hiroshi Simizu, and Nobuo Takeuchi  
National Institute for Environmental Studies,  
Tsukuba, Ibaraki 305, Japan

### Introduction

LAMP lidar<sup>1)</sup> (Large Atmospheric Multipurpose lidar) was constructed to understand the wide-area air pollution phenomena, such as long-range transportation or urban plumes. In Japan, such phenomena have characteristic scales of 10 km to 100 km, because populated areas are often surrounded by mountain ranges.

LAMP lidar has a high-power laser, a large-aperture telescope( $1.7\text{ m}^2$ ) and a high-speed scanner with high angular accuracy (0.3 mrad). Details of the system were reported earlier.

There are, however, some problems inherent to wide-area measurements:

- 1) elimination of influence from obstructions (e.g., power cables),
- 2) correction of extinction effects which cause a large attenuation of transmitted light for a long distance,
- 3) selection of appropriate measurement conditions (e.g., scan speed, scan area, range resolution, etc) according to the purpose of measurements.

Here we discuss the details of the above problems and report how to obtain high-quality image data by the LAMP lidar.

### Results

The image data presented here as an example were obtained on Feb. 8, 1982 (the weather conditions: clear, wind of 5.3 m/s, NW, the visibility of 80 km). The two-dimensional

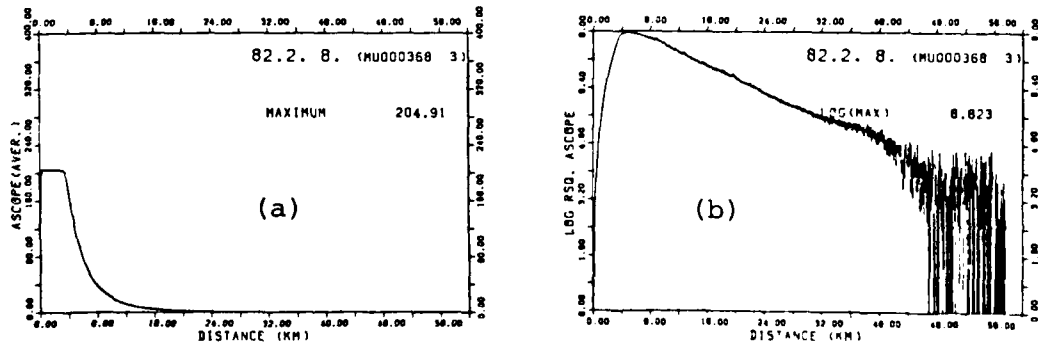


Fig.1 (a) The averaged A-scope.  
(b) The range-squared A-scope in natural logarithmic scale.

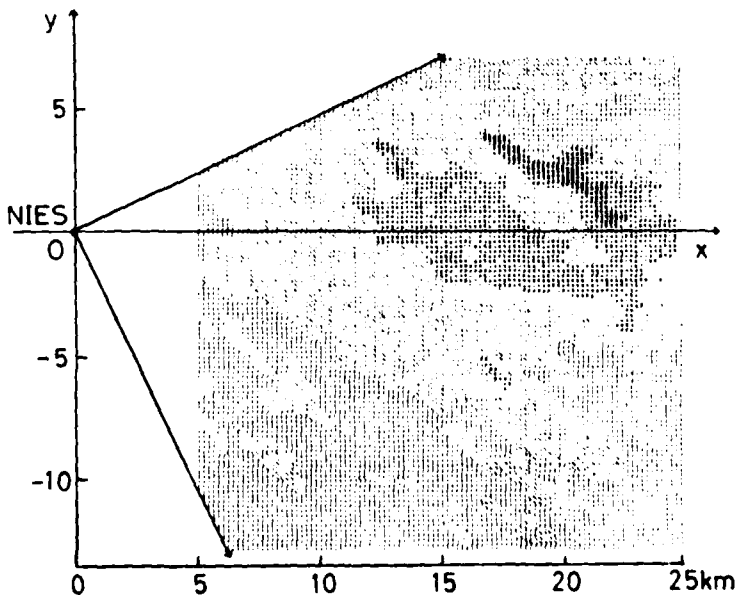
data were taken by horizontal scan from  $65^\circ$  to  $155^\circ$  ( $0^\circ$  is set to the north, clockwise from the north). One scanning required 22.5 min, which started at 10:46 a.m.. This measurement area contains an urban area (the population:100,000) and its suburbs, and a lake area. This area is one of typical satellite-city areas of the Tokyo metropolitan city.

We show the averaged A-scope for all directions in Fig.1(a). The range-squared A-scope is plotted in Fig.1(b) (the ordinate is in natural logarithmic scale). Up to 5 km, the profile is affected by the saturation of the input signal to a transient digitizer. From 5 km to 30 km, the logarithmic range-squared A-scope decreases linearly. Under an assumption of uniform extinction coefficient distribution over the scanned region, we obtained a relative aerosol concentration distribution map (Fig.2). Beyond 40 km, the signal is not reliable due to low signal-to-noise ratio (S/N). The laser powers, DC levels and area under the A-scope profile were also monitored to check the data quality.

Fig.2 presents the aerosol distribution map covering an area of  $20 \text{ km} \times 20 \text{ km}$ . This map consists of  $100 \times 100$  pixels (the lidar facility is located at the origin, the x-axis is to the east, and the y-axis is to the north). The aerosol concentration was displayed by grey level slice (ten levels).

The displayed area contains the lake Kasumigaura ( $x < 5 \text{ km}$ ,  $-2 \text{ km} < y < 2 \text{ km}$ ), urban areas ( $5 \text{ km} < x < 10 \text{ km}$ ,  $-5 \text{ km} < y < 10 \text{ km}$ ) and some factories around the point at ( $x = 15 \text{ km}$ ,  $y = 5 \text{ km}$ ). Fields and farms spread over the region  $y < -5 \text{ km}$ . The aerosol concentration distribution correlates well with these geographical features; note that the wind direction was NW.

Fig.2 The aerosol distribution map measured over a region of  $20 \text{ km} \times 20 \text{ km}$ .



### Discussion

In order to judge the quality of processed image data, we evaluated the S/N ratios at each pixel. The error  $\sigma_{ij}$  of  $c_{ij}$  at  $(i,j)$  pixel is given by

$$\sigma_{ij} = \sqrt{\frac{\sum_k (c_k - \bar{c}_{ij})^2}{N_{ij}(N_{ij} - 1)}} \quad (1)$$

where,

$$\begin{aligned} i, j &= 1, 2, \dots, 100 \text{ and} \\ k &= 1, 2, \dots, N_{ij} \end{aligned}$$

Here  $c_k$ ,  $\bar{c}_{ij}$  and  $N_{ij}$  are the relative aerosol concentration of individual measured points, the mean value of  $c_k$  in the pixel  $(i,j)$  and the number of data in the pixel  $(i,j)$ , respectively. Then S/N ratio at each pixel is given by

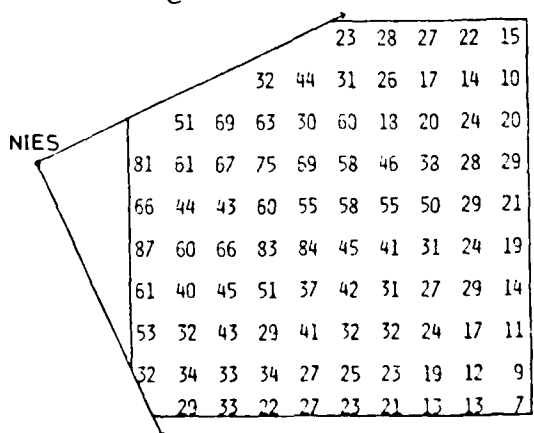
$$(S/N) = \frac{\bar{c}_{ij}}{\sigma_{ij}} \quad (2)$$

The S/N ratios averaged over  $10 \times 10$  pixels are shown in Fig.3, corresponding to Fig.2. The S/N values spread from 87 to 7, which means that signals are accurate enough to display the aerosol concentration in 10 levels.

Finally we discuss the S/N ratio taking into account various noise sources. The total S/N ratio,  $(S/N)_t$ , (we neglect suffix  $ij$  for each pixel  $(i,j)$  in the following) is given by

$$(S/N)_t = \left\{ \frac{1}{(S/N)_s^2} + \frac{\delta_\ell^2}{p} + \frac{1}{(S/N)_e^2} \right\}^{-1/2} \quad (3)$$

where,  $(S/N)_s$  and  $(S/N)_e$  are S/N ratio due to shot noise and electrically induced noise, respectively,  $\delta_\ell$  is the fluctuation of the laser power, and  $p$  is the number of laser pulses passing through each pixel. The quantity  $\delta_\ell$  is independent of distance  $R$  ( $\delta_\ell = 27\%$ ), and  $p$  is inversely proportional to the distance. In the case of Fig.2, the total S/N ratio,  $(S/N)_t$ ,



is limited by the laser power fluctuation ( $(S/N) \sim 2 \times 10^5$ ,  $\sqrt{p}/\delta \sim 170$  and  $(S/N) \sim 6.5 \times 10^3$ ) at the distance  $R = 5$  km. On the otherhand, at  $R = 25$  km,  $(S/N)$  is limited by electrically induced noise ( $(S/N) \sim 620$ ,  $\sqrt{p}/\delta \sim 76$ ,  $(S/N) \sim 16$ ). These evaluations are in good agreement with the values shown in Fig.3. This means we can extend the detection range or can shorten the measurement time by normalization of signal using the monitored power and by reduction of electrical induced noise.

In the future, we plan to examine the correlation of lidar image data with the ground-truth data, and also the relationship between the aerosol distribution with meteorological conditions and geographical factors.

#### Acknowledgement

Authors thank Mr. F.Sakurai for helping us in measurement by LAMP lidar.

#### Reference

- 1) N. Takeuchi et. al., 10th ILRC, Silver Spring, C-2(1980).

Airborne Lidar Measurements During the South Coast Air  
Basin/Southeast Desert Oxidant Transport Study

by

James L. McElroy  
Environmental Monitoring Systems Laboratory  
U.S. Environmental Protection Agency  
P. O. Box 15027  
Las Vegas, Nevada 89114

ABSTRACT

During the summer of 1981, the U.S. Environmental Protection Agency's Environmental Monitoring Systems Laboratory in Las Vegas participated with its two-frequency airborne downward-looking lidar in the South Coast Air Basin/Southeast Desert Oxidant Transport Study. The study was a cooperative program organized by the State of California's Air Resources Board; it was primarily concerned with quantifying the transport of oxidants and their precursors from the South Coast Air Basin into the adjacent high desert and low desert areas. Investigators from several Federal and State agencies, local air pollution control agencies, universities, and private contractors were involved in the field program. In this paper, the airborne lidar system is described, and the lidar data are presented and discussed in terms of the overall objectives of the study.

The two-frequency system used in the study consists of a neodymium-Yag transmitter, a 36-centimeter Newtonian telescope receiver, and a complex electronics subsystem (including a microcomputer) capable of displaying the data in real time on-board the aircraft. The laser emits light simultaneously at two frequencies, 0.53 micrometer ( $\mu\text{m}$ ) (green) and 1.06  $\mu\text{m}$  (near infrared). The data are permanently recorded on a digital magnetic tape recorder. The real time display is recorded by a video tape recorder. The laser can be fired at a variable rate from 1 pulse every 10 seconds to 10 pulses per second. At the maximum firing rate, the horizontal resolution for the cruising speed of a small twin-engine cargo aircraft (required for the lidar system) is about 10 meters. The theoretical vertical resolution of 3 meters is determined by the laser pulse width of 20 nanoseconds. Geographical positioning for the data points is provided by a dedicated Loran C navigational unit.

Discussions of lidar data collected during the study will focus on the following:

- 1) pollutant transport through the mountain passes and over the mountain slopes,
- 2) contrast between daytime and nighttime transport and the resulting impact in the desert areas,
- 3) redistribution of pollutants into elevated layers near the slopes and in major airflow convergence zones and the resulting variations from expected transport and impact in the desert areas,
- 4) interaction of elevated pollutant layers with the higher mountain slopes,

- 5) lee wave mixing to the ground in the lee of slopes and mountain passes of elevated pollutant layers, and
- 6) effects of carry-over pollutants trapped against slopes, in inland valleys, and in layers aloft.

# LIDAR IN ATMOSPHERIC DISPERSION STUDIES: SOME QUANTITATIVE ASPECTS

by

MERVYN J. LYNCH

School of Physics and Geosciences  
Western Australian Institute of Technology  
Bentley, 6102, Western Australia

and

WYNN L. EBERHARD and G.T. McNICE

Wave Propagation Laboratory  
NOAA/ERL/WPL  
325 S. Broadway  
Boulder, Colorado, 80303, USA

Lidar has proven to be a useful remote sensor in studying the dispersion of pollutants in the atmosphere under a wide range of meteorological conditions and in a variety of terrain. In these situations lidar has demonstrated that it is able to provide quantitative information on the important parameters plume centerline and the  $\sigma_y$  and  $\sigma_z$  dispersion coefficients. Further, these measurements can be determined as functions of time and mean values extracted. The value of such numbers as inputs to air quality models must be emphasised as there are few competitors that can define the physical extent of a plume over some 10 km of downwind distance on say a 10 minute timescale. In this sense the value of lidar in supporting air quality dispersion investigations seems assured for some years to come.

The issue of '*can a lidar provide more information on plume particulates?*' is more challenging and is addressed in this paper. In comparison to the majority of instruments used in air dispersion studies such as winds and temperature sensors, gas samplers, particulate samplers etc., lidar ranks rather poorly as a measuring instrument. Lidar backscatter signals typically provide a relative intensity and it is only with some difficulty that inferences about the scatterer itself can be made. Certainly, attempts to measure polydispersion size distributions and to estimate mass fluxes with other than multi-wavelength or multi-angle (e.g. bistatic) lidars are questionable. Equally, calibrating a lidar in the same sense that one calibrates a wind or temperature sensor is not trivial. Validating this calibration in a field performance is equally demanding and not yet widely demonstrated. The above matters are made somewhat more complicated if stack emissions are studied by lidar in that not only do the parameters of the scatterer change as a function of fuel burn rates but the particulates themselves change as they undergo oxidation or interact with moisture etc., in the atmosphere.

If the source parameters (e.g. particle loading, size, shape and refractive index) are controlled, then the possibility of lidar providing quantitative information on the actual concentration of particulates at downwind location is somewhat more encouraging.

The value of information on spatial concentrations of emissions is clear. Since air quality regulations are written in terms of concentrations, lidar support of air quality modelling validation programs with quantitative data on concentrations would enhance the validity and integrity of lidar as an operational instrument. Lidar data would need to agree with that from other *in situ* samplers.

Available evidence shows that lidar performance in demonstrating constancy of the integrated backscatter on a given plume at several downwind distances is a problem in itself. Clearly in these situations not all the difficulties are directly attributable to the lidar.

In dispersion studies, where particulate (and gaseous) tracers are employed to study specific aspects of dispersion dependence on meteorological conditions or terrain features, the source can be more easily controlled and in principle somewhat better characterised in terms of the nature of the particulate emissions. A major EPA sponsored study, the Small Hill Experiment at Cinder Cone Butte, Idaho is but one example where quantitative data on particulate concentrations in principle could have been determined from lidar measurements.

This paper addresses the matters of (i) lidar calibration, using a target of known reflectivity and (ii) the lidar study of plumes of particulate tracers where the physical properties of the tracer are defined. A field evaluation of the quantitative performance of the lidar is reviewed. Specific problems and recommendations for further work on this project are identified.

## PLUME DISPERSION TRACKED BY UV LIDAR

Wynn L. Eberhard and G.T. McNice  
NOAA/ERL/Wave Propagation Laboratory  
325 Broadway  
Boulder, Colorado 80303

### OVERVIEW

Lidar can play a crucial role in field experiments that hope to measure atmospheric dispersion in non-ideal but common settings, for instance over complex terrain or near land-water interfaces. The recent participation of WPL's multi-wavelength lidar in such an experiment was characterized by the successful use of a frequency-doubled ruby laser for eyesafe tracking of an oil fog plume. Plume definition in the UV was usually adequate but not equal to that possible in the red. Data processing included corrections for extinction in both the clear air and moderately dense plumes. The EPA-sponsored Plume Impingement Study at Cinder Cone Butte (CCB), Idaho, in October-November 1980 provided data for development of improved models for prediction of air quality when pollutants impinge on elevated terrain under stable (nighttime) conditions (Holzworth, 1980). The lidar data showed that the vertical dispersion parameter of the plume upwind of the hill grew as the square root of the distance from the source in slight and moderate stability.

### LIDAR SYSTEM AND DATA PROCESSING

The lidar was a calibrated multi-wavelength research lidar. The ruby laser emitted superimposed pulses at both red (.6943  $\mu\text{m}$ ) and frequency-doubled (.3472  $\mu\text{m}$ ) wavelengths at a maximum pulse rate of 0.7 Hz. Beam divergence was 1 mr full angle, and axial resolution was 7.5 m (standard deviation of signal from a point scatterer). The Newtonian receiving telescope with 70-cm diameter primary directed the scattered return through a dichroic beam splitter to photomultipliers. Biomation 8100's digitized the signals, which were recorded on magnetic tape through a NOVA 840 computer.

The use of the UV output complied with stringent eye safety constraints in both experiments. In order to measure the full vertical extent of the plume, the pulse often struck terrain occupied by persons with no eye protection. A filter of colored glass (Schott BG25) attenuated the red output strongly while passing most of the UV. The output met ANSI Z136.1 single-pulse eye safety limits at no more than 30 m range for the UV and 900 m for the residual red. Scans were therefore restricted to avoid terrain at distances closer than 1000 m. The UV channel generally achieved adequate plume definition above clear air return over most of the region of interest. The ratio of UV-to-red backscatter coefficient varied between 1 and 4 for the oil fog and was typically 9 for the ambient air.

Reduction of the lidar data is by interactive computer processing on a graphics terminal to isolate the plume's backscatter coefficient.

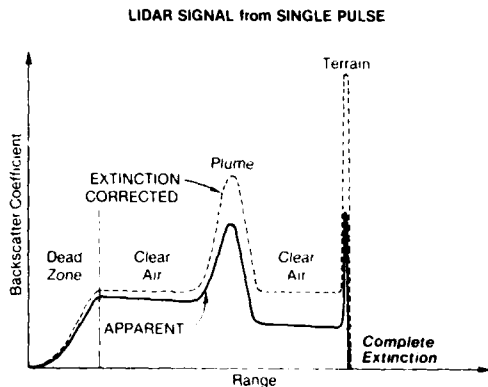


Figure 1.--Correction of lidar signal for extinction.

rected scattering profile for the pulse. This corrected profile has equal clear air backscatter coefficient on both sides of the plume.

The basic output of the CCB data for analysis by atmospheric scientists is an archive on digital magnetic tape of the two-dimensional distribution of plume backscatter coefficients plus auxiliary information for each scan. The auxiliary information includes parameters describing the section through the plume, such as centroid position in both lidar and sponsor coordinate systems. It also includes quality descriptor flags needed for proper interpretation, such as whether intervening terrain hid the bottom of the plume.

#### PLUME IMPINGEMENT STUDY

Figure 2 shows the positions at CCB of WPL instruments. Mobile cranes lifted equipment for tracer release as high as 58 m above the ground. The lidar scanned vertically in a sequence of azimuth directions to intercept the oil fog plume upwind, abreast, and in the lee of the hill. An emphasis on upwind scans had the objective of defining a "boundary condition" of plume behavior before the hill perturbed the air flow. Reduction and analysis of the large volume of lidar data are still in progress at this writing, but some tentative results are available.

Vertical dispersion under stable conditions, especially of elevated plumes, is poorly understood (Hanna et al., 1977), mainly because of limited experimental data. Some (Csanady, 1973) argue that with sufficient stability the vertical diffusion coefficient  $\sigma_z$  will asymptotically approach  $(2\sigma_w/N)$  where  $\sigma_w$  is the standard deviation of the vertical wind component at plume level, and  $N$  is the Brunt-Vaisala frequency. In contrast, the Pasquill-Gifford-Turner curves commonly used for atmospheric dispersion prediction show no tendency toward an asymptotic limit. Strong interest therefore exists in the vertical dispersion of the plume as revealed by the lidar before the flow "sensed" the hill. Figure 3 plots the vertical dispersion for the first set of

This processing includes necessary corrections for extinction in the clear air and the plume (Fig. 1) based on the method of Fernald, et al. (1972). We assume a homogeneous ambient atmosphere and determine the clear-air extinction coefficient that makes the clear air signal approximately independent of range. To correct for plume extinction, we assume that for each pulse the extinction-backscatter ratio through the plume is constant. We find the transmission of the plume by comparing the clear air signal beyond the plume with that before the plume. An iterative calculation then produces the plume's extinction-backscatter ratio and the corrected scattering profile for the pulse. This corrected profile has equal clear air backscatter coefficient on both sides of the plume.

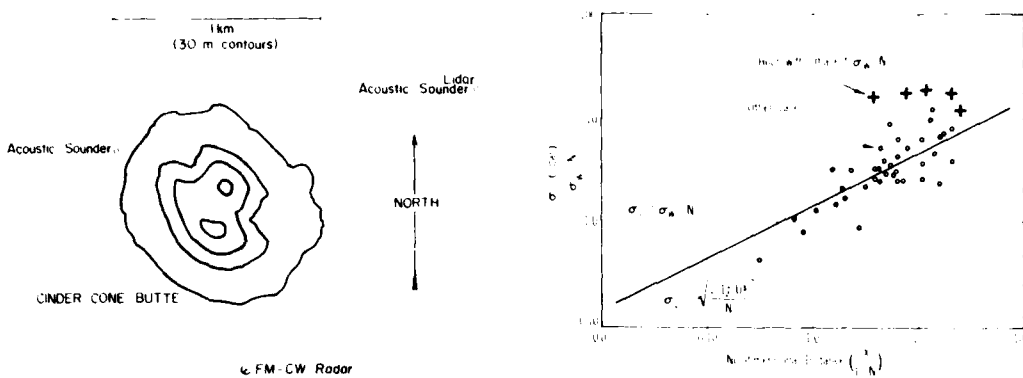


Figure 2.--Site of Plume Impingement Study. The lidar was 2 m below the outer hill contour. The oil fog generator was typically 1 km either SE or NNW of the center of the hill.

Figure 3.--Vertical dispersion upwind of Cinder Cone Butte. Parameters are: horizontal distance downwind of release  $X$ ; mean wind speed at plume height  $U$ ; Brunt-Vaisala frequency  $N$ ; vertical standard deviation of plume concentration  $\sigma_z$  and wind at plume height  $\sigma_w$ ; and vertical turbulent intensity  $I_z = \sigma_w/U$ .

experimental hours (15) processed. Environmental Research and Technology, Inc., which is carrying out model development under contract to EPA, compared the lidar data against the meteorological data. In most cases the plume grew with distance downwind during each individual experimental hour as well as in this multi-hour presentation, which suggests a square root growth law. An exception occurred during the hour of greatest stability, when no growth was evident. However, the vertical dispersion was an order of magnitude larger than the theoretical asymptotic limit. It is hoped that additional analysis of WPL lidar data from CCB and other experiments will settle this issue.

The lidar data also indicate streamline position and whether bunching occurred as flow passed over the hill. The data also reveal plume shape and proximity relative to the hillside. Figure 4 gives an example of the plume impacting the hill with higher concentrations of the tracer at the surface than would have occurred over flat terrain. The tilted plume profile resulted from shear induced by the hill, which forced the trajectories in the bottom of the plume to veer closer to the lidar than those higher.

#### ACKNOWLEDGMENTS

The U.S. Environmental Protection Agency provided financial support through the EPA-NOAA Energy/Environment Interagency Agreement. Environmental Research and Technology, Inc., conducted the CCB experiment and model development under contract to EPA.

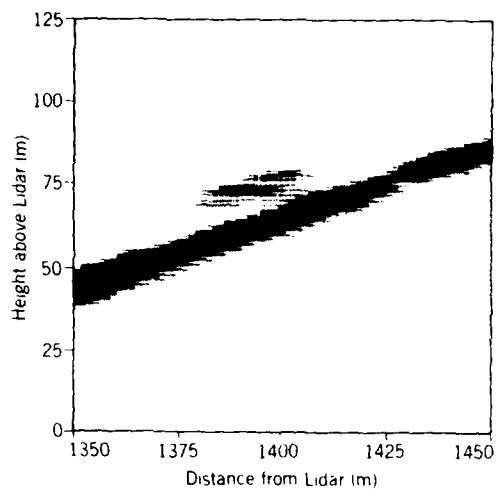


Figure 4.--Example lidar scan. The plume originated 35 m above the ground at 123° and 590 m from the center of the hill. The lidar scanned vertically at azimuth 240°, intercepting the plume in a plane roughly normal to the plume's direction of travel. The darkness of each pixel in the figure is proportional to signal strength. The broad diagonal line is the strong signal from the hillside. A single dot per pixel indicates signal equal to or less than from clear air. This lidar section shows the plume in contact with the hillside.

#### REFERENCES

Csanady, G.T., 1973: Turbulent Diffusion in the Environment. D. Reidel, 248 pp.

Fernald, S.R., B.M. Herman, and J.A. Reagan, 1972: Determination of aerosol height distributions by lidar. J. Appl. Meteorol., 11, 482-489.

Hanna, S.R., G.A. Briggs, J. Deardorff, B.A. Egan, F.A. Gifford, and F. Pasquill, 1977. AMS workshop on stability classification schemes and sigma curves--summary of recommendations. Bull. Am. Meteorol. Soc., 58, 1305-1309.

Holzworth, G.C., 1980: The EPA program for dispersion model development for sources in complex terrain. Second Joint Conference on Applications of Air Pollution Meteorology Conference Papers, 465-468, American Meteorological Society.

SUMMARIZED RESULTS OF SHIPBORNE LIDAR MEASUREMENTS CARRIED OUT DURING  
THREE YEARS OF PLUME DISPERSION OVER SEA SURFACES

by

H. Herrmann, F. Köpp, and Ch. Werner  
German Aerospace Research Establishment (DFVLR)  
Institute of Optoelectronics  
D-8031 Wessling  
Federal Republic of Germany

Summary: The dispersion of artificial aerosol plumes over sea surfaces was measured using the DFVLR-Minilidar. The distribution of the plume concentration could be derived from short-time and long-time measurements. Some effects of the aerosols and of the sea surface on the plume dispersion were estimated.

Introduction: The minilidar was widely applied to measuring problems for atmospheric physics and environment protection. One of those problems is the dispersion of aerosol plumes close to the sea surface (1). For this purpose, many artificial plumes were observed with the two minilidars on different small research vessels during three years. From the lidar results, characteristic parameters describing plume dispersion were derived.

Experiment: Estimation of the ground level concentration field of an inert pollutant downwind of a point source is generally achieved by using Sutton's formulation, the Gaussian plume model (2). The following equation is used for the concentration  $x$  at a distance  $x$  downwind from a source at the sea surface:

$$x(x,y,z) = \frac{Q}{\sigma_y \sigma_z \pi U} \exp \left\{ -\frac{1}{2} \left[ \left( \frac{y}{\sigma_y} \right)^2 + \left( \frac{z}{\sigma_z} \right)^2 \right] \right\}$$

where  $\sigma_z$  and  $\sigma_y$  are the vertical and crosswind standard deviations of the pollutant distribution,  $U$  is the wind speed, and  $Q$  is the strength of the source. Figure 1 shows a schematic distribution given by Slade (3).

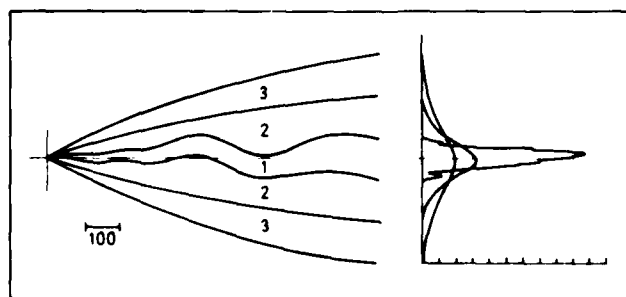


Figure 1: Schematic plume distribution (3).

Curve 1 represents the instantaneous plume, 2 is an average observation over 10 minutes, and 3 an observation over a time period of 2 hours. The relative concentrations for crosswind direction  $y$  in a distance  $x$  are shown on the right side.

For the determination of the dispersion parameters over sea surfaces, long-time measurements at a few points of the plume are necessary. Many experimental problems for the operator on a small ship could be reduced by concentrating the requirements on different parts of the dispersion.

Measurements of the instantaneous plume versus distance  $x$  from the source were the first research goal. Figure 2 shows the normalized Gaussian distribution measured at different distances  $x$  at one plume.

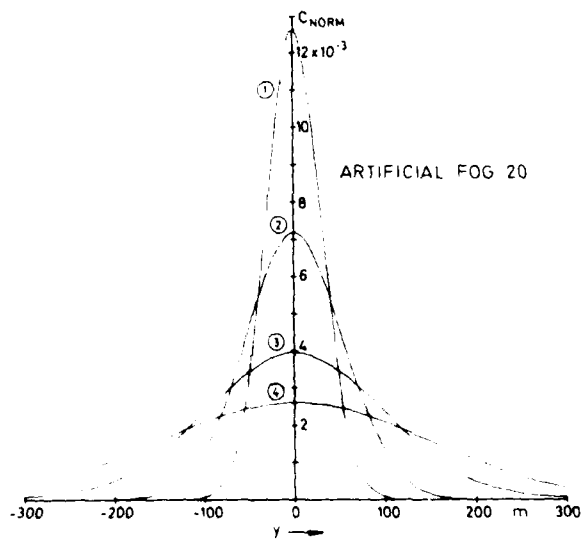


Figure 2: Normalized Gaussian distribution for a fog plume determined for four distances from the source:  
Curve 1,  $x = 1050$  m; Curve 2,  $x = 2090$  m;  
Curve 3,  $x = 2830$  m; Curve 4,  $x = 3820$  m.

Their maxima are superposed at  $y = 0$ . The dispersion of the plume grows with increasing distance from the source.

After measuring some vertical distributions of the plumes, the long-time measurements at one distance of the plume were carried out. Figure 3 shows the result which is close to that described in the literature (3).

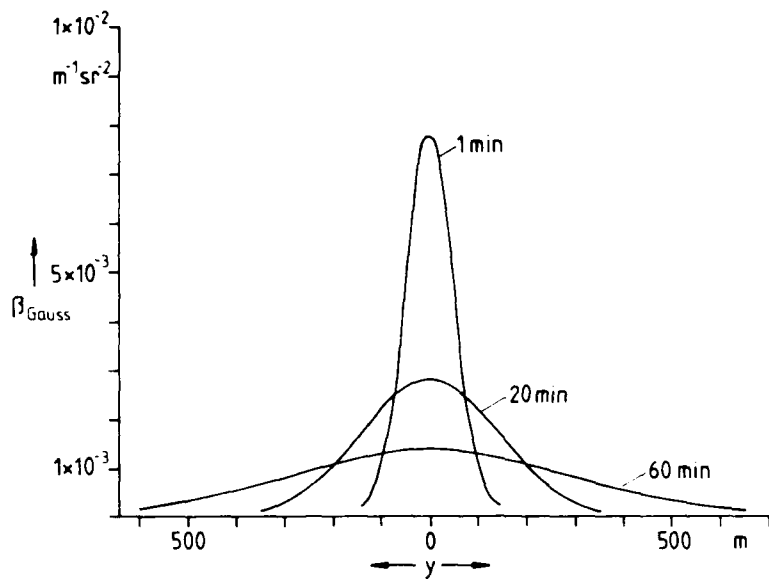


Figure 3: Normalized Gaussian distribution for a fog plume determined at a distance of 1400 m from the source for different observation times labelled at the curves. The maxima are superposed at  $y = 0$ .

Effects of the sea surface on the dispersion could be measured. One effect is caused by the different hygroscopy of the plume material, the other effect is connected to the sea surface motion. The tide effect in the North Sea could be measured under some wind conditions. Results will be reported.

#### References

- (1) H. Hermann,  
F. Köpp,  
Ch. Werner  
Remote measurements of plume dispersion over sea  
surface using the DFVLR-Minilidar, Optical Engineering  
20, 1981, 759-764.
- (2) Perkins, H. C.  
Air Pollution, McGraw-Hill, 1974.
- (3) Slade, D. H.  
Meteorology and Atomic Energy, TID-24.90 (1968).

## CLOUD MAPPING OF SCREENING AEROSOLS

B.T.N. EVANS

DEFENCE RESEARCH ESTABLISHMENT, VALCARTIER  
P.O. BOX 8800, COURCELETTE, QUEBEC, CANADA  
GOA 1R0

During recent trials a variety of data was obtained on various military screening smokes using a scanning Nd: YAG LIDAR system operating at  $1.06 \mu\text{m}$  and 100 Hz. The full description of this system will be given in another paper in the conference.

A simplified example of a mapped smoke cloud generated from burning red phosphorus is shown in Figure 1. The figure shows a horizontal slice through the cloud at about 32 s after dissemination. The contours of the estimated linear extinction coefficient can be directly related to the aerosol concentration. Since these maps can be obtained at different heights and times (< 5 s apart) the time evolution of the concentration can be monitored and measured 3-dimensionally.

Figure 2 shows a transmission contoured diagram of another red phosphorus generated cloud 40 s after burst. It is evident from this diagram that wind shear and the presence of the initial centre of burst (the lowest transmission area to the left) can be identified.

This paper will also present results on other smokes as well as cloud evolution parameters such as transmission with time, concentration with distance from the source, cloud shape and extent, etc.

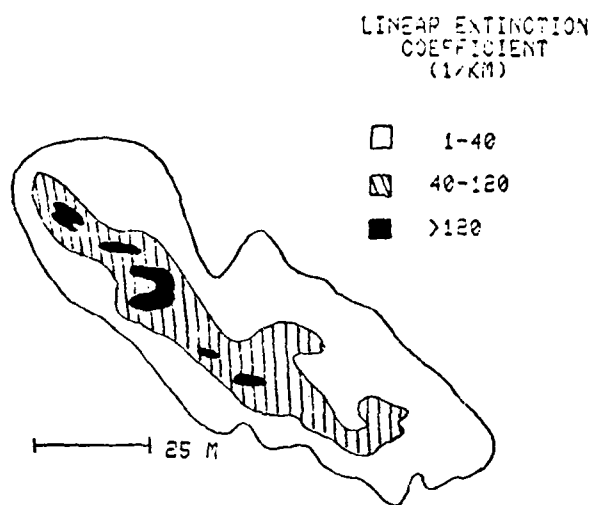


FIG. 1 SIMPLIFIED CLOUD MAP OF A RED PHOSPHORUS GENERATED SMOKE

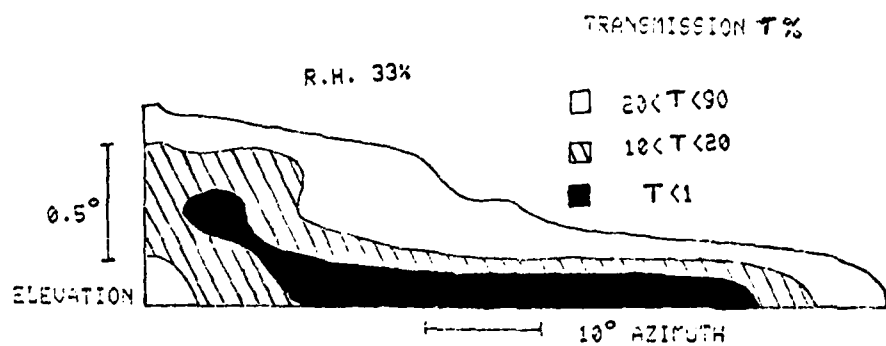


FIG. 2 TRANSMISSION CONTOUR OF RED PHOSPHORUS GENERATED SMOKE

## REFRACTIVE TURBULENCE PROFILES BY HIGH-RESOLUTION LIDAR

Ronald L. Schwiesow and Robert S. Lawrence  
NOAA Environmental Research Laboratories  
325 Broadway  
Boulder, Colorado 80303

*Intent* -- Inhomogeneities in the refractive index of the atmosphere affect the propagation of laser light used, for example, for communications links. A lidar backscatter technique may be a useful way to determine some characteristics of the vertical profile of refractive turbulence under daytime conditions. We have simulated the performance of a high-angular-resolution (essentially diffraction-limited) lidar by calculating the received image size and energy as a function of altitude for different assumed profiles of  $C_n^2$ , the refractive-index structure constant.

The measurement of path-averaged  $C_n^2$  over a horizontal path can be done with a light source and receiver at opposite ends of the path.<sup>1</sup> By the use of atmospheric backscatter as a remote source, it is possible to make an effectively single-ended, variable-path-length measurement of  $C_n^2$  along a vertical path, in analogy to the double-ended horizontal measurements, as proposed by Belen'kii and Mironov.<sup>2</sup> We have specified the form of a suitable lidar and calculated the return on the basis of various atmospheric conditions.

One application of a mobile  $C_n^2$  lidar is to survey various sites for suitability as ground stations for daytime vertical optical communication links. Preferred sites for nighttime astronomy are not necessarily best for daytime use.

*Results* -- The height profile of the image radius from the lidar scattering volume is clearly dependent on the  $C_n^2$  profile. A plot of log (altitude) vs. image radius is roughly linear; its slope depends on the value of  $C_n^2$  aloft (above 1 km), and its altitude intercept depends mostly on  $C_n^2$  at lower levels. The sensitivity of an example lidar at 488 nm is a change in slope by a factor of 4 for a change of  $C_n^2$  by a factor of 25 aloft, and a change in intercept by a factor of 10<sup>2</sup> for a change of  $C_n^2$  by a factor of 25 at lower levels. It is reasonable that the altitude intercept depends on lower level  $C_n^2$  because the intercept is another way of expressing the altitude at which image spreading from refractive index inhomogeneities becomes larger than the image radius from diffraction.

One estimate for the required signal-to-noise ratio from a given range gate is the reciprocal of the fractional increase in image radius for that gate. If we use a range gate that is 10% of the range and a 0.5-m transceiver aperture, then a 1-J transmitter pulse energy will result in an adequate daytime signal-to-noise ratio from 20 km on a single-shot basis.

The weighting function (change in image radius for a given change in  $C_n^2$  as a function of height) depends on the profile of  $C_n^2$  below the height at which the function is evaluated. This behavior, which results from the interaction of diffraction and refractive effects, is best demonstrated by considering hypothetical  $\delta$ -function  $C_n^2$  profiles.

**Technique** -- The lidar system we used for the computer simulation includes a common telescope for transmitter and receiver. This is an improvement over lidar configurations usually used in the visible<sup>2</sup> because, for the  $C_n^2$  profiling application, transmitter and receiver fields of view in the diffraction limit are matched and alignment is easier to maintain.

The  $C_n^2$  profiles for the simulation were taken from Hufnagel,<sup>3</sup> and the average model rather than the random model was used. The average model was modified by a constant multiplier and power law height dependence to produce various image radius profiles. Equations for the effect of  $C_n^2$  on image radius are in the literature.<sup>4</sup> We assumed only molecular scattering to provide a conservative estimate of available signal-to-noise values and used atmospheric backscatter and sky brightness values previously summarized.<sup>5</sup>

We conclude that a nearly diffraction-limited lidar of modest dimensions should be able to measure important aspects of the daytime  $C_n^2$  profile to an altitude of at least 20 km. Accessible aspects include the intensity scale of a profile of assumed shape and its general height dependence.

### References

1. Ting-i Wang, G.R. Ochs, and S.F. Clifford. A saturation-resistant optical scintillometer to measure  $C_n^2$ . *J. Opt. Soc. Am.* 68, 334-338 (1978).
2. M.S. Belen'kii and V.L. Mironov. Laser method of determining the turbulence parameter  $C_n^2$  on the basis of light scattering by atmospheric aerosol. *Radiophys. Quant. Electron.* 24, 206-210 (1981).
3. R.E. Hufnagel. Variations of atmospheric turbulence. Digest of Topical Meeting on Optical Propagation Through Turbulence, Boulder, CO (Opt. Soc. Am.) WA1-1 - WA1-4 (1974).
4. H.T. Yura. Signal-to-noise ratio of heterodyne lidar systems in the presence of atmospheric turbulence. *Optica Acta* 26, 627-644 (1979).
5. R.L. Schwiesow and L. Lading. Temperature profiling by Rayleigh-scattering lidar. *Appl. Opt.* 20, 1972-1979 (1981).

This work was supported in part by AFGL.

Lidar measurements of the entrainment zone and  
the turbulent kinetic energy budget of the  
atmospheric mixed layer

R. Boers, E.W. Eloranta, W.P. Hooper  
Department of Meteorology  
University of Wisconsin-Madison, WI 53706

R.L. Coulter  
Argonne National Laboratory  
Argonne, IL 60439

Lidar measurements of the thickness of the entrainment zone were derived from six case studies which included a wide range of atmospheric conditions. The entrainment zone is the outermost portion of the mixed layer confined between the maximum heights reached by only a few vigorous convective cells and by the height where the mixed layer air occupies 90-95% of the total area. The thickness of the entrainment zone was measured from pictures of RHI-scans generated by means of a color enhanced video display system. Observations were made during the day when the mixed layer depth was increasing: layer depths between 150 and 1600 meters were observed. The entrainment zone was usually 100 to 200 meters thick, with occasional values as large as 700 meters which occurred during periods of rapid mixed layer growth. Measured values of the entrainment zone thickness were compared to the predictions of parcel theory and to the values measured by Deardorff et al. (1980) in tank experiments.

The discrepancy between models that predict the daytime evolution of the mixed layer and lidar data of the mixed layer height was investigated by computing terms in the turbulent energy budget from lidar measured wind and turbulence data. The lidar measurements were supported by conventional observations made by Argonne National Laboratory researchers of temperature, wind profiles by means of pilot balloons and kyoons, and by measurements of surface heat flux and momentum flux. In addition, a network of NCAR-PAM surface stations provided measurements of surface winds used in estimating divergence rates. It is shown that during the early morning hours, turbulent energy generated by wind shear at the top of the mixed layer is comparable in magnitude to surface buoyant and mechanical production of turbulence.

Ref: J.W. Deardorff, G.E. Willis and B.H. Stockton,  
Laboratory studies of the entrainment zone of  
a convectively mixed layer. *J. Fluid. Mech.* 100, 1980, p. 41.

## CELL STRUCTURES IN THE ATMOSPHERIC MIXED LAYER OBSERVED BY A MIE LASER RADAR

Yasuhiro Sasano, Hiroshi Shimizu and Nobuo Takeuchi  
National Institute for Environmental Studies,  
Tsukuba, Ibaraki 305 Japan

Mie-scattering laser radar has been used to study the structure of the convective mixed layer in optically clear air. Two-dimensional image data obtained by scanning measurements (PPI and RHI modes) have been processed using edge-enhancement techniques to display distinct structures within the convective layer. The structures of convective cells penetrating into upper clean air were very similar to those obtained previously by sodar, radar, and FM-CW radar.

### Instruments and observations

The laser radar used was constructed for measuring wide-area air pollution phenomena (NIES LAMP lidar). It was equipped with a high-powered YAG laser (1.2 J/pulse, 25 pps) and a Cassegrainian-type telescope of 1.5 m diameter. Scanning was finely controlled with an accuracy of 0.3 mrad.

The results presented here were obtained in an experiment designed to investigate the mixed-layer structure on Nov. 12, 1981 at the National Institute for Environmental Studies, Tsukuba, Japan. On this day, the sky was clear and the wind was weak, so that mixed-layer was expected to develop. The parameters used in these laser radar measurements are shown in Table 1. The wavelength was 0.53  $\mu$ m.

Table 1. Measurement parameters

Mode	Azimuth <sup>*)</sup>	Elevation	Sampling Gate Time	Sample Word	Averaging Time	Scan Speed
RHI	-80°	0 ~ 8.9°	100 nsec	2048	2 sec	6°/min
PPI	-63 ~ -123°	1.9°	100 nsec	2048	2 sec	14°/min

<sup>\*)</sup> Angle from North (minus indicates counterclockwise direction)

### Data processing

The data stored on the magnetic tapes were processed by a HITAC M-180 computer for precise analysis. After DC-level subtraction and range-corrections were made on the received-power data, a coefficient proportional to the volume-back-scattering was obtained (this proportionality factor is due to a calibration constant and atmospheric transmittance). For simplicity, we call this coefficient an aerosol density, which is expressed as

$$C(R) \cdot P(R)R^2 = K \cdot \beta(R) \exp[-2 \int_0^R \alpha(r) dr],$$

where  $C(R)$  is the aerosol density.  $P(R)$ ,  $\beta(R)$  and  $\alpha(R)$  are the received power, the volume-backscattering coefficient and the extinction coefficient respectively.  $K$  is the system calibration constant and  $R$  is the distance.

By scanning measurements, data were obtained on an equally spaced polar-coordinate  $(R, \theta)$  mesh; they were transformed onto a Cartesian-coordinate  $(x, y)$  mesh. The aerosol density distribution on a Cartesian-coordinate is denoted as  $C(i, j)$ , where  $i=1, 2, \dots, M$  and  $j=1, 2, \dots, N$ . Mesh intervals are  $\Delta X$  for the  $i$ -direction and  $\Delta Y$  for the  $j$ -direction.

The edge enhancement is established by normalization of density gradient, which is defined as

$$G_1(i, j) = \{C(i+1, j) - C(i-1, j)\} / (2 \cdot \Delta X \bar{C}_3)$$

$$G_2(i, j) = [\{C(i+1, j) - C(i-1, j)\}^2 / (2 \cdot \Delta X)^2 + \{C(i, j+1) - C(i, j-1)\}^2 / (2 \cdot \Delta Y)^2]^{1/2} / \bar{C}_5$$

where  $\bar{C}_3$  means the average of  $C(i+1, j)$ ,  $C(i, j)$  and  $C(i-1, j)$ , and  $\bar{C}_5$  means the average of  $C(i+1, j)$ ,  $C(i, j)$ ,  $C(i-1, j)$ ,  $C(i, j+1)$  and  $C(i, j-1)$ .  $G_1$  is a one-directional gradient and  $G_2$  is a two-dimensional gradient: both are normalized by the local density. This normalization cancels the effects of the local and temporal density changes and therefore, the spatial structure of the density variation can be described only in relative terms. This also cancels the ambiguous calibration constant in the laser-radar system which is difficult to determine precisely.

Fortunately, our normalization by the local density value makes the atmospheric transmittance correction unnecessary, because the aerosol density varies more strongly with local conditions than does the transmittance term.

### Results

In Fig.1, a density gradient,  $G_1$ , distribution in a vertical plane is shown. The structure of the transition zone between the mixed layer below and clear air above is very complicated. Comparing it with those previously obtained by sodar, radar and FM-CW radar observations, it is reasonable that it shows the convective cells penetrating into the clean air above the mixed layer.

Fig.2(a) shows the aerosol density distribution obtained in the PPI mode with an elevation angle of  $1.9^\circ$ ; Fig.2(b) shows the corresponding  $G_2$  display. The aerosol density is high within the range of 8 km (below the height of 265 m) and it is low in the far range. At the range of about 9 km, some patches with high density are shown, which seem to be

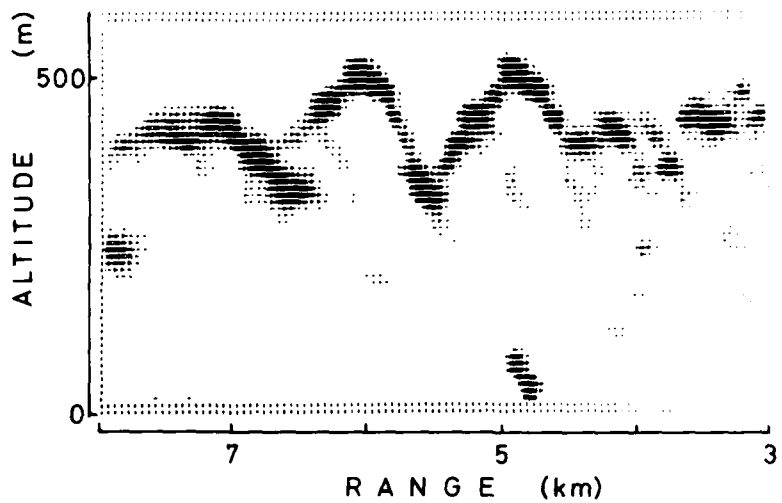


Fig.1 RHI mode displays of normalized density gradient  $G_1$ .

crosssections of penetrative cells. The  $G_2$  display clearly shows doughnut structures in the patches. These are very similar to those found by radar, which was explained as edges of moist penetrative cells.

The edge enhancement procedure proposed here allows distinct structures to be derived from the aerosol density distributions and has the advantages that it does not require an exact correction for atmospheric transmittance nor an absolute calibration for the received power. Mixed layer development can be understood and modelled by the statistics of these convective cell structures and conventional meteorological measurements, which is in execution.

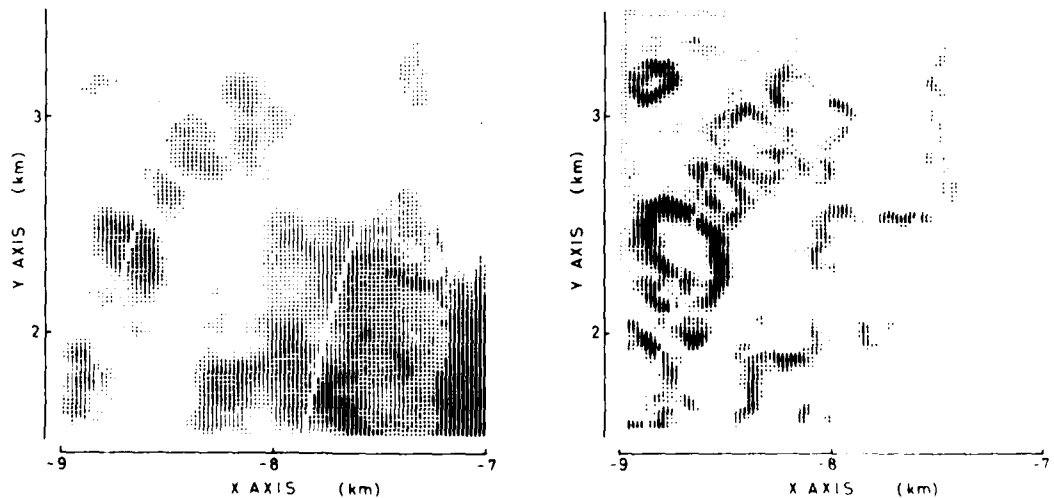


Fig.2 PPI mode displays of (a) aerosol density distribution and (b) normalized density gradient  $G_2$ . Arcs in the figures correspond to 8 km and 9 km ranges from the lidar.

## MONITORING ALPINE VALLEY WIND CIRCULATION BY AIRBORNE LIDAR

W. Renger, P. Mörl, and R. Schellhase  
German Aerospace Establishment  
Institute for Atmospheric Physics  
8031 Wessling  
F. R. Germany

The DFVLR Lidar ALEX F1 is a conventional aerosol lidar mounted on a French Falcon 20, a commercially available 13 passenger aircraft, which was modified for applications in meteorological research. The lidar is mounted above a 50 cm diameter window in the bottom of the aircraft, pointing vertically downward. The light source is a Nd-YAG laser of about 350 mJ output energy at the fundamental and simultaneously 120 mJ at the doubled wavelength. The maximum rep. rate is 10 Hz. For most applications it is limited to 5 Hz by the maximum data flow which can be accepted by the data management system and the tape recorder. Corresponding to a typical speed of 100 m/sec of the aircraft, the horizontal resolution is 20 m, and the vertical resolution is 15 m. For one wavelength operation the resolution can be improved by a factor of 2 horizontally and a factor of 10 vertically. The system was described in a paper given at the 9th ILRC, 1979. Some measurements were presented at the 10th ILRC, 1980.

To study the aerosol load of the atmosphere in the Inn valley around Innsbruck during a high pressure winter situation, several lidar flights were performed. After a cold night, enhanced concentrations of atmospheric particulates could be observed below a temperature inversion, which was blocking the exchange to the atmosphere above. During the day, the heat input of the sun caused this haze cloud to lift, and while the southerly slopes were becoming warmer, an up valley breeze was starting. The wind speed was very low and only effective in the lower few hundred meters as seen from the aerosol structure, which was made visible by the evaluation of lidar cross sections.

About 15 km west of Innsbruck where the valley narrows, the wind dropped down. The haze cloud was ascending at this point of the valley, but the polluted air was not transported to the western part of the valley. At night a typical weak breeze was blowing in the opposite direction and the haze cloud moved several km down valley. This resulted, under stable meteorological conditions, in an increase in aerosol concentration from day to day. For winter 1982 to 1983, it is planned to study these effects and the optical properties of the atmospheric aerosol in the Inn valley in cooperation with the Austrian Solar and Space Agency. We hope that our preliminary measurements will help the choice of locations for the planned instrumentation.

### References

Renger, W., Mörl, P., The German Airborne Lidar Facility - A First Stage of a Space-lab Borne System?" 9th ILRC 1979, DFVLR, Institute for Atmospheric Physics.

Renger, W., Mörl, P., Schellhase, R., Monitoring of Plume Dispersion by Airborne Lidar ALEX F1, 10th ILRC 1980, Silver Spring, MD.

Mörl, P., Reinhardt, M. E., Renger, W., Schellhase, R., The Use of the Airborne LIDAR System "ALEX F1" for Aerosol Tracing in the Lower Troposphere, Beitr. Phys. Atmosph. Vol. 54, Nov. 1981.

## AIRBORNE LIDAR MEASUREMENTS OF MIXED LAYER DYNAMICS

S. T. Shipley and E. V. Browell  
NASA Langley Research Center, Hampton, VA 23665

Airborne lidar measurements of the mixed layer were made during the summer months of 1980 and 1981 using the Ultra-Violet Differential Absorption Lidar (UV DIAL) system developed at the NASA Langley Research Center.<sup>1</sup> The UV DIAL system was operated on-board the NASA Wallops Electra aircraft to measure  $O_3$  and aerosol profiles during long-range flights over the Eastern United States as part of the EPA Persistent Elevated Pollution Episodes/Northeast Regional Oxidant Study (PEPE/NEROS) 1980 Summer Field Experiment. A subsequent Summer Experiment was conducted in 1981 to perform  $O_3$  and aerosol measurements on spatial/temporal scales not investigated during 1980. This paper confines itself to the interpretation of this lidar data set for information on mixed layer dynamics.

### 1. The 1980 PEPE/NEROS Summer Field Program

The NASA airborne UV DIAL system was used to simultaneously measure  $O_3$  and aerosol profiles over the Eastern United States in cooperation with the EPA PEPE/NEROS 1980 Summer Field Program.<sup>2</sup> Approximately 32 hours of multiple wavelength (286 nm, 300 nm, and 600 nm at 5 Hz) and an additional 10 hours of single wavelength (600 nm at 1 Hz) lidar signals were collected in the nadir viewing mode during the period from July 19 to August 13, 1980. By cooperative agreement with the EPA, this data set has been archived along with derived values for the mixed layer height and the vertical distribution of  $O_3$  at 5-min. intervals (30 km horizontal spatial resolution). A 40-min. segment of the 600 nm lidar signal archive is shown in Figure 1a. This horizontal atmospheric cross section was constructed from sequential lidar returns at a repetition rate of 1 Hz with the Electra in flight to the east over the State of Virginia at 4120 m MSL (Mean Sea Level). The entire "aerosol channel" lidar data set obtained during the PEPE/NEROS 1980 Summer Field Program has been archived with 1 Hz resolution, and a complete grey-scale atlas with graphics similar to Figure 1a has been prepared.<sup>3</sup>

In addition to mixed layer heights, the aerosol channel data set reveals information on other atmospheric properties such as the location and size of clouds, the height and horizontal distribution of stably stratified layers, and the height of the Aerosol Deliquescence Level (ADL). The ADL is identified by the change in backscattering associated with the variation of aerosol particle size with relative humidity. The 1400 EDT RADiosonde OBservation (RAOB) from IAD (Sterling, VA) on July 24, 1980, was released approximately 45 min. prior to lidar overpass, and it indicated a mixed layer height  $\sim$  1400 m AGL (Above Ground Level) with potential for non-entraining pseudo-adiabatic convection to  $\sim$  3000 m AGL. Figure 1a confirms this prediction of cloud convection to the subsidence inversion at 2660 m AGL with cloud bases at 1650 m AGL. The mixed layer height of 2660  $\pm$  150 m AGL coincides with cloud tops. The  $\pm$  150 m standard deviation corresponds to actual variations in the mixed layer height due to the upward momentum of convective eddies at the subsidence inversion. The dark bands or "shadows" in Figure 1a are regions of low signal due to the high optical attenuation encountered in clouds. The ADL at 1650 m AGL coincides with the cumulus cloud bases or Cloud Condensation Level (CCL). A lower surface heat flux over the Chesapeake Bay has delayed the convective destruction of stable layering near the inversion at 1400 m AGL.

This NASA lidar data set graphically depicts the relationship of mixed layer height to surface characteristics. For example, a cross section of the Cincinnati, Ohio, urban heat island was obtained on July 18, 1980, at 1235 EDT. An observed 200 m increase in mixed layer height over Cincinnati compared to upwind rural areas agrees with predictions using the 1200 UT Dayton, Ohio, RAOB and hourly surface temperature measurements.<sup>4</sup> As a second example, Lagrangian measurements of PEPE cross sections in the Washington, DC - Philadelphia, PA area demonstrated the insertion of a polluted continental air mass layer over the ocean mixed layer during offshore flow on July 31, 1980. Such elevated (in height) layers are capable of undisturbed long-range transport above the ocean mixed layer, and they are related to acid precipitation at downwind locations.<sup>5</sup>

## 2. Simulation for a Shuttle Lidar

The large-scale horizontal cross sections of Figure 1a can be used to simulate data for a Shuttle-borne lidar at similar wavelengths. Given a 300 km AGL Shuttle orbit with a horizontal ground velocity  $\approx 8 \text{ km s}^{-1}$  and a laser repetition rate of 10 Hz, the GE Unit Lidar for Shuttle applications<sup>6</sup> would observe the lower troposphere with a horizontal resolution approximately 8 times less than for a 1 Hz Electra aircraft system. A simulated Shuttle lidar signal was generated from the data of Figure 1a using a 45 m vertical sampling interval (an arithmetic mean over 3 UV DIAL range bins) for every eighth shot. This signal was artificially degraded using a normally distributed random number generator. The resulting Shuttle lidar simulation for the lower troposphere over Virginia on July 24, 1980, is shown in Figure 1b. It is still possible to identify the mixed layer height, the ADL, clouds and CCL, orographic features, and stable layering over the Chesapeake Bay. Clearly, a Shuttle-borne lidar system will produce signals which can be used to derive information on clouds and mixing in the lower troposphere.

## 3. The 1981 Summer Experiment

The NASA UV DIAL system was again installed on the WFC Electra aircraft for additional atmospheric measurements during the period from July 9 to August 9, 1981. Experiments included participation in the Global Tropospheric Instrument Test Flight-1 (GTIT-1), a Chesapeake Bay boundary layer experiment (Exp. I), a case study for vertical transport of  $\text{O}_3$  by clouds (Exp. II), and measurements in the vicinity of the tropopause (Exp. III). Preliminary results from GTIT-1 and Exp. III are discussed in a companion paper.<sup>7</sup> The following discussion is confined to preliminary results on boundary layer processes observed during Exp. I over the complex coastal environment of the lower Chesapeake Bay.

The airborne UV DIAL system was flown over the lower Chesapeake Bay region following the flight plan outlined in Figure 2. Lidar-derived  $\text{O}_3$  and aerosol profiles were recorded on the four major legs--AB, CD, EF, and GH--at 5 Hz during northerly flow on July 30, 1981, and during northeasterly flow on July 31, 1981. The entire flight plan was performed in approximately 80 min., and the Electra aircraft made four complete passes on a single flight. In situ measurements of  $\text{O}_3$ ,  $\text{NO}_x$ ,  $\text{SO}_2$ , winds, temperature, and dew point were measured simultaneously by other investigations at the locations shown in Figure 2. These measurements include Cessna spirals at B, H, W, X, and Y; tethered balloons at B and W; RAOBs at the Naval Air Station (NAS) and Wallops Island (WFC); and surface measurements by the

Virginia State Air Pollution Control Board (VA SAPCB) network. The 600 nm aerosol channel horizontal cross sections for legs CD, EF, and GH are shown in Figure 3 for pass 5 (1433 to 1547 EDT) on July 30, 1981. These grey-scale displays show the variation of mixed layer height over land and water during northerly flow, with well-developed sea breeze fronts near C and F. A line of clouds has formed along the Eastern Shore of Virginia near G, with general cumulus convection over land near H. The Exp. I lidar data set has been used to construct hourly plots of the mixed layer height over the lower Chesapeake Bay coastal area. These results indicate that airborne lidar systems can provide high spatial resolution measurements of the mixed layer over a complex environment like the lower Chesapeake Bay with detail comparable to that provided by models.<sup>8</sup>

An elevated stable layer that resulted from long-range transport over the ocean was encountered during flights on the morning of July 31, 1981. In situ and DIAL measurements resolved an optically thick layer over the entire region from approximately 800 to 1600 m MSL with O<sub>3</sub> levels from 80 to 100 ppb by volume. The air mass below 800 m MSL was relatively clean with surface O<sub>3</sub> levels at 40 ppb. Four Exp. I passes recorded the growth of the mixed layer over land as it rose up to and into the haze layer. Entrainment of aerosol and O<sub>3</sub> into a clean boundary layer was graphically illustrated, and the process of surface fumigation from an elevated (in height) haze layer was resolved. Under conditions of northeasterly flow, most surface fumigation occurs over and downwind of areas with high surface heat flux (H and Y). A preliminary trajectory analysis indicates that this elevated haze layer originated 1 day earlier in the Northeastern U.S. and left the coast somewhere between New Jersey and Rhode Island. The source of high O<sub>3</sub> during onshore northeasterly flow in the Norfolk, VA area has been somewhat controversial.<sup>9</sup> An airborne lidar can be used to resolve such controversy by providing information on the state and dynamics of the mixed layer under complex conditions such as a coastal environment.

#### References

1. Browell, E. V.; Carter, A. F.; Shipley, S. T.; Siviter, Jr., J. H.; Hall, W. M.; Allen, R. J.; Butler, C. J.; and Mayo, M. N., 1982: The NASA Langley Multipurpose Airborne DIAL System and Measurements of Ozone and Aerosol Profiles. To be submitted to *Applied Optics*.
2. Maddrea, Jr., G. L., and Bendura, R. J., 1981: *NASA TM 83170*.
3. Browell, E. V.; Shipley, S. T.; Carter, A. F.; Butler, C. F.; and Ismail, S., 1982: Airborne DIAL Measurements of Ozone, Aerosols, and Mixed Layer Heights during the 1980 PEPE/NEROS Summer Field Experiment (NASA TP in preparation).
4. Benkley, C. W. and Schulman, L. L., 1979: *J. Appl. Meteor.*, 18, p. 772.
5. Jickells, T.; Knap, A.; Church, T.; Galloway, J.; and Miller, J., 1982: Acid Rain on Bermuda. *Nature* (in press).
6. Greco, R. V., Editor, 1980: *NASA CR 3303*.
7. Browell, E. V.; Shipley, S. T.; Carter, A. F.; and Butler, C. F., 1982: Airborne Lidar Measurements of Ozone and Aerosol Profiles in the Troposphere and Lower Stratosphere. Eleventh International Laser Radar Conference, NASA CP-2228. (Paper C4 in this compilation.)
8. Segal, M.; McNider, R. T.; Pielke, R. A.; and McDougal, D. S., 1982: *Atmos. Environ.*, 16 (in press).
9. Salop, J. and Maier, G. F., 1978: *J. Air Poll. Control Assoc.*, 28, p. 1217; and Comments by Pasceri, R.; Predale, R.; and Peritt, A., 1979: *J. Air Poll. Control Assoc.*, 29, p. 639.

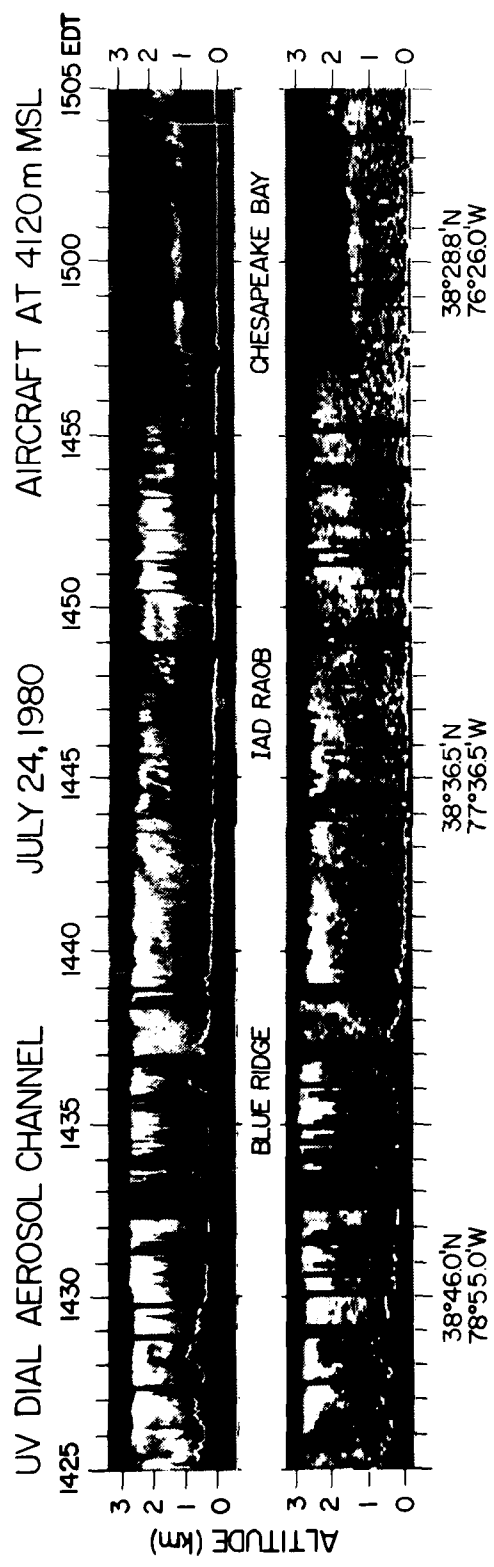
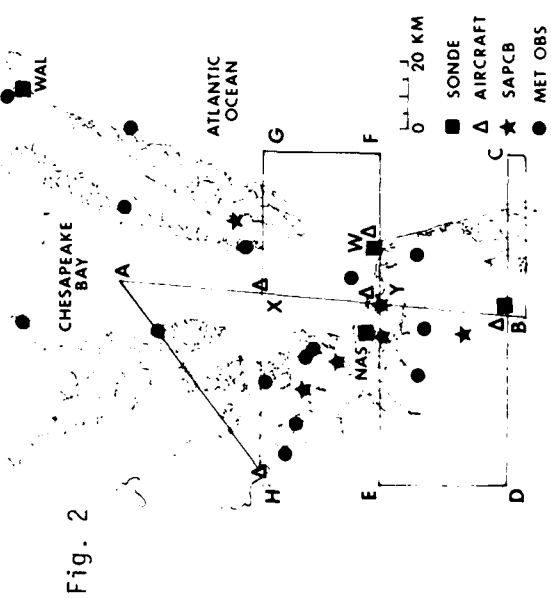


Fig. 1a (top) and 1b (bottom)



## THE ESTIMATION OF DIFFUSION PARAMETERS FROM LIDAR MEASUREMENTS

E. Asculai  
Nuclear Research Center/Negev  
Beer-Sheva, Israel

A. Cohen and M. Kleiman  
Department of Atmospheric Sciences  
The Hebrew University of Jerusalem  
Jerusalem, Israel

### ABSTRACT

Analyses of lidar returns can be used for the calculation of micrometeorological parameters.<sup>1</sup> From these measurements, the atmospheric diffusion parameters can also be calculated.

Here, we discuss the evaluation of these parameters directly from the lidar returns without deriving first the wind speed values. This is done by observing the temporal variation of eddy sizes of natural aerosol concentrations during unstable conditions.

Utilizing Giffords theories on smoke-plume photography, we were able to obtain the longitudinal diffusion parameters for the case of relative diffusion for diffusion times of 6-40 seconds. It is shown that the results of our calculations agree with the theory of relative diffusion. The comparison of the calculated constants with experimental values is presented and discussed.

### REFERENCE

1. Kunkel, K. E.; Eloranta, E.; and Weinman, J.: Remote Determination of Winds, Turbulence Spectra and Energy Dissipation Rates in the Boundary Layer From Lidar Measurements. *J. Atmos. Sci.*, v. 37, p. 978 (1980).

WIND MEASUREMENTS OF RADIAL AND TRANSVERSE COMPONENTS  
VISIBLE VERSUS INFRARED

L. Lading\*  
Case Western Reserve University  
School of Engineering  
Chemical Engineering Department  
(216) 368-4180

R.L. Schwiesow  
NOAA, Wave Propagation Laboratory  
Boulder, CO 80302

A. Skov Jensen  
Risø National Laboratory  
DK-4000 Roskilde, Denmark

$\text{CO}_2$ -laser anemometers as they are normally implemented will measure the velocity component along the optical axis [1] [2]. Systems based on visible light will normally measure the component perpendicular to the optical axis [3] [4]. Examples of measurements are given. Based on a concept introduced by Schwiesow [5] we show how the fringe and reference beam systems can be combined by using reference beam detection in a fringe type anemometer and doing the mixing electronically. An implementation is proposed.

Introducing a frequency offset and letting the angle between the beams go to zero gives the system of Schotland and Eberhard [6]. Alternatively, the radial velocity may be determined by a direct analysis of the return signal with a Fabry-Perot interferometer [7].

We have compared the theoretical minimum variances of the radial velocity estimates obtained with a reference beam system and with direct detection using a Fabry-Perot interferometer.

The uncertainties of the measured frequency shifts and thus the estimated velocities are ultimately limited by the number of photons detected during the residence time of a particle (or set of particles) in the measuring volume.

---

\* Permanent address:

Risø National Laboratory, DK-4000 Roskilde, Denmark

The variance of the estimated frequency shift  $\hat{\omega}_0$  is given by

$$\text{var} [\hat{\omega}_0] \approx \frac{1}{T\Delta\omega} \frac{(\Delta\omega)^2}{N_t^2}$$

for a reference beam system

and by

$$\text{var} [\hat{\omega}_0] \approx \frac{1}{T\Delta\omega} \frac{(\Delta\omega)^2}{N_t^2}$$

for direct detection with a F-P.

$T\Delta\omega$  is the averaging time bandwidth product for each channel of the analyzer,  $\Delta\omega$  is the frequency broadening caused by the finite residence time (or pulse length for a pulsed system. It is assumed that the analyzer bandwidth equals the signal bandwidth.  $N_t$  is the number of photons detected per residence time. Thus, everything else being equal direct detection is preferable if  $N_t < 1$ , and reference beam detection is best with  $N_t > 1$ .

These results are related to the effects of laser wavelength particularly around 0.5  $\mu\text{m}$  and 10.6  $\mu\text{m}$ . For a given laser power and transmitter/receiver aperture  $N_t$  is highest at 10.6  $\mu\text{m}$  for almost any reasonable particle size distribution, but the measuring volume is also proportional to  $\lambda^3$  and thus the spatial resolution decreases drastically with increasing wavelength. The considerations given so far are based on the assumption that a continuous signal is detected. For shorter ranges (i.e. below 100-300 m depending on particle size distribution) single burst detection is preferable: Measurements are only performed when the signal power exceeds a certain threshold.

Two examples of practical lay-outs and measurements for cw and burst detection methods are given.

## REFERENCES

1. A.J. Hughes, J.O'Shaughnessy, E.R. Pike, A. McPherson, C. Spavins, and T.H. Clifton, Long range anemometry using a  $\text{CO}_2$  laser. Opto-electronics 4, 379-384 (1972).
2. T.R. Lawrence, D.J. Wilson, C.E. Craven, I.P. Jones, R.M. Huffaker, and J.A.L. Thompson, A laser velocimeter for remote wind sensing. Rev. Sci. Instrum. 43, 512-518 (1972).
3. P.J. Bourke and C.G. Brown, Remote measurement of mean wind velocity and turbulence by laser anemometry. Opt. Laser Technol. 3, 23-25, (1971).
4. L. Lading, A. Skov Jensen, C. Fog, and H. Andersen, Time-of-flight laser anemometer for velocity measurements in the atmosphere. Appl. Opt. 17, 1486-1488 (1978).
5. R.L. Schwiesow, R.E. Cupp, M.J. Post, and R.F. Calfee, Coherent differential Doppler measurements of transverse velocity at a remote point. Appl. Opt. 16, 1145-1150 (1977), and R.L. Schwiesow, Differential Doppler velocity sensor. U.S. Patent #4, 168,906 (1979).
6. W.L. Eberhard and R.M. Schotland, Dual-frequency Doppler-lidar method of wind measurement. Appl. Opt. 19, 2967-2976 (1980).
7. G. Benedetti-Michalangeli, F. Congeduti, and G. Fiocco, Measurement of aerosol motion and wind velocity in the lower troposphere by Doppler optical radar. J. Atmos. Sci. 29, 906-910 (1972).

LIDAR OBSERVATIONS OF THE DAILY VARIATION OF  
BOUNDARY LAYER WINDS AND TURBULENCE

W.P. Hooper, E.W. Eloranta, R. Boers  
Department of Meteorology  
University of Wisconsin-Madison, WI 53706

R.L. Coulter  
Argonne National Laboratory  
Argonne, IL 60439

Lidar was used to measure wind and PBL depth for a 6 day period from 16 to 21 July 79 as part of CIRCE (the Central Illinois Rainfall Chemistry Experiment). The boundary layer depth was measured from RHI and RTI scans. These measurements compare favorably with the depths observed in Radiosonde temperature soundings. The model of Sroga et al. (1980) was used to measure the speed, direction, and RMS variation of the wind. During the data analysis, an extension to this model was discovered which reduces the random errors in the measurement of the wind component along the lidar beam.

An extensive data set with over a thousand individual wind measurements has been compiled from these lidar observations. During the daylight periods, lidar wind and depth measurements were normally made every 15 minutes. The lidar measurements of wind speed and direction are compared with radiosonde measurements and are found to be in close agreement.

This experiment includes a period of 32 hours with nearly continuous lidar measurements. These observations show wind and PBL depth evolution over a complete diurnal cycle. The nocturnal portion of these measurements, when compared with kytoon measurements, show that a scanning lidar system can measure nocturnal winds. The time-height cross sections of the nocturnal winds clearly show the transition from a daytime to a nighttime boundary layer.

Ref: J.T. Sroga, E.W. Eloranta, T. Barber, 1980: Lidar Measurements of Wind Velocity Profiles in the Boundary Layer. J. Appl. Meteor. 19, 598-605.

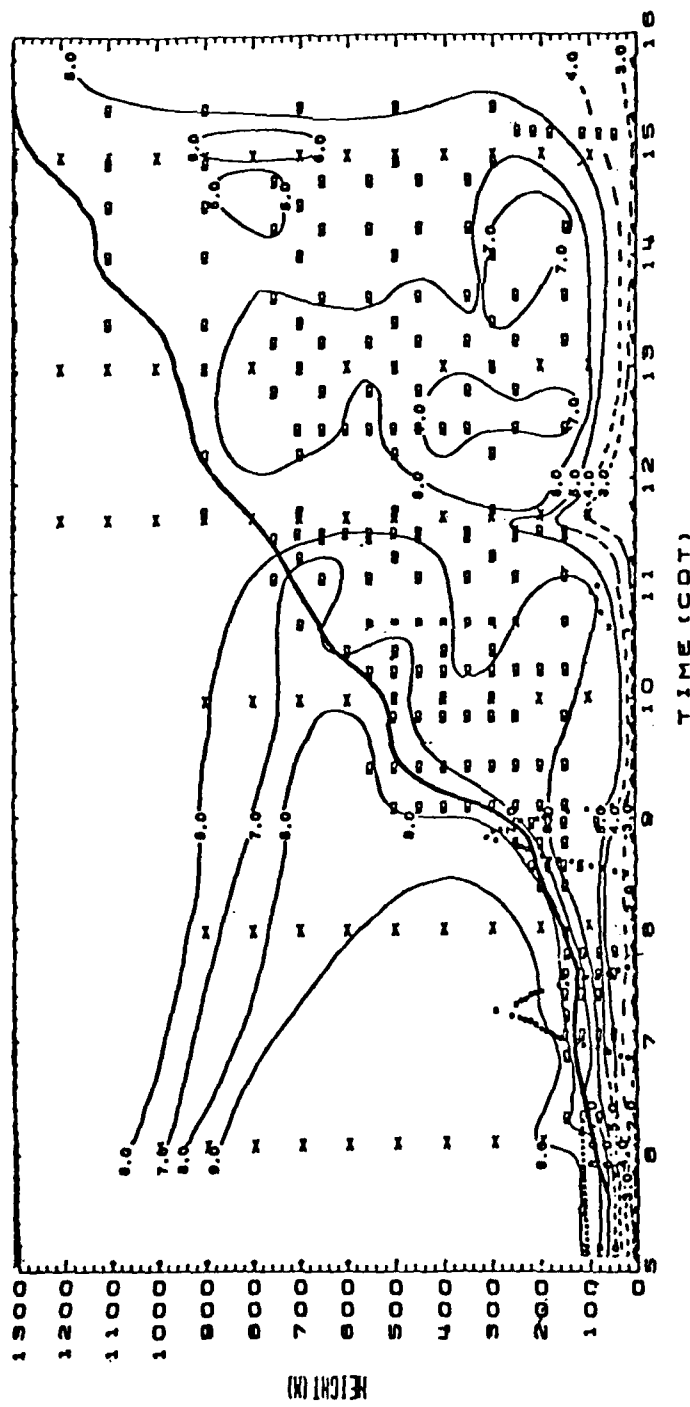


Fig. 1: Time-height cross section for the wind speed (m/s) from lidar (x), radiosonde (x), kytoon (•), and surface observations (x). The solid line represents the top of the boundary layer. The dotted line represents the top of the nocturnal haze layer. Time-height cross sections were also prepared for the direction and RMS variation of the wind. The lidar measurements were made by the University of Wisconsin lidar system. The radiosonde, kytoon, and surface measurements were provided by Argonne National Laboratory.

## Wind Comparison Measurements Between A Pulsed Doppler Lidar and Other Wind Sensors

R. Milton Huffaker and F. F. Hall, Jr.  
National Oceanic and Atmospheric Administration  
Environmental Research Laboratories  
Wave Propagation Laboratory  
Boulder, Colorado 80303

The NOAA-WPL pulsed CO<sub>2</sub> Doppler lidar system is being utilized in several atmospheric research and engineering applications such as boundary layer winds, severe storm development, wind shear monitoring, and measurement of winds aloft and along the glide slope for the Space Shuttle (STS-2) landing. An effort is in progress within the Wave Propagation Laboratory to compare the lidar wind measurements with other wind measuring sensors such as rawinsondes, microwave radar, instrumented towers, and instrumented aircraft, over as wide a range of meteorological conditions as possible.

The characteristics of the pulsed CO<sub>2</sub> Doppler lidar are as follows:

CO <sub>2</sub> TEA Transmitter	-	80 mJ
Telescope Aperture	-	.27 m
Spatial Resolution	-	.5 km
Pulse Repetition Frequency	-	10 Hz
Doppler Velocity Algorithm	-	Pulse Pair

The lidar operates in a velocity azimuth display (VAD) scan in which the laser beam is rotated around a vertical axis. The zenith angle can be varied from 15° to 90° to allow a more varied scan coverage and to match, as closely as possible, the sensitive measuring volume of the other wind sensors.

Results obtained to date indicate reasonable agreement between the lidar, an instrumented tower, Jimspheres, and rawinsondes.

MEASUREMENT OF WINDS, BACKSCATTER, AND RETURN SIGNAL  
PROPERTIES USING PULSED COHERENT LIDAR

R.M. Hardesty

NOAA/ERL/Wave Propagation Laboratory  
Boulder, Colorado 80303

Since spring 1981, the Infrared Doppler Lidar program area of NOAA's Wave Propagation Laboratory has operated a pulsed coherent CO<sub>2</sub> lidar in a variety of remote sensing applications. Designed to demonstrate the utility of coherent lidar technology as an effective tool for remote profiling of winds in the clear air, the system has also been used to measure aerosol backscatter coefficients aloft, examine statistical properties of the aerosol and hard target backscattered signals, and determine the effect of atmospheric turbulence on system performance.

The lidar system, which is entirely contained in a semitrailer, can be easily transported to a remote site and powered from standard utility lines or a portable generator. Operating in a hybrid configuration, the grating-tuned transmitter produces single longitudinal mode pulses with 80-100 mJ of energy contained in the 2  $\mu$ s effective pulse duration. Approximately 75 dB of isolation between transmitter and receiver is provided by a Brewster-angle transmit-receive plate and a 28 cm diameter, f/6, off-axis parabolic telescope. During operation the output of the signal detector is demodulated to produce complex (in-phase and quadrature) signals at baseband. These signals are digitized at a 10 MHz rate during every pulse, moved into a minicomputer for processing, and written on magnetic tape.

By directing the transmit beam out through a roof-mounted scanner, we can examine a full 360° of azimuth and from 0° to 90° of elevation angle. The 2  $\mu$ s transmit pulse length results in a minimum range resolution of approximately 300 m. System calibration indicates that usable signals for velocity and intensity measurements can be measured at 2 km range when volume backscatter coefficient levels are as low as 10<sup>-11</sup> m<sup>-1</sup> sr<sup>-1</sup>. Maximum horizontal range can be as much as 22 km.

#### Backscattered Signal Properties

Coherent lidar returns from the atmosphere undergo random fluctuations in irradiance due to speckle, which results from relative phase changes in the signals scattered by the individual aerosol particles. Our measurements indicate that the probability density function (pdf) of irradiance in the low turbulence case is exponentially distributed, consistent with a Rayleigh phasor model. As turbulence increases along the propagation path, the pdf is altered by the additional scintillations, with normalized variance increasing and mean signal level decreasing.

The characteristic time scale of the speckle-caused fluctuations is an important parameter in determining the interval required to accurately average the mean irradiance. This parameter is a function of both the transmit signal bandwidth as well as atmospheric properties such as velocity turbulence and shear. Analysis of aerosol-backscattered lidar irradiance data shows that the atmospheric effects often doubled the rate of signal fluctuation relative to returns from hard targets. This improves spectral zeroth-moment estimation, but can degrade frequency (first moment) measurements when signal-to-noise ratio (SNR) is marginal.

#### Backscatter Coefficient Measurement

Since a scarcity of information exists on the variability of the lidar volume backscattering coefficient ( $\beta$ ) in the troposphere and lower stratosphere, we have measured  $\beta$  on a daily basis throughout the year of system operation. Backscatter coefficient is calculated by measuring the SNR in the returns from the vertically pointing beam and inverting the lidar equation to solve for  $\beta$ . We typically averaged 500 to 2000 pulses to reduce the speckle-caused fluctuations in the return.

Our measurements show a marked difference in the  $\beta$  values measured over Boulder during summer and winter. During the summer we often measured  $\beta$  values of  $10^{-9} \text{ m}^{-1} \text{ sr}^{-1}$  at heights coincident with or near the tropopause. In many cases we were also able to observe returns from volcanic dust clouds in the stratosphere. During winter however, backscatter appears to fall off much more sharply with altitude, implying substantially reduced turbidity in the mid to upper troposphere. Analysis of returns from summer months indicates that the distribution of  $\beta$  values very closely approximates a lognormal distribution.

#### Wind Measurements

We determine the radial velocity of the wind by measuring the mean Doppler shift in the aerosol-backscattered signal as a function of range. Actual calculation of the mean frequency shift is done digitally using either a complex covariance or Fast Fourier Transform (FFT) algorithm. These provide good single-pulse frequency estimates at wideband SNR's as low as -0 dB (Fig. 1), enabling wind measurements to be made in the boundary layer at  $\beta$  values down to  $10^{-11} \text{ m}^{-1} \text{ sr}^{-1}$ . Figure 2 is a plot of the average FFT of an aerosol return taken while the system was vertically pointing, showing the presence of backscattered signal from heights to 10 km. We have also evaluated the effectiveness of other algorithms, such as maximum entropy and poly-pulse pair, as mean frequency estimators.

To determine the three-dimensional wind vector from the radial measurements, we employ a VAD (velocity-azimuth-display) concept, where the beam is conically scanned in azimuth around a vertical axis. Under typical conditions a plot of radial velocity versus azimuth approximates a sinusoid plus noise, with the noise resulting from measurement uncertainties as well as turbulence. We process VAD scans by finding the

sinusoid which has the best least-squares fit to the data. Average horizontal wind speed over the volume is proportional to the amplitude of the fitted sine wave, wind direction is proportional to its phase, and vertical velocity is proportional to the offset of the sinusoid around zero.

The system capability for remote wind speed measurement has been demonstrated in a number of applications. During November 1981 we provided NASA with comparison wind measurements in support of the STS-2 landing at Edwards Air Force Base. The lidar wind measurements showed close agreements with those measured using site-launched radiosondes and jimspheres. During spring and summer 1981, the lidar system participated in experimental efforts studying upslope winds, ice crystals in cirrus clouds, as well as the Joint Airport Weather Study (JAWS) with NCAR and NASA.

### Wind Measurement Error

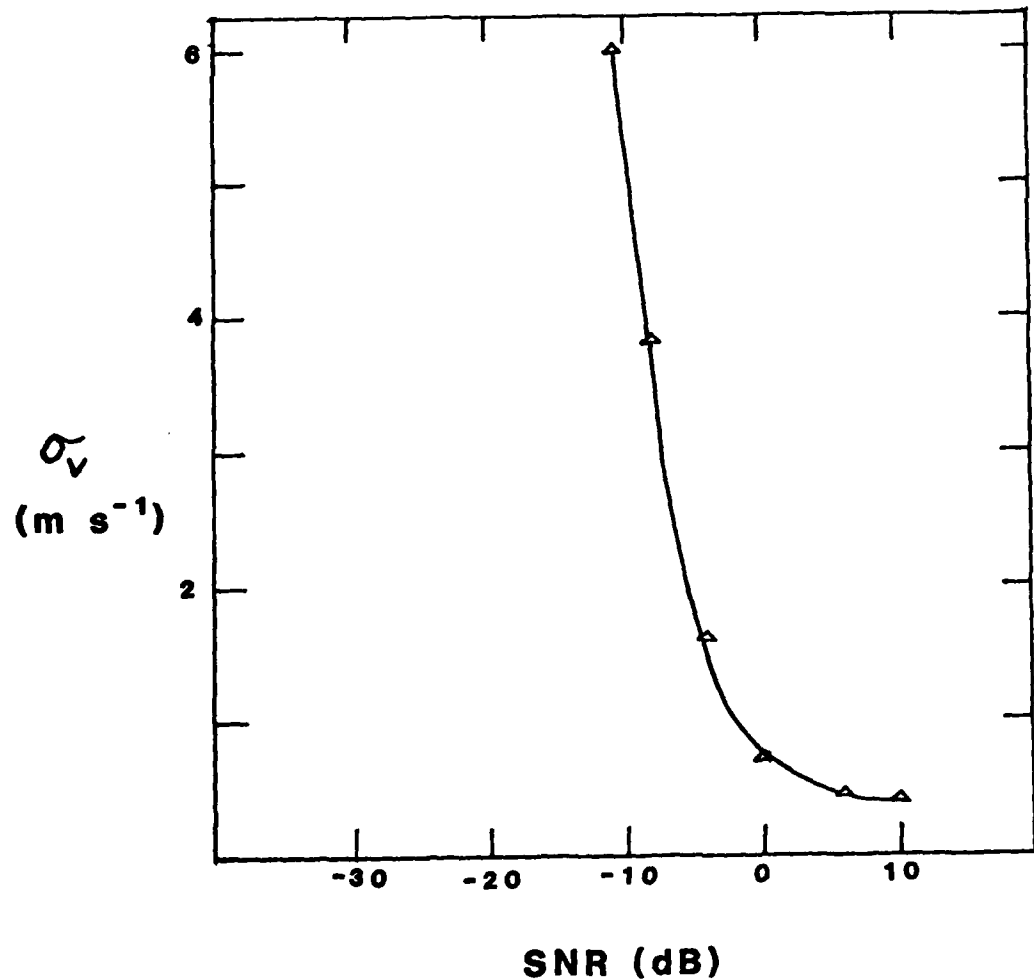


Fig. 1. Standard deviation of single pulse complex-covariance velocity measurements versus SNR for NOAA lidar.

### Aerosol Spectra

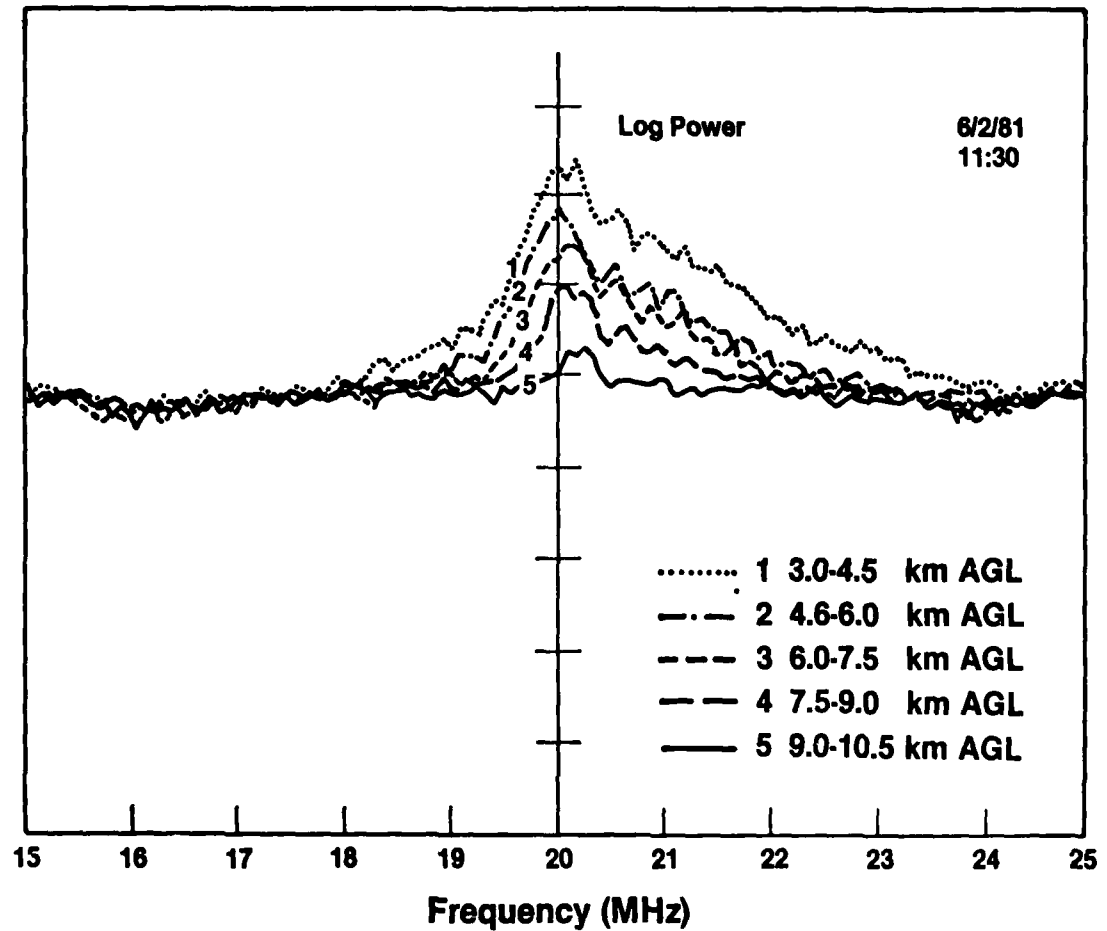


Fig. 2. Averaged spectra of aerosol-backscattered returns showing decrease in SNR with range. Note presence of signal from 10.5 km AGL, illustrating the system's capability to measure winds in the upper troposphere.

# A DIRECT LASER DOPPLER ANEMOMETER FOR REMOTE WIND SENSING

F. Köpp

German Aerospace Research Establishment (DFVLR)  
Institute of Optoelectronics  
D-8031 Wessling  
Federal Republic of Germany

The DFVLR direct Laser Doppler Anemometer (LDA) is an active system using a CO<sub>2</sub>-cw-laser for radiation source. Its output power of 5 W is focussed by a 30 cm diameter telescope into the region under investigation. Some of the radiation is backscattered by small aerosol particles drifting with wind speed through the sensing volume. The backscattered radiation is collected by the telescope and detected by coherent techniques. In that way, the Doppler shift can be extracted which directly determines the line of sight component of the wind vector.

## SYSTEM PARAMETERS OF THE LASER DOPPLER ANEMOMETER

LASER: CO <sub>2</sub> , continuous wave			
output energy	5	W	
short term stability (50 $\mu$ sec)	better 3	kHz	
LOCAL OSCILLATOR:			
energy	appr. 1	mW	
TELESCOPE:			
aperture	50	cm	
focal length	90	cm	
DETECTOR: Pb Sn Te			
sensitive area	0.25	mm <sup>2</sup>	
detectivity in cm (Hz) <sup>1/2</sup> W <sup>-1</sup>	5.7	$\cdot$ 10 <sup>10</sup>	
SYSTEM ACCURACY:			
SAW bandwidth	30	kHz	
velocity resolution	0.2	m/s	
accuracy of velocity	better 1	m/s	
accuracy of direction	appr. 5	deg	

Since the development of LDA techniques is pretty well advanced, we specified the basic system and ordered it from industry. Its properties are summarized in the table.

Two examples of wind measurements are given in Fig. 1. The measurements were carried out horizontally close to the surface, using the basic system. Focussed to 100 m range the frequency spectrum shows a sharp peak at 550 kHz, corresponding to a wind speed of 2.9 m/s. At 1000 m range a wider peak shape can be observed. That is caused by the increased length of the sensing volume (factor 100) which covers regions of different wind speeds.

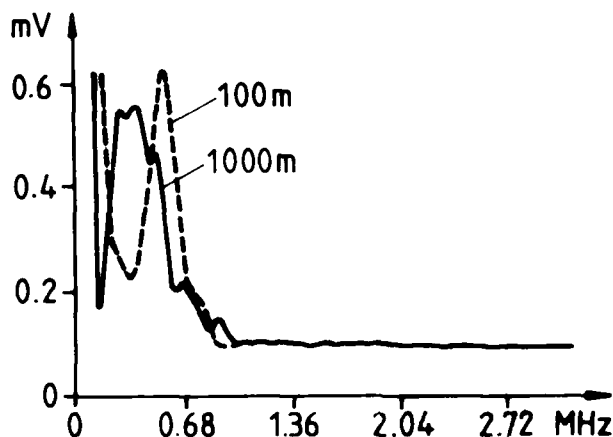


Figure 1: LDA wind measurements along a horizontal path.

As mentioned before, the basic system yields the line of sight component of the wind vector in the sensing volume. The range variation is carried out by shifting the secondary lense of the telescope automatically. All other wind components can be constructed by a certain number of line of sight components. Therefore, the basic system had to be extended by a scanning device. In Fig. 2 a schematic drawing of the scanner is shown. In front of the telescope a fixed mirror points the beam vertically upward to the second mirror which can be rotated  $360^\circ$  around the vertical axis. In that way, the full azimuth range is scanned. The third mirror can be rotated around the horizontal axis from  $0^\circ$  to  $90^\circ$  which corresponds to an elevation scan from the horizon to the zenith. Both scans together allow the system to measure at any point of the hemisphere up to more than 1 km around the LDA. The steering unit of the scanning device is very fast; position changes of  $60^\circ$  can be carried out within 1 s. Since the whole system is controlled by a processor, certain scan procedures can be performed automatically.

From the numerous possible applications of a direct LDA system we are mainly interested in profiles of wind vectors in the boundary layer and

in the propagation of wake turbulences near airfields. For the first application the velocity azimuth display (VAD) scan technique is used, whereas for the second the fingerscan is suitable. Experimental results will be presented.

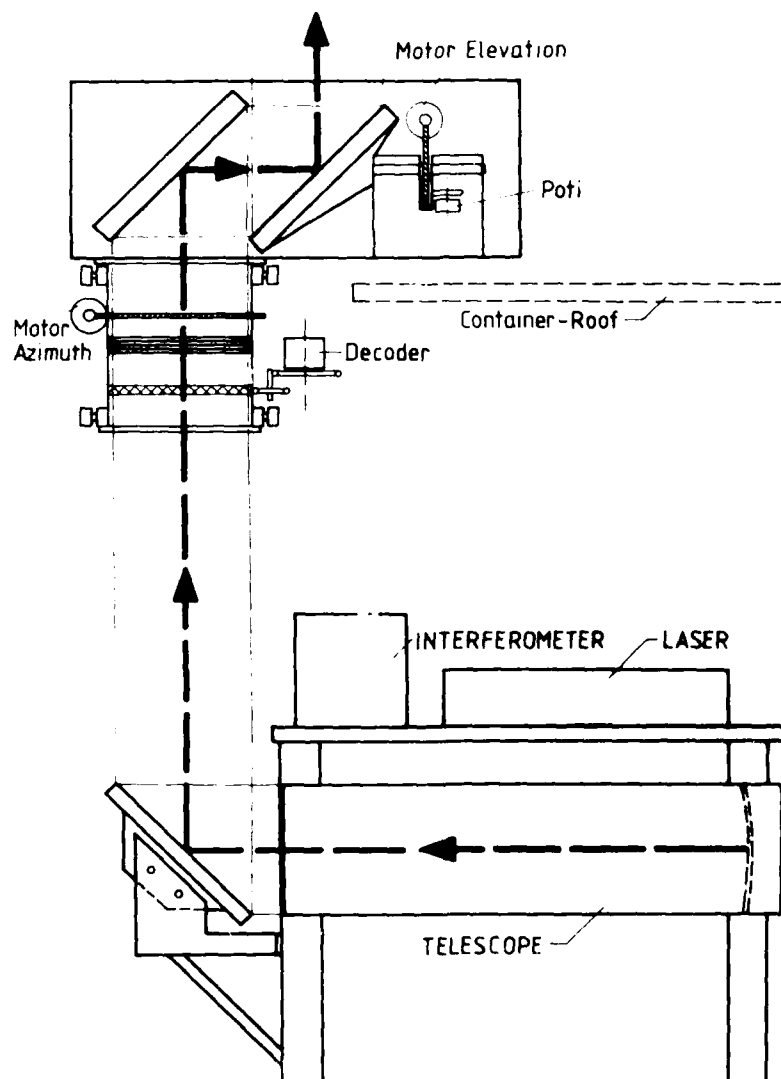


Figure 2: Scanning device for the Laser Doppler Anemometer.

AD-A116 298 NATIONAL AERONAUTICS AND SPACE ADMINISTRATION HAMPTO--ETC F/8 20/5  
ELEVENTH INTERNATIONAL LASER RADAR CONFERENCE, WISCONSIN UNIVER--ETC(U)  
JUN 82

UNCLASSIFIED NASA-L-15380

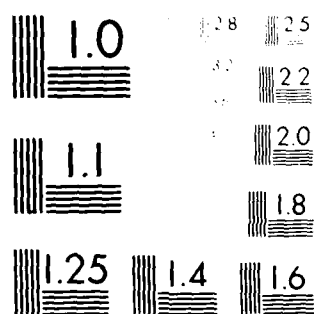
NASA-CP-2228

NL

3 of 3

40A  
16294

END  
DATE FILMED  
10782  
DTIC



McROBBY RESOLUTION TEST CHART

MEASUREMENT OF WIND USING AN AIRBORNE DOPPLER LIDAR SYSTEM  
(ADLS) - RESULTS OF 1981 CV-990 FLIGHT EXPERIMENTS

George H. Fichtl, James W. Bilbro, Daniel Fitzjarrald  
National Aeronautics and Space Administration  
George C. Marshall Space Flight Center  
Marshall Space Flight Center, AL 35812

Michael Krause  
Raytheon Company  
Electro-Optics Department  
Advanced Development Laboratories  
Sudbury, MA 01776

#### INTRODUCTION

This paper reports on a series of research flights with the ADLS installed on the NASA/Ames Convair 990, Galileo II, during the summer of 1981. These flights resulted in extensive data sets on a variety of atmospheric phenomena: boundary layer flows, gust fronts, cloud entrainment, pollution transport, and terrain effects. The test program consisted of some 21 flights ranging in duration from three to five hours for a total of eighty hours. The flights were conducted in California in the Central Valley and near the San Gorgonio Pass, in Oklahoma at the National Severe Storms Laboratory, and in Montana during the Cooperative Convective Precipitation Experiment (CCPE). A number of comparisons were obtained in the course of the flights involving towers, ground based radars, and instrumented aircraft.

#### ADLS DESCRIPTION

The ADLS is a coherent pulsed CO<sub>2</sub> Doppler lidar which operates at wavelength of 10.6  $\mu\text{m}$  and pulse length of 300 m. The system measures Doppler frequency shift line-of-sight lidar radiation backscattered from atmospheric aerosols with size of 1 to 10  $\mu\text{m}$  diameter. In this way estimates of line-of-sight component of wind velocity vector are inferred at 300 m intervals out to a range of 5 to 20 km depending on aerosol concentration. The lidar pulse prior to entering the atmosphere passes through two germanium wedges which, by means of refraction, cause a deviation in pulse direction. By rotating the two wedges, the pulse direction is scanned in a horizontal plane 20° forward and 20° aft of the telescope line of sight, which is normal to the aircraft centerline. Thus by firing the laser successively in the forward and aft directions in the horizontal, at intervals of aircraft travel distance of 50 to 150 m, fields of forward and aft line-of-sight wind velocity components are obtained which in turn can be used to infer a field of horizontal wind vectors with Nyquist wavelength of approximately 600 m. A 10 km x 10 km wind field map is produced in approximately 80 sec and is displayed in real time onboard the aircraft. The line-of-sight wind component is extracted from the backscattered radiation by employing poly-pulse-pair processing (Lee and Lee, 1980). Additional details about the ADLS are provided by Bilbro and Vaughan (1978) and Bilbro et al. (1982).

## EXPERIMENT DESCRIPTIONS

### Oklahoma Experiments

Four research flights were conducted in Oklahoma with a total of eleven hours devoted to a variety of research targets. Good data sets were obtained in the cloud-free afternoon boundary layer, in the prestorm boundary layer, at cloud base near a large storm with gust front and inflow regions, and circumnavigating one of the ground based Doppler radars at a constant range. All of the flights were made within the range of the NSSL Doppler radar based at Norman, Oklahoma, and much of the time within the area that yields dual-Doppler data when the unit, located at Cimarron, Oklahoma, was operational. During the periods without clouds, the Doppler radars and the lidar were sampling the same regions producing comparative measurements of the clear air motion. When clouds were present, the radar-measured cloud velocities are complementary to the clear air returns of the lidar obtained outside the cloud and below cloud base. Comparison of the results of these two remote measurement systems that respond to different phenomena on different space scales should be helpful in further understanding convective response to atmospheric forcing.

### Montana Experiments

Five research flights totaling 25 hours were flown in Montana in conjunction with the CCOPE. Excellent data sets of atmospheric boundary layer flows, gust fronts, and turret clouds were acquired over, and on the edge of, the CCOPE data acquisition network which consisted of Doppler radar, surface, and rawinsonde networks, and various aircraft.

Convective planetary boundary layer (PBL) experiments were flown on July 16 and 20. Chaff was released in the region of the experiments to insure that Doppler radar data would be obtained. In addition, the NCAR Queen Air 2 and Sabreliner acquired gust probe measurements by flying approximately 4 km from, parallel to, and at the same pressure altitude as the CV-990. The CV-990 flew both straight line and race track patterns at a series of altitudes between 1.2 and 4.3 km MSL. Two patterns were flown at approximately 150 m above the "top" of the boundary layer as determined by the NCAR aircraft sounding (one at the beginning of each experiment and one at the end). The remaining patterns were flown in PBL. Figures 1 and 2 provide samples of the real-time data acquired on July 16. They were taken at 3.1 and 2.3 km MSL, above and within the PBL, respectively. Above the PBL, the flow was from  $250^{\circ}$  at 5 m/s, while below, the flow direction and velocity were highly variable. These data are consistent with regard to the gross character of the flow as measured by the NCAR Queen Air.

An example of the flow field associated with a gust front is shown in Figure 3. This example is one of many acquired on July 23 from a low-level circumnavigation of a thunderstorm that occurred in the north-east section of the CCOPE network. This was an intense storm and consequently received extensive aircraft and radar coverage.

### California Experiments

Two research flights were conducted in the California Central Valley. The objective of the flights was to study the extended sea breeze circulation that is forced by the presence of the cool Pacific Ocean and strong heating of the interior valley. The valley is situated between the coastal mountains and the Sierra Nevada, and inflow is limited to a few gaps in the coastal mountains because of the strong coastal inversion. The aircraft flight track was around the perimeter of the valley near the top of the boundary layer with the lidar pointing out toward the mountains and coastal passes. In this manner, the lidar system was effective in measuring details of the flow around inflow passes, in clarifying the way that air is conducted up along the heated bordering slopes to cause outflow. Two research flights in and near the San Gorgonio Pass region of southern California investigated details of the flow that is the principal way that marine air from the Los Angeles Basin moves to the low desert region.

### REFERENCES

Bilbro, James W., and William W. Vaughan, 1978: Wind Field Measurement in the Nonprecipitous Regions Surrounding Severe Storms by an Airborne Pulsed Doppler Lidar System. Bull. Am. Meteorol. Soc., 59, 1095-1100.

Bilbro, James W., G. H. Fichtl, D. Fitzjarrald, M. Krause, 1982: Airborne Doppler Lidar Wind Field Measurements. Submitted to Bull. Am. Meteorol. Soc.

Lee, R. W., and K. A. Lee, 1980: A Poly-Pulse-Pair Signal Processor for Coherent Doppler Lidar. Topical meeting on Coherent Laser Radar for Atmospheric Sensing, Aspen, CO, July 1980.

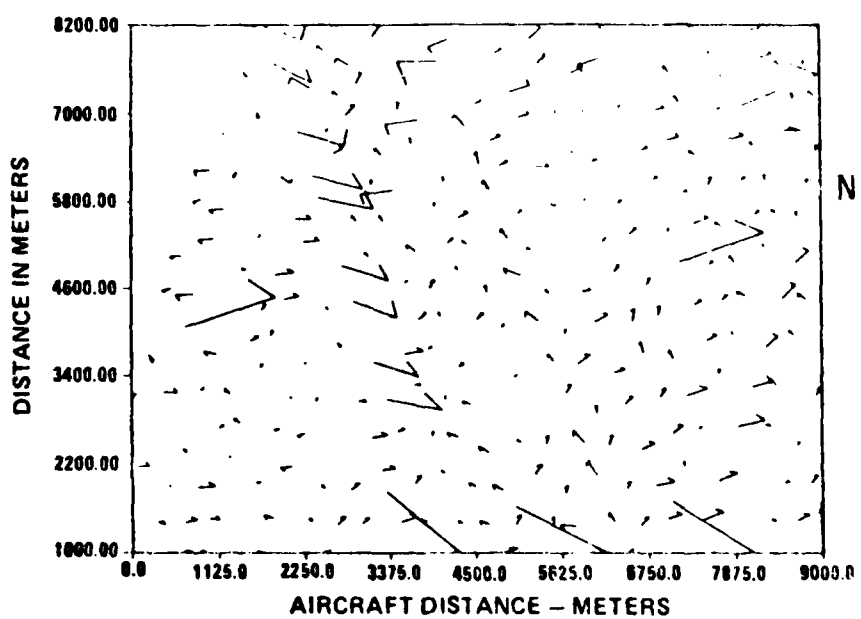


Figure 1. CCOPE flow field at 3.1 km MSL measured July 16, 1981. Vector length proportional to wind speed. 1 cm long vectors are "wild" points due to laser "moding."

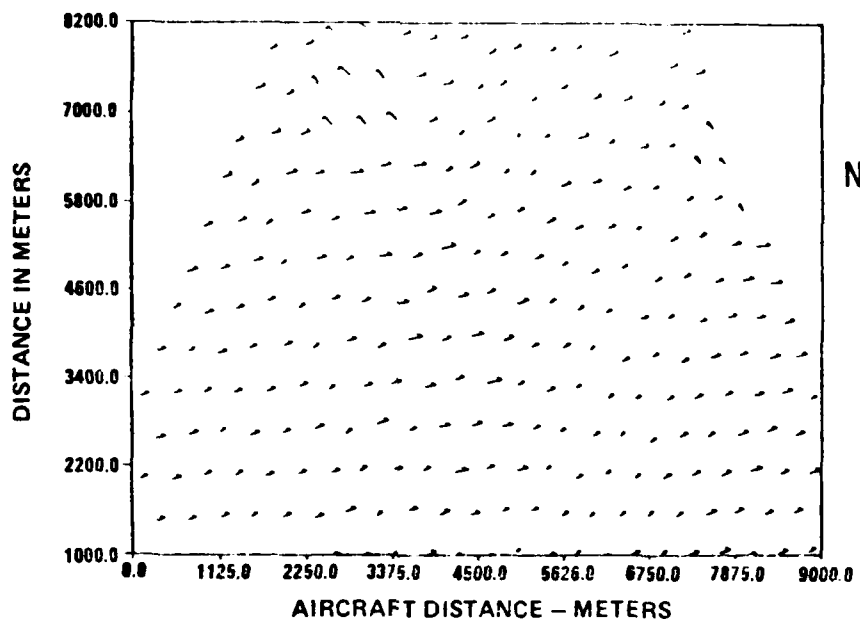


Figure 2. CCOPE flow field at 2.3 km MSL measured July 16, 1981.

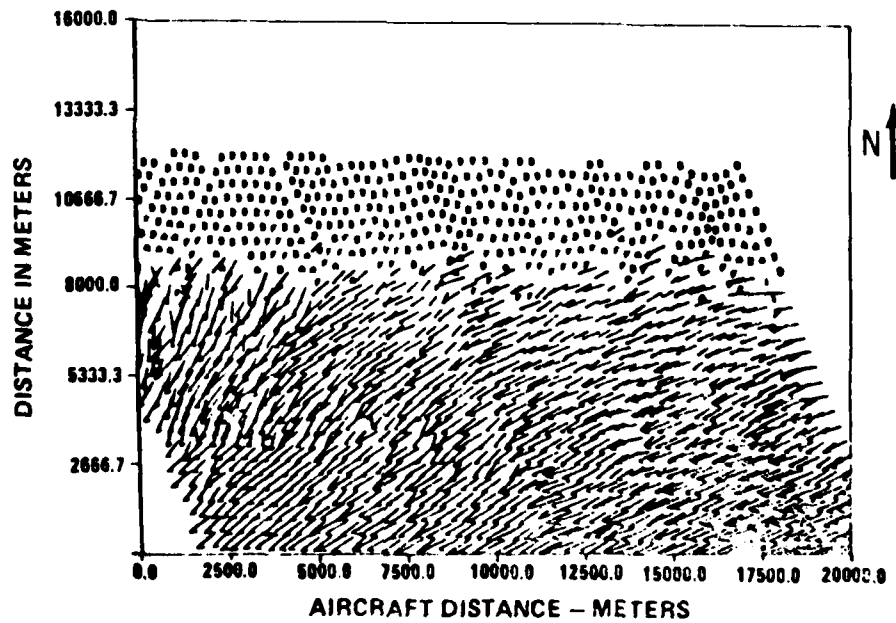


Figure 3. Example of gust front acquired at CCOPE July 23, 1981, at 1.2 km MSL.

WINDSAT/ATMOSPHERIC MULTI-USER  
LIDAR COMPATIBILITY

John S. Osmundson, Lockheed Palo Alto Research Laboratory,  
3251 Hanover Street, Palo Alto, CA 94304; R. Milton Huffaker,  
NOAA Wave Propagation Laboratory (WPL), 3100 Marine Street,  
Boulder, CO 80303; Michael McQuirk, Perkin-Elmer Corp.,  
Optical Operations Division, Main Avenue, Norwalk, CT 06856

Abstract

Recently several space-based lidar systems have been proposed. These systems include a coherent lidar, WINDSAT, proposed by the National Oceanic and Atmospheric Administration (NOAA) to measure global winds and incoherent lidars proposed by NASA Langley Research Center and the Air Force Geophysics Laboratory (AFGL) to perform atmospheric research. This paper presents results of a study<sup>1</sup> performed by Lockheed, Perkin-Elmer and NOAA to determine the feasibility of performing both incoherent and coherent missions with a single space-based lidar system. Cost efficient ways of combining incoherent and coherent applications using the same space-based lidar have been developed.

NOAA-WPL began a program to develop a pulsed CO<sub>2</sub> coherent lidar system to measure atmospheric wind several years ago. NOAA studies established the feasibility of a satellite-borne global wind measuring lidar<sup>2,3</sup> and defined the hardware for a Shuttle-borne wind measuring lidar system known as WINDSAT<sup>4</sup>. Meteorologists feel that accurate global wind measurements made on a timely basis, as could be achieved with spaceborne lidars, would allow a significant improvement in weather forecasting capability. Improved forecasting could result in large savings to many segments of the population.

NASA Langley has extensively investigated use of a Shuttle-based lidar system for atmospheric research. A NASA Atmospheric Lidar Working Group established scientific objectives and requirements for 26 atmospheric lidar experiments<sup>5</sup>, many of which address important air pollution problems. A NASA Langley study also established the feasibility of an evolutionary Shuttle-based lidar multi-user instrument to perform the 26 experiments<sup>6</sup>.

AFGL has also been active in studying techniques for determining the density of the neutral atmosphere using space-based laser radars. An AFGL study<sup>7</sup> showed the feasibility of determining atmospheric density using a lidar system very similar to that proposed by NASA Langley.

### WINDSAT Baseline

The WINDSAT design served as a baseline concept. In the WINDSAT lidar operation, a laser pulse is directed through a transmitting telescope toward the earth's atmosphere. A small fraction of the incident pulse is sent back as signal into the transceiver due to backscatter from atmospheric aerosols. Since the aerosols are moving with the wind, the signal is Doppler shifted from the transmitted frequency. The signal is heterodyne detected and the frequency shift measured, thereby giving the wind component along the transceiver line of sight.

Scanning the transmitted beam is required to cover the entire earth and to make measurements of the same locale from two different look angles. This converts line-of-sight (radial) wind components into orthogonal components parallel to the earth's surface, thereby obtaining wind direction.

The baseline WINDSAT instrument has a 1.25-m diameter, f0.95 telescope, diffraction limited with a 0.2 linear obscuration. The telescope is continuously scanned conically so that its optical axis rotates at an angle of 60° about nadir. Coherent detection requires accurate coalignment of the transmit and receive, beams and to accomplish this while scanning, requires a lag angle compensator (LAC) to bring the return signal beam back on axis. Lag angle compensation is achieved with two agile mirrors, one of which performs a first-order linear correction to the return signal, and the second which performs a second-order correction. The second mirror also corrects for laser beam wander and Shuttle perturbations. A rotating mirror is used as a transmit/receive (T/R) switch.

The WINDSAT laser is an injection-controlled unstable-resonator CO<sub>2</sub> TEA laser operating at 9.11 μm. Laser output is specified to be 10 J/pulse, 8 pulses per second, and 5 μs nominal pulse duration.

Signal and data processing provide onboard radial wind estimation in one range bin for every pulse. All the lidar data are compressed, to a 1-Mbit rate, then buffered and transmitted to ground through TDRSS for ground processing. Command and control functions are performed by two 16-bit microprocessors and two random-access memories.

### Incoherent Lidar Requirements

An incoherent lidar sends a laser pulse towards the ground at an appropriate atomic or molecular wavelength. The signal is back scattered energy from the pulse. The NASA and AFGL experiments cover a range of techniques. The fundamental requirements are the ability to cover a wide wavelength range with a variety of laser sources and detectors,

the ability to cover a field of view ranging from 0.1 to 6.0 milliradians, optical quality such that the geometric blur is less than 1/4 of the selected field of view, high system transmission at all operating wavelengths, coalignment among various transmitters and receivers, and 2-50 milliradian pointing knowledge. Switching speed for the transmit/receive switch is an issue for some of the later experiments where high-altitude measurements are desired.

The NASA multi-user telescope is non-scanning and nadir viewing, and has a 1.25-m-diameter receiving aperture. Laser sources are transmitted through small separate optics passively aligned to the receiving telescope.

The major impacts on the WINDSAT system derive from the requirements for nadir viewing and flexibility to accommodate multiple sources, detectors, and fields of view.

#### Combined WINDSAT/Atmospheric Multi-User Lidar Concepts

WINDSAT in principle is capable of making some atmospheric measurements without changes. NOAA analyzed how well the 26 NASA experiments could be performed at the WINDSAT CO<sub>2</sub> wavelength, with the WINDSAT system "as is", or with minor modifications. NOAA found that four of the atmospheric experiments plus two WINDSAT type experiments can be performed. No changes of onboard hardware are required, but minor changes in ground processing of data are implied. The remaining NASA experiments are ruled out because of laser incompatibility.

Modified WINDSAT concepts were developed which meet all of the NOAA, NASA and AFGL objectives. There were two general trades to be considered when modifying WINDSAT. First was the trade between leaving the WINDSAT telescope as configured and performing a Shuttle roll to achieve nadir viewing, or reconstructing the WINDSAT telescope to a nadir viewing device. The second trade involved a choice between common or separate T/R optics.

Four concepts encompassing all of the trade options were developed: 1) the first concept uses the WINDSAT telescope in an "as is" configuration, that is in a 60° orientation to nadir with additional sources mounted on the back of the telescope; 2) the second concept uses an "as is" telescope with added sources and detectors mounted in the lidar structure and sharing the telescope using a transmit/receive (T/R) switch; 3) the third concept reorients the telescope into a nadir viewing device, mounts the lasers separately and mounts the focal planes beneath the telescope using a selection switch; 4) the fourth concept also is a reoriented nadir-viewing telescope with lasers and detectors mounted as in concept two. The first concept is minimum cost but can perform only a few atmospheric experiments on each flight. The first

two concepts allow WINDSAT and atmospheric experiments to be performed on a time-shared basis on the same flight. The last two concepts are the most expensive, but best suited to multimission use; however, WINDSAT missions would have to be performed on separate, earlier flights before the optics are reconfigured.

This work was performed under NOAA Wave Propagation Laboratory Contract NA79 RAC-00127. Support was also provided by the NASA Langley Research Center and AFGL. The contributions of Kenneth Crumblly of NASA Langley and Donald Bedo of AFGL to this study are greatly appreciated.

#### References

1. "Atmospheric Multi-User Lidar - Global Wind Measuring Satellite System (WINDSAT) Compatibility Study," LMSC-D812354, 15 February 1982.
2. "Feasibility Study of a Satellite-Borne Lidar Global Wind Monitoring System," R.M. Huffaker, editor, NOAA Technical Memorandum ERL WPL-37, Sept. 1978.
3. "Feasibility Study of a Satellite-Borne Lidar Global Wind Monitoring System," Part II, R.M. Huffaker, et al., NOAA Technical Memorandum ERL-WPL-63, Aug. 1980.
4. "Global Wind Measuring Satellite System," LMSC-D767868, April, 1981.
5. "Shuttle Atmospheric Lidar Research Program," Final Report of Atmospheric Lidar Working Group, NASA SP-433, 1979.
6. "Atmospheric Lidar Multi-User Instrument System Definition Study," NASA Contractor Report 3303 (NAS1-15476), August, 1980.
7. "Design Study of a Laser Radar System for Spaceflight Application," AFGL-TR-79-0264, Dec., 1979.

## CONICAL LIDAR SCANNING FROM LEO - THE EFFECTS OF MESO $\beta$ AND CONVECTIVE SCALE ATMOSPHERIC PHENOMENA

G. D. Emmitt  
Visiting Scientist  
Marshall Space Flight Center  
Huntsville, AL 35812

### INTRODUCTION

The desirability of global direct wind measurements is without debate. The required accuracy and spatial/temporal resolution are, however, still to be established through model sensitivity evaluations and simulation studies. Depending upon the interests of the scientists involved, the simulations are likely to emphasize particular scales of atmospheric phenomena. This presentation will focus upon the effects of meso  $\beta$  ( $<100$  km) and convective ( $\approx 1$  km) scale features on the retrieval of wind estimates from a conically scanning lidar in a low earth orbit (LEO).

The overall objective was to develop a set of computer simulations of atmospheric conditions that will impact the performance of a satellite based Doppler lidar wind measuring system. Four of the most important atmospheric factors are 1) the three-dimensional turbulent wind field, 2) aerosol size and concentration distributions in space and time, 3) distribution of absorption gases ( $\text{CO}_2$  &  $\text{H}_2\text{O}$ ) and 4) distribution of clouds in both the horizontal and vertical.

### DESCRIPTION OF THE MODEL

The present model consists of four main modules - three-dimensional wind field, cloud field, shot selection and lidar wind estimation. The wind field is specified for any point in space by a set of continuous functions which include turbulent terms. Meso  $\beta$  wind field features are approximated with gaussian deviations from a mean vertically sheared profile. One example of a north-south cross section of a "jet" feature used to examine scanning and wind estimation techniques is shown in Figure 1. Lidar winds calculated from several shots into such a wind field are compared with the layer average winds printed on the right side of the figure.

A single cloud, random distribution of clouds or an organized array of clouds can be superimposed on the wind field. Approximate vertical velocity fields associated with individual convective cells are included.

A conical scan from a satellite at 800 km has been assumed. Figure 2 illustrates a shot distribution into a  $300 \times 300 \times 1$  km box located 600 km to the left side of a satellite ground track. This particular volume was proposed as the evaluation standard (Huffaker, 1978). However, the current model can evaluate the shots into any size box, located any distance less than 1200 km from the satellite path.

The following orbit/lidar factors have been used as inputs to the current model:

orbit height = 800 km  
satellite speed = 7.5 km/sec  
conical scan revolution rate = 15 sec/revolution  
shot frequency = 8/sec  
shot elevation from vertical = 56°  
lidar pulse length = 2 km.

With these inputs, a maximum of 32 lidar shots are possible within the reference volume. When clouds are introduced the number of shots reaching the ground are reduced. The representativeness of the wind estimate under these conditions is addressed in this research.

The two-dimensional lidar winds are calculated with the assumption that the average vertical speeds over a 300x300 km area will be very small (<10 cm/s) compared to the horizontal speeds. The validity of this assumption is being tested with the model since the number of shots (32 or less) is not great and therefore a few shots into small regions with large (>1 m/s) vertical speeds could contribute significantly to the mean wind field estimate.

With 32 shots from 32 different directions into 32 different parts of the 300x300 km area, there are 468 pairs of equations that can be solved for the horizontal wind components. With the spread contained in the information from each pulse and the presence of a horizontal wind gradient, there are 468 different U and V components calculated. Taking the unweighted mean of these calculated speeds can result in large errors and standard deviations in the estimates. Besides weighting each shot by the quality of the Doppler signal, additional weighting on the basis of shot location and azimuth was investigated.

## RESULTS

Three principal questions have been addressed so far: 1) What weighting function(s) minimizes the standard deviation in the wind estimate? 2) How many shots are needed to obtain  $\pm 1$  m/s,  $\pm 10^\circ$  accuracies? 3) What effect do lidar sample scale ( $\sim 100$  m) vertical motions have on the wind estimate?

Study of the individual solutions of the shot pairs revealed that two weighting functions may reduce the error and standard deviation in the speed estimate. One weight is a function of the horizontal distance ( $D$ ) between the shot information:

$$\text{WEIGHT 1} = 420/(420+9*D).$$

The second and more effective weighting function is based upon the angle (RDIF) between two shots being used:

$$\text{WEIGHT 2} = \text{ABS}(\text{COS}(1.57-\text{RDIF})).$$

The effects of the weighting factors were studied by using all 32 shots into the wind field of Figure 1. The results of comparing the u estimate

(unweighted, with weight 1 only, and with weight 2 only) with the actual layer averaged wind speed are shown below.

Height (km)	Unweighted 1		Weight 1		Weight 2		Reference Field	
	UT	SDU	UT	SDU	UT	SDU	RW	SDRW
.56	1.57	.99	1.57	95	1.42	.15	1.52	.22
1.68	2.12	1.80	2.11	1.73	1.86	.27	2.00	.40
2.80	2.92	3.10	2.90	2.98	2.49	.46	2.68	.68
3.91	4.04	5.02	4.01	4.83	3.37	.75	3.64	1.09
5.03	5.54	7.70	5.48	7.40	4.55	1.14	4.91	1.65
6.15	7.42	11.16	7.32	10.73	6.04	1.64	6.49	2.36
7.27	9.62	15.32	9.47	14.71	7.81	2.24	8.33	3.20
8.39	12.00	19.95	11.79	19.14	9.76	2.90	10.31	4.11
9.51	14.32	24.54	14.05	23.52	11.70	3.56	12.26	4.97
10.62	16.38	28.79	16.04	27.57	13.47	4.16	13.93	5.77

It is clear that weighting by the angle between two shots not only reduces the variance in the estimate but also reduces the error in the means. The question of the number of shots needed was approached by randomly selecting a certain number of shots from the maximum total of 32. The difference between the real wind layer average and the lidar wind estimate was then plotted against number of shots used (Figure 3). From this one test case, it seems that at least 6-8 shots are needed to get within 20% of the real wind; 15-20 shots to be within 10% of the real wind, and 25-32 shots to be within 5%. All these calculations were done using the weighting factors mentioned previously and no vertical velocities.

The effect of small scale vertical motions on the large scale ( $\approx 300$  km) horizontal wind estimate was studied by introducing either random buoyancy plumes ( $w = +5$  m/s) that are likely under strong surface heating situations or random clear air downdraft regions ( $w = -1$  m/s) near cloud boundaries. For the clear air situation, the vertical velocities introduced variance that was of nearly equal magnitude as that in the horizontal wind field. For cloudy regions the effect was similar due to the reduced number of shots used in the estimate. The greater problem of the cloud situation may be the biasing of lidar sampling towards the clear air region between storm cells where the horizontal winds are strongly affected by storm dynamics. More simulations to put bounds on this problem are planned.

In addition to expanding on the above investigations, the intention is to introduce actual case study data (e.g. prefrontal, frontal and post-frontal situations) into the simulation model and look at the correlated effects of aerosol, cloud and wind distributions.

#### REFERENCE

Huffaker, R. M. (editor), 1978: Feasibility Study of Satellite Borne Lidar Global Wind Monitoring System. NOAA Tech Memo ERL-WPL 37. pp 276.

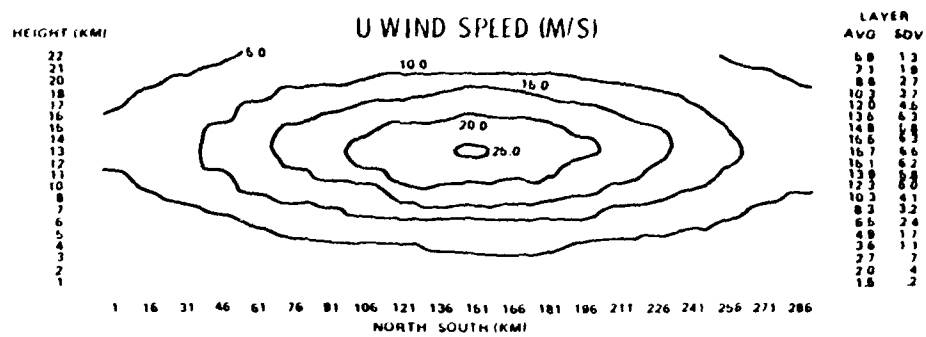


Figure 1. N-S x Section of a Simulation Wind Field

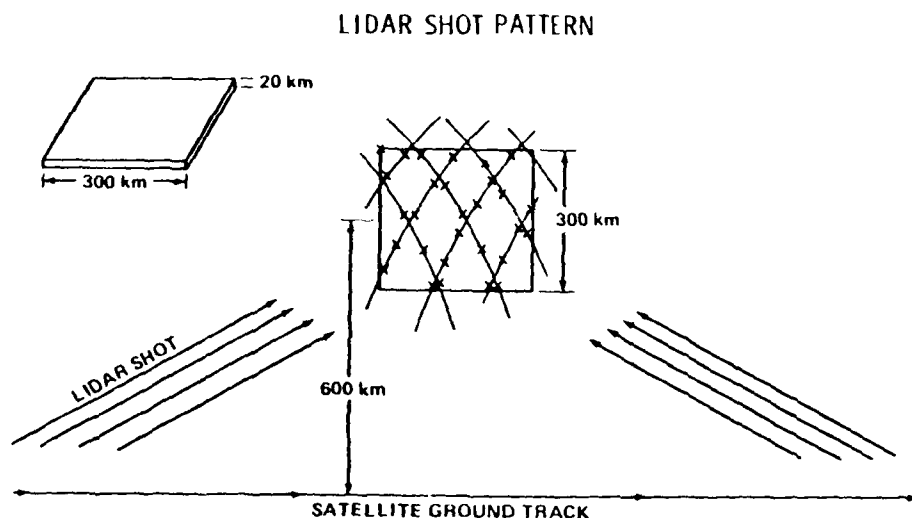


Figure 2. Shot Pattern from 800 km Orbit

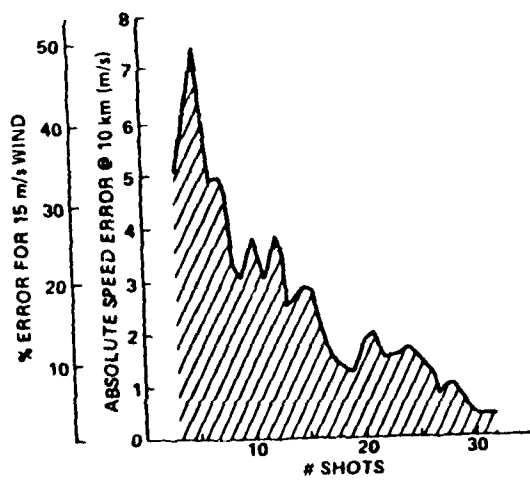


Figure 3. Shots vs. Wind Estimate Accuracy

PARTICULATE EXTINCTION AND BACKSCATTER PROPERTIES  
DETERMINED FROM LIDAR MEASUREMENTS

J. A. Reagan, C. L. Goldsmith,  
A. J. Anderson, and J. P. Garcia  
University of Arizona  
Tucson, Arizona 85721

As reported previously (Spinhirne et al., 1980), vertical profiles of particulate extinction may be determined from multiple zenith angle lidar measurements, i.e., the slant path technique. This measurement approach has been employed on a semiroutine basis over the past three years in an investigation of the optical properties of atmospheric particulates near Tucson. Preliminary results of this work were given at the last lidar conference (Reagan et al., 1980). This paper will update the previously reported results regarding observed particulate extinction profiles, mixing layer heights, mixing layer particulate optical depths, and mixing layer particulate extinction-to-backscatter ratios. In addition, results will also be presented from an intercomparative experiment which included lidar slant path measurements, tethered balloon measurements of particulate size distributions, and solar radiometer measurements of particulate spectral optical depth. These data are being analyzed to assess the extent to which lidar observed patterns in particulate extinction and backscatter may be related to specific forms of the particulate size distribution and certain ranges of the particulate refractive index.

Acknowledgments: This work has been supported by ARO Grant DAAG-29-78-G-0195 and NSF Grant ATM-8012908.

REFERENCES

Spinhirne, J. D., J. A. Reagan, and B. M. Herman, 1980: Vertical distribution of aerosol extinction cross section and inference of aerosol imaginary index in the troposphere by lidar technique. J. Appl. Meteor., 19, pp. 426-438.

Reagan, J. A., T. V. Bruhns, D. D'Souza, and G. P. Box, 1980: Extinction Properties of Tropospheric Aerosols over Tucson, Arizona as Determined by Lidar Measurements. 10th International Laser Radar Conference, Conf. Abstract, p. 3, Amer. Meteor. Soc., October 6-9, 1980, Silver Spring, MD.

## ELEVATION-SCANNING LIDAR MEASUREMENTS OF HAZE EXTINCTION AND THEIR RELATIONSHIP TO ALBEDO CHANGES

Philip B. Russell and John M. Livingston  
Atmospheric Science Center, SRI International, Menlo Park, CA 94025, USA

During the 1979 field program of the Sutro Tower Aerosol and Radiation Study (Russell et al., 1979), SRI International used a vertically scanning lidar to measure haze extinction profiles while tower-mounted radiometers measured albedo changes caused by the haze. The experimental setup is shown in Fig. 1.

The lidar measurements used the slant-path or zenith-scanning technique to derive extinction profiles. This technique has been previously used by Hamilton (1969), Reagan et al. (1977), and Spinharne et al. (1980), whose measurements were confined to twilight or nighttime. We believe this is the first application of the technique in fully sunlit conditions. The technique assumes that certain atmospheric layers (typically the clear or "clean" layers) be horizontally homogeneous. It yields the optical depths of intervening layers, which may be somewhat inhomogeneous in the horizontal, and it converts these optical depths to range-resolved extinction by assuming that the particulate backscatter-to-extinction ratio is independent of range within any turbid layers.

In the measurements reported here, two-way optical depths  $2\tau(z)$  were obtained by two solution techniques, one of which was to fit a regression line to the equation

$$\ln[S(z,\epsilon)/S(z,90^\circ)] = 2\tau(z)[m(\epsilon)-1] \quad (1)$$

where  $S(z,\epsilon)$  is the range-corrected, transmit-energy-normalized lidar signal backscattered from height  $z$  for a shot fired at elevation angle  $\epsilon$ , and  $m(\epsilon)$  is the slant-path airmass.

$$m(\epsilon) = \csc \epsilon \quad (2)$$

Fig. 2 shows signal ratios and best-fit optical depths obtained for two times of day and four different closely-spaced heights. Each of these heights is in relatively clean air above the haze boundary layer. The Rayleigh scattering gas optical depth ( $\lambda = 0.69 \mu\text{m}$ ) across all four heights is about 0.003, which is much less than the measurement errors in total (gas plus particle) optical depth shown. As expected, the height variation of measured total optical depth is not significant compared to the measurement errors. Hence, we have computed an error-weighted, height-averaged value as the best estimate of optical depth at the mean height, 1.7

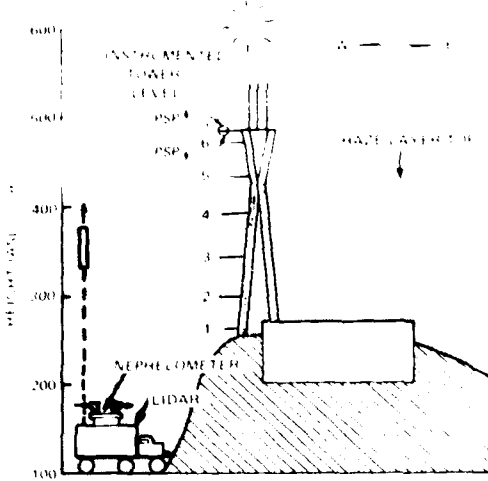
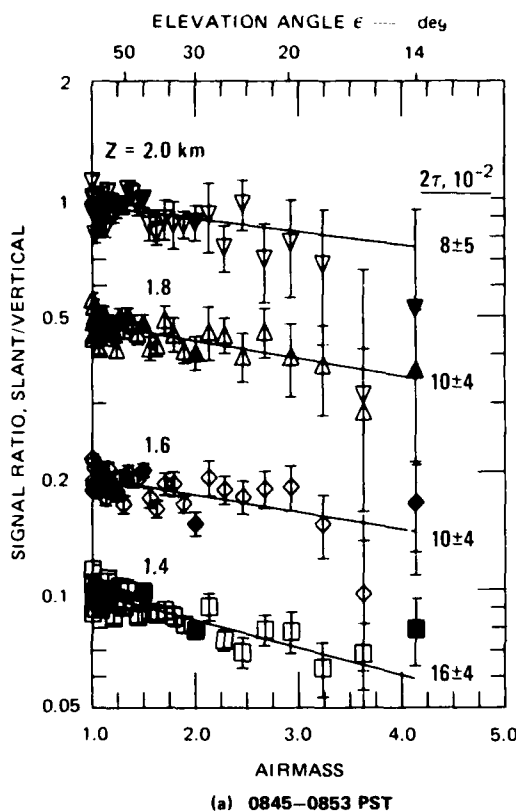


FIGURE 1 ARRANGEMENT OF INSTRUMENTS IN THE 1979 FIELD PROGRAM, MT. SUTRO TOWER AEROSOL AND RADIATION STUDY. PSP stands for precision spectral pyranometer.

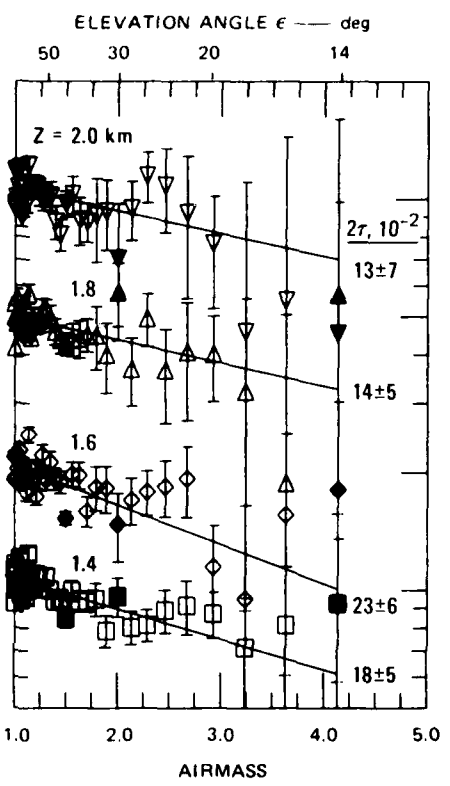
km. The results are

$$2\tau(1.7 \text{ km}) = \begin{cases} 0.12 \pm 0.02, & 0845-0853 \text{ PST} \\ 0.17 \pm 0.03, & 1402-1409 \text{ PST.} \end{cases} \quad (3)$$

$$(4)$$



(a) 0845-0853 PST



(b) 1402-1409 PST

FIGURE 2 SLANT/VERTICAL SIGNAL RATIOS AND BEST-FIT LINES. For clarity, ratios at height 1.8, 1.6, and 1.4 km have been multiplied by 0.5, 0.2, and 0.1, respectively.

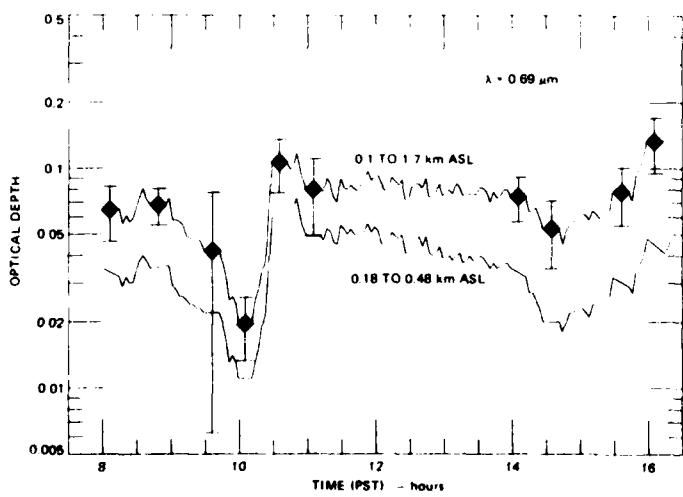


FIGURE 3

LIDAR-DERIVED PARTICULATE OPTICAL DEPTHS ( $\lambda = 0.69 \mu\text{m}$ ),  
14 NOVEMBER 1979, MT.  
SUTRO, SAN FRANCISCO  
Symbols give values measured by slant-path scans at indicated times.  
Rayleigh scattering gas optical depth  $\tau_g = 0.008$ , has been subtracted from total to obtain values shown. Curves give values derived from column backscatter measurements using backscatter-to-extinction ratios temporally interpolated between scan times.

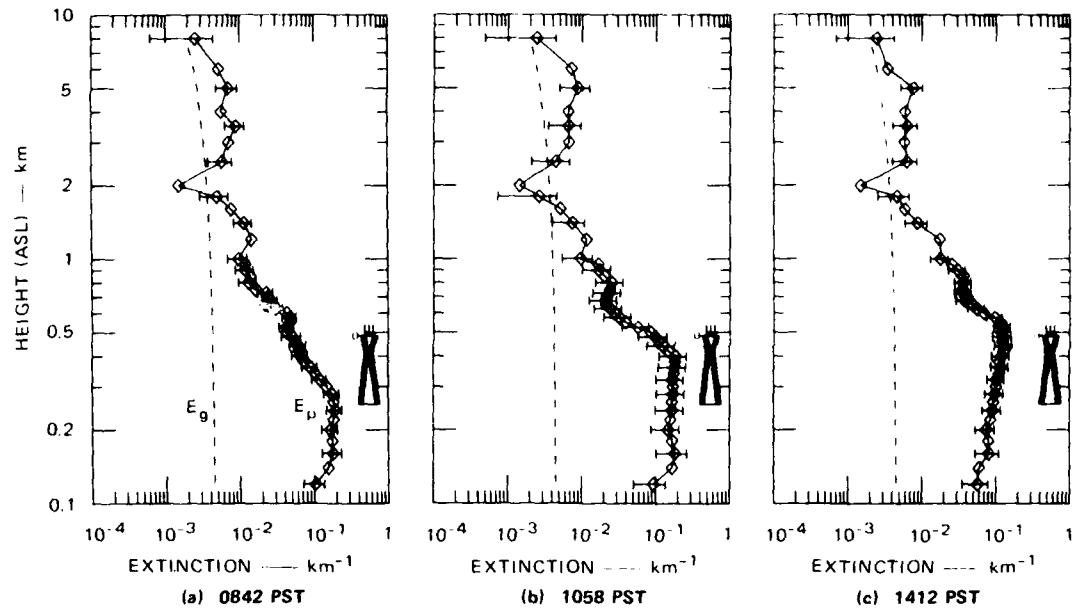


FIGURE 4 PARTICLE EXTINCTION PROFILES,  $E_p$  ( $\lambda = 0.69 \mu\text{m}$ ), MEASURED BY LIDAR AT THREE EXAMPLE TIMES, 14 NOVEMBER 1979, MT. SUTRO, SAN FRANCISCO.

The gas extinction profile  $E_g$  (dashed line), is derived from the morning radiosonde sounding at Oakland, 21 km east of the tower.

Optical depths were also computed by averaging results obtained from slant-to-vertical signal ratios for individual angles. With few exceptions, the best-fit [e.g. (3), (4)] and angle-average results agreed to within their respective errors. Fig. 3 shows optical depths obtained at ten times throughout the day by averaging the best-fit and angle-average results. The error bars ( $1\sigma$ ) reflect both the uncertainties of each method and the difference between their results.

Fig. 4 shows vertical extinction profiles obtained for three times of day, including the two times of Fig. 2. These profiles were obtained by combining boundary-layer optical depths with vertically resolved backscatter signals, assuming that the particle backscatter-to-extinction ratio is independent of height.

Vertically resolved extinction profiles, such as those shown in Fig. 4, can be integrated to obtain the optical depth of the layer between the ground and 0.48 km ASL, where our tower pyranometers were located. (See Figs. 1 and 4.) The time variation of the resulting optical depth is shown in Fig. 3.

The tower pyranometers were used to measure the albedo (integrated over all solar wavelengths) of the system consisting of the surface and the atmospheric layer below 0.48 km ASL. This albedo was measured both on the day of the lidar optical depth measurements (14 November 1979) and on two surrounding very clean days, when the atmosphere below 0.48 km ASL had negligible effect on measured albedos. Hence, the clean-day measurements yielded the surface albedo. The results for the surface ( $A_0$ ) and haze-plus-surface ( $A'_{MFAS}$ ) albedos are shown in Fig. 5.

It is of interest to inquire whether the lidar-measured haze optical depths are consistent with the haze-induced albedo changes shown in Fig. 5. Unfortunately, making this check requires information on the wavelength dependence of particle optical depth and on particle

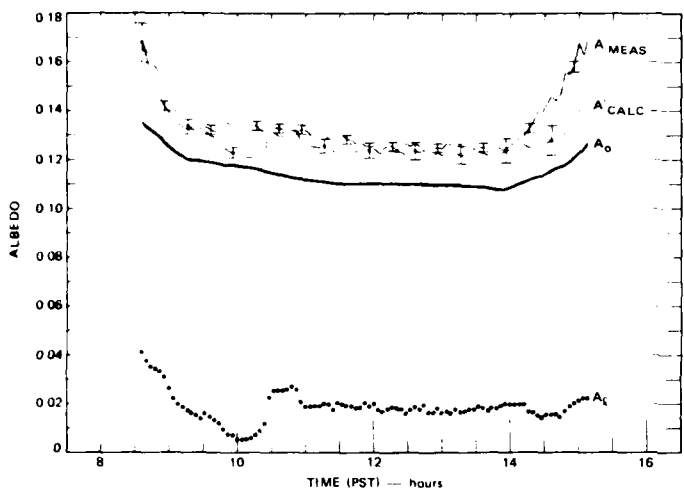


FIGURE 5

MEASURED AND CALCULATED ALBEDOS FOR MT. SUTRO, 14 NOVEMBER 1979.

$A_1$  = albedo of particle layer below tower pyranometers,  
 $A_0$  = surface albedo,  $A'$  = surface-plus-layer albedo. Error bars on  $A'$  CALC include uncertainty in optical depth (Fig. 3), but not in size distribution and refractive index.

hemispheric upscattering coefficient and single scattering albedo (also functions of wavelength), none of which were measured in this experiment. Nevertheless, it is useful to assume reasonable aerosol properties for the purpose of the check. We have assumed a power-law size distribution,  $dn/dr \sim r^{-4.5}$ , and a refractive index  $m = 1.50 - 0i$ . These assumptions are consistent with the optical depth wavelength dependence measured in a 1975 aerosol incident at Mt. Sutro, and they yield a backscatter-to-extinction ratio ( $0.03 \text{ sr}^{-1}$  at  $\lambda = 0.69 \mu\text{m}$ ) consistent with the values and uncertainties obtained in this study (0.01 to  $0.05 \text{ sr}^{-1}$ , with  $1\sigma$  uncertainties of about  $0.02 \text{ sr}^{-1}$ ). Using these assumptions and the measured optical depths in a two-stream radiative transfer calculation yields the aerosol layer ( $A_1$ ) and system ( $A'$  CALC) albedos shown in Fig. 5. In general,  $A'$  MEAS and  $A'$  CALC agree to within their respective uncertainties.

A more extensive manuscript (Russell and Livingston, 1982) is available from the authors.

*Acknowledgment.* This research was supported by a grant from the National Science Foundation, Atmospheric Research Section.

#### REFERENCES

Hamilton, P.M., 1969: Lidar measurement of backscatter and attenuation of atmospheric aerosol. *Atmos. Environ.*, 3, 221-223.

Reagan, J.A., J.D. Spinharne, D.M. Byrne, D.W. Thomson, R.G. DePena, and Y. Mamane, 1977: Atmospheric particulate properties inferred from lidar and solar radiometer observations compared with simultaneous *in situ* aircraft measurements: a case study. *J. Appl. Meteorol.*, 16, 911-928.

Russell, P.B., J.M. Livingston, and E.E. Uthe, 1979: Aerosol-induced albedo change: measurement and modeling of an incident. *J. Atmos. Sci.*, 36, 1587-1608.

Russell, P.B., and J.M. Livingston, 1982: Slant-lidar aerosol extinction measurements and their relationship to measured and calculated albedo changes. Submitted to *J. Appl. Meteorol.*

Spinharne, J.D., J.A. Reagan, and B.M. Herman, 1980: Vertical distribution of aerosol extinction cross section and inference of aerosol imaginary index in the troposphere by lidar technique. *J. Appl. Meteorol.*, 19, 426-438.

REMOTE SENSING OF ATMOSPHERIC PARTICULATE PROPERTIES BY  
JOINT LIDAR-RADIOMETER OBSERVATIONS

Qiu Jin-huan, Wang Hong-ai, Sun Jin-nui, Zhang Bei-ying, Xia Qi-lin, Hao Nan-jun, Zhang Jin-ding, Bao Ling-ming and Zhao Yan-zeng

Institute of Atmospheric Physics, Academia Sinica,  
Beijing, China

Theoretical and observational works have shown that the simultaneous solar extinction-forward scattering measurement scheme can offer more information about column aerosol size distribution than that obtained from a single extinction measurement owing to the fact that extinction is sensitive to small particles while forward scattering is sensitive to large particles. Based on the above consideration we have carried out a joint lidar-radiometer experiment since early 1982 in the north suburb of Beijing, from which the extinction coefficient profiles and column aerosol size distributions are reversed. The primary results show that:

- 1) The vertical distributions of extinction coefficient (or aerosol concentration profiles) are strongly influenced by the near ground inversion. From morning till afternoon with the disappearing of inversion the upward transport of aerosol particles results in the decrease of extinction coefficient over 1 Km.
- 2) The column aerosol size distributions are noticeably changing when the vertical mixing takes place. The number of larger particles tends to increase and that of the smaller particles tends to decrease. The former is an effect of vertical transport and the latter is probably due to the horizontal dispersion by the wind or the decrease of humidity.

## LIDAR VISIBILITY MEASUREMENTS

J.L. GAUMET

Direction de la Météorologie - EERM  
78470 MAGNY LES HAMEAUX - FRANCE

### SUMMARY

Lidar measurements of visibility in heavy fogs have been performed for the last four years by the EERM lidar group. This paper reports some results of an experimental programme conducted to design a visibility measuring device for airports. The visual ranges are measured over horizontal and slant paths by applying to the lidar signal either the slope or the transmittance method, or both.

### METHODS OF MEASUREMENTS

The visibility is determined using the classical Koschmieder's relationship :

$$V = - \log \xi / \bar{\alpha}$$

Where  $\xi$  is the contrast threshold of the eye and  $\bar{\alpha}$  is the mean extinction coefficient derived from the lidar equation.

In order to obtain this coefficient, two methods of analysis have been used : the slope and the transmittance methods.

The slope method (Collis et al. (1)) gives good results when it is applied over locally homogeneous fog regions (2). However, under patchy fog conditions, it can no longer be applied.

This is the reason why the transmittance method, proposed by Mc Manus et al. (3) and Kohl (4), has been investigated. The transmittance  $T(0, R)$  between the origine and a distance  $R$  is derived from the lidar equation without any hypothesis on the medium. These authors have described receiver systems where the range squared variation is optically eliminated.

Results obtained by another way of considering this method are presented, without any particular receiving system ; the lidar being set up in a classical coaxial configuration. The analysis consists in computing the transmittance over a range which may be located either partially before, or completely after the beam convergence point  $R_0$ . In the first case, the beam convergence factor  $f(r)$  has been determined with a very good accuracy. The transmittance between two distances  $R_1$  and  $R_2$  is given by :

$$T^2(R_1, R_2) = \frac{\int_{R_1}^{R_2} Pr^2 dr}{\int_{R_1}^{\infty} Pr^2 / f(r) dr}$$

where  $R_1 < R_o < R_2$

As the extinction coefficient is deduced from a measurement between two distances, the visibility is not the true visual range for a pilot on the glide path. This "local visibility" is used to get comparative measurements with transmissometers more easily.

#### THE LIDAR SYSTEM

The main parameters of the lidar system are summarized in table 1. As can be seen, the laser power is high and the telescope diameter is large. This is due to the fact that the transmitter and receiver were also used for Raman scattering.

<u>Transmitter</u>		
laser	ruby, 694 nm	
energy	5 joules	
repetition rate	1 ppm	
beam divergence	1 mrad	
<u>Receiver</u>		
Telescope field of view	4,5 mrad	
diameter	40 cm	
<u>Processing/display</u>		
transient recorder	Biomatique 8100	
computer facilities	Intel MDS-800	

TABLE 1

#### EXPERIMENTAL RESULTS

The slope method has been applied in various fog conditions. The validity of measurements has been checked by lidar-transmissometer comparisons over close paths. Figure 1 shows results obtained when the laser line of sight and the transmissometer baseline lie in a plane at an elevation angle of 15 degrees with respect to the horizontal. The correlation between the two instruments is good ; however, there is a lidar overestimate which has not been explained by multiple scattering effects.

The transmittance method has been applied more recently. The first results were obtained by taking into account the

beam convergence factor, under rather homogeneous fogs. They are shown in Figure 2 and will be discussed.

#### CONCLUSION

The lidar and transmissometer measurements performed by the slope method have shown a satisfactory agreement between the two instruments.

Preliminary measurements obtained with the transmittance method have been presented. These results agree well with transmissometer data ; other experiments have to be done in various fog conditions. This method is certainly an useful alternative for visibility measurements when fogs are very inhomogeneous.

#### REFERENCES

- 1 - COLLIS, VIEZEE, UTHE, OBLANAS. S.R.I., Contract N° F 19 628-70-C-0083 for AFCRL (1970).
- 2 - GAUMET, PETITPA. J. Of Applied Meteo. (to be published).
- 3 - MC MANUS ET AL. AFGL - TR - 0261 Air Force Geophysics Laboratories, Hanscom AFG, Mass (1976).
- 4 - KOHL, FLAHERTY. Conf. Abstracts Drexel University Philadelphia, Paper N° 11. (1977).

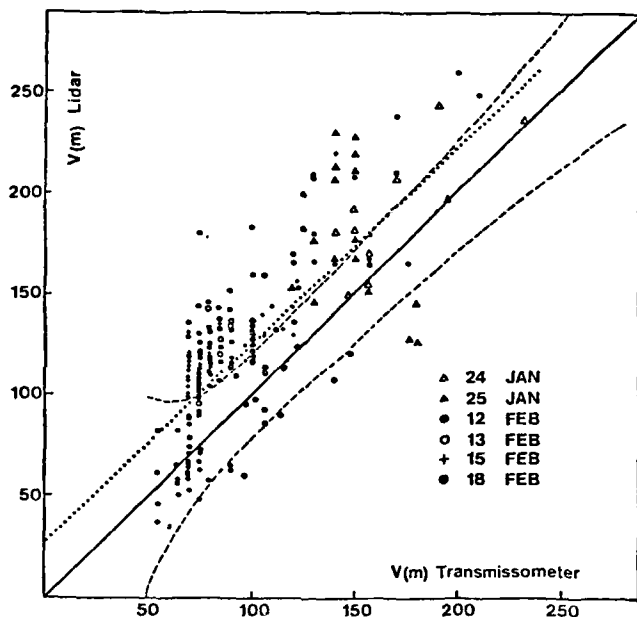


Fig. 1 : Lidar/transmissometer comparisons over the slant path ( $15^\circ$ ) (Slope method). The dotted line is the linear fit of 200 points. The dashed lines show the limits of the transmissometer error.

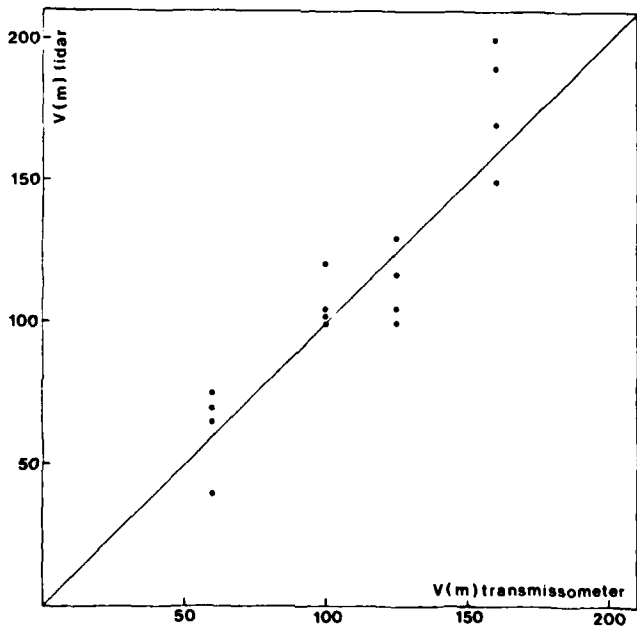


Fig. 2 : Lidar/transmissometer comparisons over the horizontal path. (Transmittance method)

## LIDAR MEASUREMENTS OF VERY DENSE FOGS

L. Stefanutti, F. Castagnoli, M. Morandi  
Istituto di Ricerca sulle Onde Elettromagnetiche del CNR  
Via Panciatichi 64  
I-50127 Firenze  
Italy

After the two lidar measurement campaigns carried out in the Po valley in the years 1978 and 1980 a new campaign was performed during the months of January and February 1982 in order to measure the extinction coefficient  $\sigma$  in fog.

Lidar measurements in fog were carried out in horizontal and slant directions. The lidar was fired at different elevation angles. The measurements were carried out in different conditions of visibility ranging from a minimum of a few meters (4-5 m standard visibility) up to 300-400 m visibility. Measurements were carried out on the following days: January 29th and 30th and February 8th, 9th, 10th, 11th, 15th, 16th, and 17th.

The extinction coefficient  $\sigma$  was measured simultaneously with a standard transmissometer and a nephelometer which were placed at approximately 200 m from the lidar. The measurements were carried out with an IROE IV lidar system (1), whose minicomputer has been expanded with a Winchester disk. Fortran IV software programs had been prepared to partially elaborate the lidar signatures on the field.

Six digital tapes each containing 460 groups of lidar signatures were recorded, each group containing 16 lidar signatures. The IROE IV lidar used two transient digitizers to collect the lidar signatures: an 8 bit Biomation 8100 and a 10 bit Biomation 1010. The Biomation 8100 was used to analyze the near signal (up to a few hundred meters) and the Biomation 1010 was used for the more remote signal. The first was operated at a sampling rate of 20 nsec while the latter was operated at a rate of 100 nsec.

The lidar was operated in a coaxial and in a semimonostatic configuration. The measurements were performed using an Nd:YAG pulsed laser operating at a pulse repetition rate of 1 Hz. The output radiation was frequency doubled. The semi-aperture of the lidar receiver could be varied from 2.5 mrad to 7 mrad. This was in order to take into account the effect of multiple scattering (2).

The lidar signatures were corrected with the different overlapping functions corresponding to each field of view. As a first approximation the overlapping functions which have been used corresponded to the ones obtained for single scattering in clear air.

The extinction coefficient  $\sigma$  was calculated by means of the slope method and the integral method. This was done for each group of signatures obtained with the same field of view.

As an example, we report here a group of range-corrected lidar signatures obtained with 3 different fields of view which have not yet been corrected with their overlapping functions (Fig. 1). Even in this case for the 3 fields of view considered, the standard visibility  $V$  varies from 80 to 22 m. With a rough extrapolation, in order to eliminate the effect of multiple scattering (see Fig. 2),

one obtains a standard visibility of approximately 8 m ( $\sigma = 0.5 \text{ m}^{-1}$ ), which was consistent with the conditions which we directly experienced. These measurements refer to February 11th at 1:17 a.m. At the same time the standard transmissometer and the nephelometer were off-scale at their lower level (minimum measurable visibility of 50 m). We obtained good results also in conditions of light fogs (visibility of the order of 100-200 m). In Fig. 3 and Fig. 4 we report such an example. Even in these conditions it is necessary to take into account the effect of multiple scattering.

Finally, by means of measurements carried out at different elevation angles, it was possible to measure the height and the structure of the fog layer.

- (1) L. Stefanutti; and L. Pantani: Optica Acta, 27, 1243-1252, 1980.
- (2) P. Bruscaglioni; L. Lachi; L. Lo Porto; L. Pantani; L. Stefanutti; and G. Zaccanti: Measurements of Multiply Scattered Radiation Contribution to Lidar and Transmissometer Signals. Eleventh International Laser Radar Conference, NASA CP-2228, 1982. (Paper II in this compilation.)

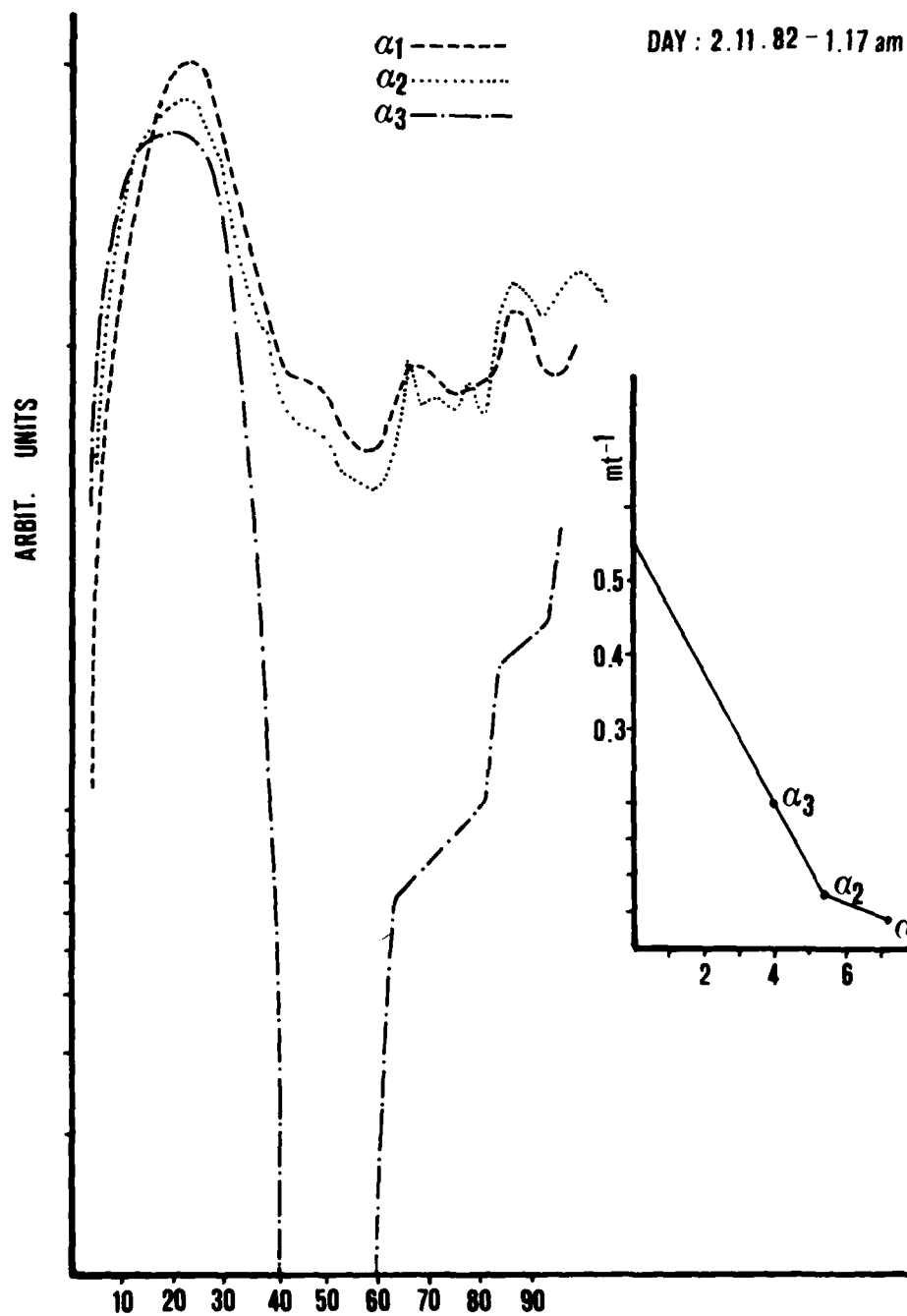


FIG.2

FIG.1

Figure 1.- Three groups of range-corrected lidar signatures with different receiver fields of view for case of very dense fog.

Figure 2.- Extinction coefficients for the 3 groups of lidar signatures. Extrapolating to zero aperture, one obtains extinction coefficient due to single scattering.

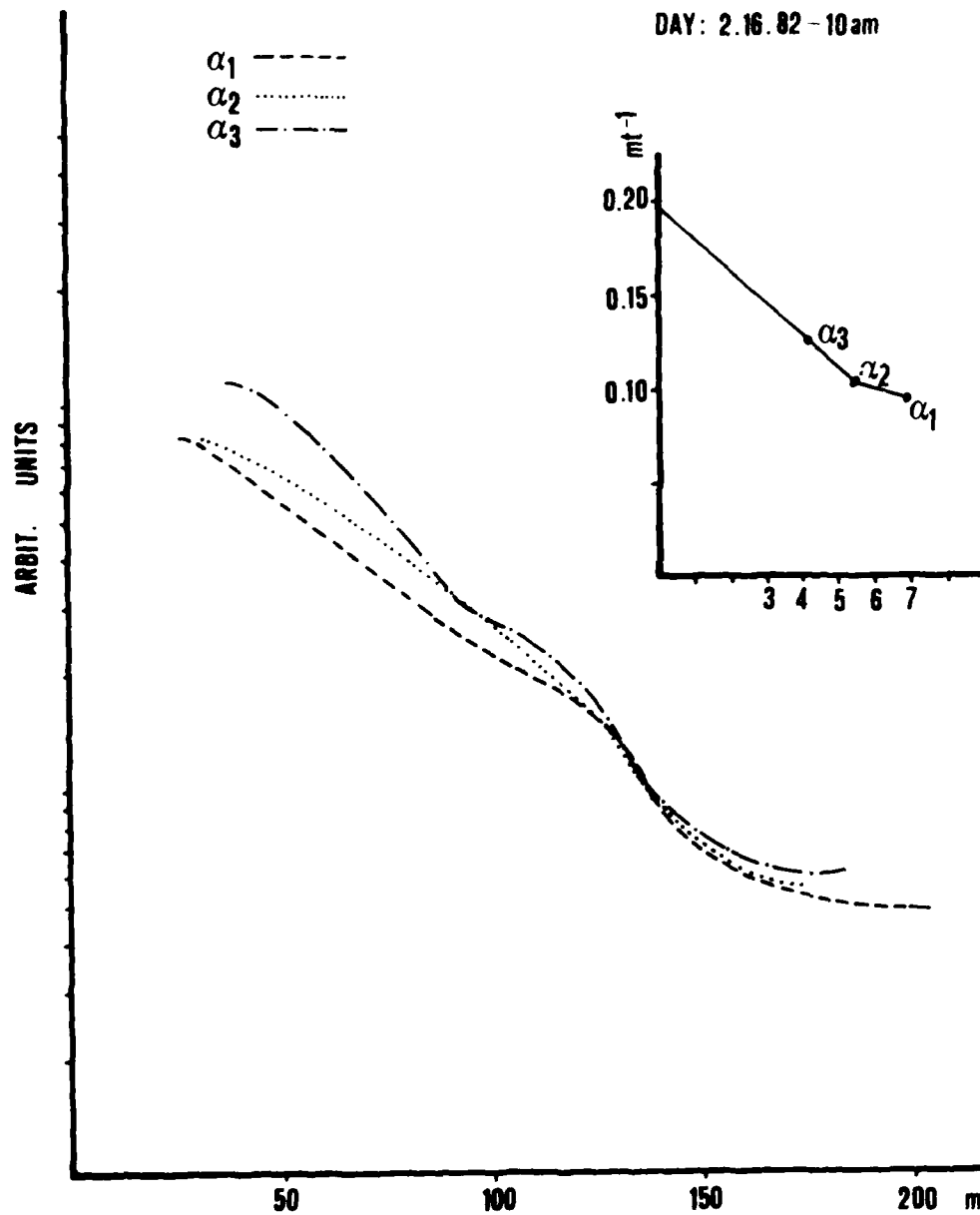


Figure 3.- Three groups of lidar signatures corrected with the clear air overlapping functions for case of light fog.

Figure 4.- Extinction coefficients for the 3 groups of lidar signatures.

# Eye-Safe Laser Slant Visual Range Measuring Device

by

Ch.Werner

German Aerospace Research Establishment (DFVLR)  
Institute of Optoelectronics  
D-8031 Wessling  
Federal Republic of Germany

Summary: An eye-safe laser ceilograph in combination with a lidar receiver was used to detect slant visual range. The system is described and test results are reported.

Introduction: Every year fog at airports renders some landing operations either difficult or impossible. In this situation it is particularly important to be able to predict the visibility along the landing glide path.

During an approach through clouds the altitude of the cloudbase and the depth of the cloud layer is of interest. These measurements are made using laser ceilographs /1/. In the case of ground fog, on the other hand, the height of the upper boundary of the mist or fog and the optical homogeneity must be known.

Many remote sensing methods are available to determine the slant visibility /2/. The modification of a laser range finder to a slant visibility detector was described /3/. Some examples of calculations of the accuracy of the two-point method under assumed atmospheric layerings are given /3/, and experimental tests with a portable lidar are reported /4/.

The limitation of the application of a slant visual range measuring device to visibilities below 2 km and up to altitudes of 100 m above ground gives two major advantages:

- 1) There is approximately no wavelength variation in the aerosol backscatter to extinction ratio.
- 2) The expected large backscatter values can be measured using lower laser output power.

Test system: The system which was tested consists of an Impulsphysics laser Ceilograph LD-WHL and a lidar receiver. The parameters of the system are listed in the table. To compare the received signals the DFVLR-minilidar was used. Two similar data systems were installed, one for the minilidar, one for the test system. A data system consists of a transient recorder, an averager, and a desk top computer. For the test system it was necessary to average over 1000 single shots; the minilidar uses 10 averaging cycles.

Table 1: System parameters of the test system

Laser transmitter

wavelength	0.906 $\mu\text{m}$
pulse energy	1.6 $\mu\text{W/s}$
output power	20 W
pulse duration	80 ns
pulse repetition rate	2.4 kHz

Receiver

mirror diameter	40 cm
photodiode	YAG 444
responsivity	0.68 A/W

Both systems have the same detector and preamplifier unit. The signal of the test system was additionally logarithmically amplified. The mirror diameters and the laser output power are different. A factor of 5400 could be calculated for which the minilidar system efficiency is better.

Test results: During two weeks in December 1981 the system was tested by measuring vertically. Figure 1 shows an oscilloscope display of the two signals versus range at visibilities above 5 km. The minilidar signal is the dashed curve.

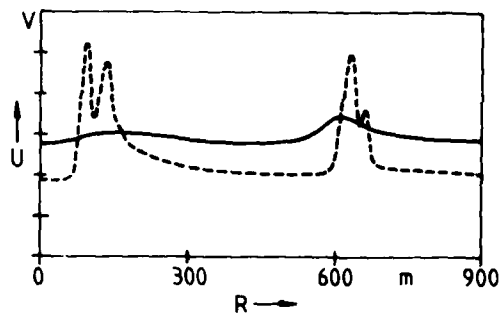


Figure 1

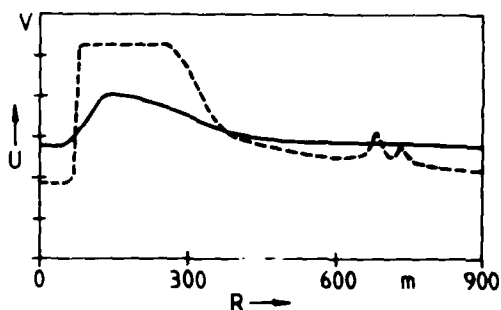


Figure 2

The cloud signal could be detected by both systems at visibility conditions above 5 km. The aerosol signal at the beginning of the test system is very weak. Figure 2 shows the signals taken 5 minutes after those of figure 1. It was snowing and the visibility was below 3 km. Now at the test system there is a very good signal, the minilidar signal was overloaded at the beginning. The cloud echo could be measured only by the minilidar.

Table 2 gives the results of a comparison. The lidar signature is calculated for different ranges using the parameters of both systems.

Table 2: Measured lidar signature versus range for two systems

range m	$\beta\tau$ $1.06\mu\text{m}$	$\text{m}^{-1}\text{sr}^{-1}$	$\beta\tau$ $0.9\mu\text{m}$
210	$6.8 \cdot 10^{-6}$		$8.1 \cdot 10^{-6}$
278	$7.8 \cdot 10^{-6}$		$7.5 \cdot 10^{-6}$
323	$2.7 \cdot 10^{-5}$		$1.4 \cdot 10^{-5}$
570	$4.9 \cdot 10^{-6}$		$3.3 \cdot 10^{-6}$

Using the slope-method /2/ one gets 2.6 km "visibility" for the minilidar; the test system gets 3.7 km for the horizontal visibility of 3.1 km.

Conclusion: It was demonstrated that an eye-safe laser transmitter as used in commercially available laser ceilographs can be used also for slant visibility detection. The system will be optimized with a better geometrical overlap at the beginning of the pulse and by using the two-point-method for data handling. A combination with the cloud base-height measuring device could simplify the system to one unit for both applications.

/1/ Manual of the Laser Ceilograph LD-WHL, 1981  
Impulsphysics GmbH, 2000 Hamburg 56

/2/ Viezee,W.  
Oblanas,G.  
Collis,R.T.H. Evaluation of the lidar technique of determining slant range visibility for aircraft landing operations  
AFCRL-RT-73-0708, Final Report, 1973

/3/ Werner,Ch. Determination of the slant range visibility from lidar signatures using the two-point-method. Optics and Laser Technology, 1981, 27-36

/4/ Werner,Ch. Results of a slant range visibility field experiment using the modified DFVLR-minilidar  
ESA-Techn. Translation -731, 1982.

Aerosol scattering and extinction measurements with LIDAR at 0,35  $\mu$ m  
and 10  $\mu$ m

Arne Hågård and Ove Steinvall  
National Defence Research Institute, Department 3  
Box 1165, S-581 11 Linköping Sweden

In order to investigate optical scattering and extinction through slant paths in the lower atmosphere we perform measurements with a Nd YAG-lidar and a  $\text{CO}_2$ -TEA lidar. The YAG laser emits 15 ns long pulses with a pulse energy of 125 mJ in the third harmonic at 355 nm. The receiver is a 20 cm diam telescope with a photomultiplier detector. The  $\text{CO}_2$ -lidar is based on a pulsed grating tuned TEA-laser and a 30 cm Newtonian telescope with a HgCdTe-detector.

Different methods for the calculation of backscattering and extinction coefficients from the lidar returns are being used and compared. The analytical inversion of the lidar equation with an initial value  $\sigma(0)$  for the extinction coefficient and the method due to Klett (Ref) are used and compared with the slope method and an iterative method. A serious drawback of the normal analytical inversion is its sensitivity to measurement errors and noise. The method due to Klett requires a value of the extinction coefficient at a remote point. For the slope method the aerosol must be assumed to be at least piecewise homogeneous. The iterative method starting with an initial value  $\sigma(0)$  leads in the limit to the same result as the analytical inversion, but can be interrupted at a suitable step before errors have grown too large.

Results from measurements with the  $\text{CO}_2$ -lidar are shown in the figure where the backscattering coefficient versus height is plotted in relative units. Values obtained as the ratio of returns from vertical and horizontal measurements are seen to be in good agreement with values obtained through inversion.

Measurements of atmospheric transmission with the lidar beams pointed at solid targets are made for comparison with the backscattering data.

So far measurements with the two lidar systems have been made independently but simultaneous measurements are planned for the near future. A laser nephelometer, which will be used with the UV-lidar to measure the  $\sigma(0)$ -value, has been designed. Laser radiation is reflected from the beam with a beam splitter and pointed through a tube with a beam trap in the opposite end. A detector with diffuse response is mounted at the wall of the tube and detects the integrated scattering from the aerosol, which is forced to flow through the tube. By alternatively using 355 nm and 532 nm (2nd harmonic) radiation in the nephelometer,  $\sigma$ -values at the two wavelengths can be obtained. Their ratio can then be used to convert data from the relatively eye-safe 355 nm-lidar to the corresponding values for the extinction at 532 nm, which can be used for slant visibility determination.

Reference: Klett J.D. Applied Optics Vol 20 No 2, p 211-220, Jan. 1981.

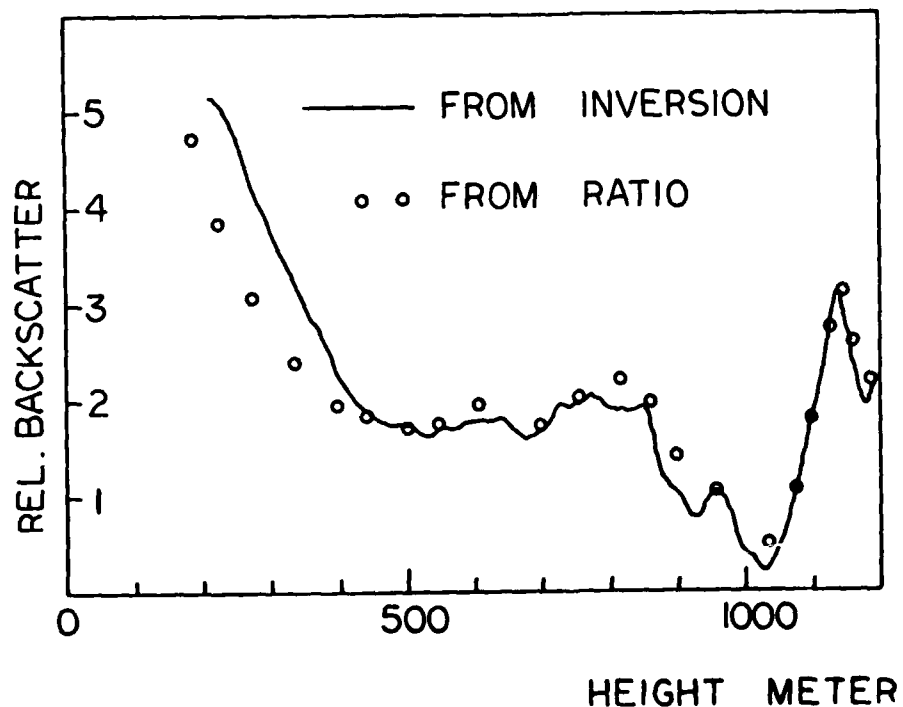


Figure. Backscattering coefficients at 10  $\mu\text{m}$  versus height, relative values.

## QUANTITATIVE LIDAR MEASUREMENT OF EXTINCTION COEFFICIENT

Edward Measure and Roberto Rubio  
US Army Atmospheric Sciences Laboratory  
White Sands Missile Range, NM 88002

### ABSTRACT

In the Fall of 1980, the US Army Atmospheric Sciences Laboratory (ASL) conducted a series of measurements of fog vertical structure in Meppen, Germany. Among the instruments present was the ASL two-color lidar. Several thousand lidar returns at 1.06 micrometers and 10.6 micrometers were digitized and recorded during the test.

A principal aim of the lidar measurements was to test the feasibility of computing quantitative fog extinction coefficients from single-ended lidar measurements. The results achieved seem to indicate that quantitative extinction coefficient measurements can be made in a highly inhomogeneous turbid atmosphere using single-ended lidar.

The problem of making quantitative measurements with lidar is a difficult one with a long history. The starting point for most attempts to extract quantitative information from lidar is the standard single-scattering lidar equation.<sup>1</sup> Until recently, all solutions to the lidar equation either were unstable or inapplicable to highly inhomogeneous atmospheres. The solution form recently developed by Klett<sup>2</sup> appears to be free of these defects. This solution has the form:

$$\sigma(r) = \frac{\exp\{[S(r) - S(r_m)]/k\}}{\sigma(r_m)^{-1} + \frac{2}{k} \int_r^{r_m} \exp\{[S(r') - S(r_m)]/k\} dr'}$$

where  $r < r_m$  and  $S(r) = \ln[r^2 P(r)]$ . In addition to the  $S(r)$  values, which are obtained directly from the lidar return, this solution also involves the boundary value extinction  $\sigma(r_m)$ . In general, it is necessary that this value either be measured independently or estimated. Results from Meppen show that even crude boundary value estimates are sufficient, under many conditions, to give good results for extinction.

It has been established that quantitative fog extinction coefficient measurements can be made using the method of Klett if sufficient extinction is present. This quantitative method, free of extreme dependence on boundary values, represents a significant advance.

<sup>1</sup>Collis, R. T. H. and P. B. Russell, Lidar Measurements of Particles and Gases by Elastic Backscattering and Differential Absorption. Topics in Applied Physics, Vol. 14, 1976, Springer-Verlag, New York.

<sup>2</sup>J. D. Klett, Appl. Opt. **20**, 211 (1981).

## QUANTITATIVE EXTINCTION MEASUREMENTS WITH THE VISIOCEILOMETER

W. J. Lentz  
US Army Atmospheric Sciences Laboratory  
Atmospheric Sensing Division  
White Sands Missile Range, NM 88002

### Abstract

In recent years lidar (Light Detection and Ranging) has made significant technical and theoretical advances. These advances have permitted the construction of a small, rugged, self-contained battery-operated lidar which measures visibility automatically without external inputs. This lidar measures cloud ceiling height and visibility from a single  $1.06\mu\text{m}$  laser pulse with a modified AN/GVS-5 laser rangefinder. Since visibility and cloud ceiling height are measured, the lidar has been dubbed a visioceilometer.<sup>1</sup>

The visibility is calculated from the extinction derived from the new Klett<sup>2</sup> solution to the lidar equation. This breakthrough in the calculation of extinction allows one to calculate extinction as a function of range even though the extinction may vary over many orders of magnitude. The lidar return is digitized and analyzed by a CCD (Charge Coupled Device) based transient recorder and CMOS microprocessor. The advances in CCD and CMOS enable a battery operated transient digitizer and processor to be technically feasible.

A recently conducted test in Meppen, Germany compared the visioceilometer against the extinction calculated from balloon borne particle counters. The following figure shows the extinction taken from several lidar shots as the balloon ascended. The agreement between the extinction calculated from the particle counter size distribution and the visioceilometer over several orders of magnitude of change indicates that the lidar is a promising tool for vertical extinction profiles.

The text will outline the Klett method of calculating extinction from the lidar return and a method of obtaining boundary values under high and low visibility cases. A number of theoretical extinction examples will be considered to define the limits of current inversion programs. Also, the critical experimental parameters which limit application of the Klett solution in the visioceilometer and other lidars will be considered. Additional experimental measurements and inversions of the lidar return to extinction will be presented.

---

<sup>1</sup>Lentz, W. J., The Visioceilometer: A Portable Visibility and Cloud Ceiling Height Lidar, ASL-TR-0105, January 1982, US Army Atmospheric Sciences Laboratory, White Sands Missile Range, NM.

<sup>2</sup>Klett, J. D., 1980, On the Analytical Inversion of Lidar Returns from an Inhomogeneous Atmosphere, ASL-CR-80-008-03, US Army Atmospheric Sciences Laboratory, White Sands Missile Range, NM.

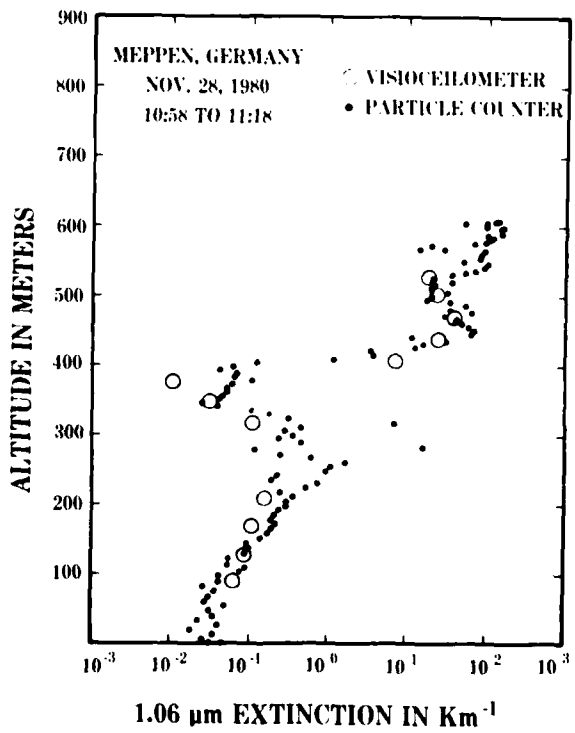


Figure 1. Visioceilometer extinction compared to extinction calculated by balloon-borne particle counter in Meppen, Germany.

## COMMENTS ON THE ANALYSIS OF ATMOSPHERIC LIDAR OBSERVATIONS

Frederick G. Fernald  
Department of Physics  
University of Denver  
Denver, Colorado 80208

### INTRODUCTION

Klett<sup>1</sup> has recently stated the solution to the lidar equation in a very convenient form for the analysis of data collected in very turbid atmospheres. His paper has prompted a restatement of the more general solution of Fernald et al<sup>2</sup> which is also applicable to mildly turbid atmospheres where both aerosol and molecular scatterers must be considered in the analysis. This has led to a simple numerical scheme for the computer analysis of lidar measurements.

### THE LIDAR EQUATION

The lidar equation for two distinct classes of scatterers is  
$$P(Z) = ECZ^2 \{ \beta_1(Z) + \beta_2(Z) \} T_1^2(Z) T_2^2(Z) \quad 1.$$

where  $P(Z)$  is the return signal from the scattering volume at slant range  $Z$ ,

$E$  is an output energy monitor pulse which is proportional to the transmitted energy,

$C$  is the calibration constant of the instrument which includes losses in the transmitting and receiving optics and the effective receiver aperture,

$\beta_1$  and  $\beta_2$  are, respectively, the aerosol and molecular backscattering cross sections at slant range  $Z$ ,

$T_1 = \exp\{-\int_0^Z \sigma_1(z) dz\}$  is the aerosol transmittance,

and  $T_2 = \exp\{-\int_0^Z \sigma_2(z) dz\}$  is the molecular atmosphere transmittance where  $\sigma_1$  and  $\sigma_2$  are, respectively, the aerosol and molecular extinction cross sections.

The molecular atmosphere scattering properties can be determined from the best available meteorological data or approximated from appropriate standard atmospheres; so that only the aerosol scattering properties remain to be determined. One further simplifying assumption is that the extinction to backscattering ratio for aerosols,  $S_1 = \sigma_1 / \beta_1$  remains constant with range. It essentially states that the size distribution and composition of the aerosol scatterers are not changing with range from the lidar and that variations in backscattering from aerosols are due to changes in their number density. This is not exceedingly restrictive. In the numerical analysis of the lidar data, the atmosphere can be divided into layers, with  $S_1$  allowed to vary among the layers. Collis and Russell,<sup>3</sup> Pinnick et al,<sup>4</sup> and Russell et al<sup>5</sup> can be referenced for values for this ratio. The corresponding ratio for the molecular scatterers is the constant

$$S_2 = \sigma_2(Z) / \beta_2(Z) = 8\pi/3$$

The solution to Eq. 1 for the aerosol backscattering cross sections (Fernald et al<sup>2</sup>) then becomes

$$\beta_1(z) = \frac{P(z)z^2 \exp\{-2(S_1-S_2)\int_0^z \beta_2(z)dz\}}{CE-2S_1 \int_0^z P(z)z^2 \exp\{-2(S_1-S_2)\int_0^{z'} \beta_2(z')dz'\}dz} + \beta_2(z) \quad 2.$$

If "a priori" information can be used to specify the value of the aerosol and molecular scattering cross sections at a specific range,  $Z_c$ , then the lidar can be "calibrated" by solving Eq. 2 for CE in terms of these scattering properties and

$$\beta_1(z) + \beta_2(z) = \frac{X(z) \exp\{-2(S_1-S_2)\int_{Z_c}^z \beta_2(z)dz\}}{\frac{X(z_c)}{\beta_1(z_c) + \beta_2(z_c)} - 2S_1 \int_{Z_c}^z X(z) \exp\{-2(S_1-S_2)\int_{Z_c}^{z'} \beta_2(z')dz'\}dz} \quad 3.$$

where  $X(z)$  is the range normalized signal  $P(z)z^2$ . The total backscattering cross section at range  $Z$  is now expressed as a function of the scattering properties at the calibration range and those of the intervening atmosphere between the ranges  $Z_c$  and  $Z$ .

Eq. 3 leads to a simple numerical integration scheme. If

$$A(I, I+1) = (S_1 - S_2) \{ \beta_2(I) + \beta_2(I+1) \} \Delta Z \quad 4.$$

is used to replace the terms that correct for the molecular atmospheric extinction between data points a slant range  $\Delta Z$  apart, then the aerosol backscattering cross section at range  $Z(I+1)$  one data step beyond the calibration range  $Z(I)$  becomes

$$\beta_1(I+1) + \beta_2(I+1) = \frac{X(I+1) \exp\{-A(I, I+1)\}}{\frac{X(I)}{\beta_1(I) + \beta_2(I)} - S_1 (X(I) + X(I+1) \exp\{-A(I, I+1)\}) \Delta Z} \quad 5.$$

Similarly, the total backscattering cross section at  $Z(I-1)$ , one step before the calibration range  $Z(I)$ , becomes

$$\beta_1(I-1) + \beta_2(I-1) = \frac{X(I-1) \exp\{+A(I-1, I)\}}{\frac{X(I)}{\beta_1(I) + \beta_2(I)} + S_1 (X(I) + X(I-1) \exp\{+A(I-1, I)\}) \Delta Z} \quad 6.$$

Similar expressions can be generated in terms of the aerosol extinction. The lidar data can, therefore, be analyzed in successive steps that can move either out or in from the assigned calibration range.

For highly turbid atmospheres ( $\sigma_1 \gg \sigma_2$ ) the two terms in the denominators of Eqs. 5 and 6 will be of comparable magnitude, and outward stepwise integration can become, as Klett<sup>1</sup> has shown, very unstable. On the other hand, inward stepwise integration is very stable and rapidly loses its dependence on the initial "guess" of the scattering cross sections attributed to the calibration range. In this sense, uncalibrated lidars can yield the extinction properties of highly turbid atmospheres.

When the aerosol and molecular scattering cross sections are of a comparable magnitude (during light to moderate air pollution events or in stratospheric studies) the second terms in the denominators of

Eqs. 5 and 6 will be considerably smaller than the first terms. Numerically stable solutions are, therefore, possible when stepping in either direction from the calibration level. Under these atmospheric conditions, the analyses will be dependent on the aerosol and molecular backscattering cross sections assigned to the calibration level. Net aerosol extinction will be small. It will be tied to the values selected for  $S_1$ , the aerosol extinction to backscattering ratio which can vary over a relatively wide range without greatly effecting the backscattering cross sections computed from Eqs. 5 and 6.

#### REFERENCES

1. J. D. Klett, *Appl. Opt.* 20, 211 (1981).
2. F. G. Fernald, B. M. Herman, and J. A. Reagan, *J. Appl. Meteor.* 11, 482 (1972).
3. R. T. H. Collis and P. B. Russell, in Laser Monitoring of the Atmosphere, E. D. Hinkley, Ed. (Springer, New York, 1976) p. 117.
4. R. G. Pinnick, J. M. Rosen, and D. J. Hofman, *J. Atmos. Sci.*, 33, 304 (1976).
5. P. B. Russell, T. J. Swissler, M. P. McCormick, W. P. Chu, J. M. Livingston, and T. J. Pepin, *J. Atmos. Sci.*, 38, 1279 (1981).

## INVESTIGATION OF AEROSOL CHARACTERISTICS USING BISTATIC LIDAR

B. V. Krishna Murthy and K. Parameswaran  
Space Physics Division  
Vikram Sarabhai Space Centre,  
Trivandrum - 695 022, India

A CW laser system with an argon-ion laser operating at 514.5 nm as transmitter has been used in a bistatic mode to investigate the physical characteristics of atmospheric aerosols. The laser power used was 0.5W and the transmitter-receiver separation was 434 m.

The scattered signal from a fixed altitude (~220 m) as a function of scattering angle was recorded by suitably choosing the transmitter and receiver elevation settings. (The polarization of the laser was such that the electric vector was parallel to the scattering plane.) The signal strength recorded was normalized for the scattering volume and range. The total volume scattering coefficient (which includes the Rayleigh and Mie scattering components) was obtained by assuming a reasonable value of the two-way atmospheric transmittance for the prevailing atmospheric condition. The dependance of the volume scatter coefficient thus obtained on the scattering angle was used to deduce the size distribution and refractive index of the aerosols by the process of iteration. In this, the Rayleigh scattering was obtained by assuming the standard atmospheric density profile applicable to the particular location (Trivandrum 8°33'N, 76°57'E). The aerosol size distribution is assumed to be of the form

$$N(r) dr = C r^{-m} \quad \text{for } 0.1 \mu\text{m} < r < 10 \mu\text{m}$$

$$N(r) dr = C 10^{-m} \quad \text{for } 0.02 \mu\text{m} < r < 0.1 \mu\text{m}$$

$$N(r) dr = 0 \quad \text{for } r < 0.02 \mu\text{m} \text{ and } r > 10 \mu\text{m}$$

where  $N(r)dr$  is the number density in the size interval  $r$  to  $r+dr$ ,  $C$  is a constant and  $m$  is the exponent. The Mie scattering coefficient is theoretically calculated as a function of scattering angle for different pairs of values of  $m$  and  $n$  (for  $m$  ranging from 3 to 6 and  $n$  ranging from 1.33 to 1.5), the refractive index which is taken to be only real at the wavelength of operation. These theoretical values were used to obtain a best fit pair of  $m$  and  $n$ . From this pair and the volume scattering coefficient corresponding to different scattering angles, the aerosol number density is obtained, making use of the fact that the Rayleigh component is zero for a scattering angle equal to 90° for the polarization used. The atmospheric transmittance was then calculated with this value of aerosol number density, assuming the number density does not change significantly with altitude. This is a valid assumption, as the planetary boundary layer (or equivalently the mixing region) is expected to extend at least up to this altitude. The new transmittance value was again used in obtaining the volume scattering coefficients. This process of iteration was continued till a consistent pair of  $m$  and  $n$  were obtained. For the observations made on Oct. 1, 1981, the values of  $m$  and  $n$  were 3 and 1.4, respectively.

With the assumption that  $m$  and  $n$  do not change with altitude, and the values of  $m$  and  $n$  obtained as described above, the aerosol-altitude profile was obtained in the altitude range of ~200 m - 2000 m by using the recorded scattered signal strengths as a function of altitude.

Polar nephelometer measurements of laser light scattering by  
non-spherical particles

Alessandro Coletti and Gerald W. Grams  
School of Geophysical Sciences  
Georgia Institute of Technology  
Atlanta, Georgia 30332

A laser polar nephelometer (Grams et al, 1975) has been used to measure the light scattered in two polarization planes by monodisperse non-spherical particles at scattering angles between 10 and 170° in 5° steps. The monodisperse aerosols were generated in the laboratory with a vibrating orifice particle generator (TSI model 53050) using solutions of non-absorbing salts such as sodium chloride, ammonium sulfate and potassium chlorate and of absorbing compounds such as nigrosine dye and methylene blue. Samples of the aerosols were collected onto filters during the measurements for subsequent analyses on a scanning electron microscope. In our experiments, the particle sizes ranged from 1 to 4  $\mu\text{m}$ , corresponding to a range of values of the Mie size parameter from 5 to 20 at the wavelength of the laser ( $\lambda=633 \text{ nm}$ ).

For both the parallel and perpendicular planes of polarization, Figure 1 shows a comparison between the phase functions computed by the Mie formulas for particles of size parameter 5 and the phase functions observed for samples of sodium chloride having approximately the same equivalent geometric cross sections. Some of the oscillations are observed in the same position for the theory (continuous lines) and for the measurements (circles and triangles) but their amplitudes are significantly different.

Since the comparison with spherical particles becomes less applicable at larger sizes, we also analyzed our phase function data, as did Pollack and Cuzzi (1980) and Hodkinson and Greenleaves (1963), as a combination of diffraction, refraction, and reflection of the incident beam. Results of these comparisons will be discussed.

REFERENCES

Grams, G. W., A. J. Descher and C. M. Wyman, 1975: Laser polar nephelometer for airborne measurements of aerosol optical properties, Opt. Eng., 14, 85-90.

Hodkinson, J. R. and I. Greenleaves, 1963: Computations of light scattering and extinction by spheres according to diffraction and geometrical optics, and some comparisons with the Mie theory, Jour. Opt. Soc. Am., 53, 577-588.

Pollack, J. B. and J. N. Cuzzi, 1980: Scattering by non-spherical particles of size comparable to a wavelength: a new semi-empirical theory and its application to tropospheric aerosol, Jour. Atmos. Sci., 37, 868-881.

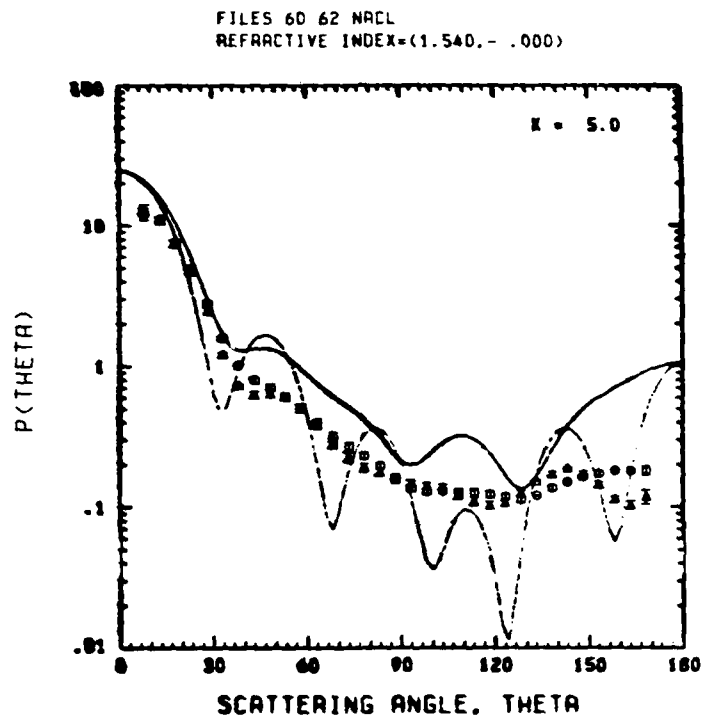


Figure 1. Light scattering phase functions on perpendicular and parallel polarization planes: circles and triangles, experimental results for non-spherical sodium chloride crystals of about  $1.3 \mu\text{m}$  diameter; continuous line, results of the Mie theory for spheres of size parameter 5.

THE MODELING OF ATMOSPHERIC AEROSOL BACKSCATTERING  
AT  $\text{CO}_2$  WAVELENGTHS

G. S. Kent, G. K. Yue, U. O. Farrukh and A. Deepak  
Institute for Atmospheric Optics and Remote Sensing (IFAORS)  
P. O. Box P, Hampton, VA 23666, USA

INTRODUCTION

Preliminary results are available from a study of the modeling of  $\beta_{10.6}$ , the aerosol backscattering coefficient at 10.6  $\mu\text{m}$ , using published data on aerosol characteristics in the free troposphere and lower stratosphere. The main problem with such modeling is concerned with our knowledge of the characteristics of the larger aerosol particles (radii  $> 1 \mu\text{m}$ ) whose presence, even in very small numbers, greatly changes the volume scattering cross-section. Factors which have been considered in this modeling, some of which are discussed quantitatively below, are the following:

1. Aerosol size distribution
2. Aerosol refractive index
3. Aerosol shape
4. Measurement uncertainties
5. Natural variations with time, height, location and meteorological conditions

Calculations have been made of  $\beta_{10.6}$  using published data on the above factors and the modified AGAUSX scattering code developed by the U.S. Army Atmospheric Sciences Laboratory and the Department of Physics, New Mexico State University.

EFFECTS OF UNCERTAINTIES IN THE AEROSOL PARAMETERS

1. Aerosol Size Distribution

It is generally recognized that the aerosol size distribution in the boundary layer is multi-modal and recently Patterson et al. (1980) have published data indicating that a similar pattern exists in the free troposphere. Independent analysis of data published by Cress (1980) for the free troposphere shows the same behavior. The mode which is responsible for the major part of the backscattering cross-section at 10.6  $\mu\text{m}$  has its maximum value of  $dV/d(\log r)$  typically around 3  $\mu\text{m}$ , but it may lie anywhere between 1 and 10  $\mu\text{m}$ . Measured particle size distributions, which do not include a significant part of this mode, are not useful for modeling backscattering at 10.6  $\mu\text{m}$  and, even when they do, considerable uncertainty occurs because of the necessity of extrapolating the distribution to larger particle sizes. This is illustrated in Table 1 which shows the effect of extrapolating such size distributions. Two methods of extrapolation have been used, a linear fit (in terms of  $\log (dN/d(\log r))$  and  $\log r$ ) to the last two measured points and a log normal fit to the last three or four measured points. The very serious problems encountered with the Gras and Laby data, which terminates at 1  $\mu\text{m}$ , are clear. Even the extrapolated values do not give a realistic value for  $\beta_{10.6}$ . In contrast, the data of Patterson et al., even though terminating at 1.8  $\mu\text{m}$ , includes an

appreciable fraction of the large particle mode and gives a useful value for  $\beta_{10.6}$ . The difference between the values calculated from the data of Cress and Patterson *et al.* probably represents a real atmospheric variation.

#### 2. Aerosol Refractive Index

A standard model for tropospheric aerosols assumes them to consist of 70% dust, 29% water soluble and 1% soot. It is also likely that the smaller particles are mainly water soluble, while the larger particles responsible for infrared scattering are mainly clay and silicate dust. Considerable literature exists on the refractive index of the materials and its variation with wavelength. The stratospheric aerosol is believed to be mainly sulfuric acid with an admixture of volcanic ash immediately after an eruption. Table 2 shows the effect of changing composition on modeled  $\beta_{10.6}$  values for typical aerosol size distributions. The effect of different compositions is to change  $\beta_{10.6}$  by a factor of two or three.

#### 3. Aerosol Shape

Several recent studies of the effects of irregular aerosol shape on backscattering have shown that uncritical use of Mie theory can lead to erroneous values. Most published data is on the effects at visible wavelengths and there is considerable spread in the quantitative estimates of the effect. It seems possible that  $\beta_{10.6}$  calculated from Mie theory may be too large by a factor of from 2 to 10 depending upon the shape of the irregular particle.

#### 4. Measurement Uncertainties

Measurement uncertainties may arise both from sampling problems and from errors in the technique itself. The former is aggravated by the fact that it is the larger and less common particles that determine  $\beta_{10.6}$ . Sampling errors for these larger particles cause calculated values of  $\beta_{10.6}$  to vary over a range of 2:1 in the troposphere and by as much as an order of magnitude for some stratospheric data. Analysis of aerosol size distributions obtained by different sizing techniques (Gras and Ayers, 1979) also shows an order of magnitude variation in  $\beta_{10.6}$  calculated for stratospheric aerosols.

#### 5. Natural Variations

The most considerable natural variation in both aerosol characteristics and  $\beta_{10.6}$  is that with altitude, and modeled values of  $\beta_{10.6}$  vary from about  $3 \times 10^{-9} \rightarrow 3 \times 10^{-8} \text{ m}^{-1} \text{ sr}^{-1}$ , just above the boundary layer, to  $3 \times 10^{-11} \rightarrow 3 \times 10^{-10} \text{ m}^{-1} \text{ sr}^{-1}$  in the stratosphere. The atmosphere clearly shows much structure, with sharp vertical layering and temporal variation associated with aerosol history. Measurements made by different workers, at different times and locations, are still in insufficient quantity to separate, easily, natural differences from measurement differences, except after major changes, such as those produced by volcanic eruptions.

#### COMPARISON OF THEORETICAL AND EXPERIMENTAL VALUES FOR $\beta_{10.6}$

Figure 1 shows the results of modeling, compared with experimental values measured by the airborne CO<sub>2</sub> lidar system operated by NASA Marshall Space Flight Center. The modeled values are based on aerosol measurements made over Europe in May 1976, selected because these

measurements were made out to a 5  $\mu\text{m}$  particle radius. The lidar flights were made over the continental U.S.A. in July, 1981. In spite of the fact that the measurements were made over different continents, the agreement between theory and experiment is relatively good, particularly at the 6 km level. At lower levels some of the differences may possibly be due to humidity effects, which have not been included in these calculations.

#### ACKNOWLEDGMENTS

This work was carried out under Contract NAS8-34427 with NASA Marshall Space Flight Center. We are grateful to Mr. J. D. Bilbro of NASA Marshall Space Flight Center for supplying the experimental profiles shown in Fig. 1.

#### REFERENCES

Cress, T. S., Airborne measurement of aerosol size distributions over northern Europe. Volume 1. Spring and Fall, 1976, Summer 1977. Air Force Geophysical Laboratory, Hanscom Field, Mass. U.S.A., Environmental Research Paper No. 702, 29 May 1980.

Gras, J. L., and Ayers, G. P., On sizing impacted sulfuric acid aerosol particles, *J. Appl. Meteor.* 18, 634-638, 1979.

Gras, J. L., and Laby, J. E., Southern Hemisphere stratospheric aerosol measurements 3. Size distribution 1974-1979, *J. Geophys. Res.* 86, 9767-9775, 1981.

Patterson, E. M., Kiang, C. S., Delany, A. C., Wartburg, A. F., Leslie, A.C.D., and Huebert, B. J., Global measurements of aerosols in remote continental and marine regions: Concentrations, Size distributions, and Optical properties, *J. Geophys. Res.* 85, 7361-7375, 1980.

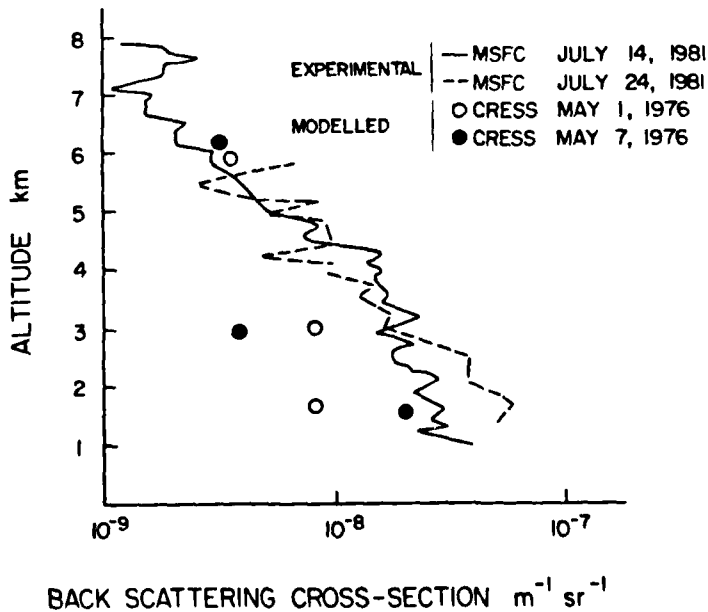


Figure 1. Comparison of experimentally and theoretically derived values of  $\beta_{10.6}$ . The modeled values have been calculated assuming a refractive index corresponding to silicate dust.

TABLE 1: EFFECT OF EXTRAPOLATION ON THE CALCULATED VALUES OF  $\beta_{10.6}$ 

Data Source	Maximum Particle Radius Measured	Altitude	$\beta_{10.6}$ ( $10^{-9} \text{ m}^{-1} \text{ sr}^{-1}$ )		
			No. Extrap.	Log-normal Extrap.	Linear Extrap.
Cress, 1980	5 $\mu\text{m}$	6 km	1.78	1.93	2.11
Gras & Laby 1981	1 $\mu\text{m}$	4-10 km	0.017	not possible	0.16
Patterson et al. 1980	1.8 $\mu\text{m}$	5 km	0.60	0.66	0.72

TABLE 2: A COMPARISON OF  $\beta_{10.6}$  VALUES CALCULATED FROM THE SAME AEROSOL SIZE DISTRIBUTION BUT WITH DIFFERENT REFRACTIVE INDICES<sup>1</sup>

Date	Height (km)	$\beta_{10.6}$ ( $10^{-9} \text{ m}^{-1} \text{ sr}^{-1}$ )							
		75% $\text{H}_2\text{SO}_4$ (1.737 - 0.273)		dust (1.620 - 0.120)		water soluble (1.760 - 0.07)		soot (2.22 - 0.73)	
		No extrapolation	with extrapolation	No extrapolation	with extrapolation	No extrapolation	with extrapolation	No extrapolation	with extrapolation
May 1 1976 (Flt 1)	16	7.80	8.38	7.02	7.90	11.65	17.24	18.32	19.55
	3.1	7.56	8.13	6.85	7.72	11.41	17.00	17.72	18.94
	5.9	3.30	3.82	3.06	3.86	5.50	10.44	7.83	8.90
May 7 1976 (Flt 1)	1.45	7.84	11.24	6.95	11.99	12.42	38.38	18.36	25.37
	3.0	2.60	3.13	2.34	3.15	3.97	8.59	6.07	7.15
	6.0	1.97	2.40	1.78	2.43	3.07	6.77	4.62	5.49

<sup>1</sup>The aerosol size distributions are given by Cress [AFGL-TR-80-0178 (1980)].

CO<sub>2</sub> LIDAR FOR ATMOSPHERIC OPTICAL  
MEASUREMENTS IN THE 8-12  $\mu$ m WINDOW REGION

D. M. Winker and R. M. Schotland

Institute of Atmospheric Physics  
University of Arizona  
Tucson, Arizona 85721

The optical properties of the atmospheric 8-12  $\mu$ m window region are of importance both from the standpoint of the design of lidar operating in this region and from general radiative transfer considerations. At the present time there is a scarcity of data relating to the radiative properties of the desert aerosol in this spectral region. With this in mind, an incoherent CO<sub>2</sub> lidar system is being developed to obtain measurements of atmospheric transmission and volume backscattering cross sections using the slant path technique which has been developed at the University of Arizona.

The lidar system is based on a grating-tuned CO<sub>2</sub> TEA-laser operating at 1Hz with pulse energies of up to several joules. The unstable resonator design gives a beam divergence of 0.7mr. A range of 5km horizontally and 3km vertically is expected, with a range resolution of 100 meters, allowing observation to be made to the top of the mixing layer. The receiver is a .44m diameter Newtonian telescope coupled to a HgCdTe detector. The transmitter and receiver are mounted coaxially and a large plane mirror is used to scan the beams in elevation.

Output from the detector is amplified by a 4 stage switched-gain (gain stage of 12) amplifier with 5 MHz bandwidth and 100 dB usable dynamic range and then digitized in real time by a 12 bit A/D converter. A back-up system using a logging amplifier in place of the switched gain amplifier is also under development. A PDP 1103 controls laser firing and mirror scan, stores the digitized returns and housekeeping information on each shot, and is also used for analysis of the data.

Results obtained to date and the algorithm employed will be discussed.

APPLICATION OF COHERENT ANTI-STOKES RAMAN SCATTERING TO  
DROPLET CHARACTERISTIC MEASUREMENTS IN THE MIE SIZE RANGE

Abraham Gross and John Cooney

Department of Physics and Atmospheric Science, Drexel  
University, Philadelphia, Pennsylvania 19104.

In the comparison between theory and experiment of droplet growth by condensation the value of the sticking coefficient is only roughly estimated (Ref. 1). To get a better estimate we need to know both the growth rate and the exact temperature of the drops at the same time. Growth rate can be determined by the regular Mie scattering. We seek a light-scattering mechanism which can provide a knowledge of temperature changes during growth. By such means it will be possible to arrive at an experimental value of the sticking coefficient. Of the various optical diagnostic techniques, Coherent Anti-Stokes Raman Spectroscopy (CARS) is considered to be promising for making temperature measurements in the bulk. The objective of this work is to study the feasibility and advantages of CARS as a valid diagnostic tool in droplets of 1.0 to 20 microns in size.

In CARS radiation, two waves of high intensity and frequencies  $w_1$  and  $w_2$  are mixed in a medium to produce a new coherent wave at frequency  $w_3=2w_1-w_2$ . This third signal is enhanced if  $w_1-w_2=w_v$  where  $w_v$  is a Raman active resonance in the medium. In the bulk the properties of CARS, in contrast with spontaneous Raman, are mainly high-signal level and small-signal beam divergence.

It would be incorrect to assume that the CARS signal intensity and spatial distribution from droplets are similar to those from the bulk (Refs. 2-3). The signal is affected by the geometrical and optical properties of the droplets. To begin with, these properties influence the local internal (elastic) electric fields which interact with the medium to create the CARS radiation at  $w_3$ . The particle size and refractive index now shape the  $w_3$  radiation as it emerges from the spherical boundary and give it a distinct spatial distribution of intensity. Thus, the resulting CARS scattering total cross section as well as the differential cross section from a droplet are shown to differ significantly from that of the bulk for equivalent volumes.

To determine the CARS field produced in the droplet, two plane waves at  $w_1$  and  $w_2$  are allowed to fall on the

droplet. As a result two internal fields arise, each one equivalent to ordinary Mie scattering. The source for the CARS field at  $w_3$  is the third-order nonlinear optical susceptibility (Ref. 4). From such an interaction the third-order dipole moment per unit volume arises. Incidentally, the third-order susceptibility depends in part on the population of the various energy states, and here is the source of the temperature dependence which enters as the thermal equilibrium Boltzman factor.

The third-order electric dipole moment so derived is the source that generates the local CARS field at  $w_3$  through the Maxwell equations.

At the frequency  $w_3$  the field inside the sphere can be written as the sum of two fields. One is a particular solution of the source equation. It is generated by all the oscillating third-order induced dipoles at the frequency  $w_3$ . To calculate this portion of the  $w_3$  field, one has to perform a Green's function integration of the source dipole  $P(3)$  over the entire volume of the sphere. The other component of the  $w_3$  field is a general solution for the homogeneous Maxwell's equations. The latter is introduced to facilitate the matching of the boundary conditions. All fields are expanded in multipole fields (also called vector spherical harmonics).

The coefficients of expansion for the CARS field that is scattered outside the droplet are obtained by the use of the standard boundary conditions requiring the tangential components of  $E$  and  $H$  to be continuous at the droplet's surface.

The results for CARS scattering intensities from droplets are calculated for benzene (Ref. 5), but can be performed for any other material for which adequate information about the third-order susceptibility exists. Among the more interesting results of these calculations are the values of the total CARS intensity scattered from droplets as compared with CARS power scattered from equivalent mass in the bulk form. For size parameters greater than 4.0, scattering intensities are shown to reach values of 30 greater than an equivalent material in the bulk form. The calculation also indicates that to maximize the scattering efficiency, one should use parallel incident beams.

The CARS differential scattering cross sections from droplets resemble in their gross features the Mie patterns but differ from it in some vital respects. The CARS intensity has extra-sharp minima at angles not predicted by any Mie scattering minimum. Furthermore, the CARS

intensity in the forward direction relative to the backward scattering is reduced.

In conclusion, the results show that when CARS is observed from small droplets, the scattering depends sensitively upon the characteristics of the droplets and differs from the bulk in shape and magnitude. On the one hand, the CARS radiation from droplets, as opposed to the bulk, is nondirective with complicated angular dependence. On the other hand, for certain sizes it is augmented in its total magnitude by almost two orders of magnitude. This indicates that in using CARS for measurements on droplets one has to consider the effect of the size, refractive index, and scattering angle.

#### References

1. J.C. Carstens and J.M. Carter, Proc. Int. Coll. on Drops and Bubbles, Cal Tech/JPL, (Ed. D. J. Collins, M.S. Plesset and M.M. Saffren), pp. 529-552 (1974).
2. H. Chew, P.J. McNulty, M. Kerker, Phys. Rev. A 13, 396 (1976).
3. H. Chew, M. Scully, M. Kerker, P.J. McNulty, and D.D. Cooke, J. Opt. Soc. Am. 68, 1686 (1979).
4. J. W. Nibler and G. V. Knighten, in "Raman Spectroscopy of Gases and Liquids" A. Weber, ed. (Springer-Verlag, New-York, 1979) pp. 253-299.
5. M.D. Levenson and N. Bloemberger, Phys. Rev. B 10, 4447 (1974).

ALGORITHM FOR OBTAINING AEROSOL BACKSCATTER  
CROSS-SECTION DISTRIBUTION WITH AN LDV\*

L. Z. Kennedy and H. B. Jeffreys  
Applied Research, Inc., P. O. Box 194  
Huntsville, AL 35804

An algorithm for obtaining the backscatter cross-section (bcs) distribution from cw LDV data at 10.6 microns has been developed. The LDV system must be focused so that single-particle signals dominate. A histogram of peak backscatter signals from single particles can be used to deconvolve the bcs distribution from the focal-volume sensitivity topology. This is accomplished by choosing, from a family of bcs distributions  $D(\sigma)$ , the one which best satisfies the equation

$$N(s) = L \int_{\sigma_L}^{\sigma_H} D(\sigma) A(s/\sigma) d\sigma$$

where

$\sigma$  = backscatter cross section

$s$  = peak single-particle signal

$N(s)$  = number of peak signals at  $s$

$A(s/\sigma)$  = focal-volume area which yields a peak signal  $s$  when penetrated by a particle with bcs  $\sigma$

$\sigma_H, \sigma_L$  = practical upper and lower bcs limits.

The simplicity of this formulation results from the LDV configuration, which is aircraft-based with optic axis perpendicular to the flight direction. Hence

$L$  = flight distance during data run.

The areas  $A(s/\sigma)$  must be known or obtained by calibration. Determining sensitivity profiles of the focal volume with a spinning wire yields these areas.

Knowledge of the bcs distribution provides information on aerosol constituents and size distribution, and also yields the backscatter coefficient for the LDV volume mode (as opposed to single-particle mode) of measurement.

---

\*Work supported by Marshall Space Flight Center, NASA.

Measurements of Multiply Scattered Radiation Contribution to Lidar  
and Transmissometer Signals

P.Bruscaglioni<sup>x</sup>, L.Lachi<sup>x</sup>, L.Lo Porto<sup>x</sup>, L.Pantani<sup>xx</sup>, L.Stefanutti<sup>xx</sup>,  
G.Zaccanti<sup>x</sup>

<sup>x</sup> Università di Firenze, <sup>xx</sup>IROE-CNR, Via Panciatichi, 64, Firenze, Italy

Lidar signatures and signals received by transmissometers can be analyzed in order to deduce the atmospheric extinction coefficient. In the case of dense fogs the contribution of multiply scattered radiation to Lidar received power, or of the forward diffused power to the transmissometer signals, must be generally taken into account.

A Lidar and a transmissometer have been assembled (1,2), for which the field of view angles of the receivers can be changed in steps. The instruments were used for field measurement campaigns, made with the aim to study multiple scattering effects, since it is recognized that these effects are strongly dependent on the aperture angles of the receivers.

While analyzing the Lidar returns one has to take into account the so-called form factor affecting the singly back scattered radiation. An analogous factor can be introduced to treat the contributions of higher orders of scattering. These factors have been computed, for several scattering function models, by using a particular form of the Monte Carlo method allowing us to examine the power received by elements of the receiver area placed off the symmetry axis of the coaxial apparatus.

An analysis has been made of some cases of Lidar signatures obtained for not too low visibility conditions, for which an assumption was made that first and second scattering effects could only be considered.

A simple theoretical scheme, actually only valid for homogeneous fogs, indicates that in such conditions the signal S received by the Lidar can be approximated as: (3)

$$S = S_1 (1 + \alpha a \sigma R)$$

where  $S_1$  is the signal due to singly scattered radiation,  $\alpha$  is the semi-aperture angle of the receiver,  $\sigma$  is the extinction coefficient,  $R$  is the Lidar range and  $a$  is a constant depending on the medium scattering function.

The analysis of the signatures showed that the values of the constant  $a$  obtained by using the above mentioned relation, is of the order of magnitude expected for water fogs. This applies when the visibility is greater than about 200 m.

- 1) L. Stefanutti, L. Pantani: *Optica Acta* 27, 1243, 1980
- 2) P. Bruscaglioni et al.: Rept. IV/A/2.14, Università di Firenze (December 1980)
- 3) P. Bruscaglioni et al.: *Optica Acta* 27, 1229, 1980.

LIDAR MULTIPLE RAMAN-MIE SCATTERING FROM A CLOUD

by

SMADAR EGERT, ARIEL COHEN AND MOSHE KLEIMAN  
Department of Atmospheric  
Sciences

The Hebrew University of Jerusalem

Raman shifted laser-radar echoes from clouds are attenuated due to the cloud droplets' extinction. However, multiple scattering effects in the presence of high optical-depth values in the cloud are adding to the expected signal from given altitudes. Such multiple scattering processes occur between any Raman molecular scattering ( $N_2$ ,  $O_2$  or any other gas with known spatial distribution) and any water droplet (or between a water droplet and a molecule) both contained within the field of view of the lidar system. In the case of double scattering, only two consecutive scatterings are taken into account, the first being within the transmitter field of view and the second within the receiving-system field of view. This case is valid for intermediate optical-depth values (0.1 to 0.4). The presence of a cloud acts as a "mirror" for the Raman scattering effect for all Raman scattering events occurring between the lidar and the cloud in both directions.

Here we present results of theoretical calculations for this effect and the expected contribution of the double scattering effect vs. the single scattering signal. The calculations are performed for a Deirmendjian C2 cloud and for 3 values of the receiving system field of view.

Results of field measurements are also presented and discussed.

2-D Laser Propagation Calculations  
Using Neutron Transport Methods

S. A. W. Gerstl and A. Zardecki  
Theoretical Division  
Los Alamos National Laboratory, University of California  
Los Alamos, NM 87545

and

R. C. Shirkey  
Atmospheric Sciences Laboratory  
White Sands Missile Range  
New Mexico 88002

ABSTRACT

The general applicability of modern neutron transport methods to the analysis of radiative transfer problems in the atmosphere has been demonstrated in Ref. 1 with special emphasis on one-dimensional geometries in non-homogeneous atmospheres. This paper describes a two-dimensional model calculation to quantify the radiation field that is generated by multiple scattering and target reflection when a 1.06  $\mu\text{m}$  laser beam propagates through an atmosphere that contains haze and smoke.

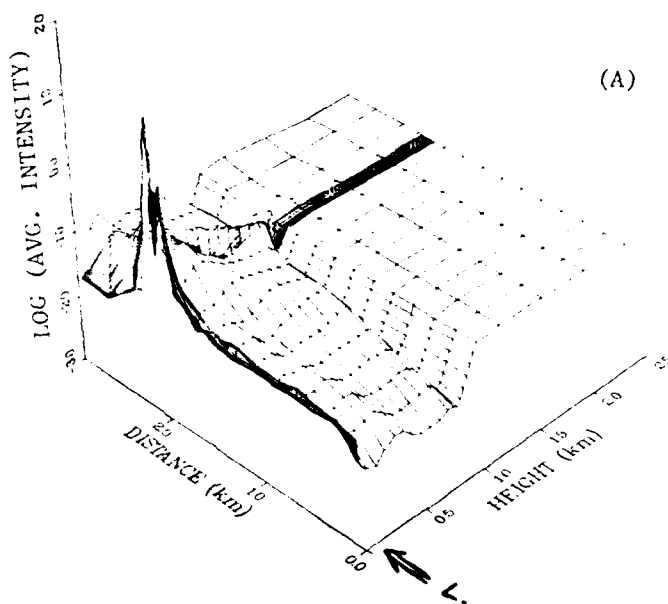
The two-dimensional radiative transfer equation is solved numerically by a finite-element discrete-ordinates ( $S_N$ ) method which is a variant of Chandrasekhar's discrete-ordinates method and is widely used to solve radiation transport problems for neutrons and gamma rays in nuclear systems. The general purpose code TWOTRAN<sup>2</sup>, which was originally developed by Los Alamos National Laboratory for nuclear radiation shielding applications, has been adapted to radiative transfer calculations of laser and solar radiation in realistic atmospheres. The rigorous solution of the fully two-dimensional radiative transfer equation is carried out iteratively until a pre-specified convergence criterion for the radiance at all spatial mesh points is achieved without resorting to a small-angle or other low-order (e.g. diffusion) approximation. All orders of multiple scattering are included and the highly forward peaked scattering characteristics of aerosols and smoke particulates are taken into account by using anisotropic scattering phase functions and other electro-optical data evaluated by the Atmospheric Sciences Laboratory<sup>3</sup>.

Figures 1 A and B show the result of a typical calculation where the spatial distribution of scattered radiation in the vicinity of the laser beam and its target is given up to distances of several kilometers under steady state conditions. In this model, a  $1.06 \mu\text{m}$  laser beam is pointed horizontally (along the axis labelled "Distance") at a reflective target (albedo 0.5) that is located at a distance of 2100 m from the beam source. As a realistic atmosphere we assume a homogeneous distribution of haze with a visual range of 10 km at  $0.55 \mu\text{m}$ . In addition, a smoke cloud of 50 m depth and 50 m height is assumed to be located between the laser beam source and target at 2000 m distance from the source. To study the influence of solar background radiation we include a solar boundary source at the top of our model at 2.5 km height but assume also the existence of a 200 m thick homogeneous cloud layer (Deirmendjian water cloud C1 distribution) with cloud top at 1000 m height and total optical depth of 5.

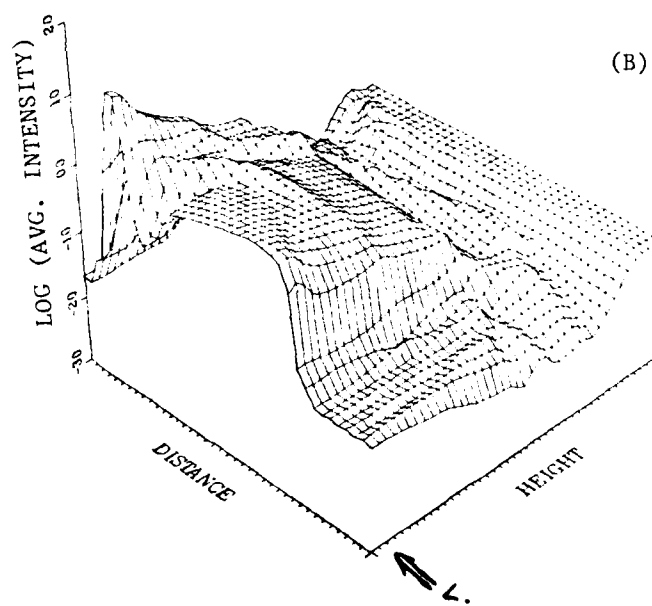
In the logarithmic plots of Figs. 1 A and B the average intensity (radiance integrated over all angles) of the scattered and reflected laser radiation is given at every two-dimensional spatial mesh point. The direct beam intensity is omitted. Dominant features in the plots are (a) the intensity peaks due to the target reflection and due to the multiple scattering in the smoke cloud, and (b) the intensity trough due to the rain cloud. Both figures show the same data; however, Fig. A is to scale, while the spatial scale in Fig. B is intentionally distorted to show more detail. The distortion represents every (non-equidistant) spatial mesh in Fig. B as if it were equally spaced. This feature allows the intensity "peak" created by the smoke cloud to be broadened and more easily recognizable in Fig. B. The optical depth of the smoke cloud for these sample results was 2.0. Additional results for more and less opaque smoke clouds will also be presented. In addition, the ratio of multiple scattered radiation to the directly reflected laser radiation as received in a detector with narrow field of view will be given.

#### References

1. S. A. W. Gerstl, "Application of Modern Neutron Transport Methods to Atmospheric Radiative Transfer," Int. Rad. Symp., Aug. 11-16, 1980, Fort Collins, CO, pp. 500-502 of Extended Abstracts.
2. K. D. Lathrop and F. W. Brinkley, "TWOTRAN Code for Two-Dimensional Transport," Los Alamos National Lab. report LA-4848-MS, July 1973.
3. R. C. Shirkey and S. G. O'Brien, "EOSAEL 80 Volume II Users Manual," Atmospheric Sciences Laboratory report ASL-TR-0073, White Sands Missile Range, NM, Jan. 1981.



(A)



(B)

Fig. 1: Average intensity (radiance integrated over all angles) of scattered and reflected radiation, in arbitrary units. Spatial dimensions in Fig. A are to scale. In Fig. B the spatial mesh is stretched in smoke and target locations. Wavelength  $\lambda=1.06 \mu\text{m}$ ; optical depth of smoke cloud = 2.0; of water cloud = 5; haze visual range = 10 km.

LIDAR STUDIES OF POLARIZATION  
ANISOTROPY IN MULTIPLE BACKSCATTERING  
S.R. PAL and A.I. CARSWELL  
YORK UNIVERSITY  
4700 KEELE ST.  
DOWNSVIEW, ONTARIO, CANADA, M3J 1P3

Our lidar investigations of clouds and of particulate suspensions have revealed some interesting features of multiple scattering that could be exploited to infer size information from backscatter polarization measurement.<sup>1</sup> The total multiple scattering in the backscatter field shows a characteristic build-up with pulse penetration and with increase in attenuation coefficient. However, the distribution of multiple scattering, polarized parallel and perpendicular to the polarization direction of the linearly polarized transmitted pulse, is found to be anisotropically distributed in the region surrounding the illuminated volume. This anisotropy is found to have a relationship with the size of the scattering particles and the probing wavelength. For sizes comparable to the wavelength the parallel polarized backscatter intensity is found to concentrate along the direction of polarization and orthogonal to it with the regions at azimuths of 45° showing very low intensity. The cross-polarized backscatter however shows intensity concentrated along the 45° directions with minima of intensity along and orthogonal to the initial polarization direction.

For particles much smaller than the probing wavelength the parallel polarized multiply backscattered radiation shows enhancement along the axis orthogonal to the initial polarization direction and negligible intensity along it. However the perpendicular polarization component of multiple scattering still exhibits maximum intensity in the directions at 45°. These features provide a potential method for deducing the size distribution of the scatterer from the spatial distribution of the polarization of the multiply-scattered signal.

In this paper we present our recent results on the evaluation of this method. Both lidar measurements and theoretical calculations for

spherical particles are presented. One interesting result of the analysis is that the calculations of single scattering using Mie phase functions for specific size parameters do exhibit the anisotropic polarization characteristics. The effects are most clearly evident at scattering angles around 90 degrees. Thus it appears that the polarization features observed in the multiple scattering are caused by these larger angle ( $\approx 90^\circ$ ) scattering events. This finding is particularly important since most multiple scattering calculations tend to favour scattering events in the near forward and near backward directions.

To extend the laboratory procedures into lidar measurements we introduced sector-shaped aperture slides in the lidar receiver focal plane. The sectors were designed to block all single scattering and to pass only a narrow angular field of the pure multiple scattering. This sector was aligned at different orientation angles in the focal plane in successive measurements. To study the polarization quantitatively, several receiver channels were used simultaneously with different combinations of sector orientations and polarizers.

Clouds were studied with this arrangement and all exhibited pronounced anisotropy in the backscattered multiple scattering. These results will be presented and discussed.

#### REFERENCE

1. A. I. Carswell and S. R. Pal, *Appl. Opt.* 19, 4123, 1980.

LASER BACKSCATTERING FROM DENSE  
WATER DROPLET CLOUDS

A.I. CARSWELL, R.B. SMITH, S.R. PAL, R. DUBINSKY  
DEPT. OF PHYSICS AND CRESS  
YORK UNIVERSITY  
4700 KEELE ST.

DOWNSVIEW, ONTARIO, CANADA, M3J 1P3

Laboratory studies of the propagation and scattering of laser beams in dense water droplet clouds have been undertaken for several years in our laboratory and in this paper a summary of recent results is presented. The work has been extended to investigate the wavelength dependence of the extinction and the backscattering. Wavelengths in the visible and near IR from several laser sources have been used .

In the backscattering measurements, the polarization characteristics have been measured at several wavelengths using a linearly polarized incident beam. The linear depolarization ratio (the ratio of the signals polarized perpendicular and parallel to the incident beam polarization direction) is found to exhibit some wavelength dependence. This dependence appears to arise from changes of the proportions of multiple and single scattering in the total backscattered signal at different wavelengths rather than from a change in the characteristics of the multiple scattering itself. This dependence, which is similar to that noted previously in atmospheric lidar returns, can be explained on the basis of diffraction theory and effects of receiver field of view.

In another series of experiments range-resolved measurements of the backscattering from water droplet clouds have been undertaken in the laboratory system. In lidar probing of the atmosphere the range resolution is one of the most important attributes of the system and it is obtained by using short pulses and performing a time-of-flight analysis via the lidar equation to provide range-resolved information from the backscattered signal. To use a similar approach in the laboratory would require the use of very short pulses and very wide bandwidth electronics because of the small distances involved. We have adopted an alternative approach which

utilizes selective chopping of the laser beam within the cloud and phase sensitive detection of the scattered radiation. We have used, for example, a pair of rotating chopper blades at different depths in the cloud along with a lock-in amplifier to measure the backscattered signal (including the polarization information) from thin slabs of cloud located at various distances within the cloud. In this way it has been possible to study the evolution of the scattered signal as it penetrates into the cloud. Since the laboratory clouds can be made to be very homogeneous and their properties can be carefully measured, it is possible to use such range resolved information to improve the analysis of beam propagation in very turbid media. Our initial measurements have shown the value of the technique and demonstrate that range resolutions of a few centimeters are readily obtained. Range resolved data are presented for measurements of the total backscattered signal and for the linear depolarization ratio which clearly shows the build-up of multiple scattering with increasing penetration depth.

Joint Polarization Lidar and  $K_{\mu}$ -band Radar  
Cloud Observations

Kenneth Sassen

University of Utah, Department of Meteorology  
Salt Lake City, Utah 84112

During the month of January 1982 the Mobile Polarization Lidar Facility of the University of Utah participated in the Colorado Orographic Seeding Experiment (COSE) in Steamboat Springs, Colorado. Gathered for this research program were an impressive array of remote sensing systems, including the ruby lidar, a dual-wavelength passive microwave radiometer, vertically-pointing  $K_{\mu}$ - and  $K_a$ -band radars and a scanning C-band radar. In addition, research aircraft, radiosonde, and ground-truth precipitation data were also collected. Co-located with the lidar at a mountain-base station (2.1 km MSL) were the microwave radiometer, with channels to detect emissions from both vapor and liquid water, and the 1.8 cm wavelength  $K_{\mu}$ -band radar.

Following a description of the new Mobile Polarization Lidar Facility, data comparisons which dramatically illustrate the differences and overlaps in sensitivities to hydrometeors of the remote sensors will be presented. As both the use of  $K$ -band radars and passive microwave radiometers have been stressed recently for incorporation into orographic cloud modification operations, their performance in this regard based on lidar data comparisons will be evaluated. Preliminary analysis has revealed that the polarization lidar observations can be considerably more sensitive to the presence of cloud liquid water and ice clouds composed of small or diluted concentrations of ice crystals, although, as expected, strong optical attenuation in snowfall or dense water clouds would often limit the range of lidar probing. Presented in Figure 1 is a comparison of lidar and  $K_{\mu}$ -band radar (vertically-pointing) data obtained over a 3½ hour period from a layer cloud associated with a frontal cloud band which illustrates some of these findings. In this case, it was only during a few periods that optical attenuation appeared to seriously limit the range of lidar operations (generally corresponding to times with radar reflectivities  $> 5$  to 10 dBZ), while particularly near the end of this period the radar failed to detect an ice cloud that lidar measurements show was ~3.5 km thick.

Another interesting finding that has implications for both lidar and radar operations is that layers of uniformly oriented ice crystals were identified from the lidar returns during several storms. Such regions could be identified by scanning the lidar several degrees away from the vertical direction, so that the non-depolarized specular reflections were no longer received, but a preliminary comparison with  $K_{\mu}$ -band returns suggests that the radar reflectivities were anomalously enhanced by the same ice crystal orientation effects. The effects of such microphysical processes on the remote sensor returns and comparisons of liquid water detection by the lidar and microwave radiometer will be fully discussed.

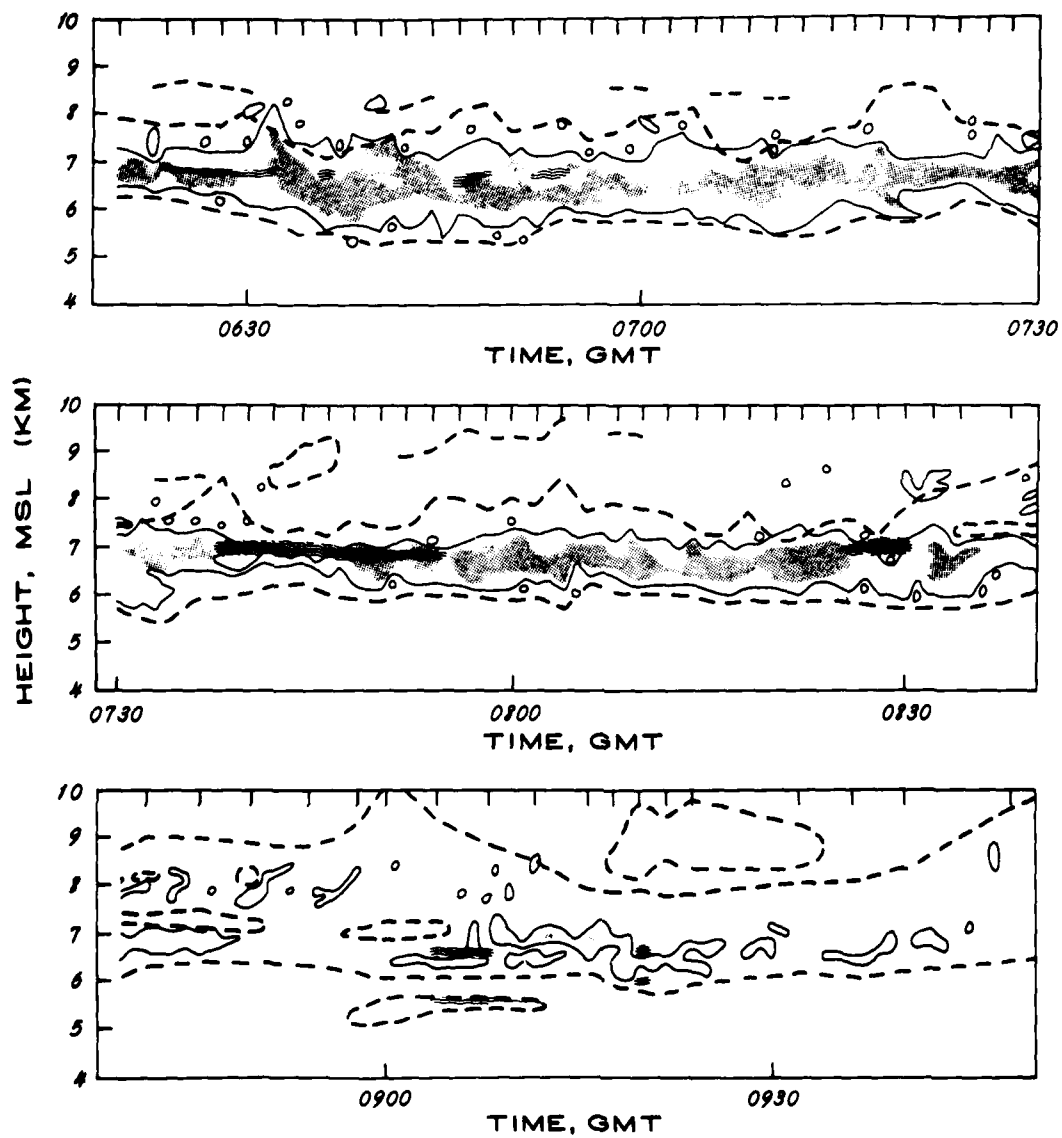


Figure 1. A time versus height comparison of vertically-pointing ruby lidar and K<sub>u</sub>-band radar data representing a segment of a frontal cloud band passage over Steamboat Springs, Colorado. The envelopes of lidar and radar ( $> -15$  dBZ) returns are shown as dashed and solid lines, respectively. The discontinuous dashed lines represent weak, intermittent laser returns from higher-level cloud tops or layers. Stippled areas define radar reflectivities  $> 5$  dBZ, and regions with wavy lines show the presence of liquid water-containing cloud layers as identified through laser depolarization measurements (collected at the times indicated by the vertical lines along the top margin).

MEASUREMENT OF THE STOKES PARAMETERS FOR CIRRUS CLOUDS  
USING INCOHERENT AND COHERENT LIDAR SYSTEMS

Ingar Singstad  
University of Bergen, Norway\*

\*Guest Worker, National Oceanic and Atmospheric Administration  
Environmental Research Laboratories  
Wave Propagation Laboratory  
Boulder, Colorado 80303

Cirrus cloud cover is of importance in understanding atmospheric radiation and the heat budget of the earth. The radiation properties of the cirrus clouds depend on several factors, such as shape, orientation and size distribution of the ice crystals and on bulk properties such as ceiling height and thickness of the clouds. One interesting aspect of the cirrus clouds is the question about the alignment of the ice crystals.

Fluid dynamical experiments have shown that needle shaped crystals fall with the long axis (the optical axis) horizontally and that hexagonal plates fall vertically with the flat face down. The plates then have the optical axis oriented vertically. This fact will have consequences for the polarization properties of the backscattered laser light from an aligned population of ice crystals.

By using a rotating polarizer and a quarter-wave plate, one can obtain the four Stokes parameters for the reflected light when the clouds are illuminated with a polarized laser beam (Houston and Carswell, 1978). In lidar experiments, the Stokes parameters frequently are expressed in terms of the parameters for the polarization ellipse. They are the rotational angle  $\chi$ , which is the angle between the major axis of the ellipse and the direction of the incident polarized light, and the ellipticity  $\epsilon = \pm b/a$ . Here  $a$  and  $b$  are the major and minor axis of the ellipse, respectively. The depolarization ratio  $\delta$  is an important parameter, defined as  $P_1/P_{11}$ .  $P_{11}$  and  $P_1$  are the backscattered intensities measured parallel and perpendicular to the emitted laser light.

Ice crystals are double refracting; therefore, there generally is an elliptical contribution in the backscattered light due to scattering inside the crystals. Furthermore, the ice crystals are optically positive and this produces  $\epsilon > 0$ . The magnitude of  $\epsilon$  depends on the crystal size, shape, orientation of the optical axis and the ratio between the thickness of the crystal and the laser wavelength. The rotational angle  $\chi$ , too, depends on the size of the crystal and the laser wavelength.

The polarization plane may be changed by internal reflection in the ice crystals. The depolarization ratio  $\delta$  can be used to discriminate between water and ice phases in clouds, supposing a randomly oriented ice particle population. However, scattering from horizontally aligned plates will also result in  $\delta = 0$ .

Generally, the backscattering from aligned plates results in  $\epsilon = 0$ ,  $\delta = 0$ , and  $\chi = \text{constant}$ .  $\chi$  will vary through the cloud if the crystal dimensions change. For horizontally aligned needles we have  $\epsilon > 0$ ,  $\delta > 0$ , and  $\chi = \text{constant}$ . The Stokes parameters may thus be very useful when interpreting lidar data from clouds.

At the University of Bergen, Norway, we have a two-channel, incoherent, ruby lidar system. Two laser pulses in about 1/2 minute provide the necessary data on the Stokes parameters, even if several shots may be needed because of the counting statistics. We have found that typical depolarization ratios for winter cirrus clouds are between 0.35 and 0.7. The data are obtained with the beam propagated vertically. The Stokes parameter data indicate that the ice crystals basically are randomly oriented. A few examples can be interpreted as oriented needles. The signature of oriented plates was not found in the data. As mentioned, plates with a horizontal orientation result in  $\delta = 0$ . Tilting the laser beam produces elliptically reflected light and  $\delta > 0$ . This was shown by Platt et al. (1978) using the NOAA incoherent lidar.

The field of view of an incoherent lidar is about 1 mrad as compared to less than 0.1 mrad for the NOAA coherent system. Consequently, one should expect relatively stronger specular reflection from aligned plates with a coherent system than with an incoherent one. Besides, the contribution from multiple scattered photons is negligible with a coherent system. At a wavelength of  $10.6 \mu\text{m}$ , the contribution from internal reflection in the crystals will be small.

At NOAA, we plan to use the coherent Doppler lidar for Stokes parameter measurements in the study of cirrus clouds and alignment of the ice crystals. Furthermore, the Doppler lidar facilities can measure the fall velocities of the ice crystals from the cirrus clouds.

The Stokes parameters are obtained by rotating a quarter-wave plate while keeping the polarizer fixed. In a coherent system, the local oscillator beam picks out the polarization component of the reflected beam and thus works as a polarizer. Preliminary results of the experiment will be presented at the conference.

#### References:

1. Houston, J. D. and A. I. Carswell, 1978, *Appl. Opt.* 17, 619-20.
2. Platt, C.M.R., N. L. Abshire, and G. T. McNice, 1978, *J. Appl. Meteor.* 17, 1220-24.

LIDAR  
OBSERVATIONS OF CLOUD TOP STRUCTURE  
AND SCATTERING POLARIZATION

J. D. Spinhirne and M. Z. Hansen  
NASA/Goddard Space Flight Center, Code 913  
Greenbelt, Maryland 20771

Over the past several years a cloud lidar system (CLS) has been deployed on high altitude aircraft cloud observation missions. The instrumentation configuration and some initial data acquired in Fall 1979 have been previously reported.<sup>1,2</sup> In May-June 1981 a further set of flights were undertaken in conjunction with the large scale CCOPE experiment. A modified configuration, shown in Fig. 1, was employed for these later flights. The major additions to the instrument were a 1064 nm detector to supplement the dual polarization 532 nm detectors and also an increase to a 20 MHz data acquisition bandwidth.

The acquired data includes a wide variety of cloud top structure and scattering polarization observations. These encompass high, low and middle cloud groupings of various types. Several cases of multiple overflights of developing cumulonimbus have been acquired. These data graphically present the height resolved structure of storms in a manner not previously realized. The polarization diversity of the signal return is seen to delineate ice-water phase changes at upper cloud boundaries and also, to some extent, changes in crystal types. Although airborne cloud lidar data will not supplant in-situ observations for cloud physics and storm development studies, it can be shown that our data provides a useful adjunct to in-situ and other remote sensing observations. In several cases during the 1981 CCOPE observations, simultaneous cloud particle measurements were obtained by aircraft underflying the CLS.

Analysis development is in progress to obtain the maximum interpretation of the dual polarization, dual wavelength cloud lidar data in terms of physical cloud particle parameters. A major application of the cloud lidar measurements will be to corroborate simultaneous passive remote sensing observations. A summary of results obtained by the CLS to date is to be presented.

### References

1. Spinhirne, J. D., M. Z. Hansen and L. O. Caudill, 1982; Cloud top remote sensing by airborne lidar, Appl. Opt., (in press).
2. Hansen, M. Z., J. D. Spinhirne and L. O. Caudill, 1980; Application of a high altitude cloud top lidar sensor, Tenth ILRC, Silver Spring, Maryland.

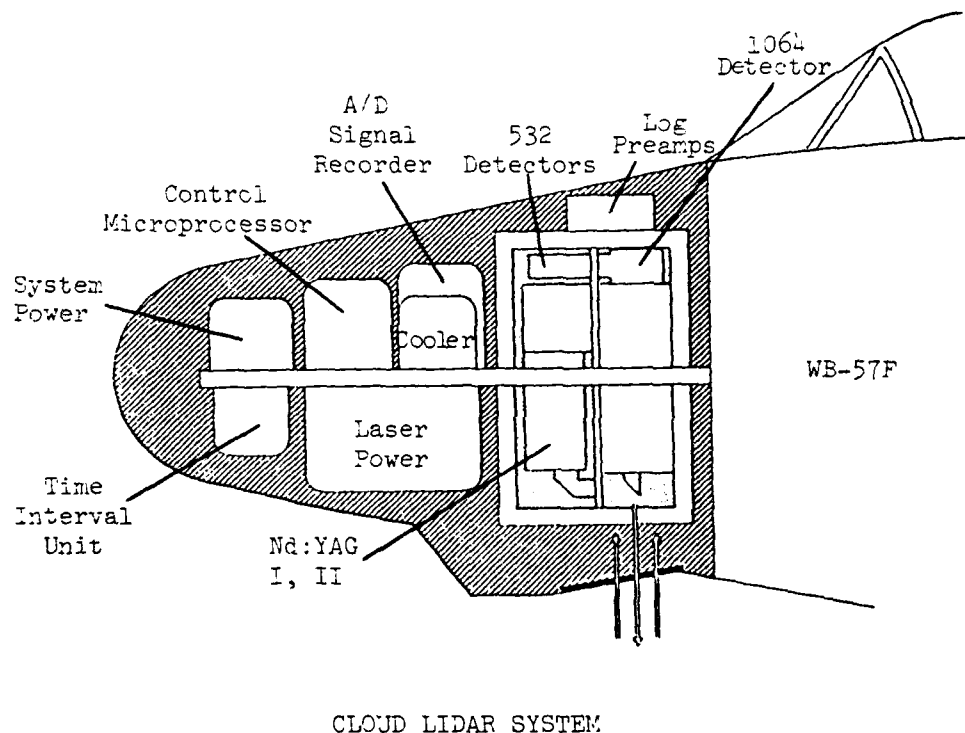


Figure 1

A PATH-AVERAGED LASER RAIN GAUGE FOR  
SATELLITE/EARTH COMMUNICATIONS APPLICATIONS

D. J. Fang and C. H. Chen

COMSAT Laboratories  
22300 Comsat Drive  
Clarksburg, Maryland 20871

In satellite communications systems utilizing automatic power control and/or polarization compensation networks, a knowledge of instantaneous area rainfall information is essential. This knowledge cannot be supplied by a conventional tipping bucket rain gauge, which has a slow response and a low saturation level. The paper examines laser sensing techniques for the development of a high precision/fast resolution rain gauge using an HeNe laser. Optical configurations, detection schemes and data acquisition and processing algorithms are presented. Preliminary field trial results in determining instantaneous rain rates and raindrop size distributions are summarized. It is established that such an optical system can sample precipitation accurately, not only in the far field region, but also in the near field. Applications in modern satellite communications systems are outlined.

## LIDAR BACKSCATTER MEASUREMENTS IN FALLING SNOW

G. Davidson, A. Bogdan, D. McCaffrey  
PhotoMetrics, Inc.\* Woburn, MA, 01801

John D. Mill  
Air Force Geophysics Laboratory  
Hanscom Air Force Base, MA, 01731

Measurements were made during December 1981 and January 1982 of backscatter in falling snow at a field location near Burlington, Vermont. These measurements were performed as part of a coordinated measurements program, entitled SNOW ONE-A, which included many other optical and non-optical correlated experiments. The lidar measurements utilized a frequency-doubled Nd:Yag laser yielding 15 mJ pulses at 0.53  $\mu$ m at a 20 Hz pulse rate. The use of the lidar allowed slant-path (near-horizontal to zenith) measurements of range-resolved backscatter to be made, from which extinction in snow could be deduced.

In general, data was taken as sets of returns averaged over 1 to 25 seconds. Individual returns were digitized with 10 bit resolution at a 10 MHz rate. The data was reduced in near real time and stored on disk. Analysis is being performed using the Klett<sup>1</sup> method to determine extinction coefficients.

Preliminary lidar extinction results are being compared to results of measurements taken by a visible transmissometer operating at 0.55  $\mu$ m. The transmissometer operated over a 300 m horizontal path some distance from the lidar path.

---

\*This work was sponsored by Air Force Geophysics Laboratory

<sup>1</sup>J. D. Klett, Appl. Opt. 20, 211(1981)

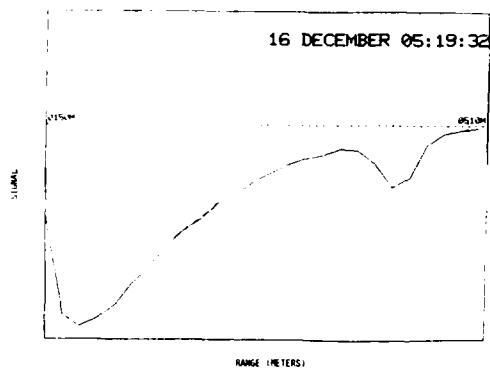


Fig. 1. Lidar Return

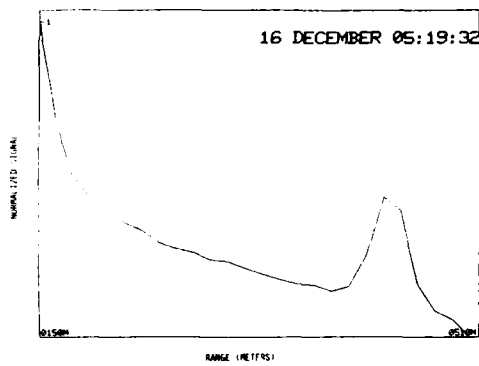


Fig. 2. Corrected Return

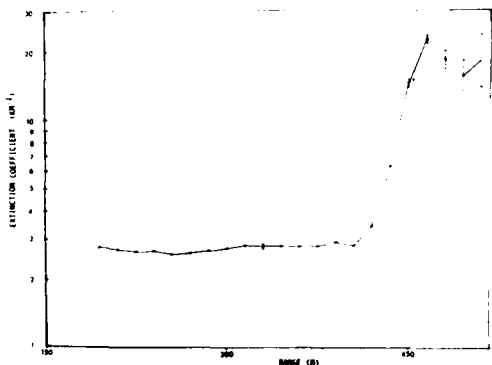


Fig. 3. Extinction

Figure 1 shows a return signal in moderate snowfall averaged over 128 laser pulses (6.4 sec). The lidar was pointing at an angle of  $45^\circ$  with respect to the horizontal. In the figure, signal strength increases in the negative direction. The initial increase is due to gain switching of the photomultiplier tube. The increase in signal near a range of 450 m is due to backscatter from a cloud at an altitude of approximately 320 m.

Figure 2 is the same data corrected for gain and the  $1/r^2$  signal dependence, and normalized to the 150 m return signal.

Figure 3 shows the computed extinction coefficient as a function of range. This particular falling snow condition has an extinction coefficient of  $\approx 2.8 \text{ km}^{-1}$ . Preliminary data from the visible transmissometer yields a value of  $\approx 4.8 \text{ km}^{-1}$  in the horizontal direction at this time. Extinction within the cloud shows a value of  $\approx 20 \text{ km}^{-1}$ .

Additional lidar data under a variety of precipitation conditions will be presented.

## PHASE FUNCTION MEASUREMENTS OF SNOW CRYSTALS

L.W. Winchester, Jr.  
Keweenaw Research Center  
Michigan Technological University  
Houghton, Michigan 49931

With the expanding use of electro-optical devices in both military and civilian areas, an understanding of the scattering of light by snow crystals is needed to assess the performance of electro-optical systems in blowing and falling snow. Since the orientation of the snow crystals as well as their size and shape must be considered when calculating scattering, the phase functions of various types of snow crystals are needed in order to compute the transmission through a snowy atmosphere. The snow crystal phase functions are also of importance in problems involving radiative transfer in cloud atmospheres, since high altitude clouds consist mainly of ice crystals.

Previous experimental studies of the phase function of ice crystals have been concerned with artificial ice crystals. Huffman and Thursby (1969) used a polar nephelometer employing a filtered xenon arc lamp as a source operating at 0.55 micrometers to measure scattering from microscopic ice crystals grown in a refrigerated chamber. They reported that the phase functions of hexagonal plates, hexagonal columns and irregular ice crystals were identical at angles less than 130°. Compared with calculations using Mie theory for equivalent spheres, the ice crystals produced more lateral scattering, i.e. scattering in the angular range of 60° to 130°. Since the phase function  $f(\theta)$  is normalized as shown below,

$$1 = \frac{1}{2} \int_0^{\pi} f(\theta) d\theta$$

the increase in lateral scattering must be accompanied by a corresponding decrease in forward scattering and/or back-scattering. Haloes at 22° and 46° have been reported by Dugin et al. (1971), Nikiforova et al. (1977) and Volkovitskiy et al (1980) for artificial ice crystals.

Since the experimental studies have shown that the phase functions of snow crystals, with the possible exception of graupel, cannot be approximated using Mie theory computations for spheres with either equivalent area or equivalent volume, it is necessary to examine other methods of obtaining the phase function of snow crystals. A polar nephelometer has been constructed at the Keweenaw Research Center to measure the phase function of various types and sizes of particles. A helium-neon laser

operating at a wavelength of 0.6328 micrometers is used as a light source and two photomultiplier tubes mounted on moveable arms are used as detectors. Snow crystals are brought through a vertical chute leading from the roof to the scattering volume located above the pivot of the two arms by creating a slightly reduced pressure in the laboratory. The rate at which particles are brought into the scattering volume is controlled by regulating a pressure gradient between the room and the outside. Scattered light is collected by a lens placed in front of each photomultiplier and focused onto the photocathode. The reference arm is placed at an angle of 15° while the measurement arm is used to measure the phase function. As a snowflake falls through the laser beam a pulse is observed at the output of each phototube. Coincidence of pulses from both the reference and measurement phototubes is used to ascertain that the snowflake did pass through the scattering volume and not a part of the laser path visible to only one photomultiplier. To insure that the snow crystals do not change phase during the experiment, the room is allowed to cool to the outside temperature.

The phase function of ice circular cylinders was measured during an intense snow storm on November 15, 1980. The measurements were made with unpolarized light since a complete set of polarized measurements would require at least four hours. Data were taken between 10° and 170° in 5° intervals. At each scattering angle, a minimum of 51 events were recorded. The cylinders fell with their axes oriented in a vertical direction. Ice crystals were collected and examined after every fourth set of phase function measurements. The crystal size and shape remained constant during the two-hour experiment. The crystals were circular cylinders with an average length of 2.1 millimeters and an average radius of .125 millimeters. Very little riming was observed. Comparison of crystal size and shape measurements in the laboratory and outside showed that the system which delivered the crystals to the scattering volume had no effect on the crystal size or shape. The phase function values were determined by averaging the measurements at each scattering angle and then normalizing at 10°. The standard deviation at each point is plotted as an error bar. The phase function in Fig. 1 shows a deeper minimum and less lateral scattering than the measurements of Huffman and Thursby (1969). This is consistent with the snow crystals observed in this study being much larger than the artificial ice crystals used in all other studies as more energy goes into forward scattering for larger particles.

Liou (1972) has developed a straightforward method for computing the phase function of circular cylinders. The wave vector of the incident radiation was assumed to be perpendicular to the cylinder axis and the scattered intensities were summed over all possible polarization combinations. The result, shown in Fig. 1, has been averaged over a 5°

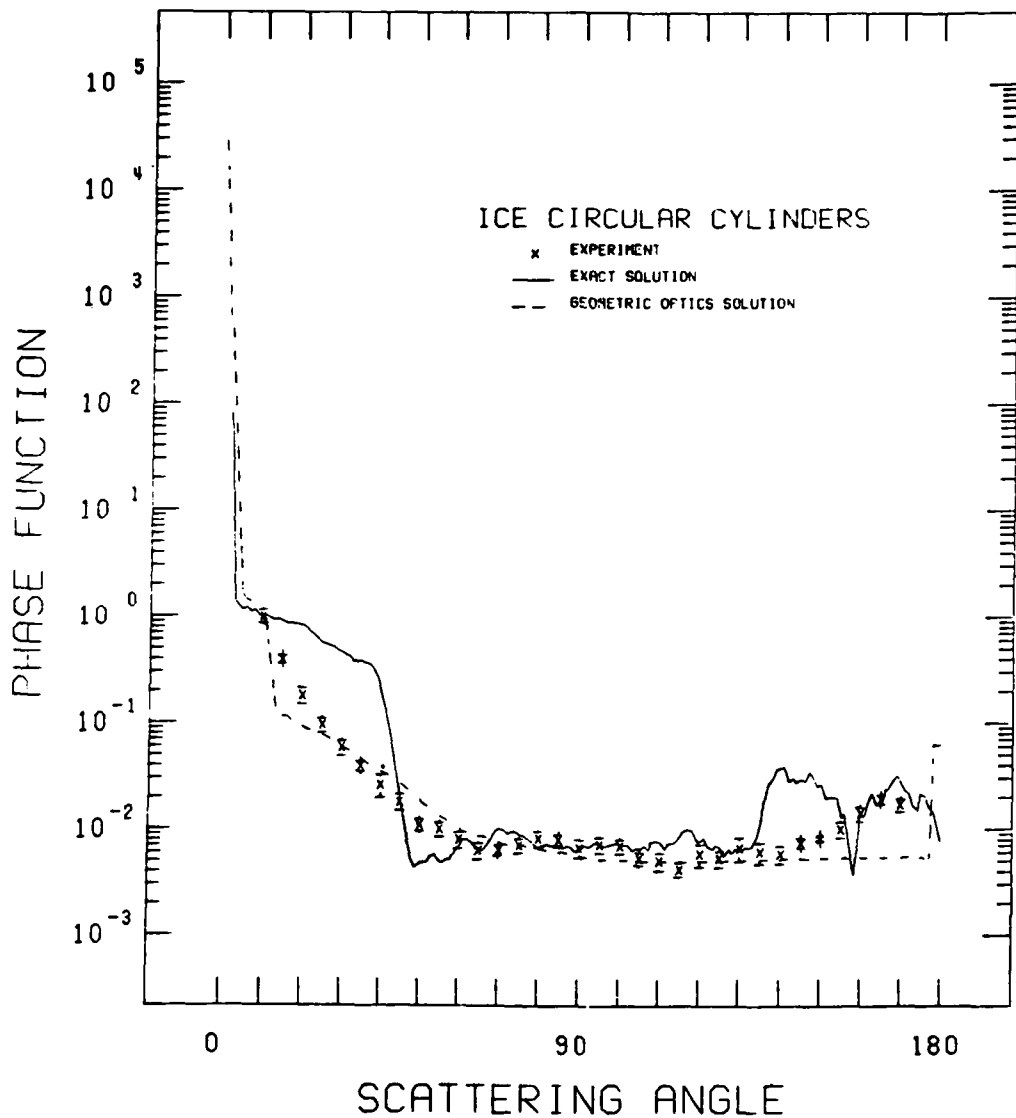


Fig. 1. Comparison of experimental measurements with computations

collection angle and normalized at  $10^\circ$ . The exact calculation using the method of Liou (1972) predicts much more scattering between  $10^\circ$  and  $40^\circ$  and icebows at  $143^\circ$  and  $168^\circ$ . The computed phase function has some structure between  $70^\circ$  and  $130^\circ$ , but it does not match the structure shown by the data. The general intensity level of the lateral scattering does agree with experiment as does the intensity of back-scattering near  $160^\circ$ .

Several ray tracing methods have been reported for hexagonal platelets and hexagonal columns (Jacobowitz, 1971; Wendling et al., 1979; Liou and Coleman, 1980). These methods follow the internal path of a ray inside the ice crystal

for up to six internal reflections. Since natural ice crystals such as snow are formed by successive deposition and scavenging it is reasonable to assume that each crystal is made up of many small domains. In the case of the circular cylinder some of the domains may be annular with the crystals resembling the rings of a tree. There is considerable scattering and absorption of light at the domain interfaces. A ray tracing model for a circular cylinder oriented with the cylinder axis vertical was used to obtain a geometric optics solution for the phase functions. The method follows each ray path through the crystal and assumes that radiation not exiting the crystal on the first pass is lost. The externally reflected and transmitted components are studied for 6000 equally spaced rays incident on the cylinder. A single rectangular diffraction pattern is then added to give the phase function which has been normalized at  $10^\circ$ . The result is shown as the dashed curve in Fig. 1. The agreement between the ray tracing solution and the data is quite reasonable at scattering angles less than  $140^\circ$ . In the geometrical optics approximation the backscattering from a cylinder is concentrated near  $180^\circ$  instead of in a broad peak as seen in the data. The broadening of the backscattering is attributed to rays which have undergone two internal reflections and to surface roughness.

#### References

Dugin, V.P., B.M. Golubitskiy, S.O. Mirumyants, P.I. Paramoniv, and M.V. Tantashov, *Atmos. Oceanic Phys.* 7 581 (1971)

Huffman, P.J. and W.R. Thursby, Jr., *J. Atmos. Sci.* 26 1073 (1969)

Jacobowitz, H. *J. Quant. Spectrosc. Radiat. Transfer* 11 691 (1971)

Liou, K.-N., *Appl. Optics* 11 667 (1972)

Liou, K.-N. and R.F. Coleman, *Light Scattering by Irregularly Shaped Particles*, D.W. Schuerman, ed., Plenum, New York, p.207 (1980)

Nikiforova, N.K., L.N. Pavlova, A.G. Petrushin, V.P. Synkov, and O.A. Volkovitskiy, *J. Aerosol Sci.* 8 243 (1977)

Volkovitskiy, O.A., L.N. Pavlova, and A.G. Petrushin, *Atmos. Oceanic Phys.* 16 156 (1980)

Wendling, P., R. Wendling, and H.K. Weickmann, *Appl. Optics* 18 2663 (1979)

## AUTHOR INDEX

The paper numbers are preceded by the capital letter designation of the session in which the papers were presented (see Contents). Page numbers are given in parentheses.

Alden, M., C6 (67)  
Anderson, A. J., H1 (191)  
Asai, Kazuhiro, D2 (95)  
Asculai, E., F6 (165)  
  
Baba, Hiroshi, D6 (108)  
Bair, C. H., C10 (82)  
Bao Ling-ming, H3 (196)  
Bedo, D. E., B1 (21)  
Bilbro, James W., D12 (123), G6 (179)  
Boers, R., F2 (156), G2 (169)  
Bogdan, A., I10 (245)  
Brockman, P., C10 (82)  
Browell, E. V., B6 (34), C4 (60), F5 (161)  
Brun, C., B8 (41)  
Bruscaglioni, P., I1 (228)  
Bufton, J. L., A7 (17)  
Burlamacchi, P., D14 (129)  
Butler, C. F., B6 (34), C4 (60)  
  
Cahen, C., B7 (37)  
Capitini, R., B8 (41), C7 (70)  
Carnuth, W., A3 (4)  
Carswell, A. I., I4 (234), I5 (236)  
Carter, A. F., B6 (34), C4 (60)  
Castagnoli, F., H5 (201)  
Cecchi, G., D14 (129)  
Champion, K. S. W., B1 (21)  
Chandler, R., D12 (123)  
Chen, C. H., I9 (244)  
Churchill, David K., D5 (104)  
Clem, D., B9 (45)  
Cohen, Ariel, F6 (165), I2 (230)  
Coletti, Alessandro, H12 (217)  
Cooney, John, H15 (224)  
Cotnoir, L., B4 (30)  
Coulter, R. L., F2 (156), G2 (169)  
Cvijin, P. Vujkovic, C2 (55)  
  
Davidson, G., I10 (245)  
Deepak, A., H13 (219)  
DeFeo, William E., C5 (64)  
DiMarzio, C., D12 (123)  
Dombrowski, Mark, B3 (26)  
Dubinsky, R., I5 (236)  
  
Eberhard, Wynn L., E3 (143), E4 (145)  
Edner, H., C6 (67)  
Egert, Smadar, I2 (230)  
Eloranta, E. W., D8 (113), F2 (156), G2 (169)  
Emmitt, G. D., G8 (187)  
Evans, B. T. N., D10 (120), E6 (152)  
  
Fang, D. J., I9 (244)  
Farrukh, U. O., H13 (219)  
Fernald, Frederick G., H10 (213)  
Fichtl, George H., G6 (179)  
Fitzjarrald, Daniel, G6 (179)  
Flamant, P. H., D1 (91)  
Fredricksson, K., C1 (47)  
Funk, W., A3 (4)  
  
Garcia, J. P., H1 (191)  
Gardner, C. S., A7 (17)  
Gaumet, J. L., H4 (197)  
Gehlhaar, U., D13 (127)  
Gerstl, S. A. W., I3 (231)  
Goad, Joseph H., Jr., A6 (14)  
Goela, J. S., D11 (122)  
Goldsmith, C. L., H1 (191)  
Grams, Gerald W., H12 (217)  
Gross, Abraham, H15 (224)  
  
Hagard, Arne, H7 (208)  
Hall, F. F., Jr., G3 (171)  
Hall, W. M., B6 (34)  
Hansen, M. Z., B9 (45), I8 (242)  
Hao Nan-jun, H3 (196)  
Hardesty, R. Michael, D5 (104), G4 (172)  
Hasson, V., D7 (111)  
Heaps, William S., C8 (75)  
Herrmann, H., E5 (149)  
Hertz, H., C1 (47)  
Hess, R. V., C10 (82)  
Hofmann, D. J., A5 (13)  
Hooper, W. P., F2 (156), G2 (169)  
Houston, D., D10 (120)  
Hu Yu-liang, B5 (33)  
Huang Qi-rong, B5 (33)

Huang Zhong-fang, B5 (33)  
 Huffaker, R. Milton, G3 (171), G7 (183)

Igarashi, Takashi, D2 (95)  
 Itabe, Toshikazu, D2 (95)

Jäger, H., A3 (4), A5 (13)  
 Jeffreys, H. B., H16 (227)  
 Jensen, A. Skov, G1 (166)  
 Jin Hui-shu, B5 (33)  
 Joos, E., C7 (70)

Kavaya, M. J., D1 (91)  
 Keeler, R. Jeffrey, D5 (104)  
 Kennedy, L. Z., H16 (227)  
 Kent, G. S., A4 (8), H13 (219)  
 Killinger, Dennis K., C5 (64), C11 (87)  
 Kleiman, Moshe, F6 (165), I2 (230)  
 Kluchert, R. E., D10 (120)  
 Koga, Ryuji, C3 (56)  
 Kondo, Masamichi, D6 (108)  
 Köpp, F., E5 (149), G5 (176)  
 Korb, C. Laurence, B3 (26), C9 (78)  
 Kosaka, Megumi, C3 (56)  
 Krause, Michael, D12 (123), G6 (179)  
 Krishna Murthy, B. V., H11 (216)

Lachi, L., I1 (228)  
 Lading, L., G1 (166)  
 Lawrence, Robert S., F1 (154)  
 Lawrence, T. R., D4 (103)  
 Lebow, P., B4 (30)  
 Lefrere, J., B2 (23), B7 (37)  
 Lentz, W. J., H9 (211)  
 Lesne, J-L., B7 (37)  
 Livingston, John M., H2 (192)  
 Lo Porto, L., I1 (228)  
 Lynch, Mervyn J., E3 (143)

Matsui, Ichiro, E1 (137)  
 Mayo, M. N., B6 (34)  
 Mazzinghi, P., D14 (129)  
 McCaffrey, D., I10 (245)  
 McCormick, M. P., A2 (2), A4 (8)  
 McElroy, James L., E2 (141)  
 McNice, G. T., E3 (143), E4 (145)  
 McQuirk, Michael, G7 (183)  
 Measure, Edward, H8 (210)  
 Megie, G., B2 (23)  
 Melfi, S. H., B9 (45)  
 Menyuk, C. R., C11 (87)  
 Menyuk, Norman, C5 (64), C11 (87)  
 Menzies, R. T., D1 (91)

Michelin, J-M., B7 (37)  
 Mill, John D., I10 (245)  
 Morandi, M., H5 (201)  
 Mörl, P., F4 (160)

Nakane, Hideaki, E1 (137)

O'Reilly, J., D12 (123)  
 Osborn, M., A1 (1)  
 Osmundson, John S., G7 (183)

Pal, S. R., I4 (236), I5 (236)  
 Pantani, L., D14 (129), I1 (228)  
 Parameswaran, K., H11 (216)  
 Petheram, John C., D3 (99)  
 Philip, M. T., A4 (8)  
 Pippi, I., D14 (129)

Qui Jin-huan, H3 (196)

Reagan, J. A., H1 (191)  
 Reiter, R., A3 (4), A5 (13)  
 Renaut, D., B8 (41), C7 (70)  
 Renger, W., F4 (160)  
 Roesler, F. L., D8 (113)  
 Rosen, J. M., A5 (13)  
 Rosenberg, A., B4 (30)  
 Rubio, Roberto, H8 (210)  
 Russell, Philip B., H2 (192)

Sakurai, Katsumi, D6 (108)  
 Sano, Hiroya, C3 (56)  
 Sasano, Yasuhiro, E1 (137), F3 (157)  
 Sassen, Kenneth, I6 (238)  
 Scheilhase, R., F4 (160)  
 Schotland, R. M., H14 (223)  
 Schwemmer, Geary, B3 (26)  
 Schwiesow, Ronald L., F1 (154), G1 (166)  
 Sechrist, C. F., Jr., A7 (17)  
 Shaw, K., D12 (123)  
 She, C. Y., D9 (117)  
 Shimizu, Hiroshi, D9 (117), F3 (157)  
 Shinohara, Koji, C3 (56)  
 Shipley, S. T., C4 (60), F5 (161)  
 Shirkey, R. C., I3 (231)  
 Simizu, Hiroshi, E1 (137)  
 Singstad, Ingvar, I7 (240)  
 Siviter, J. H., Jr., B6 (34)  
 Smith, R. B., I5 (236)  
 Spinhirne, J. D., B9 (45), I8 (242)  
 Sroga, J. T., D8 (113)  
 Stefanutti, L., H5 (201), I1 (228)  
 Steinvall, Ove, H6 (208)

Strobel, S., B4 (30)  
Sugimoto, Nobuo, D6 (108), E1 (137)  
Sun Jin-hui, H3 (196)  
Svanberg, S., C6 (67)  
Swirbalus, R. A., B1 (21)  
Swissler, T. J., A1 (1)

Takeuchi, Nobuo, D6 (108), E1 (137),  
F3 (157)  
Taylor, S. E., D15 (132)  
Thomas, E. L., D15 (132)  
Van Dijk, J. W., D3 (99)  
Wang Hong-qi, H3 (196)  
Weng, Chi Y., C9 (78)  
Werner, Ch., E5 (149), H6 (205)

Wilkerson, T. D., B4 (30), B6 (34)  
Winchester, L. W., Jr., I11 (247)  
Winker, D. M., H14 (223)  
Wu Shao-ming, B5 (33)  
Xia Qi-lin, H3 (196)  
Yue, G. K., H13 (219)  
Zaccanti, G., I1 (228)  
Zardecki, A., I3 (231)  
Zhang Bei-ying, H3 (196)  
Zhang Chun-lin, B5 (33)  
Zhang Jin-ding, H3 (196)  
Zhao, Yan-zeng, B5 (33), H3 (196)  
Zheng Si-ping, B5 (33)

1. Report No. NASA CP-2228	2. Government Accession No. <i>AD-A116 294</i>	3. Recipient's Catalog No.	
4. Title and Subtitle  ELEVENTH INTERNATIONAL LASER RADAR CONFERENCE	5. Report Date June 1982	6. Performing Organization Code 665-40-40-10	
7. Author(s)	8. Performing Organization R No. L-15380	10. Work Unit No.	
9. Performing Organization Name and Address  NASA Langley Research Center Hampton, VA 23665	11. Contract or Grant No.	13. Type of Report and Period Covered Conference Publication	
12. Sponsoring Agency Name and Address  Space Science and Engineering Center University of Wisconsin American Meteorological Society U.S. Air Force National Aeronautics and Space Administration	14. Sponsoring Agency Code		
15. Supplementary Notes			
16. Abstract  This publication contains abstracts of papers presented at the Eleventh International Laser Radar Conference, held at the University of Wisconsin-Madison, June 21-25, 1982. Eighty-nine papers were presented. The topics of the conference sessions were	<ol style="list-style-type: none"> <li>1. Middle atmospheric measurements</li> <li>2. Meteorological parameters: temperature, density, humidity</li> <li>3. Trace gases by Raman and DIAL techniques</li> <li>4. Techniques and technology</li> <li>5. Plume dispersion</li> <li>6. Boundary layer dynamics</li> <li>7. Wind measurements</li> <li>8. Visibility and aerosol properties</li> <li>9. Multiple scattering, clouds, and hydrometers</li> </ol> <p>This conference manifests a maturing technology. The abstracts discuss measurements of properties from the Earth's ocean surface to the mesosphere, made with techniques ranging from elastic and inelastic scattering to Doppler shifts and differential absorption.</p>		
17. Key Words (Suggested by Author(s))  Lidar Laser radar Remote sensing Atmospheric measurements	18. Distribution Statement  Unclassified - Unlimited  Subject Category 35		
19. Security Classif. (of this report) Unclassified	20. Security Classif. (of this page) Unclassified	21. No. of Pages 267	22. Price A12

For sale by the National Technical Information Service, Springfield, Virginia 22161

NASA-Langley, 1982

